The Age-Metallicity-Velocity relation in the nearby disk

Borja Anguiano

Potsdam 2012

To my Father, my Galaxy

Leibniz Institute for Astrophysics Potsdam
Arbeitsgruppe "Milky Way and the Local Volume"

The Age-Metallicity-Velocity relation in the nearby disk

Dissertation
zur Erlangung des akademischen Grades
"doctor rerum naturalium"
(Dr. rer. nat.)
in der Wissenschaftsdisziplin "Astrophysik"
der Universität Potsdam

eingereicht an der
Mathematisch–Naturwissenschaftlichen Fakultät
der Universität Potsdam

von
Borja Anguiano
Corella (Navarra), Spanien

Potsdam, den 28. März 2012

Erstgutachter: Prof. Dr. Matthias Steinmetz
Betreuer: Prof. Dr. Matthias Steinmetz & Prof. Dr. Kenneth C. Freeman

Contents

List of Figures

List of Tables

Allgemeinverständliche Zusammenfassung

In der vorliegenden Arbeit wurden die Alters-Metallizitäts- und Alters-Geschwindigkeits-Beziehungen von der Sternen in der näheren Umgebung der Sonne untersucht. Dazu wurde, auf Grundlage der Sternkataloge des RAdial Velocity Experiments (RAVE) und der Genf-Kopenhagen-Himmelsdurchmusterung (GCS), eine sorgfältig definierte Auswahl von Unterriesensternen erstellt. Zur genaueren Bestimmung der Sterneigenschaften wurden alle Kandidaten mit dem Doppelstrahl-Spektrographen des ANU 2,3m Teleskops am Siding Spring Observatorium (Australien) nach beobachtet. Mit den Ergebnissen konnte die Stichprobe bereinigt und das Alter der Sterne mit großer Genauigkeit abgeschätzt werden. Insgesamt wurden dafür 1253 Spektren im Bereich von 3200 Å bis 6200 Å mit geringer Auflösung (R = 400) vermessen. Im Gegensatz zu Standardanalyseverfahren wurden die Spektren in dieser Studie flusskalibriert um sie dann mit einem empirischen Katalog von Sternspektren zu vergleichen und somit die wahrscheinlichsten Sternparameter zu erhalten. Dieser Ansatz stellt eine neue, vielfältig anwendbare Auswertungsmethode von Spektren niedriger Auflösung da. Für eine Untergruppe der Stichprobe konnten die ermittelten Parameter, effektive Temperatur $T_{\rm eff}$, Metallizität [m/H] und Oberflächengravitation $\log g$, mit denen des PASTEL Katalogs verglichen werden. Die Standardabweichungen betragen jeweils 145 K, 0,16 und 0,23 dex. Neben den oben genannten Parametern konnten für einen Großteil der Stichprobe auch die Häufigkeitsverhältnisse [Mg/Fe] und [Ca/Fe] bestimmt werden. Anhand ihrer Position im Hertzsprung-Russell-Diagramm konnte, mittels theoretischer Isochronen, auch das wahrscheinlichste Alter der Sterne ermittelt werden. Dabei wurden die Messfehler der Sternparameter als normalverteilt angenommen, ansonsten aber keinerlei Annahmen bezüglich der ursprünglichen Massenfunktion (IMF), der Verteilungfunktion von Metallen oder der Sternentstehungsrate getroffen. Es wird gezeigt, dass Unterriesenstern gut geeignet sind um das Alter der Milchstraße zu bestimmen und dass für circa 80% der Stichprobe ein mittlere Messunsicherheit von weniger als 1,5 Giga-Jahren erzielt werden konnte. Das so ermittelte Ensemble von Sternparameter wurde statistisch ausgewertet. Dabei zeigte sich, dass die Alters-Metallizitäts-Beziehung eine intrinsische Dispersion von 0,14 dex in den Metallhäufigkeiten aufweist. Dieser Wert um einen Faktor zwei kleiner als bisher in der Literatur veröffentlichte Werte. Die mittlere Metallizität weist als Funktion von abnehmenden Sternaltern, einen geringen, aber konstanten Anstieg auf. Für zur Dünnen Scheibe zugehörige Sterne lässt sich außerdem eine Korrelation des Sternalters und der Häufigkeit von α-Elementen zeigen: während Sterne mit einem Alter von etwa 5 Giga-Jahren einen, im Vergleich zur Sonne, nur leicht erhöhten Wert für [α/Fe] aufweisen ($\sim$ 0,02 dex), wurden bei den ältesten Sternen Werte um 0,1 dex gemessen. Diese Ergebnisse deuten auf einen geringeren Einfluß von Radialmigration in der Galaktischen Scheibe hin als vielfach in der Literatur angenommen. Eine Analyse der Metallizität-Geschwindigkeits-Beziehung der Stichprobe ergab, dass für

Sterne mit [m/H] im Bereich von -0,6 dex bis 0,2 dex, die drei Geschwindigkeitskomponenten U, V und W keinerlei Korrelation mit der Metallizität aufweisen. Für Sterne der Dünnen Scheibe ist auch die mittlere Rotationsgeschwindkeit um das Galaktische Zentrum nicht mit [m/H] korreliert. Die Geschwindigkeitsdispersion ist für Sterne mit [m/H] > -0,5 dex in etwa konstant, während sie für metallarme Sterne ([m/H] < -0,7 dex), mit abnehmender Metallhäufigkeit, in allen drei Geschwindigkeitskomponenten deutlich ansteigt. Eine solche Alters-Geschwindigkeitsdispersions-Beziehung legt nahe, dass das dynamische Aufheizen der Dünnen Scheibe überwiegend in den ersten drei Giga-Jahren stattfindet und dass die dafür verantwortlichen Prozesse bei einer Geschwindigkeitsdispersion von etwa 20 km s^{-1} stark an Effektivität verlieren. Ineffiziente Aufheizung der Sternpopulationen durch kurzlebige Spiralarme während der gesamten Lebensdauer der Milchstraße in Kombination mit einer effektiven Aufheizung durch massereiche Molekülwolken in ihrer Entstehungsphase könnte ein solches Verhalten hervorrufen. Zusätzlich wurde auch die Form des Geschwindigkeitsellipsoiden untersucht. Für Sterne der Dünnen Scheibe ergibt sich $\sigma_U : \sigma_V : \sigma_W \sim 1.0{:}0.7{:}0.5$ und für Sterne der Dicken Scheibe $\sigma_U : \sigma_V : \sigma_W \sim 1.0{:}1.0{:}0.7$. Anhand der Ergebnisse dieser Studie lassen sich Entstehungsszenarien für die Dicke Scheibe, wie, zum Beispiel durch die Akkretion einer Satellitengalaxie, nicht ausschließen.

Abstract

The age-metallicity and the age-velocity relation in the nearby Galactic disk is investigated using a sample of subgiants. The sample was carefully selected from the *RAdial Velocity Experiment (RAVE)* and the *Geneva-Copenhagen Survey (GCS)*. Further observations were needed to improve the stellar parameters in order to clean the sample and get accurate ages. We obtained a total of 1253 low resolution spectra from the Double Beam Spectrograph (DBS) on the ANU 2.3-m telescope in Siding Spring Observatory (Australia). The resolving power was 400, with a spectral range from 3200 to 6200 Å. We derive the stellar parameters via flux calibrated spectra using an empirical stellar library (MILES). This technique provides a widely applicable new method of deriving stellar parameters from low resolution spectrophotometry. A comparison between T_{eff}, [m/H] and log g derived in this work and those in a high-resolution catalogue (PASTEL) present a rms $\sim$ 145 K, 0.16 and 0.23 dex respectively. We also estimate [Mg/Fe] and [Ca/Fe] from spectrophotometry using the abundances ratios obtained in de Castro Milone et al. (2011) and Venn et al. (2004) as reference. We determine the age of stars via isochrones fitting. Adopting a Gaussian probability density for T_{eff}, log g and [m/H] centered at the measured values we determine the probability density distribution for the age. The procedure makes no assumption on the initial mass function, the metallicity distribution, or the star formation rate. We demostrate that subgiants are suitable for dating the Galaxy and we find that around 80% of the stars present a total relative error lower than 1.5 Gyr. We derive an age-metallicity relation with an intrinsic cosmic dispersion in metal abundances of 0.14 dex, a factor of two smaller than that found by Edvardsson et al. (1993), Nordström et al. (2004), Casagrande et al. (2011). The mean metallicity shows a slow, steady increase with time. We also find a relation between the α-elements and the age for the thin disk stars. Stars around 5.0 Gyr old present [α/Fe] slighly higher than solar ($\sim$ +0.02) while the oldest thin disk stars show values around +0.1 dex. For the thick disk stars we find values from +0.1 dex up to +0.3 dex in [α/Fe]. These results suggest a less need for radial migration in the Galactic disk. The metallicity-velocity relation shows that U, V and W velocities are independent of metallicity for a range between +0.2 and -0.6 dex. We also find that the mean rotational velocity is independent of the metallicity for the thin disk. Furthermore, the velocity dispersion remains roughly constant for a metallicity range from +0.2 to -0.5 dex. For metal-poor stars ([m/H] $<$ -0.7 dex) the velocity dispersion clearly increase for the three velocity components. The age-velocity dispersion relation shows that the heating for the thin disk take place for the first $\sim$ 3.0 Gyr, and then saturates when $\sigma_w \sim$ 20 km s^{-1}. This result is consistent with inefficient heating caused by scattering from tightly wound transient spiral structure and with the very efficient heating mechanism caused by the GMCs during the first 3.0 Gyr. We find an abrupt increase of the velocity dispersion for stars older than 10.0 Gyr. The shape of the velocity ellipsoid is also investigated. For the thin disk we find $\sigma_U : \sigma_V : \sigma_W \sim$ 1.0:0.7:0.5 and for the thick disk, $\sigma_U : \sigma_V : \sigma_W \sim$

1.0:1.0:0.7. Mechanisms of formation of the thick disk such as accretion events remain compatible with our findings.

Chapter 1

The Galactic disk

"It appears that δ Eri and possibly μ Her are not abnormal in composition or velocity. If they are older than anything else in the Galaxy, the simple relations [between age, velocity dispersion, and chemical composition] I proposed yesterday would have to be abandoned."

Martin Schwarzschild (1958)

1.1 Introduction

We have spent more than half a century trying to understand how the metallicity distribution and the space motions of the stars in the Galactic disk evolve with time. Despite the huge amount of effort done by the astronomical community in this aspect, the relation between chemical composition, kinematics and age is still controversial. In this chapter we make a review about what we (do not) know about the chemical and kinematical evolution of the Galactic disk in the solar vicinity. We also present very briefly the strategy we follow in this thesis to address the age-metallicity and age-velocity relation problem.

1.2 The formation of a galaxy disk in a cosmological context

It is commonly believed that all cosmic structure grew from small fluctuations generated at very early times in a flat Universe which today consists of 72% dark energy, 23.5% dark matter[1] and 4.5% ordinary baryons. The cosmic microwave background (CMB) sky shows

[1]Dark energy and dark matter are both a hypothetical form of energy and matter respectively. There are not direct observational evidences for their existence but we need them to explain that the Universe

that the Universe was very nearly uniform when it was only 0.4 Myr old (Bennett et al. (2011)). Today we know that gravity is the main driver in the formation and evolution of the structures we see in the present Universe but also complex and strongly nonlinear physical processes appear to play an important role. *Dark matter halos* are the basic nonlinear units. It is widely believed that these dark halos present a universal cusped density profile (Navarro et al. (1997)) in a simulated universe dominated by Cold Dark Matter, the so called ΛCDM cosmology. Simple models for disk formation show that the angular momentum predicted for collapsing dark halos is sufficient for them to create a disk population (Steinmetz & Muller (1995), Mo et al. (1998)). However, direct simulations have been struggling to confirm this picture (Navarro & Benz (1991), Klypin et al. (2002)). New generations of simulations have improved the numerical resolution and have introduced better implementations of feedback, presumably from stellar winds and supernovae (Scannapieco et al. (2008)). Note also that in ΛCDM context, 95% of dark haloes with final, present-day mass of 10^{12} $M_{\odot}$ experienced a merger with a satellite of mass 5 $\times 10^{10}$ $M_{\odot}$ (Stewart et al. (2008)). Despite this, no cosmological simulation has so far been able to produce a present-day disk galaxy with a bulge-to-disk mass ratio much less than one in a proper ΛCDM context and such galaxies are common in the real Universe; our own Galaxy is a good example (see White (2009) and Wyse (2009b) for more details). Recently, Guedes et al. (2011) claim that using a new cosmological N-body/smooth particle hydrodynamic simulation of extreme dynamic range found that a close analog of a Milky Way disk galaxy arises naturally.

From the observational point of view, new techniques like integral field near-infrared spectrographs fed by adaptive optics are providing unprecedented views of gas motion within galaxies at redshift z = 2 - 3, when the Universe showed a peak rate forming stars. These galaxies show a complex picture in kinematics, with inflows, rotation within extended and nearly always thick disks, mergers, and galaxy-wide outflows (see Pettini (2009) and Genzel (2009) for more details).

1.3 Disk dichotomy: the thin and thick Galactic disk

The Milky Way is a spiral galaxy and the Galaxy has several recognizable structural components that probably appeared at different stages in the galaxy formation process. We describe here very briefly two of the main Galactic components: the thin and the thick disk.

The *thin disk* is still forming stars and its oldest stars are around 10 Gyr old (Wyse (2009a)). The thin disk is believed to be the end product of the quiescent dissipation of most of the baryons and contains almost all of the baryonic angular momentum

is expanding at an accelerating rate, the rotation curve of spiral galaxies and the time scales in galaxy formation and an amount of other indirect observational evidences. Understanding the *genesis* of this energy and matter respectively is one the most important challenges of our days.

(Freeman & Bland-Hawthorn (2002)). The exponential thin disk presents a vertical scale height of about 300 pc (Chang et al. (2011)). The younger stars of the disk show a radial abundance gradient of about -0.06 dex kpc^{-1} (Luck et al. (2006), Lemasle et al. (2008)). In the outer disk, for the older stars, the abundance gradient appears to be even stronger (-0.5 dex kpc^{-1}). The radial abundance gradient in the Galaxy flattens for R > 12 kpc at an [Fe/H] value of $\sim$ -0.5 (Carney et al. (2005)).

Many studies have attempted to chart the spiral arm pattern of the Milky Way in several tracers. Many of them follow a 4-armed spiral pattern, while others only using 2 arms (see Englmaier et al. (2011) and references therein). Nakanishi & Sofue (2006) recovered the 3D distribution of the molecular gas in the Milky Way, the area beyond the Galactic centre was excluded. The face-on view is compatible with a 4-armed spiral pattern.

The *thick disk* may be one of the most significant components for studying signatures of galaxy formation because it presents a snap-frozen relic of the state of the (heated) early disk. The thick disk in the Milky Way was discovered by Gilmore & Reid (1983); its scale height is still uncertain but is probably about 1000 pc. Its stars are older than 10 Gyr and are significantly more metal poor than the stars of the thin disk. It also rotates slower than the thin disk and their stars present a higher velocity dispersion (Wyse (2009a)). Most thick disk stars have metallicity values between about -0.5 dex and -1.0 dex and are enhanced in α-elements relative to Fe (e.g. Gratton et al. (1996), Bensby et al. (2007), Fuhrmann (2008)). Recently, Navarro et al. (2011) show that when the abundances of Fe, α elements and the r-process element Eu are considered together, stars separate neatly into two groups that delineate the traditional thin and thick disk components of the Milky Way. The formation of the thick disk is an open question. The thick disk is a very significant component for studying Galaxy formation, because it presents a kinematically and chemically recognizable relic of the early Galaxy. Several formation mechanisms have been proposed (see Freeman (2011) for more details). In the last chapter of this thesis we discuss these mechanisms together with our findings. The existence of the thick disk is well accepted in the astronomical community, but recently Bovy et al. (2011) claim that the bimodal distribution in α-elements associated with the thin and thick disk is an artifact of selection effects on the data sets.

One the main goal of this thesis is to address how the metallicity distribution and the stellar velocity dispersions in the disk have evolved with time. In the next sections we will see that these basic observational constraints on the properties of the Galactic disk are still uncertain due to the difficulty of measuring ages for individual stars.

1.4 Chemical evolution of the Galactic disk

Stellar abundances as functions of age, the called age-metallicity relation (AMR), is the fossil record of the chemical evolution and enrichment history of the disk. The AMR is an important observational constraints on models of the evolution of the Galaxy. It shows how

stellar formation has enriched in the interstellar medium (ISM) over time. This relation depends on the star formation rate, the chemical yields, the efficiency of recycling, gas infall and outflow and the amount of mixing in the gas. Due to this continuing enrichment, one might expect to find that old stars are likely to be more metal-poor than younger stars. However, the AMR in the Milky Way disk is still not well known. There are several studies and one can find remarkable disagreement between them.

One of the first studies on the AMR was made by Twarog (1980). This work presents an AMR in the solar neighborhood derived from four-colors and Hβ photometry of 329 southern F dwarfs. For the age determination theoretical isochrones were used. He found that the metallicity increases from -1.0 dex at 13 Gyr to -0.03 dex at the age of the Sun ($\sim$ 4.5 Gyr) and to +0.1 dex for stars forming now. This sample shows a smooth increasing relation with an average scatter of 0.12 dex. The sample from Twarog was reanalyzed subsequently by two different groups. Carlberg et al. (1985) have found a very flat AMR, probably because they have cut from the sample all stars with metallicities lower than -0.5 dex. On the other hand, Meusinger et al. (1991) used updated isochrones and a metallicity calibration and found an AMR very similar to that of Twarog. Nissen et al. (1985) using spectroscopy metallicities for 29 F dwarfs, found a higher scatter in the AMR.

One of the most significant works on the relation between abundances and ages was done by Edvardsson et al. (1993). They analyzed high-resolution spectroscopic of 189 carefully selected disk stars. They measured very accurate spectroscopic abundances (Δ[X/Fe] $\sim$ 0.05 dex) and the ages were computed via isochrones fitting. Edvardsson et al. (1993) found that the slope of [Fe/H] vs age over the the life time of the disk is very flat with a large scatter in metallicity at all ages. This scatter ($\sigma_{[Fe/H]} = 0.21$ dex) for star with ages < 10 Gyr has not been clearly demonstrated for field stars before, but is known for open clusters (Friel et al. 2002). This result casts doubts about the real meaning of the age-metallicity relation. If the scatter is real it is difficult to explain without breaking some of assumptions that Galactic chemical evolution models usually make. Ng & Bertelli (1998) computed new ages for the stars from the Edvardsson et al. (1993) data set using updated isochrones, and the dispersion in metallicity was reduced. Garnett & Kobulnicky (2000) studied the Edvardsson et al. (1993) sample as function of distance. Stars closer than 30 pc presented an AMR with considerable scatter while stars between 30 and 80 pc present an strong correlation between metallicity and age.

Subsequent investigations by Feltzing et al. (2001) and Ibukiyama & Arimoto (2002) find similar conclusions to Edvardsson et al. (1993). Feltzing et al. (2001) use 5828 dwarf and sub-dwarf stars from the Hipparcos Catalogue (stars with a relative error in the parallax less than 25% and $M_V < 4.4$). They derive stellar ages from evolutionary tracks and metallicities from Strömgren photometry. The main impressions from their AMR are the large spread both in age and metallicity. They found a pronounced structure around 2 Gyr and stars that are metal-rich, i.e. [Fe/H] > 0.0, and old (t > 10 Gyr). If this result is real, it indicates that the star formation history (SFH) of the disk has been complex with regions that reached a high metallicity in a short time. Ibukiyama & Arimoto (2002)

derive an AMR for 1658 solar neighbourhood stars (1382 thin disk stars, 229 thick disk stars and 47 halo stars, according to their orbital parameters) with accurate distance from Hipparcos. They present large errors in metallicity due to inhomogeneous data taken from different authors. The thin disk AMR has a considerable scatter, larger than expected from observational errors. The mean metallicity is almost constant from 1 to 14 Gyr. The scatter decreases towards younger stars. Ibukiyama & Arimoto (2002) compared their results with the AMR of Edvardsson et al. (1993) for the thin disk. For stars younger than 10 Gyr they found a similar pattern. For the stars older than 10 Gyr, the AMR includes more metal rich stars than that of Edvardsson et al. (1993), although the parameters of these old stars have larger errors. For the thick disk AMR, Ibukiyama & Arimoto (2002) found that the average age of thick disk stars is around 8.0 Gyr, the mean metallicity is <[Fe/H]> = -0.5 and the scatter is larger than that for a thin disk. All these studies determined the stellar ages using isochrones.

Rocha-Pinto et al. (2000a) used chromospheric emission with a new metallicity dependent chromospheric activity-age relation (Rocha-Pinto & Maciel 1998) to estimate the ages of 525 nearby dwarfs. They estimated the metallicities from *uvby* data. Rocha-Pinto et al. (2000a) derive an AMR which shows similar mean trend found by previous studies but the intrinsic cosmic dispersion in metal abundances is around 0.13 dex, a factor of two smaller than that found by Edvardsson et al. (1993). They found an average [Fe/H] = -0.48 dex at around 13.5 Gyr. This metallicity is higher than the corresponding values found by Twarog (1980) and Edvardsson et al. (1993), and would indicate significant pre-enrichment of the gas before the formation of the first stars in the disk. The metallicity dispersion in this work suggests that the ISM has been enrichment in an homogeneous way by metals ejected from evolving stars. This evolution picture is also in good agreement with Twarog (1980) and Meusinger et al. (1991) but does not explain the huge dispersion found in Edvardsson et al. (1993).

A recent contribution on this problem is *The Geneva-Copenhagen survey of the Solar neighbourhood* (see Nordström et al. (2004), Holmberg et al. (2007), Holmberg et al. (2009), Casagrande et al. (2011)). They present determinations of metallicity (Strömgren *uvbyβ* photometry), rotation, age, kinematics and Galactic orbits for a complete, magnitude-limited and kinematically unbiased sample of 16682 F and G dwarfs stars from Hipparcos catalogue. Despite all the re-analysis on the stellar parameters determination done by Holmberg et al. (2007), Holmberg et al. (2009) and Casagrande et al. (2011) the AMR from this survey shows little variation in mean metallicity with a broad dispersion for a given age.

Haywood (2006) reviews the uncertainties in the AMR. He shows that recent studies of AMR from Strömgren photometric surveys are dominated by noise due to systematic biases in metallicities and effective temperatures. He evaluated these biases and present a new AMR. This AMR shows that ages less than 3.0 Gyr, the dispersion in metallicity is about 0.1 dex which, having in mind the uncertainties in the derived metallicities, is compatible with the small cosmic dispersion measured in ISM. He found that populations

become progressively older and more metal-rich ([Fe/H] > +0.0 dex at ages greater than 5.0 Gyr). He also confirmed an AMR in the thick disk. He concluded that this new picture of the solar neighbourhood presents dynamical effects and complexity of the age-metallicity distribution, rather than a general view of high metallicity dispersion at all ages. However, Soubiran et al. (2008) present an AMR where there is no young star with a metallicity lower than -0.32, and no old star with a metallicity higher than -0.13, contrary to common findings in samples of dwarfs, as for instance in Feltzing et al. (2001), Nordström et al. (2004), Casagrande et al. (2011). Soubiran et al. (2008) concluded that this results is an important property of their sample, because the existence of old, metal-rich stars is often mentioned to explain the large dispersion of the AMR (Haywood (2006)).

One could conclude from here that the AMR is still controversial, mainly because to get precise stellar ages for the field stars is difficult (see chapter 4). The shape of the AMR is a fundamental constraint on the chemo-dinamical evolution models (see chapter 5 for more details).

1.5 The kinematical evolution of the Galactic disk

Another tool to study the evolution of the Galaxy is the space motions of the stars as a function of age. It lets us probe the dynamical evolution of the disk. The age-velocity diagrams reflect the slow increase of the random velocities with age due to the heating of the disk by massive objects such as spiral arms or giant molecular clouds. These kinds of studies are fundamental to understand the local dynamics of the disk. However, there is not yet agreement on the observational properties of the age-velocity relation (AVR). Also, the main responsible mechanism for the heating of the disk is not yet understood, and this comes mainly from the disagreement between the observed dispersion from several authors.

Roman (1950) was one of the first, more than half a century ago, to discovered the connection between the kinematics and chemistry of stars. Wielen (1977) found that the stellar velocity dispersion increases steadily for all time, $\sigma \sim t^{0.25-0.55}$. Another view (e.g. Stromgren (1987), Quillen & Garnett (2001), Soubiran et al. (2008)) is that the heating takes place for the first 2.0 - 3.0 Gyr, but then saturates when σ_W reaches 20 km/s, because the stars of higher velocity dispersion spend most of their orbital time away from the Galactic plane where the sources of heating lie. A jump is apparent for stars with ages > 9 Gyr which is generally interpreted to be the signature of the thick disk. Recently, Casagrande et al. (2011), using improved astrophysical parameters for the Geneva-Copenhagen Survey found a picture in which the disk has undergone continual heating over the past ∼ 10 Gyr. Several disk heating mechanisms have been proposed; massive perturbers of the disk from the Galactic halo (Wielen (1977)), molecular clouds (Lacey 1984), transient spiral arms (e.g. Sellwood & Carlberg (1984), Binney & Lacey (1988)), the resonance overlap of multiple spiral patterns (Minchev & Quillen 2006), disrupting

satellite galaxies (Toth & Ostriker (1992), Velazquez & White (1999), Villalobos & Helmi (2008), House et al. (2011)). The role of the different mechanisms are not yet completely well understood, mainly due to the discrepancies in the AVR mentioned above. See chapter 5 for a further discussion.

1.6 The Age-Metallicity-Velocity Relation project

As described above, previous studies have found a diverse range of chemical and kinematical relations with stellar ages for the Galactic disk. The discrepancies are the main motivation for this thesis. How the nearby disk stars have evolved with time over the past 10 Gyr remains a crucial open question. Very likely much of the difference in view goes back to the difficulty of measuring stellar ages and it is in this point where we aimed to we improve over the earlier work.

The new generation of spectroscopy surveys bring new opportunities to understand the formation and evolution of the Galaxy through their stellar components. One of the most important surveys in our days is the RAdial Velocity Experiment (RAVE)[2]. The survey is conducted in the Ca-triplet region and provides accurate radial velocities, cross-matched proper motions, stellar atmosphere parameters and distances for hundreds of thousand stars (Steinmetz et al. (2006), Zwitter et al. (2008), Siebert et al. (2011), Boeche et al. (2011)). In this thesis we present a new derivation of the AMR and AVR using carefully selected *subgiant stars* from RAVE and Geneva-Copenhagen survey. Subgiants are suitable stars for dating the Galaxy as the isochrones separate well in the M_V/log g - log T_{eff} plane, enabling accurate stellar age determination. From the RAVE survey we have selected about 2000 subgiants candidates using a first estimate of stellar parameters and $\sim$ 500 single star subgiants from the Geneva-Copenhagen survey. Further observations were needed to improve the stellar parameters in order to clean the sample and get accurate ages. We obtained 1253 low resolution spectra from the Double Beam Spectrograph (DBS) on the ANU 2.3-m telescope in Siding Spring Observatory (Australia). The resolving power was 400, with a spectral range from 3200 to 6200 Å. Spectroscopy observations and data reduction techniques can provide accurate values for gravity through comparison of low resolution spectra with recent grids of synthetic flux spectra (Bessell 2007). We derived the stellar parameters via chi-squared statistic using synthetic model atmospheres (Munari et al. 2005) and empirical stellar libraries (Sánchez-Blázquez et al. 2006). This technique provides a widely applicable new method of deriving stellar parameters from low resolution spectrophotometry. Stellar ages are crucial to place the observed chemical and kinematical properties in an evolutionary context. The most common method for deriving ages of stars is via isochrones, however not all stars can be dated in this way. Moreover, we find in this thesis remarkable differences between different authors and techniques. To derive the age of our subgiants we use the log g - T_{eff} plane. 10% error in parallax or 0.1 dex in log g

[2]http://www.rave-survey.aip.de/rave/

correspond to 2.0 Gyr in age uncertainty. For the older stars the error in age could be up to 3.0 Gyr (Thorén et al. 2004).

This thesis is organized as follows: The AMR and AVR problem together with the main goal of this thesis is described in detail in this chapter. Sample definition, observations and data reduction is described in the second chapter. In chapter 3, we investigate the determination of the fundamental stellar parameters via flux calibrated spectra. In chapter 4, we attempt to explore the value of subgiants for dating the Galaxy, we also compare different methods and techniques for the determination of the age of stars. In chapter 5, the AMR and AVR are presented together with a discussion of its interpretation. The last chapter presents a brief summary of the present thesis and future work.

Chapter 2

Sample definition, observations and data reduction

2.1 Introduction

In this chapter we describe the data selection from the RAVE and Geneva-Copenhagen Survey. We also describe the data acquisition with the DBS instrument in the ANU 2.3 m telescope in Siding Spring Observatory. Data reduction, flux calibration and independent check on the flux calibration using DDO bands is also discussed.

2.2 Sample definition

Subgiants are suitable stars for dating the Galaxy as the isochrones separate well in the M_V/log g - log T_{eff} plane. The age of the individual stars are probably the main source of error together with bias in the selection sample in the discrepancies commented in the previous chapter. From the RAVE survey we have selected around 2000 subgiant candidates using a first estimate of stellar parameters and around 400 non-binaries subgiants from the Geneva-Copenhagen survey in the M_V - T_{eff} plane.

2.2.1 Geneva-Copenhagen Survey (GCS)

The Geneva-Copenhagen survey of the solar neighborhood present new determinations of metallicity, rotation, age, kinematics, and Galactic orbits for a complete, magnitude-limited, and kinematically unbiased sample of 16682 nearby F and G dwarf stars. Accurate radial-velocity observations for nearly 13500 stars allow identification of most of

the binary stars in the sample and, together with published *uvbyβ* photometry, Hipparcos parallaxes, Tycho-2 proper motions, and a few earlier radial velocities, complete the kinematic information for 14139 stars Nordström et al. (2004). Recently, Holmberg et al. (2007) re-examined and verified the temperature, metallicity, distance, and reddening calibrations for the *uvbyβ* system using V-K photometry, angular diameters, high-resolution spectroscopy and Hipparcos parallaxes.

We have selected a sample of subgiants according to the following criteria:

$3.69 < \log T_{eff} < 3.76$

$M_V < 5.0$

M_V = -31.25 log T_{eff} + 121.66 (avoid MS)

We also selected non-binaries and stars with negative declination. A total of 404 stars (no binaries) were selected according to our selection criteria. For these stars we know Hipparcos parallaxes and accurate kinematics (Nordström et al. (2004), Holmberg et al. (2007)).

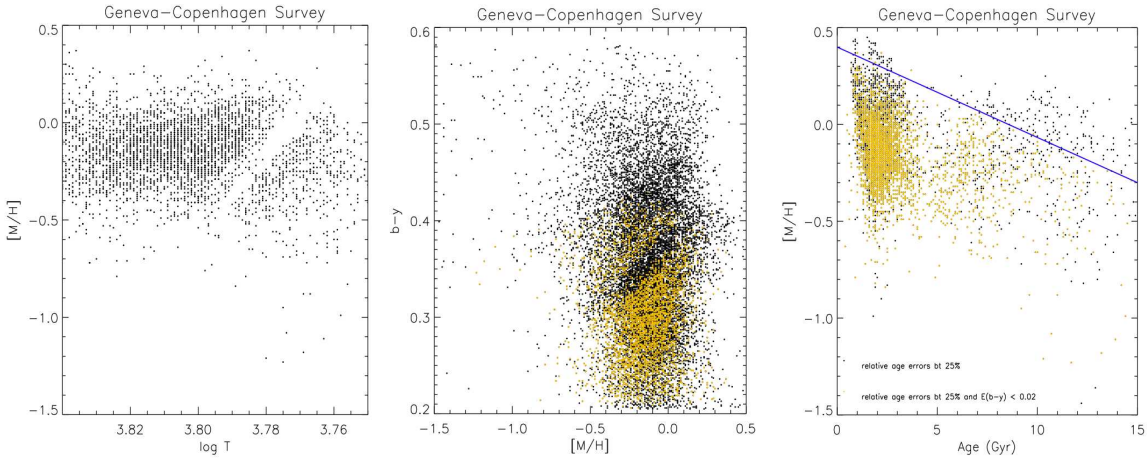

Figure 2.1: Temperature-metallicity, color-metallicity and age-metallicity relation. The left panel shows a clear gap in the log T - [m/H] diagram after selecting stars with E(b-y) < 0.02. Middle: the color-metallicity diagram shows the whole catalogue (black dots) and the stars with E(b-y) < 0.02 (yellow dots). The gap is evident after the reddening cut. The right panel shows the AMR for stars with an age error < 25% (black dots) and stars with age error < 25% and E(b-y) < 0.02 (yellow dots). The reddening cut excludes systematically old and metal-rich stars. The blue line emphasizes the exclusion.

During the selection processes we found systematic effects in the GCS catalogue that affect these data this data. Fig. 2.1 show how the cuts in reddening and the errors in the age could modify the shape of the age-metallicity relation excluding, systematically, old metal-rich stars. We also find a clear "gap" in the stellar parameters space. This effect

could be driven by the new *uvby* calibrations introduced by Holmberg et al. (2007) in the GCS.

2.2.2 The RAdial Velocity Experiment (RAVE)

The RAdial Velocity Experiment (RAVE) is a large southern hemisphere spectroscopy Galactic survey. RAVE uses the 6dF multi-fiber spectroscopic facility at the UK Schmidt telescope of the Anglo-Australian Observatory in Siding Spring, Australia. RAVE is a magnitude limited spectroscopic survey in the range $9 < I < 13$ working on the wavelength range of 8410 to 8795 Angstrom at a resolution of R = 7500. To date, RAVE has collected more than 520,000 spectra. For more details see Steinmetz et al. (2006), Zwitter et al. (2008) and Siebert et al. (2011).

We have selected a sample of sub-giants according to the following criteria:

$9.0 < I < 12.0$ (RAVE input)

$3.5 < \log g < 4.1$

$3.69 < \log T_{eff} < 3.75$

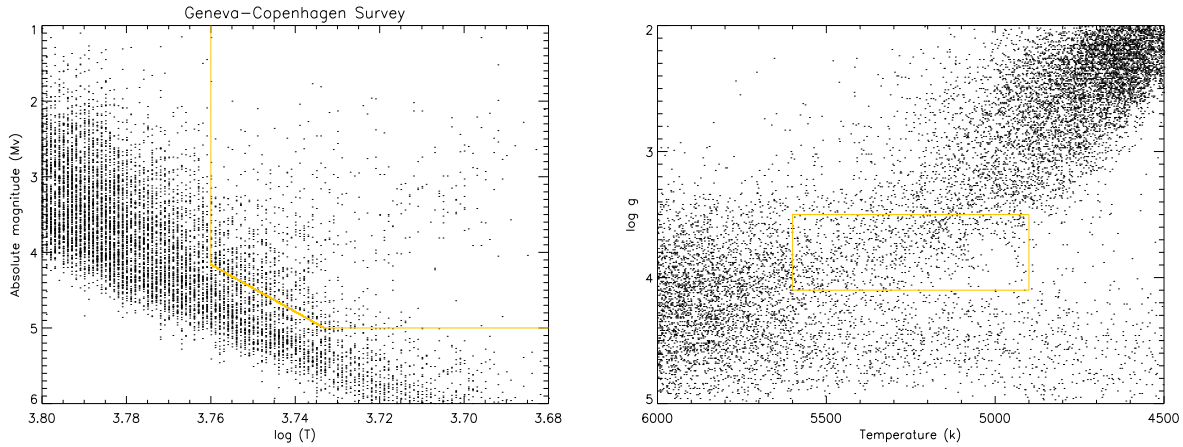

Figure 2.2: On the left the absolute magnitude-temperature plane from the GCS. The yellow are indicate the selected stars. On the right the log g - temperature plane from the RAVE survey, again the yellow area indicate the selected subgiants.

We have selected around 2000 stars with accurate radial velocities, proper motions and first estimate of stellar parameters (Steinmetz et al. (2006), Zwitter et al. (2008)).

2.3 Observations

Optical spectra of 1262 subgiants candidates were taken with the Dual-Beam Spectrograph (DBS) in the ANU 2.3 m telescope at Siding Spring Observatory (SSO) during a three years period from 2007 to 2010.

2.3.1 Siding Spring Observatory

SSO is Australia's premier facility for optical and infrared astronomy. The observatory is part of the Research School of Astronomy & Astrophysics (RSAA) at the Australian National University (ANU). The observatory is situated 1165 meters above sea level in the Warrumbungle National Park, near Coonabarabran in the central west region of New South Wales, Australia. The latitude and longitude of the site are: 31°16′24″S and 149°03′52″E.

The site conditions of the observatory show little seasonal variation, with an average of 2110 hours (64%) useable throughout the year[1]. Wood et al. (1995) using a differential image motion monitor (DIMM) measurements showed that the most common free air seeing value at SSO is 1.2″. They found the best seeing was about 0.6″ for a brief interval of a few hours (See Fig. 2.3). Recently measurements from the AAT in an interval of time of 5 years show that 68% of the time, the seeing is less than 1.75″ (Keller et al. (2007)).

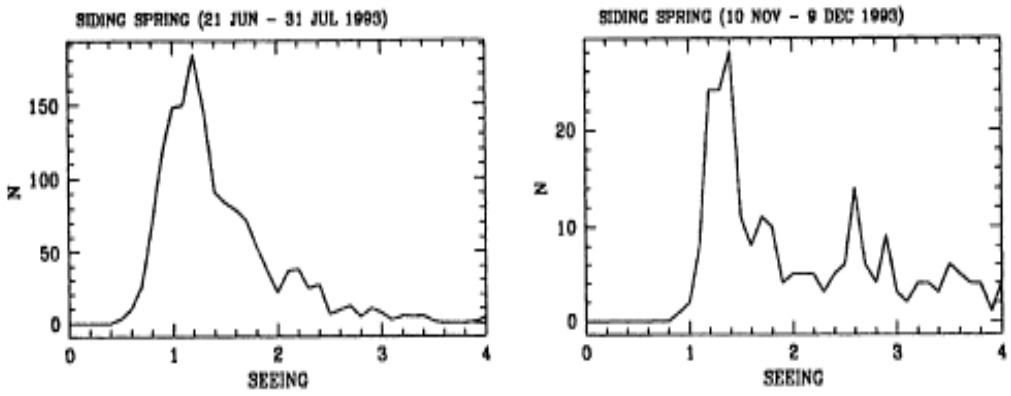

Figure 2.3: Histograms of seeing measures in arcsec at Siding Spring for the dates indicated Wood et al. (1995). There is clearly a peak around 1.2″.

Payne (1985) used a series of selected standard stars at different air masses to measure the atmospheric extinction of the site. The extinction in the U and B band is -0.19 and

[1]Data from the weather logs of the Anglo-Australian Telescope (AAT) from 2000-2005 Keller et al. (2007)

-0.31 mag per airmass. Payne (1985) measured also the sky brightness of the site using the contribution due to the background taking readings offset either side of each standard. In Fig. 2.4 we can see the atmospheric extinction results and the raw sky V-band night brightness for the site.

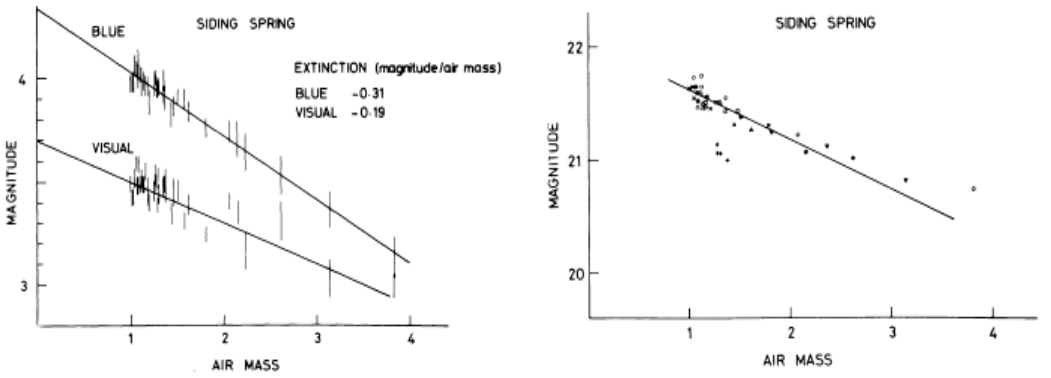

Figure 2.4: On the left the behaviour of the extinction in the B and V bands at Siding Spring on the 26.05.1985. On the right the raw V-band night sky brightness plotted against air mass in magnitudes per arcsec^2 due to the background stars, zodiacal light and the airglow (Payne (1985)).

SSO has several telescopes including the 2.3m Advanced Technology Telescope, the 3.9m Anglo-Australian Telescope, 2m Faulkes Telescope, the 1.24m UK Schmidt Telescope, two Boller & Chivens Cassegrains 1m and 0.6m along with the 0.5m Automatic Patrol Telescope, 0.6m Uppsala Schmidt Telescope and a 1.35m survey telescope called SkyMapper.

2.3.2 ANU 2.3 m telescope

The ANU 2.3 m telescope also called the Advanced Technology Telescope is a 2.3 meters aperture telescope with altitude-azimuth mounting and rotating building. It was constructed by the Australian National University (ANU) in the early 1980's at SSO. The telescope has an f/2.05 paraboloidal primary and f/7.85 Cassegrain secondary mirror. This configuration provides fields of 6.62 arcmin at two Nasmyth foci and a Cassegrain focus (Rodgers et al. (1988)). In Table 2.1 we summarize some properties of the primary and the secondary mirrors.

At present there are three instrument available in the telescope, the Wide Field Spectrograph (WiFeS), Imager and Echelle. There are also three decommissioned instruments, the Double Beam Spectrograph (DBS), the Cryogenic Array Spectrometer/Imager (CASPIR) and the Tiptilt Infrared Secondary. All the data in this research project comes from the DBS instrument.

Primary	Secondary
2.3 m, f/2.05 primary mirror	0.3 m, f/7.85 secondary for Nasmyth
4715 mm focal length	18056 mm focal length
2300 mm outside diameter	Plate scale : 4.964 arcsec/mm
500 mm diameter central hole	80 mm diameter (6.62″) unvignetted field of view
3.973 m^2 collecting area	0.3 m, f/7.85 tip-tilt secondary for Cassegrain (18056 mm focal length)

Table 2.1: Some specifications for the ANU 2.3 m telescope.

2.3.3 The Double Beam Spectrograph (DBS)

The Dual-Beam Spectrograph is an optical spectrograph, it was mounted at the Nasmyth A focus of the ANU 2.3 m telescope. The visible waveband ranges from 3200 Å to 9000 Å. It is split by a dichroic at around 6000 Å and feeds two essentially similar spectrographs, with red and blue optimized detectors respectively. The full slit length is 6.7 arcmin and gratings are available with rulings of 158 to 1200 line per mm, giving dispersions of between 4 and 0.6 Å/pixel. In Table 2.2 we present some characteristic of the instrument.

Telescope scale	5.02″/mm
Unvignetted field telescope + slit	80 mm = 6.7′
Collimator focal length	2812 mm
Camera focal length	232 mm
Beam	152 mm
Imaging scale	1″/mm
Across dispersion	0.015 pixel = 0.91″

Table 2.2: Some numbers for the Dual-Beam Spectrograph.

The spectral range could be as large as the CCD detector's quantum response. The double spectrograph uses a different type of CCD detector in each arm; each CCD is optimized according with the quantum response for their particular wavelength coverage, hence the DBS is a versatile intermediate-resolution spectrograph with maximum versatility in the choice of resolution and with maximum efficiency over the wavelength range available.

2.3.4 Observation strategy and data acquisition

For our observations we use the blue arm of the DBS instrument mounted in the ANU 2.3 m telescope with a long slit of 5″ width and the 300B grating, giving a spectral resolution of $R = \lambda/\Delta\lambda \sim 400$. The recorded spectra cover the wavelength range from 3200 Å to 6200 Å. The second order contribution to the red end of the wavelength band 3200-6200 Å is negligible. Observations consist of a sequence of target exposure, standard stars,

calibration lamps, flats and bias. An important goal of the project is to get a good relative flux calibration.

The angle of the slit on the sky is an important issue. Stars away from the zenith are affected by differential refraction, i.e. a variation of the angle of refraction of a light ray as a function of its wavelength cause by the Earth's atmosphere. Note that when observing away from the zenith, atmospheric dispersion is inevitable. To correct this effect we placed the slit parallel to the direction of atmosphere dispersion, i.e aligning the slit at the parallactic angle. In this way we avoid to record incorrect intensities as a function of wavelength that could spoil our flux calibration.

During the observational campaign we used a wide slit of 5″. A wide slit assures that 100% of the star light is collected (the seeing is worse at the UV end than at the red end, and we did not want to lose UV light relative to red light because of worse seeing at the UV end) and mitigates tracking problems and differential refraction that could affect the calibration.

We have collected standard stars with the same instrumental setup including the slit width every night. We have observed the same standard stars covering a big range of airmass during the same night, allowing us to control the atmosphere extinction in the observed spectra. Tab. 2.3 lists the optical spectrophotometry standard stars from the Oke (1990) and Hamuy et al. (1994) catalogues used for our observations.

Star name	RA (h m s)	DEC (d ' ")	V mag	Spec. type
LTT7987	20 10 57.38	-30 13 01.2	12.23	DA
LTT1020	01 54 49.68	-27 28 29.7	11.52	G
EG21	03 10 30.98	-68 36 02.2	11.38	DA
LTT3864	10 32 13.90	-35 37 42.4	12.17	F
LTT1788	03 48 22.17	-39 08 33.6	13.16	F
EG274	16 23 33.75	-39 13 47.5	11.03	DA
Feige110	23 19 58.39	-05 09 55.8	11.82	DOp

Table 2.3: A few standard stars that have been used in the observations. Data from Oke (1990) and Hamuy (1992, 1994) catalogues.

The stars selected from the GCS cover magnitudes $5 < m_V < 10$. The stars in the RAVE survey have a range in the I band from 9 to 12 magnitudes. In order to get a very high signal-to-noise (S/N $>$ 100) for the whole sample, we have used different exposure times for the different stars. The exposures run from seconds to a few hundred seconds depending on the visual magnitude of the star. The "CCD equation" (Mortara & Fowler (1981)) shows the S/N of a measurement made with a CCD.

$$\frac{S}{N} = \frac{N_P}{\sqrt{N_P + n_{pix}(N_S + N_D + N_R^2)}} \tag{2.1}$$

where N_P is the signal term and is the number of photons collected from the object. The noise terms are the $\sqrt{N}$ plus n_{pix} (number of pixels under consideration for the S/N) time N_S (the total number of photons per pixel from the background or sky), N_D (total number of dark current electrons per pixel), and N_R^2 (total number of electrons per pixel resulting from the read noise). For bright sources, as the case of our objects, we could simplify the equation above. For bright objects the S/N errors are dominated by the source itself, which means that the total noise $\sqrt{N_P + n_{pix}(N_S + N_D + N_R^2)}$ is controlled by the first noise term, N_P. The CCD equation becomes

$$\frac{S}{N} \sim \frac{N}{\sqrt{N}} = \sqrt{N} \tag{2.2}$$

thus, the signal to noise is similar to the Poisson error which includes the photon noise from the source itself.

How does the integration time control the S/N of our observed object? Strictly speaking N_P is really N $\times$ t, where N is the count rate in electrons per second for the photons from the observed object i.e., $N_P \times$ G (gain of the CCD in electrons/ADU) and t is the CCD integration time. We can write the following,

$$\frac{S}{N} = \frac{Nt}{\sqrt{Nt + n_{pix}(N_S t + N_D t + N_R^2)}} \tag{2.3}$$

where the integration time is also implicit in the noise quantities. We get an important relation for S/N,

$$\frac{S}{N} \sim \sqrt{Nt} \tag{2.4}$$

thus the S/N is proportional to the squared root of the integration time. Solving Eq. 2.3 for t we find

$$t = \frac{-B + \sqrt{B^2 - 4AC}}{2A} \tag{2.5}$$

where

$$A = N^2; B = -(S/N)^2(N + n_{pix}(N_S + N_D)); C = -(S/N)^2 n_{pix} N_R^2 \tag{2.6}$$

These expressions above allow us to compute roughly the S/N of our observed objects. Standard objects are fainter than program stars (V $\sim$ 12), to get a good S/N these stars present exposure times of a few minutes.

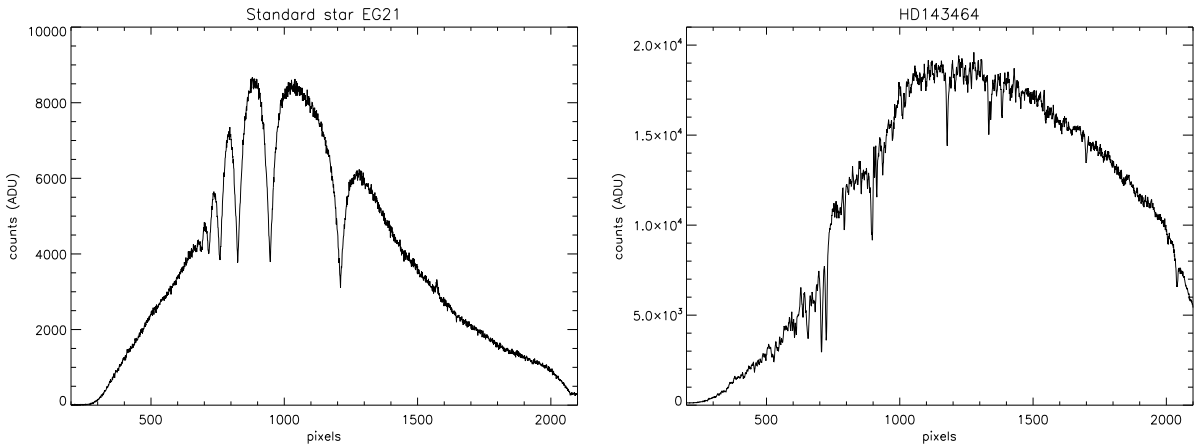

Figure 2.5: Counts per pixel for a standard and a program star respectively. For EG21 the peak of the light distribution in the wavelength range of work is around 9000 ADUs while for HD143464 is almost 20000 ADUs.

In Fig. 2.5 we show two raw spectra: EG21[2] is a standard star and HD143464 a program star. Our program stars cover a small range in temperature, from 4900 K to 6000 K (G spectral type stars). According to *Wien's displacement law*, there is an inverse relationship between the wavelength of the peak of the emission of a black body and its temperature when expressed as a function of wavelength.

$$\lambda_{max} = \frac{b}{T} \tag{2.7}$$

in the above equation λ_{max} is the peak wavelength, T is the absolute temperature of the blackbody, and b is a constant of proportionality called Wien's displacement constant, equal to 2.897×10^6 nm K. Hence the peak of the emission of our stars is around 5500 Å. For this wavelength a typical value for the signal-to-noise is S/N $\sim$ 130 and we have a S/N $\sim$ 80 for the Ca II H & K region around 3950 Å.

Spectra for a total of 1262 program stars has been collected. The *seeing* of the night is not a constant factor, in fact the final resolution of the spectra is controlled by the atmosphere conditions of the site. This effect is stronger when using a wide slit. In the next chapter we explain a new method we have developed to control the resolution of every single spectrum using the Power Spectrum in the Fourier space. Control the resolution allow us to degrade the stellar models to the exact resolution of the observed spectrum.

Finally a CuHe arc lamp was used for the wavelength calibration of the observed stars.

[2]During the observation time at the ANU 2.3 m telescope Prof. Ken Freeman called "the spider" to this kind of white dwarfs due to the very broad hydrogen lines. The broad lines remind him of the Huntsman's legs, a very common spider in Australia

There are plenty of emission lines in this arc lamp covering the wavelength range 3200 - 6200 Å. We took a couple of arc lamp spectra at the beginning and at the end of the run. Five bias and five flat fields (for the flat field we use the projection of a lamp on a screen: we needed to saturate the red part in order to get a good level of counts in the blue. That means we have two sets of flat fields, one for the blue and one for the red) have also been taken in the beginning and at the end of every single night for data reduction purposes.

2.4 Data reduction

A CCD image reduction uses a basic set of images that form the core of the reduction process. Our basic set of images consists of two calibration frames -bias and flat field- and the spectra of the objects. While performing the data reduction we have to keep in mind that bias subtraction and flat-fielding could add noise to the data. As an equation, the reduction process can be expressed as

$$Reduced = \frac{Object - Bias}{Flat - Bias} \tag{2.8}$$

For reduction purposes we use *IRAF*, the Image Reduction and Analysis Facility (IRAF), a general purpose software system for the reduction and analysis of astronomical data. IRAF is written and supported by the IRAF programming group at the National Optical Astronomy Observatories (NOAO) in Tucson, Arizona (USA).

2.4.1 Bias subtraction

A CCD image contains a "bias", a pedestal level of several hundred ADU's[3]. The bias image has an exposure time of zero-seconds and allow us to determine this pedestal level. The rms value of the bias level is the CCD read noise, the bias contains the DC offset level, the overscan, and the variation of that level.

In order to properly sample these variations in a statistical sense, we have collected five bias frames in the beginning of the run and 5 bias at the end of the observations every night. We have examined the statistic in every bias. In Tab. 2.4 we show that the mean and the standard deviation of the bias keep roughly constant for all frames. From the bias statistics of the images of every night we have subtracted the bias as a constant number for all the images, taking the mean value of the ten total bias frames observed every night. We control the bias level without adding noise to the data.

[3]The gain of a CCD determines how the amount of charge collected in each pixel will be assigned to a digital number in the final image, the number of electrons needed to produce one ADU (Analog-to-Digital) step within the A/D converter.

Bias frame	mean (ADUs)	stdev (ADUs)
1	1607	133.5
2	1604	110.9
3	1604	109.2
4	1604	108.2
5	1603	107.2

Table 2.4: Statistics for some bias frames on January 2007

2.4.2 Flat field correction

Flat-fielding in spectroscopy is used to correct the pixel-to-pixel high spatial frequency variation in response (i.e., in both directions). We have used a projector lamp to get a uniformly illuminated calibration image, i.e., a flat field image. Each row of a flat spectrum is illuminated by light of a different wavelength and our spectral range is larger than 3000 Å. Hence to get a good level of counts in the blue region (3200 - 4200 Å) of the spectrum we need to saturate flat frames in the red region. To deal with this problem we collected flat-fields with different exposure times, every night: we obtained six frames with five seconds (to get a good S/N in the red) and six with 30 seconds exposure time (to get a good S/N in the blue). Also the variation of the quantum efficiency within the CCD pixels are wavelength dependent. We need to work out a flat frame with an average value of 1.00 that is "spectrally flat".

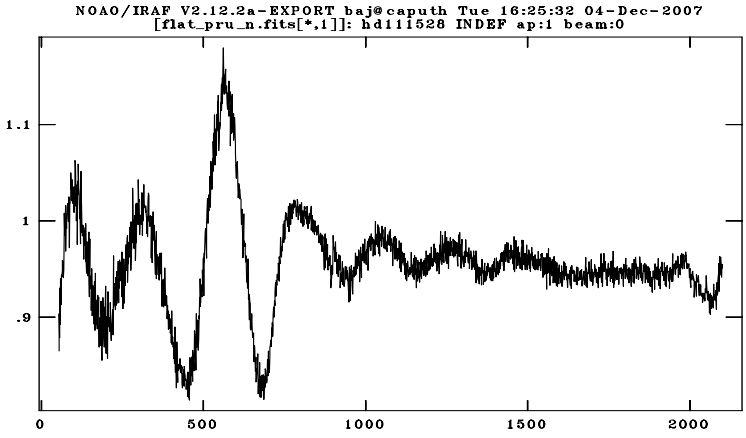

Figure 2.6: A zoomed-in tracing across the normalized flat-field, after fit the "blue flat" and the "red flat", parallel to the dispersion direction.

Fig. 2.6 shows the normalized flat-field we would use for correction purposes. Note the feature around the pixel 850, this feature arises from the fit between the "blue flat" and the "red flat". Note also the significant variations from the average value of 1.00 we see

for the "blue flat". For these reasons we decided do not correct for flat-field.

2.4.3 Scattered light

We may find some light well away from the "right" position of focus for photons of their wavelength due to imperfections in the mirrors and in the gratings or pieces of dust in the air. These scattered light results in a systematic error in the line strength and shape measurements that could drive a bad extraction of the spectra.

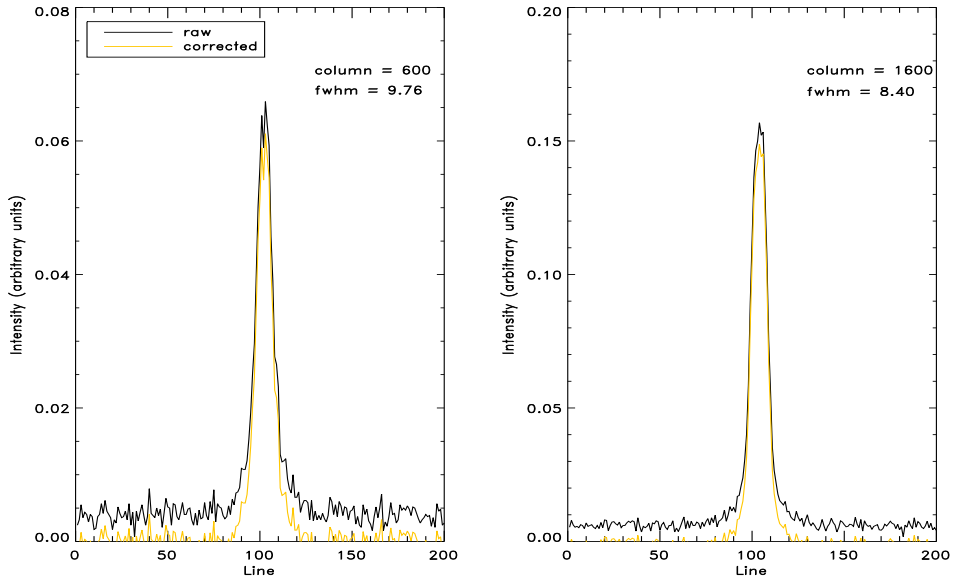

Figure 2.7: Intensity of the stellar profile versus lines in pixels for the column 600 (blue) and 1600 (red) respectively. Note the differences in the stellar profile before and after the scattered correction.

Our goal is to get a robust extracted spectrum. This scattered light modified the stellar profile along the dispersion axis (see Fig. 2.7). We have corrected the so-called linearly scattered light that arises from the grating and the slit and goes in the direction of dispersion. We are using the task from IRAF called *apscatter*. The task allow us to extract, smooth and subtract the scattered light by using the light outside the apertures defining the two dimensional observed spectra. First we select the apertures to study the scattered light. Second we set the fitting parameters for the scattered light functions both across and along the dispersion interactively. We avoid sky lines like [OI] to make the fit.

2.4.4 Extracting the spectra

Once we have our spectra reduced and the scattered light subtracted, the next step is to extract the spectra. First we determine the aperture, the object's part of the tracing and second the background, the sky region we use for subtraction. It traces the spectrum and sums it up in a mono-dimensional line.

The extraction algorithm used by IRAF is variance-weighted (optimal), developed by Horne (1986). The weight that is used to compute the sum in the optimal extraction, is inversely proportional to its statistical uncertainty. In order to estimate the variance image we use the READ-NOISE and the GAIN parameters of the CCD.

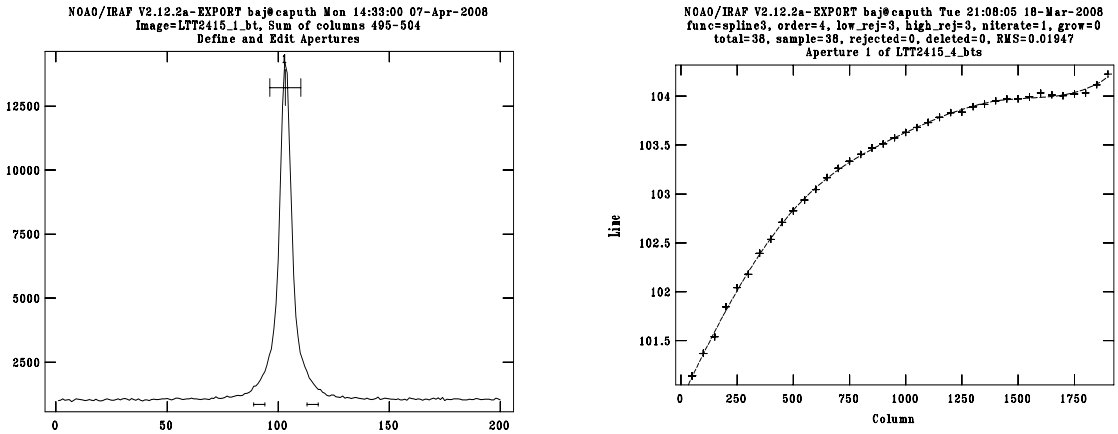

Figure 2.8: Left: A perpendicular cut to the dispersion axis. We see the location and width of the spatial profile. In the top of the profile we show the aperture we use for the extraction. Right: Tracing the spectrum along the dispersion axis. Note how a spline3 function of order 4 does a good job fitting the trace.

There are some parameters that controll the extraction aperture where we define the exact spatial center of the stellar profile along the dispersion axis. In our case we have defined the spatial center at column 500 pixels, the number of columns run from 0 to 2000 pixels. The reason why we use the column 500 is because we don't want to lose light in the blue. Note in Fig. 2.7 the difference in the FWHM for the stellar profile at column 600 and 1600. Another important parameter is the profile width that is the base-to-base size of the stellar profile which should be close to the FWHM of the spectrum. To improve the extraction we increase the number of lines to average when finding the center of the spatial profile. To get a good tracing we increased the step size along the dispersion axis.

Background subtraction

Our spectra are contaminated by the sky lines from the Earth's atmosphere and also by sky continuum, that gets bright when the moon is up. To control these lines and correct our spectra, we need to specify the location of the background regions, either side of the star, relative to the center of the spatial profile. Ten pixels have been used on both sides to control the background. We take the median, which helps to clean out cosmic rays in the region, of the adjacent points within each background window and we use these values to fit the background using a *chebyshev* function of order 2.

Cosmic rays

In several cases, especially for stars with long exposure time, we found cosmic rays in the spectra of the stars. To clean them we used a task called *splot*. This task removes the cosmic ray by interpolating between near points around the cosmic ray area.

2.5 Calibration

In this section we discuss the steps we have done to get our spectra calibrated in wavelength and flux. These calibrations are fundamental to get the stellar parameters for our objects. We also test the accuracy of the flux calibration using David Dunlap Observatory (DDO) bands.

2.5.1 Wavelength calibration

Our goal is to calibrate the pixel scale of our spectra into a wavelength scale. Using the spectrum for a CuHe lamp we determined the dispersion solution we use to convert from pixels to Angstroms.

We used the task *identify* to identify the emission lines from the CuHe arc lamp with their laboratory wavelength and to fit a function to these data. We used the line-list provided by SSO and obtain fits with a RMS $\sim$ 0.2 Å. Finally we applied the dispersion solution to our program objects using the task *dispcor*.

2.5.2 Flux calibration

We now wish to have the axis of ADUs or counts converted into flux units such as *ergs* $s^{-1}cm^{-2}\AA^{-1}$. To get an accurate flux calibration we have secured every night spectra of standard stars at different zenith distances, i.e. different airmass.

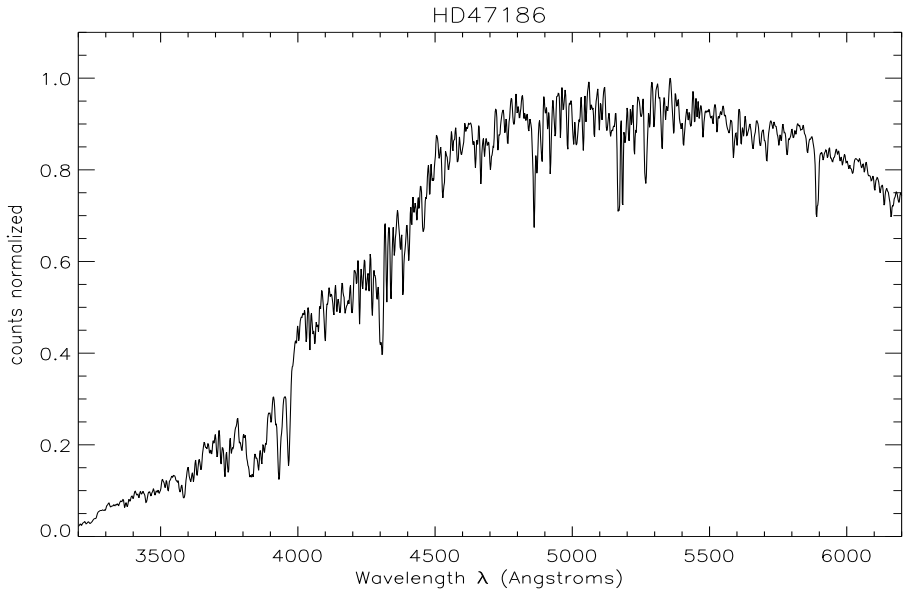

Figure 2.9: The star HD47186 calibrated in wavelength.

The goal is to calibrate the CCD response, the system telescope plus spectrograph throughput and control for atmosphere extinction. The steps we have done to get the flux calibration are: 1) using a tabular compilation we take the energy distribution of the standard stars we observed, 2) we correct the energy distribution for wavelength dependent atmospheric extinction, 3) we compare it to the energy distribution of the observed spectrum and finally, 4) using this comparison we derive the function that gives the response of the instrument in function of wavelength.

Optical spectrophotometry standard stars

As we have mentioned in Sect. 2.3.4 we collected standard stars covering a large range of airmass during the night. The spectrophotometry standard stars come from the Oke (1990) and Hamuy et al. (1994) catalogues.

Oke (1990) Spectrophotometric Standards catalogue: this catalogue provides absolute spectral energy distributions covering the wavelength range 3200 to 9200 Å in AB magnitudes[4] for 25 stars. The measurements were made with the Double Beam Spectrograph of the Hale 5 m telescope. The reduced magnitudes are tabulated at 1 Å intervals from 3300 to 4700 Å and at 2 Å intervals from 4700 to 9200 Å. Colina & Bohlin (1994) tabulate the differences between the original Oke fluxes, in terms of synthesized B and V magnitudes, and Landolt photometry for each star individually and the AB magnitudes were converted

[4]ABMAG = -2.5 log(Fν) - 48.59

to flux units.

Hamuy et al. spectrophotometric standards: this catalogue consists of 10 secondary spectrophotometric standards (from Taylor (1984)) and 19 tertiary spectrophotometric standards from the lists of Stone & Baldwin (1983) and Stone (1977). Hamuy et al. (1994) present AB magnitudes for the 10 secondary standards at 16 Å intervals from 3300 to about 10400 Å and for the 19 tertiary standards at 50 Å intervals from 3300 to about 10300 Å.

For practical and traditional reasons the star Vega (HD 172167, HR 7001 or α Lyrae) is the primary standard star. The fluxes and energy distributions of the secondary and tertiary standard stars mentioned above have been determinated through measurements relative to Vega. The absolute measurement of the flux of Vega is determinated by comparing Vega with a source of radiant energy whose monochromatic flux is known, like a blackbody at a specified temperature. See Hayes (1985) for details.

Flux calibration and correction for atmospheric extinction

We use the task *standard* to determine the calibration pass-band. The observed standard stars are integrated over calibrated bandpasses, the task creates a file along with the associated calibration fluxes. The fluxes are obtained from tabulated standard star calibration files based on the magnitude and spectral type of the star.

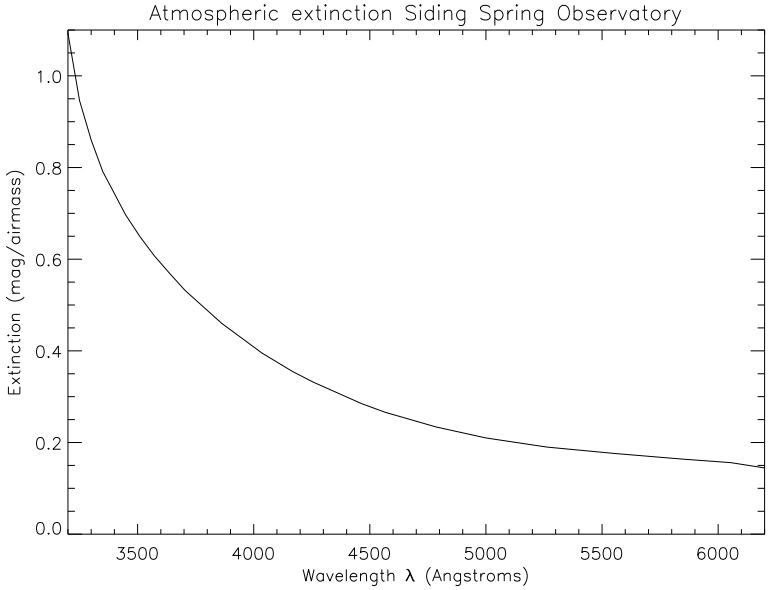

Figure 2.10: Atmospheric extinction at Siding Spring Observatory in the optical wavelength range.

standard uses a model for extinction created by Hayes & Latham (1975). Rayleigh

scattering by molecules, aerosol scattering and molecular absorption are considered the three main sources of extinction in the Earth's atmosphere. Each of these has its own wavelength dependence; roughly speaking the overall extinction behaves like $A(\lambda) \propto \lambda^{-4}$. See Fig. 2.10 for the extinction curve at SSO.

The calibration files consist of lines with wavelengths, calibration magnitudes and bandpass widths. The magnitudes are AB defined as

$$ABmag = -2.5 \log(F_\nu) - 48.60 \tag{2.9}$$

the flux F_ν is in erg/cm^2/s/Hz. $ABmag$ is converted to absolute flux per unit frequency using the parameter F_{ν_0} defined by

$$F_\nu = F_{\nu_0} 10^{(-0.4 ABmag)} \tag{2.10}$$

The default value of F_{ν_0} was chosen such that Vega at 5556 Å has an AB magnitude of 0.0336 and a flux of 3.52×10^{-20} erg/cm^2/s/Hz.

Once we have recorded the response of each standard star, we want to find a proper wavelength dependence of instrumental sensitivity and atmosphere transparency. We have combined several standard stars observed at different airmasses to solve simultaneously for the sensitivity and is also possible to derive an adjustment to the standard extinction curve. When the sky conditions are poor and the standard star observations are obtained during periods of variable transparency, we shifted all stars to the star with the highest sensitivity curve so that they have the same average sensitivity. To control this process we use the IRAF task *sensfunc*.

The calibration factor at each point is given by

$$C = 2.5 \log(O/(TBF)) + AE \tag{2.11}$$

where O is the observed counts in a bandpass of an observation, T is the exposure time of the observation, B is the bandpass width (50 Å), F is the flux per Angstrom at the bandpass for the standard star, A is the airmass of the observation, and E is the extinction at the bandpass. Thus, C is the ratio of the observed count rate per Angstrom corrected by some extinction curve to the expected flux expressed in magnitudes. The goal is to fit the observations to the following relation

$$C = S(W) + AE(W) \tag{2.12}$$

where W is wavelength, S(W) is the sensitivity function, and E(W) is a residual extinction function relative to the extinction used in Eq. 2.11. The residual sensitivity is defined by

$$R = C - S(W) - AE(W) \tag{2.13}$$

In our calibration the usual RMS for R is around 0.1. That indicates we are be able to get a good fit for the sensitivity function. Finally we use *calibrate* to apply the flux calibration to all stars using the calibration explained above.

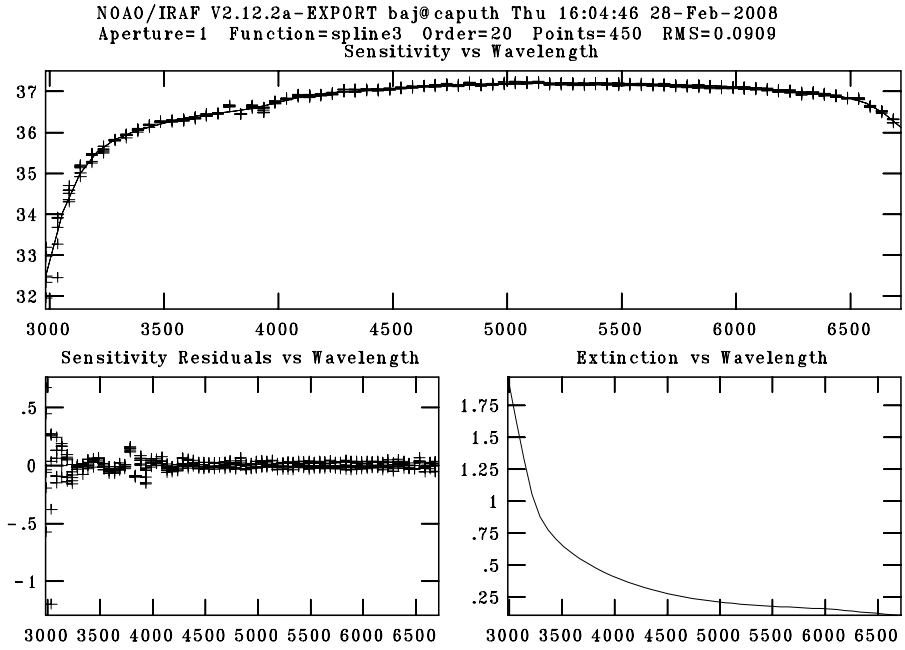

Figure 2.11: The sensitivity function versus wavelength. The function used to fit the instrumental response has usually very high orders. Here we use a spline3 with order 20. The units for the y-axis in the sensitivity panels are magnitude while for the extinction panel are magnitude/arimass. For the x-axis the units are Å.

After the calibration, we have a spectrum as observed from outside the atmosphere with an ideal uniformly sensitive detector, telescope, spectrograph. For a good flux determination we need to observe the standard stars under photometric conditions. Periods of thin clouds and bad seeing could vary the sensitivity curve by a constant factor assuming that the cause of the variations has no color effect. Variations in transparency are usually grey, unless there is bushfire smoke in the air; that would modify the shape of the sensitivity curve. In the next figures we show how the conditions of the night affect to the flux calibration.

Our targets were observed with an airmass close to 1.00 (zenith positions). We see in Fig. 2.12 a standard star flux calibrated for different values in airmass. An important point here is that the calibration shows small variations with the airmass for a clear night and a good seeing.

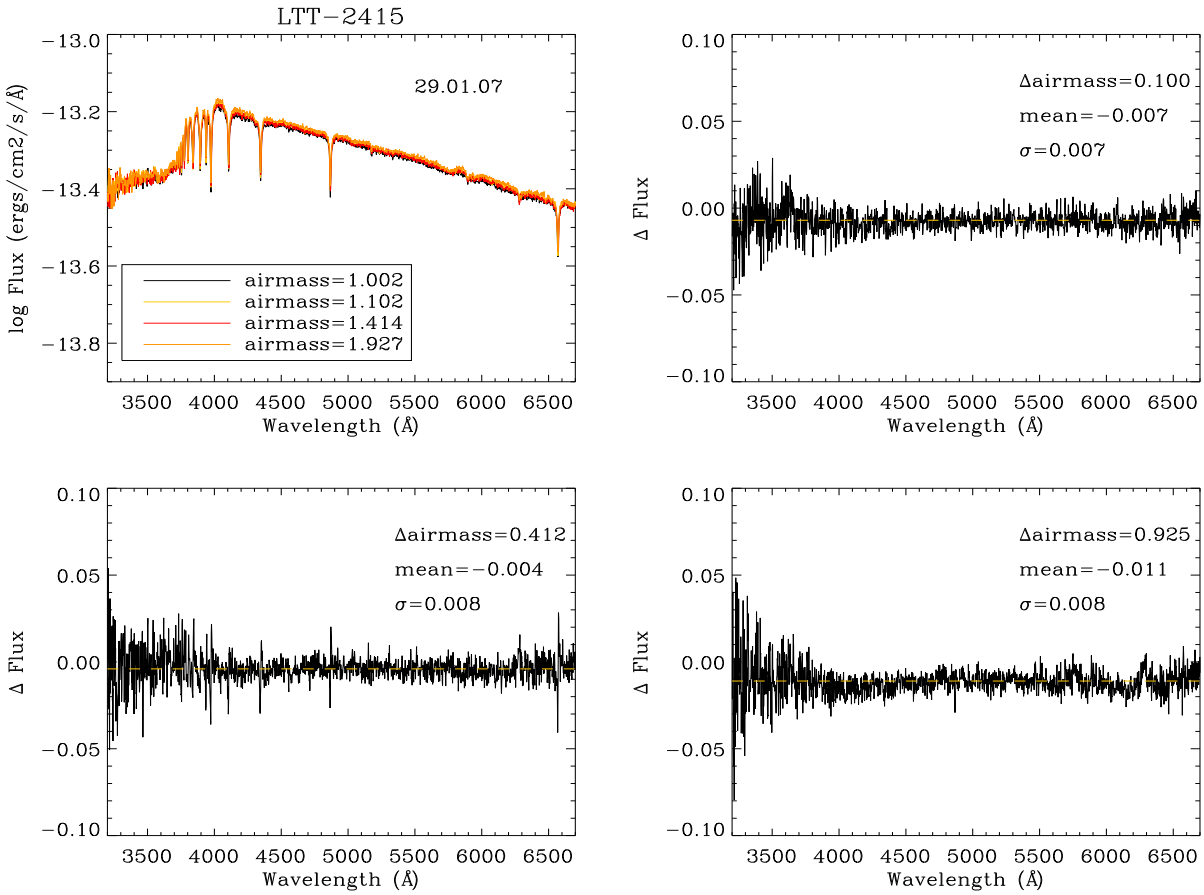

Figure 2.12: The standard stars LTT2415 flux calibrated for four different values of airmass. Note the good sky conditions for that night as the flux calibration is independent of the airmass.

It is important that we do not find remarkable differences in the shape of the flux distribution along the wavelength range when the sky conditions are poor or when our stars are far from the zenith (see Fig. 2.13). As we will see in the next chapter we use the shape of the spectra calibrated in flux to get the stellar parameters.

2.5.3 DDO photometry: Testing the accuracy of the flux calibration

We have tested the accuracy of the flux calibration using David Dunlap Observatory (DDO) bands. We got three different DDO bands directly from the flux calibrated spectra and we have tried to test how precise the flux calibration is by comparison with existing standard stars from two catalogues with this photometric system.

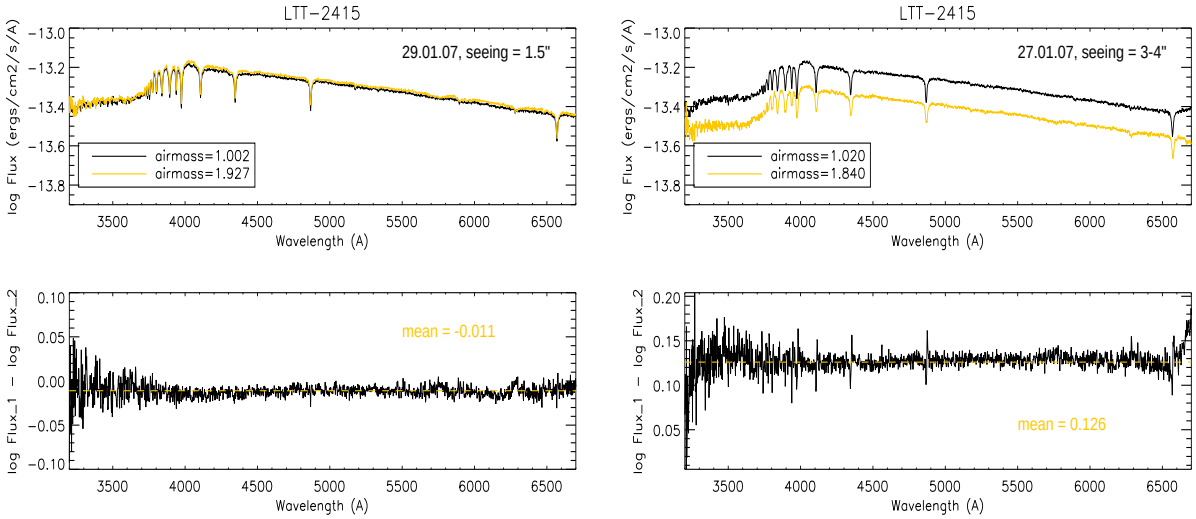

Figure 2.13: Left: LTT2415 flux calibrated for a night when the seeing was quite good. Right: The same stars for two different airmasses for a night with a very bad seeing. Note how the relative flux is shifted by almost for a constant factor keeping the shape of the energy distribution.

David Dunlap Observatory (DDO) photometric system

McClure & van den Bergh (1968) developed the DDO photometric system at the David Dunlap Observatory. The system consists of six intermediate bands defined as: *48*, centered at 4886 Å, *45*, centered at 4517 Å, *42*, centered at 4257 Å, *41*, centered at 4166 Å, *38*^{b}, centered at 3800 Å, *35*, centered at 3469 Å. A sixth filter, *51*, centered at 5150 Å, was defined by Clark & McClure (1979).

DDO	λ_{eff}/Å	FWHM/Å
45	4517	76
42	4257	73
41	4166	83
38	3800	172
35	3490	370

Table 2.5: Filter characteristics of intermediate-band DDO system. Data published in McClure & van den Bergh (1968).

The DDO standard stars: McClure & Forrester (1981) catalogue: The catalogue present 2196 bright G and K stars in the DDO photometric system selected from the Bright Star Catalogue (Hoffleit (1964)) and Eggen (1964) catalogue. Color indices are formed from measurements through each of the filter bandpasses. The colors presented are C(45-48), C(42-45), C(41-42), C(38-41), C(35-38) and they are defined as follow

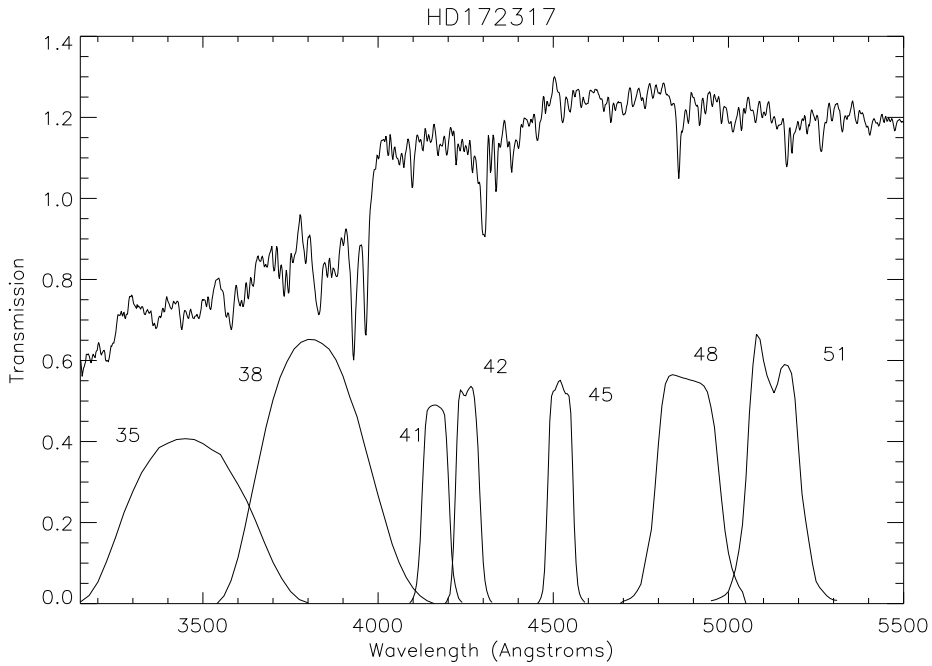

Figure 2.14: The flux calibrated spectrum of HD172317 with the filter transmission vs wavelength of the DDO bandpasses as given by McClure (1976) and Clark & McClure (1979). We normalized the transmission being 100% just 1.00.

$$C(A-B) = 2.5\log(I_B/I_A) \tag{2.14}$$

where I_A and I_B are the deflections, corrected for atmospheric absorption, through the A and B filter.

We have 20 stars in common with this catalogue. Following the shape of the DDO bands represented in Fig. 2.14 we compute the color indices directly from our spectra using the very familiar relation between magnitude and flux

$$m_A = -2.5\log(F_A) \tag{2.15}$$

In Fig. 2.15 we compare the values obtained in the color indices from our spectra with the values collected in McClure & Forrester (1981) catalogue. We get a good correlation between our values and the catalogue with small RMS values (< 0.02 mag) for all the color indices, indicating that the flux calibration is quite precise when comparing with photometric catalogues. We have derived the color transformation equations between the two systems by fitting a least-square fit taking into account the errors in the colors from the McClure & Forrester (1981) catalogue:

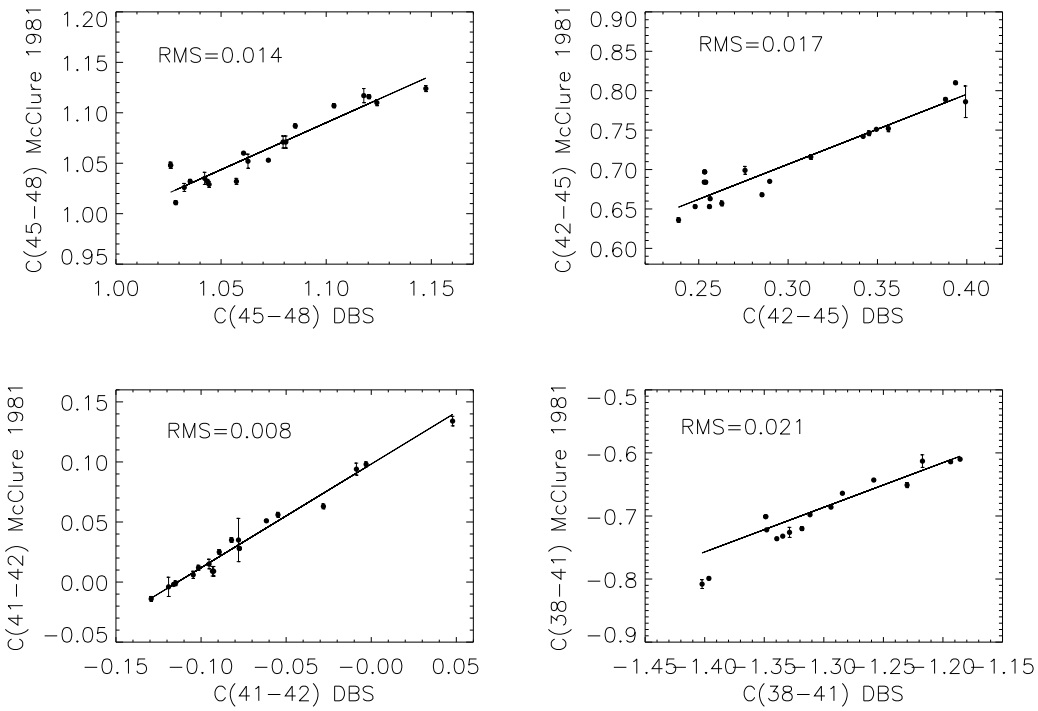

Figure 2.15: Comparison between the color indices derived from our spectra and the color indices from McClure & Forrester (1981) for 20 stars in common. We have found a very good correlation between the colors derived from the spectra and the photometric catalogue with a small RMS for all the colors. The line represents a first-order polynomial least-square fit.

DDO index	zero-point	scale factor
C(45-48)	0.065 ± 0.017	0.931 ± 0.016
C(42-45)	0.440 ± 0.027	0.888 ± 0.008
C(41-42)	0.098 ± 0.001	0.863 ± 0.012
C(38-41)	0.234 ± 0.007	0.708 ± 0.006

Table 2.6: Calibration of the DDO colors with respect to the standard stars from McClure & Forrester (1981).

We have mentioned above that the differential refraction, the atmosphere extinction and the *seeing* of the night could spoil the flux calibration. These effects are more severe for the blue wavelength. We have payed special attention to the color C(35-38). The DDO bands *35* and *38* cover the blue region of the spectra going from 3100 Å to 4200 Å. See Fig. 2.14. Hence the behaviour of this color gives us a good test for the blue wavelength.

The result using the color C(35-38) from the DBS and the McClure & Forrester (1981)

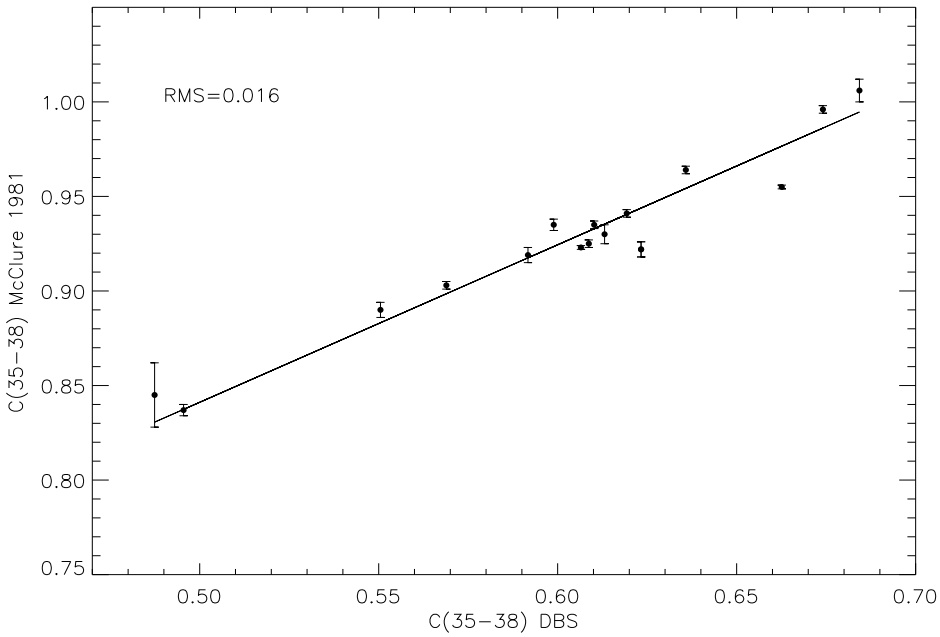

Figure 2.16: Comparison between the DDO color C(35-38) derived from our spectra and the color indices from McClure & Forrester (1981) for 20 common stars. The correlation between the color derived from the spectra and the photometric catalogue presents a quite small RMS. The line represents a least-square fit.

presents a good correlation, being the RMS = 0.016 mag. See Fig. 2.16. These results secure our flux calibration for the blue region of our spectra. We also have derived the color transformation equations between the two systems being the zero-point 0.425 ± 0.005 and the scale factor 0.833 ± 0.008.

One of the purpose of the DDO photometric system was to determine the spectral types and luminosities of a wide range of stars. An important color-color diagram in the DDO system is C(45-48) vs C(42-45). The color C(45-48) is quite sensitive to surface gravity for late-type stars, mainly due to MgH absorption region for the filter 48. The index C(42-45) measure the break in the continuum of late-type stars due to the G band of CH and other nearby lines and the G band break is primarily sensitive to the temperature of the star. See Tripicco & Bell (1991) for more details about getting the stellar parameters via DDO photometry.

In Fig. 2.17 we show the color-color diagram for C(45-48) vs C(42-45). We clearly see how the color C(45-48) separates between giants and dwarfs, i.e. this color is sensitive to gravity. Note also how C(42-45) drives the temperature of the stars (the temperature range we see here is between $\sim$ 4200 K and $\sim$ 6000 K). Using our data we fill the gap between dwarf and giant stars present in McClure & Forrester (1981), these stars are mainly

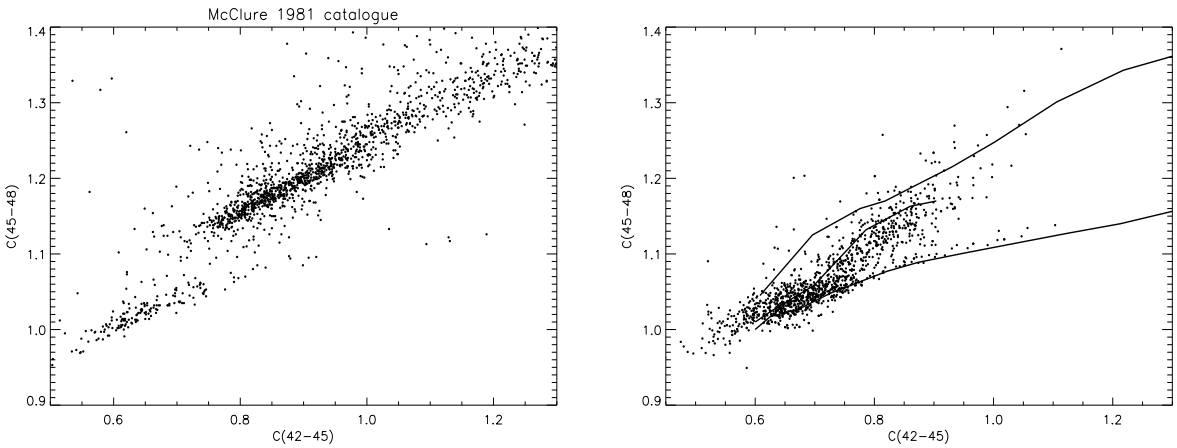

Figure 2.17: Left: C(42-45) versus C(45-48) for the stars in the McClure & Forrester (1981) catalogue. The color-color diagram clearly shows the separation between dwarfs and giants. Right: The DDO indices C(42-45) versus C(45-48) derived from the spectrophotometry for the selected sample. The *lines* represent the luminosity class V, IV and III (from *bottom* to *top*) from the mean values of the DDO indices for MK spectral classes listed in the catalogue of homogeneous photometry of bright stars from McClure & Forrester (1981).

subgiants. These results secure the flux calibration we have made for our targets and show a good roadmap for the subgiants in our sample.

The DDO standard stars: Mermilliod & Nitschelm (1989) catalogue: The catalogue consists of 8034 measurements of 6138 stars. It includes, when measured, the magnitude of the filter 48, and the six color indices C(48-51), C(45-48), C(42-45), C(41-42), C(38-41) and C(35-38). We have 62 stars in common with this catalogue. Unfortunately there is data for the color C(48-51) for just two stars, hence we cannot make a proper study for this color.

In Fig. 2.18 we make the same plots as before but now using the standards from a new catalogue, Mermilliod & Nitschelm (1989) catalogue. We get a good correlation between our values and the catalogue with small RMS values for all the color indices. We have two independent test for our flux calibration. Both indicate that the flux calibration works quite well being relatively precise when comparing them with photometric catalogues. We have derived the color transformation equations between the two systems by fitting a least-square fit taking into account the errors in the colors from the Mermilliod & Nitschelm (1989) catalogue.

Again we have payed attention to the colors mapping the region between 3200 Å and 4200 Å (see Fig. 2.19). We find a good relation between our colors and the colors from the standards with a RMS = 0.026 mag. The zero-point of the transformation and the scale factor are 0.441 ± 0.018 and 0.797 ± 0.029 respectively.

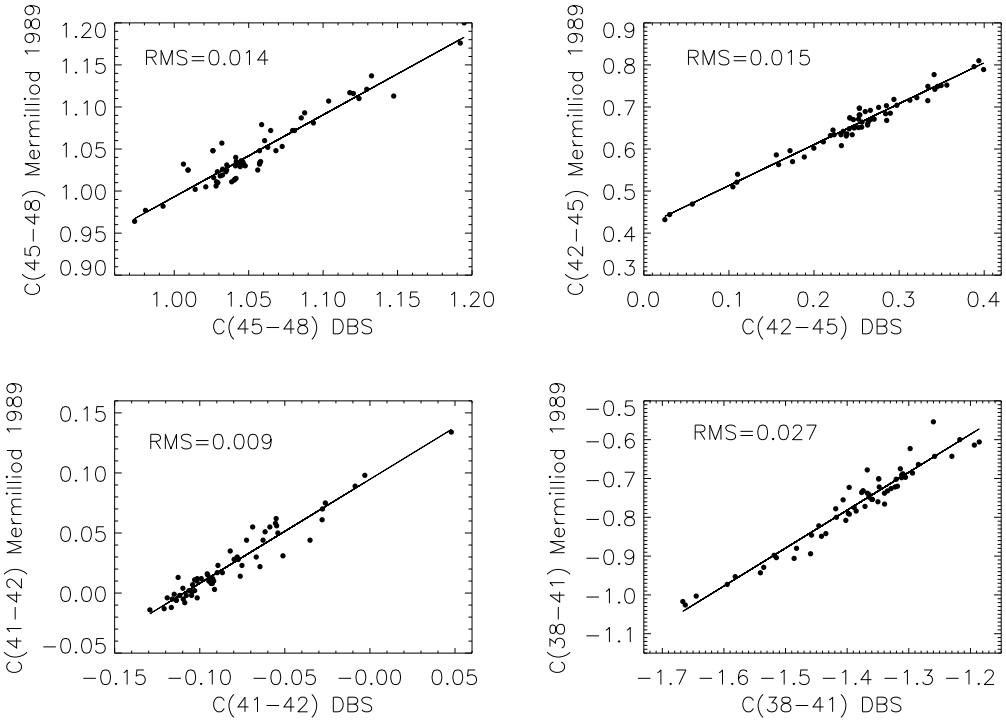

Figure 2.18: Comparison between the color indices derived from our spectra and the color indices from Mermilliod & Nitschelm (1989) for 62 common stars. We have found a strong correlation between the colors derived from the spectra and the photometric catalogue with a small RMS for all the colors. The line represents a first-order polynomial least-square fit.

DDO index	zero-point	scale factor
C(45-48)	0.018 ± 0.043	0.974 ± 0.041
C(42-45)	0.415 ± 0.006	0.973 ± 0.024
C(41-42)	0.094 ± 0.002	0.865 ± 0.031
C(38-41)	0.586 ± 0.046	0.977 ± 0.033

Table 2.7: Calibration of the DDO colors with respect to the standard stars from Mermilliod & Nitschelm (1989).

As mentioned above, we have two independent tests for our flux calibration. We developed the tests using the DDO colors from our spectra and the standards stars observed in Mermilliod & Nitschelm (1989) and McClure & Forrester (1981) catalogue. Both studies indicate that the flux calibration is robust and precise. The color bands we used cover almost the whole spectral range we have for the observed spectra, going from 3100 Å to 5100 Å.

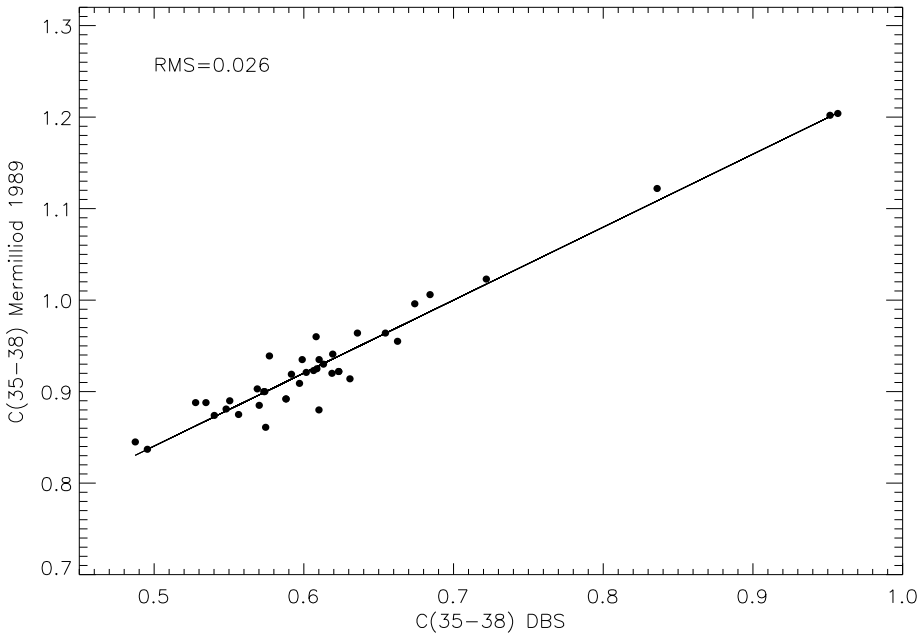

Figure 2.19: A comparison between the DDO color C(35-38) derived from our spectra and the color indices from McClure & Forrester (1981) for 20 common stars. The correlation between the color derived from the spectra and the photometric catalogue results in a small RMS. The line is a least-square fit.

Photon noise

We checked the photon noise for the DDO colors from our spectrophotometry. We want to check if the expected photon noise for these bands is negligible. The photon noise is an inherent natural variation of the incident photon flux and this noise is distributed according to a Poisson distribution. For the band 45 we can write

$$m_{45} = 2.5 \log N_{45} \tag{2.16}$$

where N_{45} is the level of counts in that band. For a noise of N_{45} we have $\sigma_{N_{45}} = \sqrt{N_{45}}$. Being the error for the magnitude

$$\sigma_{m_{45}} = \frac{1.086}{\sqrt{N_{45}}} \tag{2.17}$$

hence for the color C(42-45) we have that the photon noise is

$$\sigma_{C(42-45)} = 1.086(\frac{1}{N_{42}} + \frac{1}{N_{45}})^{1/2} \tag{2.18}$$

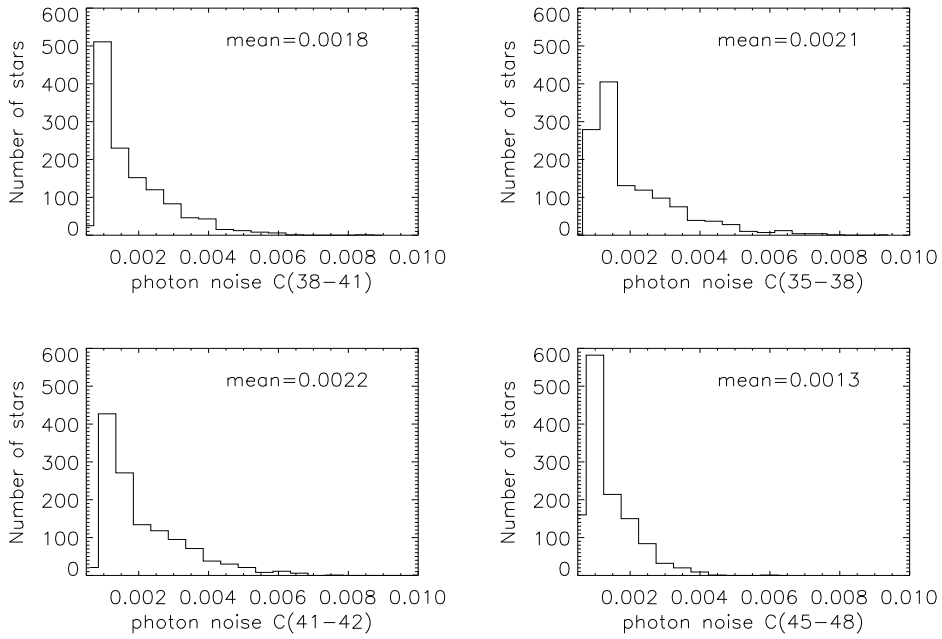

Figure 2.20: Photon noise distribution for four different colors. We indicate the mean value of the distribution.

In Fig. 2.20 we show the photon noise distribution for four different colors. We find that the expected photon noise for these bands is much smaller than the expected systematic uncertainties.

Chapter 3

Stellar parameters from Spectrophotometry

3.1 Introduction

In this chapter we discuss in detail the strategy used to determine the stellar atmosphere parameters via synthetic and empirical spectral libraries. We also discuss the corrections that we have to apply to our spectra before they can be compared to models.

3.2 Radial Velocity

The observed frequencies of photons are shifted from their emitted frequencies when a source of radiation moves from an observer. This effect is called *Doppler shift*. We need to measure this displacement and shift the spectra to the rest frame before they can be compared to models.

The radial velocity of a star, i.e. the velocity along the line of sight, have frequency ν_0 in the rest of frame of the star but we will detect these photons at frequency

$$\nu = (1 - \beta)\gamma\nu_0 \tag{3.1}$$

where $\beta \equiv v_r/\mathrm{c}$ and $\gamma \equiv (1 - \beta^2)^{-1/2}$ and c is the velocity of light. For our stars we have the lowest order in v_r/c hence $\gamma = 1$. The frequency shift is

$$\triangle\, \nu \equiv \nu - \nu_0 = -\beta\nu_0 \tag{3.2}$$

for the wavelengths $\lambda = c/\nu$ we have that $\triangle\lambda/\lambda_0 = -\triangle\, \nu/\nu_0$ hence

Temperature (K)	$4500 \leq T_{eff} \leq 6000$ K (steps of 250 K)
Gravity (cgs units)	$3.0 \leq \log g \leq 4.5$ (steps of 0.5 dex)
Metallicity	-1.5 $\leq [M/H] \leq$ 0.5 (steps of 0.5 dex)
Rotation velocity	2 km/s
Enhancement	$[\alpha/\mathrm{Fe}] = 0.0$
Micro-turbulent velocity	2 km/s
Resolution (FWHM of the PSF)	$1.0 \leq$ FWHM (Å) ≤ 14.0

Table 3.1: Range of properties for the selected templates. We degrade the templates by Gaussian convolution to lower resolving powers from the library with dispersion of 1 Å/pix.

$$\triangle \lambda = \frac{v_r}{c}\lambda_0 \tag{3.3}$$

Our goal is to measure the radial velocity of our stars to shift the spectra to the rest frame for the comparison with the synthetic spectral libraries. We are not going to use the RV value from the low resolution spectra. In fact, we did not take many arcs during the night, because we were not really trying to measure RV and there will be some drift in wavelength during the night, up to about one Å ($\sim$ 60 km/s). The RVs for this project come from GCS and RAVE.

We use a standard cross-correlation procedure (Tonry & Davis (1979)) to determine the wavelength offset needed to shift the stellar spectrum to zero velocity. We use the package *XCSAO* for IRAF (Kurtz & Mink (1998)). Measuring RVs using cross-correlation techniques relies on the availability of accurate stellar templates to correlate with the observed spectra. Our sample covers a small range in temperature and gravity and a quite large range in metallicity. Due to the low resolution of the observed spectra we fix the rotational and the micro-turbulent velocity of the templates. We use the library of theoretical spectra from Munari et al. (2005). This library contains 51,288 synthetic spectra at resolving powers R_P = 20 000, 11 500 (GAIA), 8500 (RAVE), 2000 (SLOAN) and uniform dispersions of 1 and 10 Å/pixel constructed using the Kurucz model atmosphere code (ATLAS). It covers an extensive range of physical conditions of the stellar atmosphere and it covers a wavelength range from 2500 10500 Å. In Tab. 3.1 we present the characteristics of the selected templates.

When computing the RVs the whole spectral range was used, from 3200 Å to 6200 Å. Prior to the RV determination, the spectra are continuum normalized using a cubic spline of order 3. Subtraction preserves the relative amplitudes for the lines in the data and the correct S/N behavior in the cross-correlation. A cosine-bell filter is used to minimize the effects of (high-frequency) noise. The last steps are rebinning and the RV is calculated by fitting a parabola to the top of the correlation peak.

In Fig. 3.1 we see the behaviour of the RV with respect to the R coefficient (Tonry & Davis (1979)) for different resolutions in the template spectra. The R coefficient, defined in

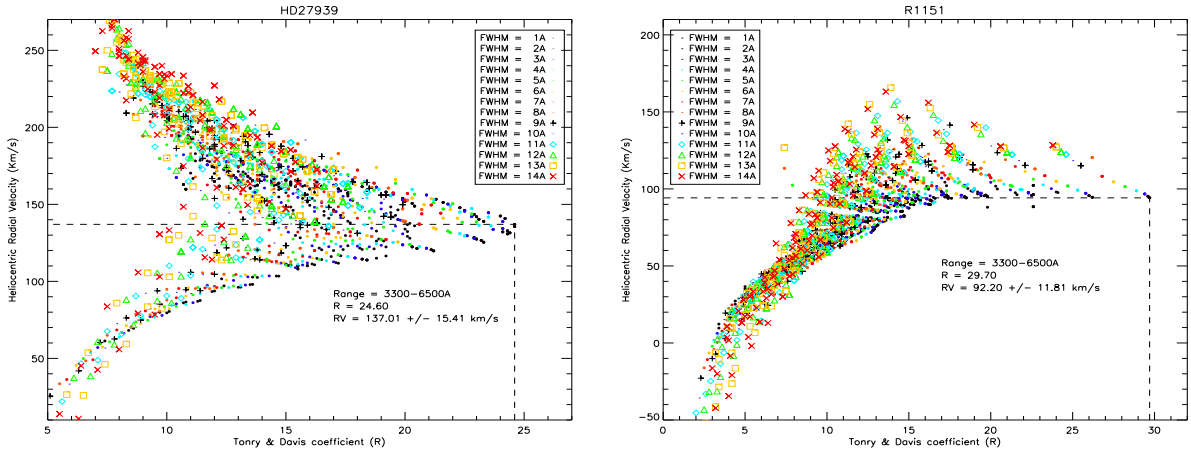

Figure 3.1: RV versus the R coefficient (Tonry & Davis (1979)) for different resolutions in the template spectra.

Tonry & Davis (1979) as the ratio of the height of the true peak to the average peak, could be treated as a reliability empirical confidence measure (Kurtz & Mink (1998)). Fig. 3.1 shows that the templates with higher resolution present the higher value for the R coefficient. The filter we use to compute the RV also degrades the spectra to about 10 Å resolution. The choice of filter does have an effect on the derived RV. The R coefficient should always be higher if you include more high frequency data, but this is good only if the high frequencies are dominated by real data and not by photon noise. The formal accuracies we are getting are about as good as can be expected at this resolution. One pixel ~ 2 Å $= 120$ km/s at 5000 Å so we are getting formal errors of about 0.2 pixels.

3.3 Synthetic stellar atmospheres

Stellar electromagnetic fluxes supply the most detailed information we can obtain from stars. With the present limitations in available computer power, one has to use geometrically simple 1D hydrostatic model atmospheres to compare in detail the very large amounts of opacity data necessary to describe the radiative energy transport in stellar photospheres with observations (Gustafsson et al. (2008)). Recently, time-dependent, 3D, hydrodynamical model atmospheres have started to be employed for stellar abundance purposes, with large differences compared with 1D modeling found in particular for metal-poor stars (e.g. Asplund (2005)).

3.3.1 The formation of the continuum and the absorption lines

Here we review, very briefly, the basic and fundamental ingredients to build the spectrum of a star. The concepts described below are presented in more detail in the textbooks of Mihalas (1978) and Bšhm-Vitense (1990). The bulk of stellar radiation come from the *photosphere*. The optical depths for continuum radiation in this layer is between about 0.01 and a few[1]. The optical depth τ_λ represents the number of mean free paths of radiation traveling vertically outwards before it escapes from the star. We write

$$\tau_\lambda(z) = \int_z^\infty \kappa(z)\rho(z)dz \tag{3.4}$$

the optical depth is related to the geometrical height z above an arbitrary layer. In the expression above ρ is the mass density and κ the mass absorption coefficient or *opacity*. The effective temperature is a fundamental parameter to describe the photosphere of a star. The T_{eff} we measure in a star is equal to the actual (kinetic) temperature at $\tau \sim 2/3$.

For stars hotter than 10^4 K the atmospheric opacity comes mainly from photo-ionization of hydrogen atoms in different excitations levels. This effect gives rise to absorption in the Lyman ($\lambda \leq 912$ Å), Balmer ($\lambda \leq 3646$ Å), Paschen ($\lambda \leq 8208$ Å) etc. continua. In cooler stars like the Sun the main opacity in the optical region come from negative hydrogen ions

$$H^- + h\nu(\geq 0.75eV) \rightarrow H + e^- \tag{3.5}$$

H^- opacity varies smoothly with wavelength and does not lead to significant departures from a black-body-like continuum in the optical and near IR range. In local thermodynamic equilibrium (LTE), the relative population of protons, neutral hydrogen atoms and H^- ions are as predicted by the Saha-Boltzmann equations

$$\frac{n_i}{n_j} = \frac{g_i}{g_j} e^{-(E_i - E_j)/KT} = \frac{g_i}{g_j} 10^{-\theta\chi_{ij}} \tag{3.6}$$

g_i, g_j are the statistical weights of two atomic levels, χ_{ij} is the difference in excitation potential in volts and $\theta = 5040/T$ and

$$\frac{n_+ n_e}{n_0} = 2\frac{u_+}{u_0}\left(\frac{m_e kT}{2\pi\hbar^2}\right)^{3/2} e^{-E_I/kT} \tag{3.7}$$

or

[1] A stellar atmosphere is optically thick when the optical depth is bigger than 1, and optically thin when is lower.

$$log\frac{n_+}{n_0} = log(\frac{u_+}{u_0}) + 9.08 - 2.5log\theta - \theta I - logP_e \tag{3.8}$$

I is the ionization potential in volts and the u_s are partition functions[2]. P_e is the electron pressure. At solar-like temperatures and abundances, almost all the free electrons come from easily ionized metals (Na, Mg, Al, Si, Ca, Fe) leading to an electron pressure that is about 10^{-4} times the gas pressure.

The processes of absorption in LTE is governed by Planck's law for specific intensity

$$I_\nu d\nu = B_\nu(T)d\nu \equiv \frac{2h\nu^3}{c^2}\frac{d\nu}{e^{(h\nu/kT)} - 1} \tag{3.9}$$

this expression is often referred to as "pure absorption". Considering the simple case of a plane parallel grey atmosphere in radiative equilibrium, where κ the opacity is independent of wavelength, we get some insight into the structure of stellar atmosphere.

Let I(τ,θ) be the specific intensity (integrated over all wavelengths) traveling outwards at an angle θ to the normal. Traveling through a layer with vertical thickness dz, it loses I dτ/μ from absorption, being $\mu \equiv \cos\theta$ and gains j dz$/\mu \equiv$ S dτ/μ from emission, where j(τ) is the emission per unit solid angle per unit volume and S(τ) $\equiv$ j$/\kappa\rho$ is called the *source function*. We write the transfer equation as follow

$$\mu\frac{\partial I}{\partial \tau} = I - S \tag{3.10}$$

Integrating Eq. 3.10 over solid angles and dividing by 4π we obtain

$$\mu\frac{\partial H}{\partial \tau} = J - S \tag{3.11}$$

where J(τ) $\equiv \int$ I d$\omega \equiv 1/2 \int_{-1}^{1}$ I dτ is the mean intensity angle-averaged and H $\equiv \int$ I μ d$\omega/4\pi \equiv 1/2 \int_{-1}^{1}$ I μ dμ is known as the *Eddington flux*; we can write the actual flux like $\sigma T_{eff}^4 \equiv \pi F \equiv 4\pi H$. The flux is constant in radiative equilibrium, so

$$S = J \tag{3.12}$$

and in LTE,

[2]In statistical mechanics, the partition function, encodes the statistical properties of a system in thermodynamic equilibrium. It is a function of temperature and other parameters, such as the volume enclosing a gas.

$$S = B(T) = \sigma T^4/\pi \tag{3.13}$$

Eq. 3.13 is called the Stefan's law. Multiplying Eq. 3.10 by μ and integrating over solid angles, we have

$$\mu\frac{\partial K}{\partial \tau} = H \tag{3.14}$$

where K $\equiv 1/2 \int_{-1}^{1}$ I $\mu^2 d\mu$. We can set

$$K = \frac{1}{3}J \tag{3.15}$$

Eq. 3.15 is called *Eddington's approximation*. From Eq. 3.12 to Eq. 3.15

$$J = S = B = 3H\tau + const. \tag{3.16}$$

We obtain a simple boundary condition at the surface by assuming I(τ=0,μ >0) = const. (i.e. limb-darkening is neglected), I(τ=0,μ <0) = 0. Then J(τ=0) = 2H and we have

$$S = J = H(2 + 3\tau) \tag{3.17}$$

and in LTE using πF = 4πH = σT$^4_{eff}$

$$T^4 = T^4_{eff}(\frac{1}{2} + \frac{3}{4}\tau) \tag{3.18}$$

Eq. 3.18 gives a first approximation to the temperature structure of an atmosphere in radiative equilibrium.

Integrating the radiative transfer equation, Eq. 3.10, we can get the specific intensity at an angle θ to the normal

$$I_\lambda(0,\mu) = \int_0^\infty B_\lambda[T(\tau_\lambda)]e^{-\tau_\lambda/\mu}d\tau_\lambda/\mu \tag{3.19}$$

and the flux from

$$F_\lambda(0) = 2\int_0^1 I_\lambda(0,\mu)\mu \tag{3.20}$$

In the Eddington-Barbier approximation one has simply

$$I_\lambda(0,\mu) \simeq B_\lambda(\tau_\lambda = \mu) \tag{3.21}$$

and

$$F_\lambda(0) \simeq B_\lambda(\tau_\lambda = 2/3) \tag{3.22}$$

Molecules, ions and atoms present in the stars atmosphere provide additional opacity at wavelengths corresponding to specific atomic transitions; giving narrow absorption lines with intensities related to the abundances of the relevant elements. Another process involved in the production of absorption lines is the *scattering*. These processes are often treated in LTE, this is only a simplifying approximation which works well for specific cases. However there are regions in the atmosphere of the stars, like the stellar chromospheres, that present large departures from LTE. We have seen that LTE holds if the occupation numbers can all be described by the Boltzmann formula for the kinetic temperature. For a given transition the source function is always given by the Planck function for the excitation temperature for the two levels involved in the transition. In *non-LTE (NLTE)* conditions we will find different excitation temperatures for different pairs of energy levels.

Deviation from LTE occurs in hot stars due to the discontinuities in the continuous absorption coefficients, especially in the UV, where most of the flux is emitted. In the photosphere of cool stars where the radiation field does not deviate much from the Planck function the LTE approximation works well. Mihalas et al. (1978) have shown that the LTE approximation is not too bad for all main sequence stars and giants with $T_{eff} <$ 25000 K. However, processes like *resonance scattering*, *overionization*, *photon pumping* and *photon suction* are pure NLTE effects and they play a relevant role in spectral line formation. For more details about NLTE effects see Asplund (2005) and references therein.

3.3.2 Stellar atmospheres models: the art of modelling the atmosphere of a star

The derivation of precise element abundances and main stellar parameters requires realistic models of the stellar atmospheres and the spectrum formation processes. The determination of the atmosphere parameters are therefore never more trustworthy than the models used to analyze the observations. The main source of uncertainties in stellar abundances analyses come from inadequacies in the line formation modeling and the input atomic and molecular physics (Asplund (2005)). Briefly, calculating a *model atmosphere* is normally based on radiative and convective equilibrium, together with hydrostatic equilibrium. This gives the run of physical parameters with optical depth at some chosen wavelength, using as input parameters T_{eff}, the surface gravity g and the chemical composition. Effects of

line opacity (line blanketing) on the structure of the atmosphere need to be allowed as well as parameters to describe rotational and micro-turbulent velocity. The *flux distribution* or *synthetic spectra* is the emergent flux predicted by a model atmosphere.

An enormous amount of work has been done since the first grids of line-blanketed, model atmospheres for late-type stars were published (Carbon & Gingerich (1969)). There has been a remarkable improvement for atomic and molecular absorption. Accurate continuous absorption coefficients for a number of heavy elements have been calculated within the Opacity Project (Seaton et al. (1994)), and the Iron Project (Bautista (1997)). Thanks to the effort of Kurucz, line lists[3] with transition probabilities for millions of lines of heavy elements have been calculated. See, for example, *Vienna Atomic Line Database*, VALD (Stempels et al. (2001). Extensive line lists have been calculated for most diatomic and polyatomic molecules that contribute to the opacity in stellar atmospheres. The lists are based on laboratory measurements of wavelengths and *gf* values[4].

In the last years it has been possible to relax the traditional assumptions of plane-parallel stratification in homogenous layers, of stationary hydrostatic equilibrium, mixing-length convection and local thermodynamic equilibrium (LTE). Grids of spherically-symmetric-models for giants and supergiants were made by Plez et al. (1992). Dynamic pulsating model atmospheres for cool giants have been developed by Wood (1979) and Bowen (1988). Nordlund & Dravins (1990), Stein & Nordlund (1998), Asplund et al. (1999) developed 3D simulations with proper hydrodynamics and radiation fields taken into account for solar-type stars, and Freytag (2001) developed full *star-in-a-box* models for supergiants. These simulations show a striking agreement with observations of solar granulation and spectral line profiles for solar type stars, and clearly demonstrate the qualitative difference between traditional 1D models and reality. Due to the great number of atomic and molecular species affecting the radiative field a consistent treatment of radiative transfer in models for late-type stars without making the assumption of LTE is complicated. From the first attempt to construct a reasonably realistic non-LTE model for a late-type star (the Sun) made by Anderson (1989), the development of algorithms and computers has now made it possible to calculate grids of such models. The lack of accurate collision cross sections is still a major problem in these efforts. For more details and references see Gustafsson et al. (2008).

Overview of synthetic stellar libraries

The majority of model atmosphere available are classical, in the sense they are one-dimensional, i.e., spherically symmetric or plane-parallel, with LTE assumed and treat

[3] http://kurucz.harvard.edu

[4] *gf* is the product of the oscillator strength f of an atomic transition and the statistical weight g of the lower level. Also known as weighted oscillator strength.

convection using the standard mixing-length theory[5]. There are interesting reviews of the current synthetic stellar libraries done by Bertone (2005) and Martins & Coelho (2007). Bertone (2005) present a very handy compilation of the synthetic stellar libraries available (see his Table 1) indicating the resolving power, the dispersion, the geometry adopted, the mixing length parameter used and the stellar parameters covered.

Martins & Coelho (2007) tested the accuracy of different synthetic stellar and empirical libraries. Martins & Coelho (2007) compared *Coelho* (Coelho et al. (2005)), *Martins* (Martins et al. (2005)) and *Munari* (Munari et al. (2005)) libraries with three empirical libraries: *Indo-US* (Valdes et al. (2004)), *MILES* (Sánchez-Blázquez et al. (2006)) and *Elodie* (Prugniel & Soubiran (2001)). Martins & Coelho (2007) compared the model predictions with an empirical color-temperature relation published by Worthey & Lee (2011) and they found that all the models are bluer in the B-V and H-K plane with respect to the empirical calibration. Martins & Coelho (2007) also found that the atmosphere models are systematically worse for the very cool stars and the blue region of the spectra. Models do still not reproduce molecular lines at low temperatures very well and Martins & Coelho (2007) highlight the effect of different choices of atomic and molecular line lists, especially in the blue region of the spectrum. Fig. 2 in Bertone (2005) shows the spectral energy distribution of three models from the Brott, MARCS and Munari spectral libraries, from the mid-UV to the near infrared. The different theoretical models differ clearly in the spectral region from 3000 Å to 4000 Å for cool stars ($T_{eff} < 4500$ K).

The stars we use for this project cover a small range in temperature being mainly solar-type stars. For that reason we have compared a Sun spectrum versus two close synthetic model from Munari et al. (2005) and Coelho et al. (2005). The Sun is the closest star to us and therefore the best understood star from both the observational and theoretical side. The main stellar parameters of the Sun are 5777 K for T_{eff}, 4.44 for log g, 0.0 for [m/H] and $[\alpha/Fe] = 0.0$ (Stix (2004)).

The spectrum of the Sun in Fig. 3.2 comes from Colina et al. (1996). The ultraviolet and optical spectrum is based on absolute flux measurements from satellites and from the ground. We degrade the spectrum to the resolution of the program stars for a comparison with the models. Both models, Munari (Munari et al. (2005)) and Coelho (Coelho et al. (2005)) do not reproduce the blue range of the optical spectrum of the Sun. Both models show a higher flux value compared to the Sun spectrum. We need to have in mind that a very precise flux calibration in the blue is always difficult. In the blue the uncertainty of the flux could increase up to about 20% due to the variability of the solar energy. Martins & Coelho (2007) conclude that for stars with $T_{eff} \leq 7000$ K, the library by Coelho et al. (2005) is the one with best average performance. However, from Fig. 3.2 we have that the Munari model matches the observed Sun spectrum better than Coelho. Edvardsson (2008) also compared observed versus predicted stellar flux distributions of solar-type stars. The results strongly suggest that there are systematic errors in the ultra-

[5]The mixing-length theory was introduced in ATLAS6 code by Kurucz (1979), and is a phenomenological approach to convection.

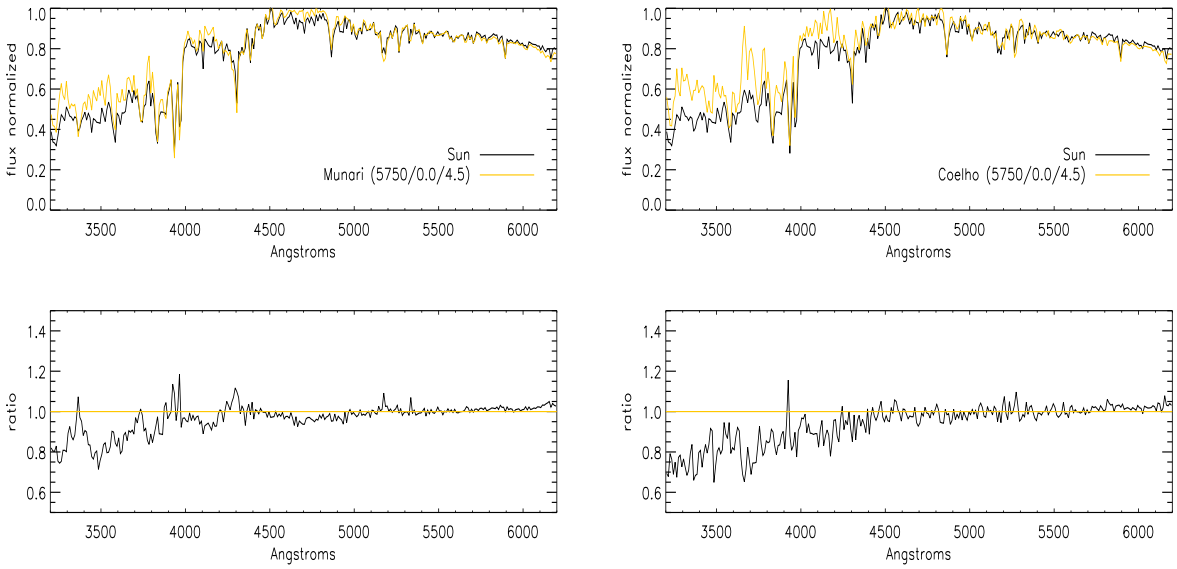

Figure 3.2: Left: the spectral energy distribution of the Sun from Colina et al. (1996) (black line) and close model from Munari spectral library (yellow line). The model is systematically worse in the blue region. Right: Comparison between the Sun from Colina et al. (1996) (black line) and a close model from Coelho spectral library (yellow line). Note the clear discrepancies in the blue region of the spectra.

violet and blue opacities used in the construction of the model atmospheres.

Fig. 3.3 shows a comparison between the Sun spectrum from Thuillier et al. (2004) and stellar atmosphere models from different libraries. Clearly, the models present discrepancies with respect to the Sun spectrum for wavelengths < 4500 Å.

3.4 Derivation of the atmosphere parameters of the observed stars

Bessell (2007) has shown that simple spectroscopic observations can yield accurate values for *log g* through comparison of the Balmer jumps of low-resolution spectra with recent grids of synthetic flux spectra. Blueward of 3636 Å, the continuous opacity is mainly H^-, whereas redward it is H^- plus H I. As *log g* decreases, the H^- opacity decreases and the size of the Balmer discontinuity increases. Bessell (2007), using the Munari et al. (2005) library to measure the Balmer jump, concludes that if the effective temperature of the FGK star is known to within 100 K, the Balmer jump will yield an effective gravity to about 0.2 dex. That is one of the main reasons why we have decided to use *Munari* for our studies. We have mentioned above that there are no huge differences between the stellar

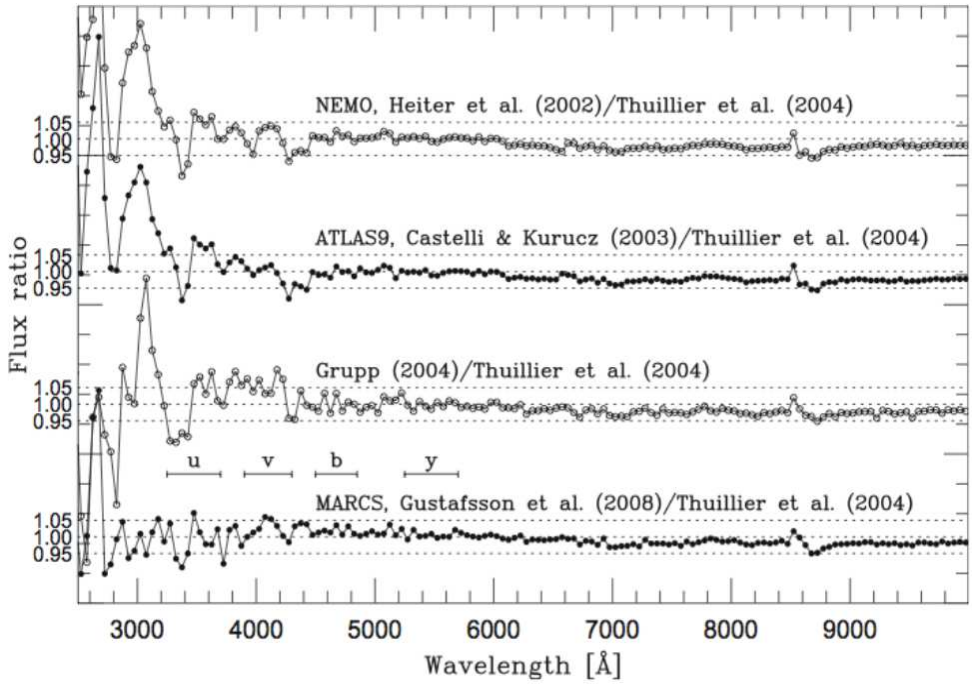

Figure 3.3: Solar photospheric model fluxes (NEMO, ATLAS9, Grupp, MARCS) compared with observations (Thuillier et al. (2004)). The dominating portions of the Strömgren *uvby* photometric passbands are also indicated (figure from Edvardsson (2008)).

synthetic libraries currently available. However, the problems mentioned above about the systematic errors in the blue opacities of the model atmospheres and the fact that the sensitivity of most spectrographs and CCDs decreases rapidly below 3600 Å could be a handicap in order to get accurate stellar parameters via flux calibrated spectra. We have also explored an empirical library, MILES (Sánchez-Blázquez et al. (2006)), to determine the atmosphere parameters of the observed stars. In this section we describe the results we have found using both libraries as well as the different methods employed. We describe in more detail the libraries used.

3.4.1 An extensive library of 2500-10500 Å synthetic spectra

Munari et al. (2005) present a complete library of synthetic spectra based on Kurucz's codes that covers the 2500-10500 Å wavelength range at resolving powers from high resolution to 2000 and uniform dispersions of 1 and 10 Å/pix. The whole library was computed using the SYNTHE code by Kurucz (Kurucz & Avrett (1981)). To calculate this library a new opacity distribution functions (ODFNEW models) from Castelli & Kurucz (2003) were adopted.

The adoption of new ODFs, replacing of the solar abundances from Anders & Grevesse

Temperature (K)	$4500 \leq T_{eff} \leq 6500$ K (steps of 250 K)
Gravity (cgs units)	$1.0 \leq \log g \leq 5.0$ (steps of 0.5 dex)
Metallicity	-2.5 $\leq [M/H] \leq$ 0.5 (steps of 0.5 dex)
Rotation velocity	2 km/s
Enhancement	$[\alpha/\mathrm{Fe}] = 0.0, +0.4$
Micro-turbulent velocity	2 km/s
Dispersion	1 $\mathring{A}$/px
Flux calibrated	erg cm^{-2} s^{-1} $\mathring{A}^{-1}$

Table 3.2: Range of properties for the selected templates we use to get the stellar parameters of our targets.

(1989) with those from Grevesse & Sauval (1998), and with improvements in the molecular opacities including the adoption of the molecular line-lists of TiO by Schwenke (1998) and of H_2O by Kurucz (1999). The ODFNEW models were computed with the overshooting option for the mixing-length convection switched off. Munari et al. (2005) claim that analysis in several papers have demonstrated that for stars with active convection ($T_{eff} < 9000$ K) the no-overshooting convection treatment provides better agreement with the observations than the overshooting case does. The no-overshooting models used to create this library were computed for a mixing-length parameter up to a scale height of 1.25. Munari et al. (2005) argue that this value allows to fit the observed solar irradiance, contrary to what we have seen in this thesis (see Fig. 3.2). This library used the Kurucz atomic and molecular line-lists (Kurucz (1992a)). Several molecules were taken into account, including C_2, CN, CO, CH, NH, SiH, SiO, MgH and OH and for stars cooler than 5000 K the TiO molecular lines (from Grevesse & Sauval (1998)) were included in the computation.

Our targets were selected as subgiants candidates, the range in temperature and gravity is small (G IV stars). We have selected a number of templates according to our need. In Tab. 3.2 we present the characteristics of the selected templates. We use stellar spectra with fixed values in rotational velocity and micro-turbulent velocity. The resolution of the observed spectra is quite small hence variations in these parameters are extremely hard to see. We explored spectra at the used resolution with different values in micro-turbulent and rotational velocity and we did not note significant changes. In general the effects of rotation on the continuous spectrum are small but the spectral lines could show significant changes by the relative Doppler shifts of the stellar disk. The effect of rotation is often called the rotational broadening; the spectral lines appear more broad for stars with high velocity rotation. Rapid rotation is normal for hot stars while slow rotation is seen for cool stars (e.g. Soderblom (1982), Royer et al. (2002)). In the case of subgiants they show a wide range of rotation rates for stars hotter than G0 IV, but slow rotation for cooler stars (Royer et al. (2002)). A typical rotation rate in the G-star region for evolved stars is $\leq$ 5-8 km/s (Gray & Toner (1987)). In this study we fixed the value of the rotational velocity for the theoretical atmosphere models to 2 km/s. The micro-turbulent (ζ) is small-scale mass motions, these small-scale velocities produce Doppler shifts and the effects are line

broadening. Evidences point toward ζ increasing toward higher luminosities, from 0.0 to 1.5 km/s for dwarfs up to 5 km/s in supergiants Gray (2008). In our study we use the models with $\zeta = 2$ km/s.

The main goal is to determinate the stellar parameters from the flux calibrated observed spectra using the theoretical model atmospheres as a reference system. We are covering a large spectral range, running from 3200 to 6200 Å. In the next figures we explore how sensitive the different spectral features are to the main atmospheric parameters (T_{eff}, [m/H], log g and [α/Fe]).

The effective temperature is defined by

$$T_{eff} = (\frac{L}{4\pi R^2 \sigma})^{1/4} \tag{3.23}$$

where L is the total luminosity, R the radius of the star and σ the Stefan-Boltzmann constant. T_{eff} is the measure of the temperature of the gas that forms the bulk of the stellar atmosphere.

The surface gravity (g) is calculated by

$$g = \frac{GM}{R^2} \tag{3.24}$$

where M is the mass of the star and G is the gravitational constant. The surface gravity fixes the pressure gradient in the atmosphere and largely determines the densities at which spectral lines are formed.

The chemical composition of the atmosphere determines the relative strengths of spectral lines of the different atomic species present. We can characterize the chemical composition of a star by quoting the abundance relative to hydrogen of any heavy element, for example Fe. Stars rich in Fe tend to be rich in other elements heavier than helium. The iron abundance, denoted [Fe/H], is defined to be

$$[Fe/H] = log_{10}(\frac{n(Fe)}{n(H)})_{star} - log_{10}(\frac{n(Fe)}{n(H)})_{\odot} \tag{3.25}$$

where n(X) is the number of X atoms per unit volume. Note that we define the abundances of a star with respect the abundances in the Sun[6]. We often refer to *metallicity*, denoted [m/H], to account for the complete chemical composition (elements heavier than He) of an object.

[6]The solar chemical composition has recently undergone a drastic revision, in particular in terms of the C, N, O and Ne abundances that have been lowered by almost a factor of two (Asplund (2008)).

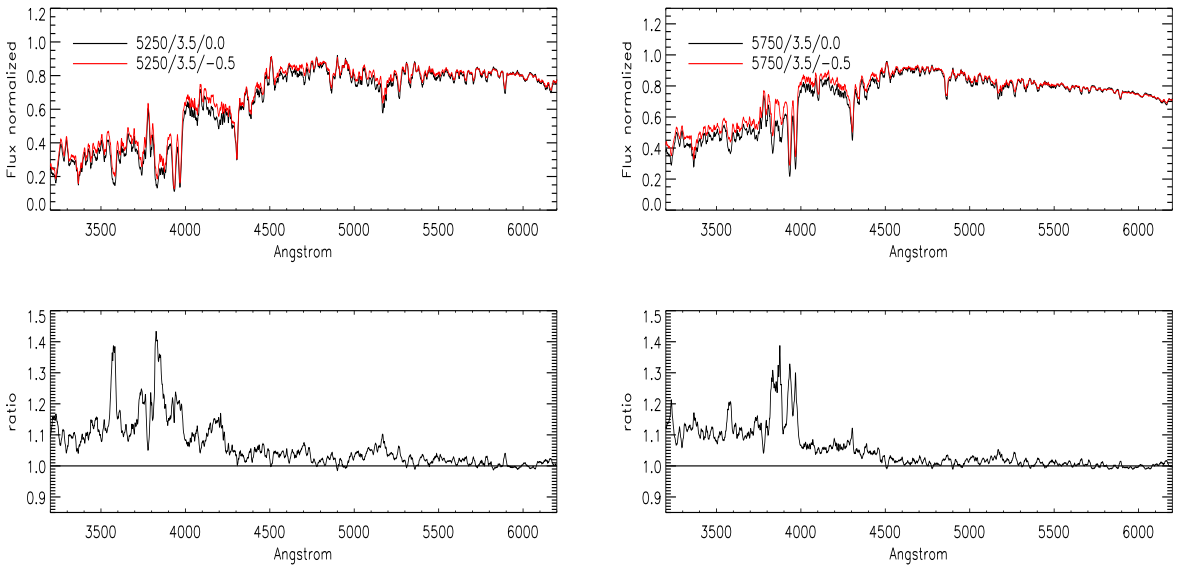

Figure 3.4: Comparison between spectra with the same temperature (5250 K and 5750 K respectively) and gravity but different metallicity ([m/H] = 0.0/-0.5) at solar alpha abundances. The metallicity information shows up clearly between 3200 and 4500 Å.

In Fig. 3.4 there are clearly a couple of features very sensitive to metallicity. There is one between 3540 Å and 3600 Å. In this region there are four strong absorption lines that in our spectra appear blended due to the low resolution. The main lines are Fe I 3565, Ni I 3566, Fe I 3570, Mn I 3570, Cr I 3571, Fe I 3574 [7]. We find another important feature between 3800 Å and 3900 Å. In this range the main absorption lines are Fe I 3859, 3872. We also note that the Ca II H & K lines at 3933 and 3968 Å carry metallicity information. The spectral range from 4400 to 6200 Å is not carrying much metallicity information.

Fig. 3.5 shows that the UV region of the spectrum (3200 - 4100 Å) is pretty sensitive to gravity. We find also that Mg I b 5183 line (Mg b triplet) is strongly dependent on gravity. There are two Na I 5889, 5895 lines blended due to the low resolution carrying gravity information as we see in the figure.

In Fig. 3.6 the shape of the whole spectra changes when we modify the temperature. The slope between 4400 Å to 6200 Å is a clear indicator of the temperature of the star. We also find that the UV region shows a dependency with temperature. This behaviour of the spectrum in the UV presents a significant degeneracy between metallicity and temperature as we will see below when representing the χ^2 contour plots in the two-dimensional parameters space.

[7] We use the Sun spectrum at R = 350.000 from *The Interactive Database of Spectral Standard Star Atlases* to get the lines information (Lobel (2008)).

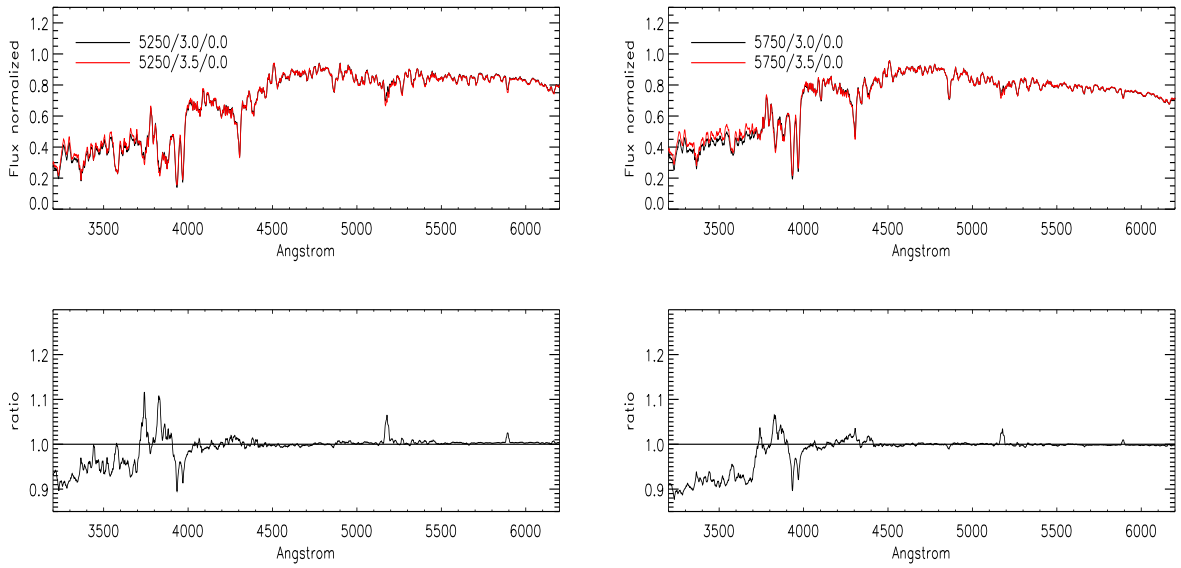

Figure 3.5: Comparison between spectra with the same temperature (5250 K and 5750 K respectively) and metallicity but different gravity (log g = 3.0/3.5) at solar alpha abundances. There is gravity information in the blue range of the spectra and some features like Mgb and NaD lines are also sensitive to gravity.

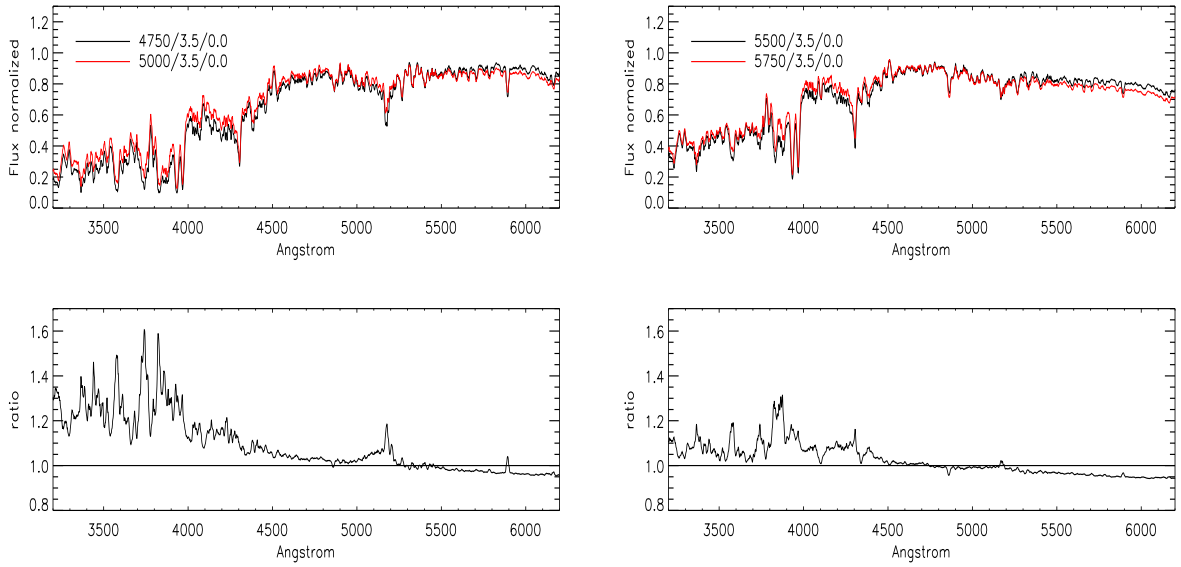

Figure 3.6: Comparison between spectra with the same metallicity and gravity but different temperature (T_{eff} = 4750/5000/5500/5750) at solar alpha abundances.

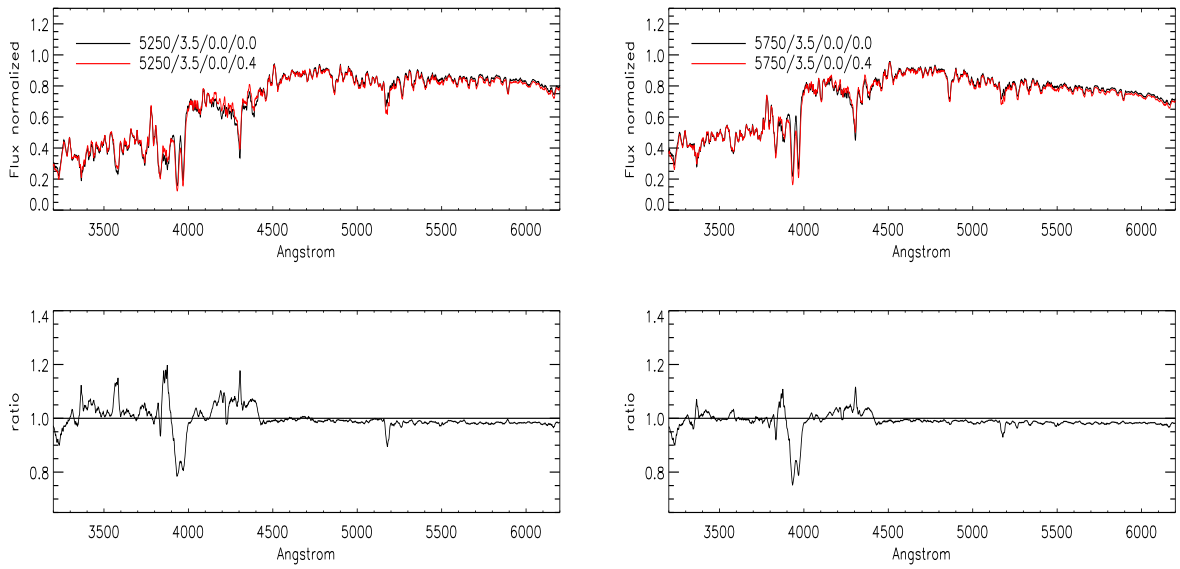

Figure 3.7: Comparison between spectra with the same temperature, metallicity and gravity but different [alpha/Fe] (0.0/+0.4). On the left for a spectrum with T_{eff} = 5250 K and on the right for a spectrum with T_{eff} = 5750 K.

Alpha elements are Z $\leq$ 22: O, Ne, Mg, Si, S, Ar, Ca, Ti. They are synthesized by alpha-capture in the silicon fusing[8] precursor state to Type II supernovae. Silicon and calcium are purely alpha process elements. Magnesium can be burned by proton capture reactions.

The abundance of alpha elements in stars is usually expressed in a logarithmic manner

$$[\alpha/Fe] = log_{10}(\frac{n(\alpha)}{n(Fe)})_{star} - log_{10}(\frac{n(\alpha)}{n(Fe)})_{\odot} \tag{3.26}$$

where n(X) is the number of X atoms per unit volume. In Fig. 3.7 we try to understand the sensitive part of the optical spectrum to [alpha/Fe]. Ca and Mg lines show a clear variation when we modified the [alpha/Fe] abundances. Note also that the G-band around 4300 Å is quite sensitive to the alpha elements.

[8]In astrophysics, silicon burning is a brief sequence of nuclear fusion reactions that occur in massive stars ($M_{star} \geq 8$ $M_{\odot}$). Silicon burning is the final stage of fusion for massive stars that have run out of the fuels that power them for their long lives in the main sequence

3.4.2 Medium-resolution Isaac Newton Telescope library of empirical spectra (MILES)

Recently, many new empirical libraries suitable to stellar population synthesis have been made available with improved spectral resolution and parameter coverage: e.g. STELIB (Le Borgne et al. (2003)), UVES POP (Jehin et al. (2005)), Indo-US (Valdes et al. (2004)), ELODIE (Prugniel & Soubiran (2001)), MILES (Sánchez-Blázquez et al. (2006)) and NGSL (Gregg et al. (2004)). For this study we are using the MILES library. MILES was carefully created trying to fill the major gaps in T_{eff}, [m/H] and log g presented in other empirical libraries. MILES also presents a careful treatment in the flux calibration. An inconvenience with this library is that the spectral range of our data starts at 3200 Å while the library starts at 3525 Å.

The library consist of 985 models spanning a large range in atmospheric parameters. The spectra were obtained at the 2.5m INT telescope and cover the range 3525-7500 Å at 2.3 Å (FWHM) spectral resolution [9] (Sánchez-Blázquez et al. (2006)). The library contains stars with a wide range of stellar parameters. The spectral type of the stars goes from O to M, the library covers all luminosity classes and a wide distribution of metallicities (-2.7 $<$ [m/H] $<$ 1.0). The sample selection are field stars from the solar neighborhood. These stars are covering a wide range in age (from open clusters) and different metallicities (from Galactic globular clusters) are also included. In addition, with the aim of filling gaps and enlarging the parameter-space coverage, stars from additional compilations were carefully selected (see Sánchez-Blázquez et al. (2006) and references therein).

A reliable flux calibration for the MILES library was obtained by using several spectrophotometric standards (BD+33 2642, G 60-54, BD+28 4211, HD 93521 and BD+75 325) observed each night at different air-masses. A special effort was made to avoid the selective flux losses due to the differential refraction observing through a 6-arcsec slit. Sánchez-Blázquez et al. (2006) also made a correction of the second-order contamination at the red end $\lambda > 6700$ Å. Cenarro et al. (2007) constructed a larger, homogenous set of atmospheric parameters for the stars in MILES library. They defined an initial reference system against which other sources are calibrated and corrected for systematic differences. MILES uses the work by Soubiran et al. (1998) as initial standard source, since they compute self-consistent atmospheric parameters for a total of 211 echelle spectra of stars with $4000 < T_{eff} < 6300$ K over a wide range of log g and [Fe/H] following the method developed by Katz et al. (1998). The method relies on the least-square comparison of the spectrum of a target star to a library of 211 spectra of reference stars for which the atmospheric parameters are well known and which were observed with the same instrument. Tests performed with the library allow to estimate the internal accuracy to be 86 K, 0.28 dex and 0.16 dex for T_{eff}, log g, [Fe/H] for a target star with S/N = 100 (Katz et al. (1998)). Given that the stellar sample in Soubiran et al. (1998) does not comprise all stars

[9] Beifiori et al. (2010) found that the MILES resolution has previously been slightly overestimated. They derived a new spectral resolution of 2.54 Å FWHM, instead of the nominal 2.3 Å.

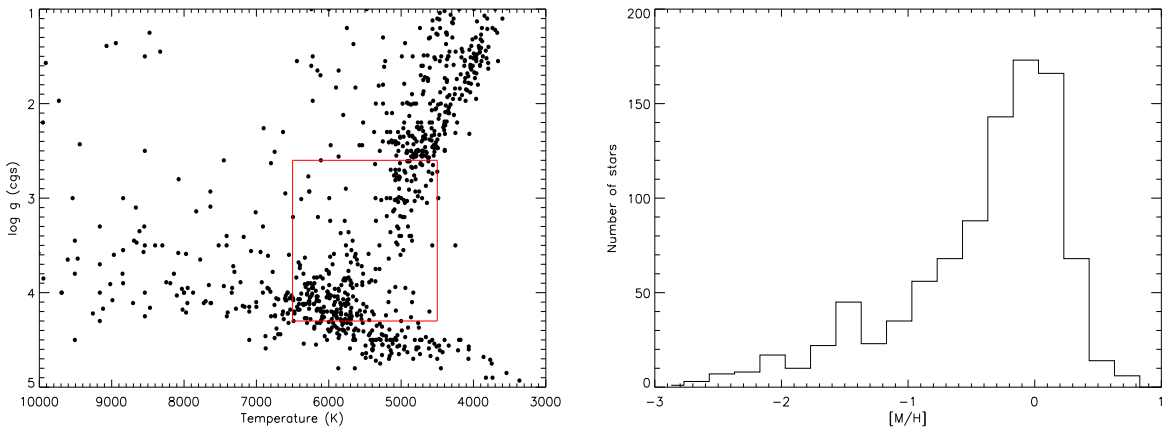

Figure 3.8: On the left: gravity-temperature diagram of the library stars. The red box indicates the subgiant region in the gravity-temperature plane. Note that for the present study the region of interest is even smaller (5000 < T_{eff} < 5700 K and 3.4 < log g < 4.1). On the right: the metallicity distribution function for the MILES library.

in MILES, they updated the compilation of atmospheric parameters by including data from recent publications and extending the search to all field stars in MILES. See Table 4 in Cenarro et al. (2007) for the references of the catalogues used in the compilation. Original sources giving any of the three atmospheric parameters for MILES stars were calibrated and bootstrapped against the reference system making use of all stars in common between both samples. The atmospheric parameters for the cluster stars have also been revised and updated according to recent metallicity scales, colour-temperature relations and improved set of isochrones. See Cenarro et al. (2007) and Cenarro et al. (2001b) for details.

In Fig. 3.9 there is a good agreement between the Sun spectrum from Colina et al. (1996) and a close model from MILES library with T_{eff} = 5750 K, [m/H] = 0.0 and log g = 4.5. Note that a small systematic shift arise in the blue region of the spectrum ($\lambda \leq$ 3900 Å). This effect could be due to flux calibration issues as in this case both spectra are empirical. Recently, Prugniel et al. (2011) have redetermined the atmospheric parameters of MILES stars in order to improve the homogeneity and accuracy using ELODIE (Prugniel & Soubiran (2001)) as reference. To determine the atmospheric parameters, Prugniel et al. (2011) compared the observed MILES spectra with templates built from the ELODIE library via χ^2 minimization. They emphasize they obtain precisions of 60 K, 0.13, and 0.05 dex, respectively, for T_{eff}, log g, and [Fe/H] for the FGK stars.

Fig. 3.10 and Fig. 3.11 show the comparison between the stellar parameters derived by Cenarro et al. (2007) and Prugniel et al. (2011). There are no systematic effects between the two samples but they show a significant scatter for the three parameters.

In Fig. 3.12 we represent the gravities and temperatures for MILES stars derived by

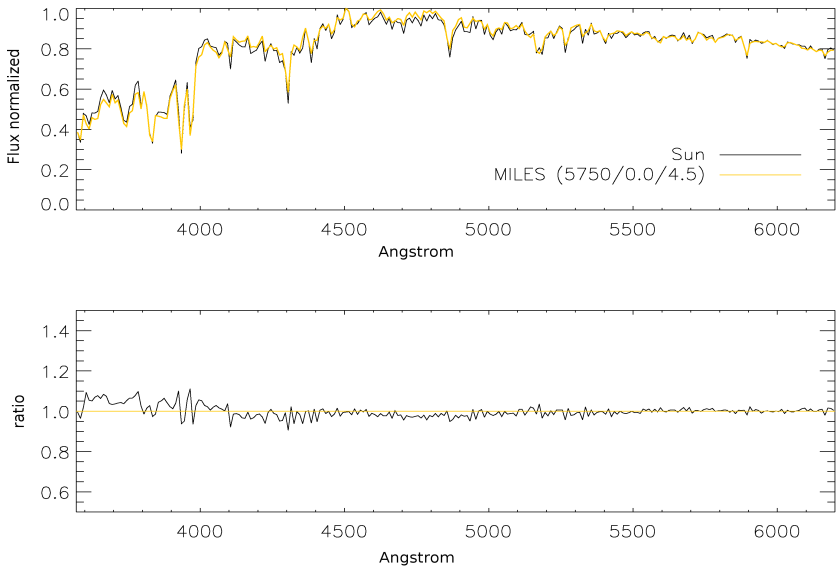

Figure 3.9: Comparison between the Sun spectrum from Colina et al. (1996) and close model from MILES library. The temperature, the metallicity and the gravity of the spectrum from the library are indicated on the legend (T_{eff}/[m/H]/log g). In the second panel we show the ratio between both spectra.

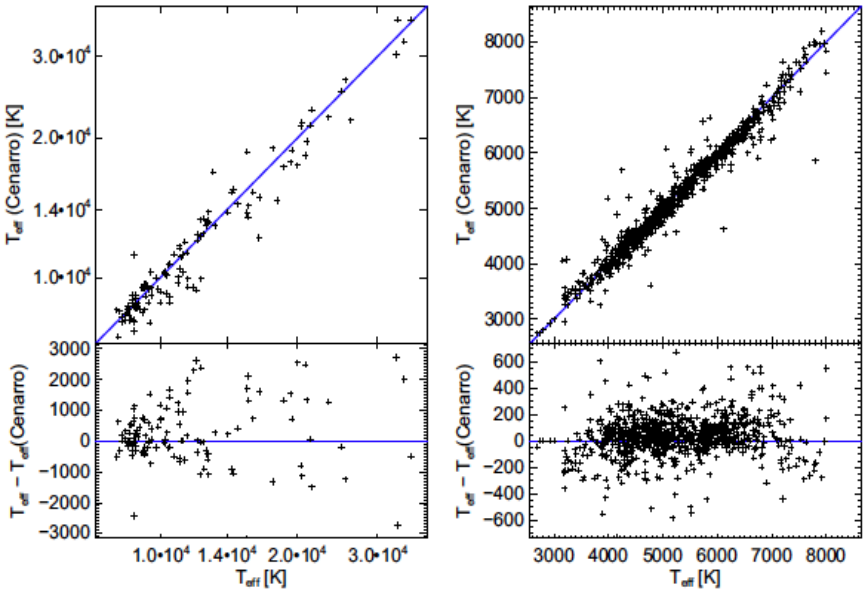

Figure 3.10: Comparison of the measured atmospheric parameters of the Prugniel et al. (2011) and Cenarro et al. (2007) compilations, for hot and cool T_{eff} respectively.

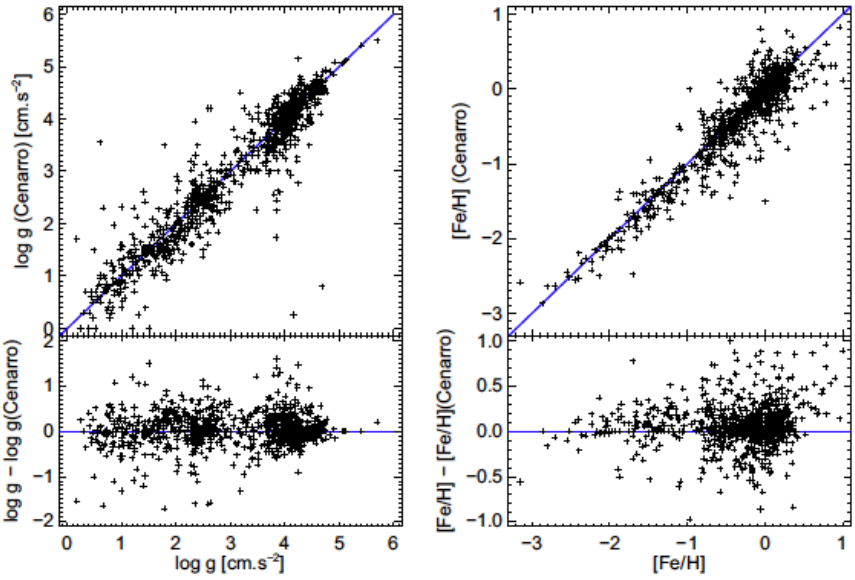

Figure 3.11: Comparison of the measured atmospheric parameters, log g and [Fe/H], of the Prugniel et al. (2011) and Cenarro et al. (2007) compilations.

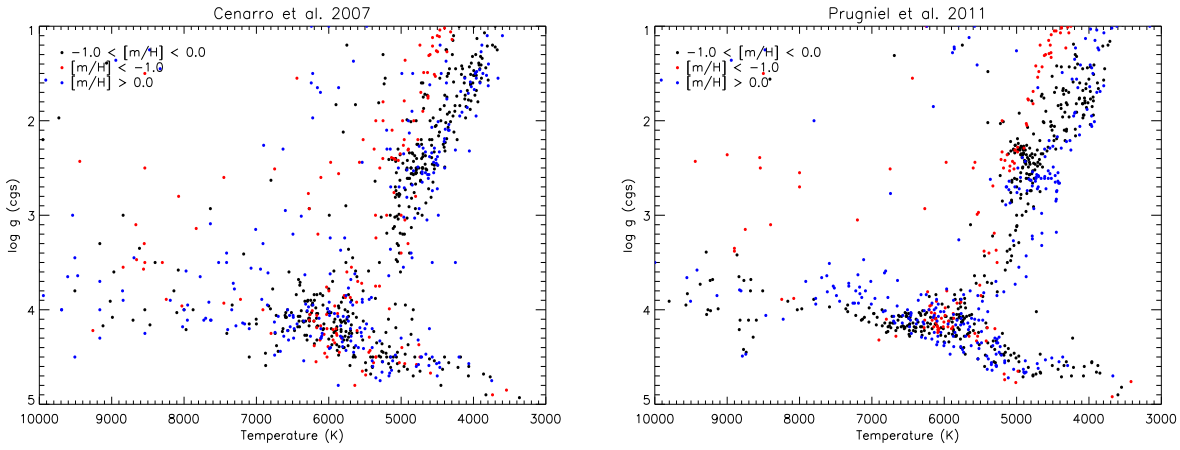

Figure 3.12: The temperature-gravity diagram for MILES stars derived by Cenarro et al. (2007) and Prugniel et al. (2011) color-coded according to the metallicity of the stars ([m/H] > 0.0 (blue), -1.0 < [m/H] < 0.0 (black) and [m/H] < -1.0 (red)).

Cenarro et al. (2007) and Prugniel et al. (2011) color-coded according to the metallicity of the stars. Both stellar parameters show clearly the main sequence, the subgiant branch and the red giant branch. Prugniel et al. (2011) show a more evident red clump region around log g $\sim$ 2.7 and T_{eff} $\sim$ 4900 K. The new stellar parameters from Prugniel et al. (2011) presents a smaller scatter suggesting that the stellar parameters are more accurate

that the ones from Cenarro et al. (2007).

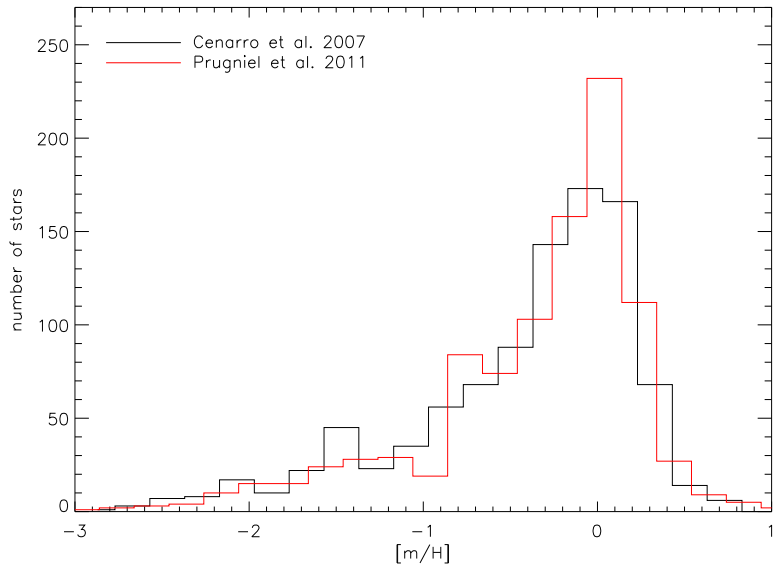

Figure 3.13: Metallicity distribution functions for the metallicities derived by Cenarro et al. (2007) (black) and the metallicities derived by Prugniel et al. (2011) (red).

Fig. 3.13 show the metallicity distribution functions for the metallicities derived by Cenarro et al. (2007) (black) and the metallicities derived by Prugniel et al. (2011) (red). Both distributions present a similar shape and a peak around solar metallicity but the metallicities from Prugniel et al. (2011) show a more prominent peak at solar abundances.

3.4.3 Spectral resolution: Exploring the power spectrum

The Fourier concepts have been widely applied in astrophysics, in particular in spectroscopic techniques, e.g. analysis of line profiles, spectrograph resolution, studies of line absorption coefficients, astrophysical time-series analysis, restoration of astronomical data, cross-correlation analysis, convolutions, etc. In the present work the low resolution spectra were acquired using a wide slit. The final resolution of the spectra depends on the width of the slit and the conditions of the night (*seeing*). The *seeing* is variable and we need to have the model atmosphere and data at the same resolution before we match them. We have developed a new method to determine the final resolution of the observed spectra using a close model in the Fourier space using the Power Spectrum.

The Fourier transform: Basic concepts

One can describe a physical process in the space domain, by the values of a quantity h as a function of position x (meters), e.g., h(x). H will be a function of inverse wavelength (cycles per meter). We take a function h(x) and write

$$H(\sigma) = \int_{-\infty}^{\infty} h(x) e^{2\pi i \sigma x}\, dx \tag{3.27}$$

The new function, H(σ), is the *Fourier transform* of h(x). The variables x and σ are called a Fourier pair. We can write the inverse transform

$$h(x) = \int_{-\infty}^{\infty} H(\sigma) e^{-2\pi i \sigma x}\, d\sigma \tag{3.28}$$

In the physical world of stars we assume the Fourier transform exists because not all functions have this kind of transforms. We can use Euler's expression, e^{ix} = cos x + isin x, to expand Eq. 3.27. Provided that h(x) is a complex function, h(x) = h_R(x) + ih_I(x), with h_R(x) the real and h_I(x) the imaginary component. In the general case we have that h(x) and H(σ) are complex function. In our case h(x) is the spectrum of a star and it may be a real function. Being h_I(x) = 0, we have

$$H(\sigma) = \int_{-\infty}^{\infty} h_R(x) cos 2\pi x\sigma\, dx + i \int_{-\infty}^{\infty} h_R(x) sin 2\pi x\sigma\, dx \tag{3.29}$$

The Fourier transforms of our spectra will be a complex functions, H(σ) = H_R(σ) + iH_I(σ); where the amplitude is

$$|H(\sigma)| = (H_R(\sigma)^2 + H_I(\sigma)^2)^{1/2} \tag{3.30}$$

and the phase

$$tan\phi = \frac{H_I(\sigma)}{H_R(\sigma)} \tag{3.31}$$

Parseval's theorem

The total power is defined by

$$TotalPower = \int_{-\infty}^{\infty} |h(x)|^2\, dx = \int_{-\infty}^{\infty} |H(\sigma)|^2\, d\sigma \tag{3.32}$$

and is the same whether we work it in the position domain or in the inverse wavelength domain. This results is the Parseval's theorem. When h(x) is a real function, as in the case of our spectra, the total power is

$$P_h(\sigma) = 2|H(\sigma)|^2 \tag{3.33}$$

We are effectively trying to estimate the smoothing of the spectrum over wavelength caused by the unknown seeing, so we can match the synthetic spectra properly to our observed spectra.

The Fourier transform of discretely sampled data

We have seen basics concepts about the Fourier transform for a continuos signal. In the most common experiments, the function h(x) is sampled at evenly spaced intervals. If Δ represents the position interval between consecutive samples, we could write

$$h_n = h(n\Delta x) n = ..., -2, -1, 0, 1, 2, ... \tag{3.34}$$

Let's call the spectrum that we have measured s(x) and write

$$s(x) = III(x)h(x) \tag{3.35}$$

where h(x) is the true spectrum and multiplication by III(x) gives the discrete sampling. III(x) is called the Shah function and is defined by

$$III(x) = \sum_{n=-\infty}^{\infty} \delta(x - n\Delta x) \tag{3.36}$$

where n is an integer and δ(x) is the delta function. The Shah function is also called the sampling symbol. Furthermore of sampling data we record data in a window. When we take a stellar spectrum, it extends from x_1 to x_2. We can express the windows in the data string by multiplication with a box, b(x), where the width is equal to the window limits of our observations. Our spectral data in Eq. 3.37 become

$$s(x) = b(x)III(x)h(x) \tag{3.37}$$

the function s(x) is our spectrum, sampled and bounded. However, when we measure the spectrum, the instruments imprint their signature on the observations. This footprint is called the δ-function response or the instrumental profile, I(x). We can rewrite Eq. 3.37 to include I(x)

$$s(x) = b(x)III(x)h(x) * I(x) \tag{3.38}$$

In the end, our measured spectrum is bounded, sampled and blurred[10]

Sampling and aliasing

For a sampling interval Δ, there is a frequency called the *Nyquist critical frequency* (f_c),

$$f_c \equiv \frac{1}{2\Delta} \tag{3.39}$$

The basic signal is effectively band-limited by the characteristics of the physical processes producing it. In our case, the signal band-limit is fixed by the characteristic widths of the spectral lines. According to the *sampling theorem*, a continuous function h(x), sampled at an interval Δ with a bandwidth limited to frequencies smaller than f_c, is determined by its samples h_n:

$$h(x) = \Delta \sum_{n=-\infty}^{\infty} h_n \frac{sin[2\pi f_c(x - n\Delta)}{\pi(x - n\Delta)} \tag{3.40}$$

What happens if a continuous function that is not bandwidth limited is sampled below the Nyquist critical frequency? In that case, it turns out that all of the power spectral density that lies outside of the frequency range $f_c < f < f_c$ is spuriously moved into that range. This phenomenon is called *aliasing*. Hence, the important issue is that no frequencies above the Nyquist frequency should be present in the data - the instrument should remove them before they get to the detector. Once they get to the detector, we cannot get rid of them.

The final resolution of the observed spectra

The use of a wide slit in our observation has an impact in the final resolution of the data. As mentioned above the *seeing* during the night drives the final resolution. If the source is extended due to the seeing and covers the whole slit the resolution is determined by the slit width but if the source is not covering the whole slit the seeing controls the final resolution. We need to degrade the models to the observed resolution to get a good match in order to secure the stellar atmosphere parameters. We have used Fourier space to understand the behaviour and the impact of the conditions of the night on the final resolution of the observed spectra.

[10]The convolution of the two functions, denoted g(x)∗h(x), is defined by $g * h = \int_{-\infty}^{\infty} g(x_1)h(x - x_1)\, dx_1$.

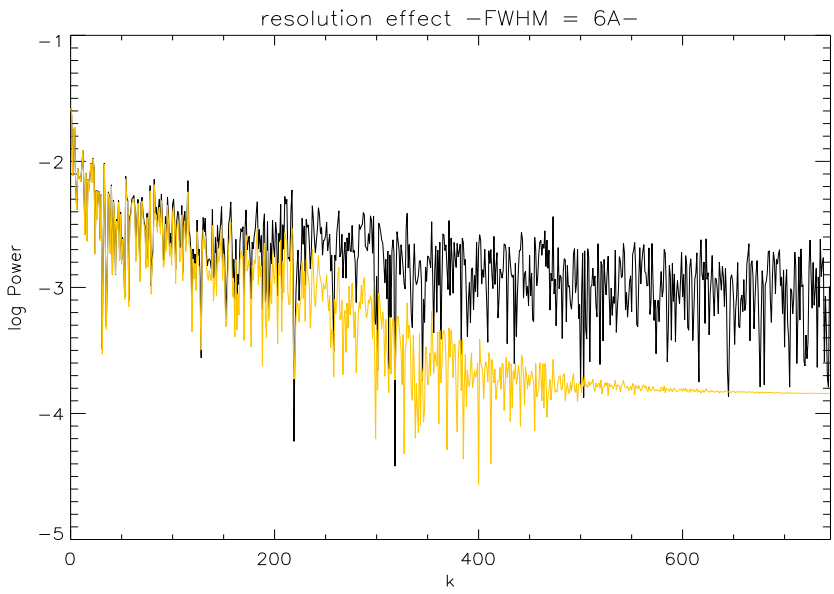

Figure 3.14: Power spectrum with different resolution. The original (black) and the degraded (yellow) show a clear different behaviour in the Fourier space.

The Power Spectrum (PS) is very sensitive to changes in the resolution of the spectrum (Fig. 3.14). To compute the Fourier transform of the spectra we use the algorithm called *Fast Fourier Transformation (FFT)*, see Press (1993) for details. The PS is computed via the Parseval's theorem for real functions discussed above. First, with the models described in Sect. 3.4.1 we find the close model from the raw library that matches the observed spectra using a simple minimum distances method in the Euclidean space $\Re^n$. We are fitting N data points from the observed spectrum (x_i,y_i) = 0,...,N - 1, to a model that has, in this case, just three adjustable parameters (T_{eff},[m/H],log g); a_j, j = 0,1,2. The model predicts a functional relationship between the measured independent and dependent variables, for this specific case we can write

$$y(x) = y(x|T_{eff}, [m/H], logg) \tag{3.41}$$

minimizing over a_0, a_1, a_2 we use a least-squared fit,

$$\sum_{i=0}^{N-1} [y_i - y(x_i|T_{eff}, [m/H], logg)]^2 \tag{3.42}$$

Once we find the best match we degrade the model at different resolutions from 2 Å to 15 Å (FWHM) in steps of 0.1 Å by convolving the model with a Gaussian profile. We work out the PS and using a minimum distances method we get the best fit in the Fourier

domain, i.e. we get the FWHM of the Gaussian we need to degrade the model to the exact resolution of the observed spectrum. In this case the adjustable parameter is just the FWHM (Å) of the Gaussian (T_{eff}, [m/H] and log g are just fixed). We can write

$$\sum_{i=0}^{N-1}[y_i - y(x_i|FWHM)]^2 \tag{3.43}$$

To get the resolution we use the range in wavenumber from $15 < k < 250$. For scaling the two spectra we use a small range from 2 to 20 in k. The pixel scale of the spectra is about 1.96 Å/pix. In the best seeing, the resolution could be as good as about 2.2 pixels, FWHM $\sim$ 4 Å (set by the seeing), and in the worst seeing it will be about 12 Å (set by the slit width). This is a big range and it indicates the importance to know the effective resolution for each spectrum to get a good match to the model spectra.

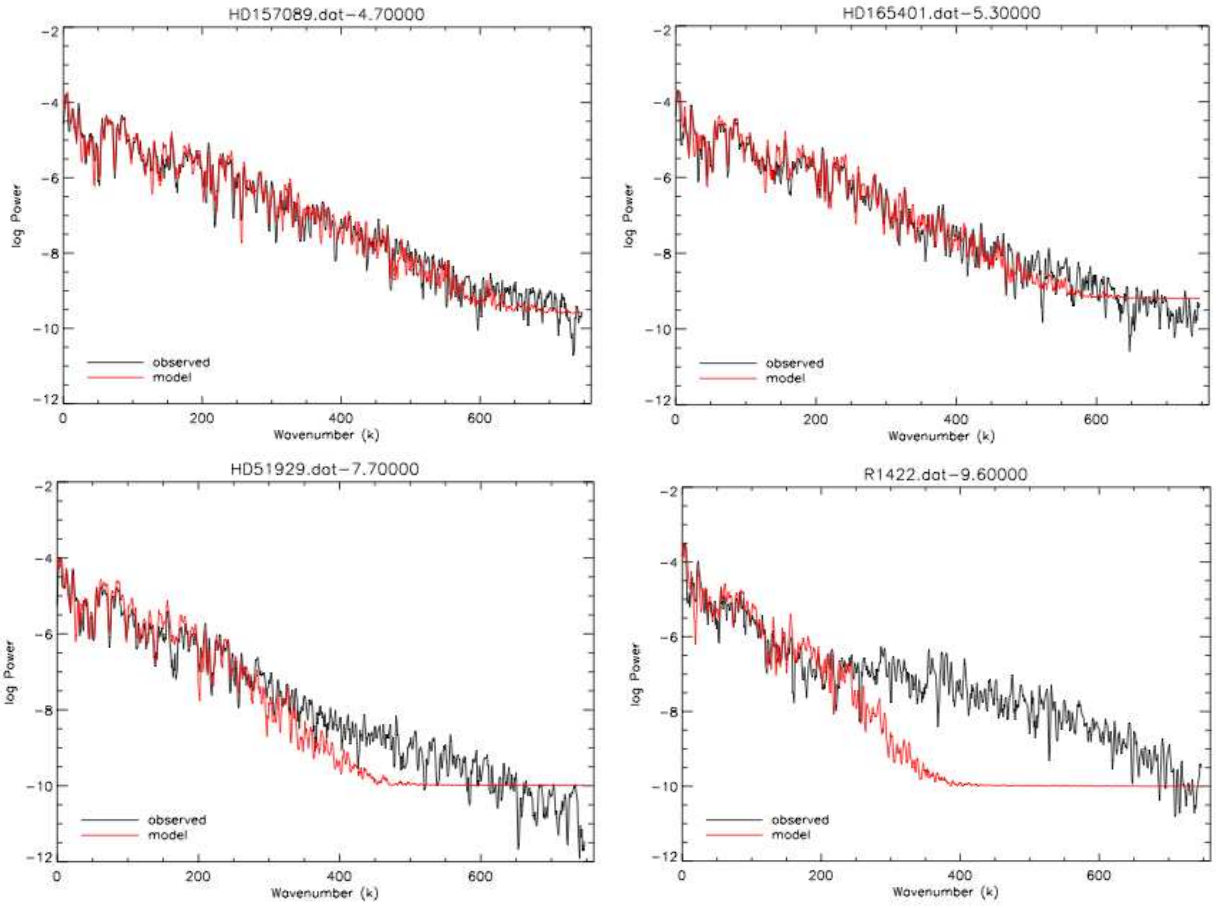

Figure 3.15: Power Spectrum of four different observed stars and a close model at different resolution. The FWHM of the model convolution is listed behind the star name at the top.

The method is very sensitive and we get an accuracy of 0.1 Å for the FWHM. In Fig. 3.15 we show how our method works for four different stars. The red line is the best match model to the observed stars in the Fourier space having the resolution as a free parameter. The noisy appearance of the PS arises from the beating of the sinusoidal components necessary to reproduce the spacing between the spectral lines (Brault & White (1971)). In the Fourier domain the signal dominates at high frequencies while the noise-contaminated signal appears for low frequencies. We see this effect clearly in Fig. 3.15, the model (red line) is noise free, and for low frequencies the PS shows a constant value. To measure the photon noise we take the mean value of the power in the range $725 < k < 740$, here the PS is nearly flat and comes almost entirely from photon noise, and we add this value to the model. However, even taking the photon noise into account we find a shift in power for some stars affecting the match between the observed star and the model. We found out that differences between the first and the last value of the model in the real domain could present some problems in the edge coming from the Fourier transformation of the spectra. To avoid this problem we have developed a kind of normalization that sets the edge of model to zero before the Fourier transformation.

Fig. 3.15 shows two stars with a very good seeing (top), FWHM = 4.7 and 5.3 Å respectively. There is one star that present quite low resolution (FWHM = 9.6 Å), note that the bad-seeing stars have excess power between $300 < k < 500$ approximately. This "bump" in power is an artifact of the slit. On nights with bad seeing the slit starts to be fully iluminated due to the broad *point spread function* (PSF[11]) of the star.

The PSF of the slit works like a top-hat function. Let us call to this function b(x),

$$b(x) = \begin{cases} 0 & \text{if } -W/2 > x > W/2 \\ 1 & \text{if } -W/2 \leq x \leq W/2 \end{cases} \tag{3.44}$$

The Fourier transform of b(x) is,

$$B(f) = W(\frac{sin(\pi W f)}{\pi W f}) = W sinc(\pi W f) \tag{3.45}$$

In our case W is the width of the slit (5" $\sim$ 6 px $\sim$ 12 Å). We need to convolve the PSF with contributions from the telescope optics (including seeing) and the spectrograph optics. When the seeing is very bad or the slit is completely illuminated (arc lamp) we could describe the behaviour in the Fourier space using the convolution between B(f) and G(f). For the arc or very bad seeing we have

[11]The point spread function (PSF) describes the response of an imaging system to a point source.

$$H(f) = B(f) * G(f) = [Wsinc(\pi W f)][exp(-2\pi^2\sigma^2 f^2)] \tag{3.46}$$

where σ = FWHM/2.35. According to Eq. 3.46 there is a relation between the number of lobes and the width of the slit. The sinc function is equal to zero at n/W.

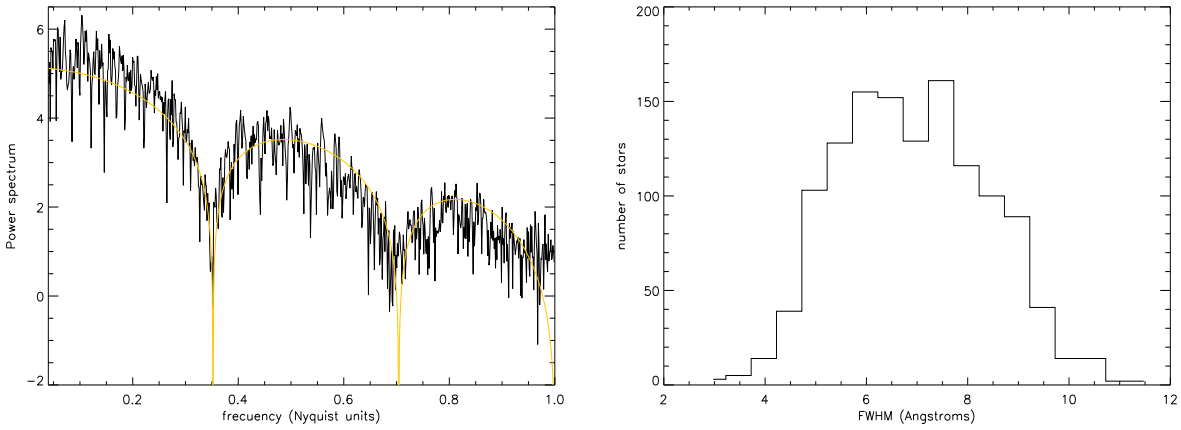

Figure 3.16: Left: Power Spectrum of the arc lamp and the representation of the function H(f) (yellow) described on the text. Right: Distribution of the FWHM (Å) for the whole sample. The final resolution of the observed stars cover a big range in FWHM.

The function H(f) from Eq. 3.46 presents a good agreement with the PS from the observational spectrum of an arc (Fig. 3.16). We see clearly the lobes coming from the behaviour of the slit as a sinc function in the Fourier domain. When the seeing is quite bad we see these lobes appearing in the PS of the observed stars due to the slit. See the star with FWHM = 9.6 in Fig. 3.15. On the right side of Fig. 3.16 we present the distribution of the resolution in for the whole sample of observed stars. As mention above the final resolution covers a big range going from FWHM $\sim$ 4 to 11 Å. With this method we are able to degrade the models to the exact resolution of the observed spectra taking account the effect of the earth's atmosphere on the observed stars.

We have some stars in common with the empirical library mentioned in Sect. 3.4.2. These stars in common present an excellent opportunity to test the PS method developed in the present work. Using the procedure described above we take the spectra from the empirical library as model. The resolution of the library is higher (FWHM $\sim$ 2.5 Å) than the theoretical resolution of the data. We can see the results in Fig. 3.17; our resolution method is be able to reproduce the final resolution of the observed stars and hence we can degradate the model to the resolution we need for the comparison. Fig. 3.17 shows that there is a very good agreement between the data and the library, indicating that the PS method can accurately correct for the resolution effects.

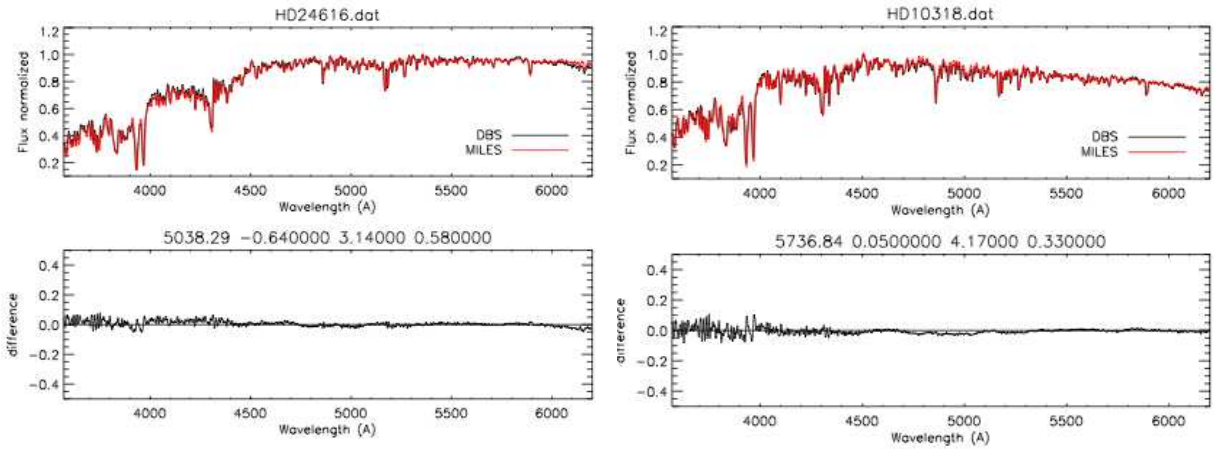

Figure 3.17: Comparison between the same stars observed in the present work and the MILES library, HD24616 and HD10318 respectively. T_{eff}, [m/H], log g and [Mg/Fe] are listed for both stars.

3.4.4 Stellar parameters: the minimum chi-square method

The observed spectra are flux calibrated, shifted to a rest frame and we have estimated their individual resolution, hence we are in a good position to compare the stellar atmosphere models with the observational data. The direct comparison between the two spectra is done by a chi-square minimization technique we describe below.

3.4.5 χ^2 test

The chi-square statistic describes the goodness-of-fit of the data to the model. If the observed numbers in each of k bins are O_i, and the expected values from the model are E_i, then the chi-square statistics is

$$\chi^2 = \sum_{i=1}^{k} \frac{(O_i - E_i)^2}{E_i} \tag{3.47}$$

Rather than picking specific features, we make optimal usage of the entire measured signal. The minimum chi-square method of model fitting consists of minimizing the chi-squared statistic by varying the parameters of the model. In this case the parameters of the model are just three, T_{eff}, [m/H] and log g. For [α/Fe] we use the MILES library and the work done by de Castro Milone et al. (2011) to get the [Mg/Fe] for the MILES stars. We will describe this method later. Another free parameter we should take into account is the reddening on the observed stars. In practice, the parameter search is easy enough

as long as the number of free parameters in less than four (Wall & Jenkins (2003), Avni (1976)).

Strong covariances between the free parameters are manifested when four or more parameters are used and one should use more sophisticated procedures. For that reason we are also treating the reddening independently using the Schlegel dust maps (Schlegel et al. (1998)) as explained later. The parallel between χ^2 and weighted least squares is evident; the statistic is the squares of the residuals weighted, in our case, by the observed spectra. A low S/N is a real handicap for the χ^2 minimization method. Our spectra have a very high S/N, > 100 at 5500 Å.

3.4.6 Stellar parameters using a synthetic library

We get a first guess of the stellar parameters using a theoretical library (Munari et al. (2005)). The selected templates are described in Tab. 3.2; the models are flux calibrated and the steps are ΔT_{eff} = 250 K, Δ[m/H] = 0.5 dex, Δlog g = 0.5 dex and [α/Fe] = 0.0/0.4 dex.

In general, there is a good agreement between the models and the observed spectra, however we find regions where the differences between the models and the observed spectra are up to 20%. Fig. 3.18 shows four observed spectra and the closest model via χ^2 minimization. The Ca II H & K lines are usually stronger in the models than in the observed stars. For very metal-poor stars ([m/H] $\leq$ -1.0) we find the opposite situation; the models have weaker Ca II lines than the observed ones. The G-band region around 4300 Å shows also some discrepancies between the empirical results and the models. We also find discrepancies in the very blue region. Note that for this exercise we do not correct the observed stars for reddening. We treat this problem in the next section, first we interpolate the library in smaller steps for the atmospheric parameters and we explore the results coming out from this exercise.

The library has large steps in the main stellar parameters (see Tab. 3.2). We use a *cubic spline* interpolation per wavelength to get steps in T_{eff} of 50 K and 0.1 dex in [m/H] and log g respectively. Spline interpolation uses low-degree polynomials in each of the intervals, and chooses the polynomial pieces such that they fit smoothly together (Press (1993)). Spline interpolation is often preferred to polynomial interpolation because it yields similar results, even when using low-degree polynomials, while avoiding Runge's phenomenon[12] for higher degrees. Zwitter et al. (2004) shows that linear interpolation is accurate to $\sim$ 10 % of the grid step. Zwitter et al. (2004) conclude that linear interpolation itself does not introduce errors exceeding 25 K in temperature (for $T_{eff} \leq$ 10 000 K) and 0.05 dex in [m/H] or log g. We have explored the impact of the interpolated theoretical library and the stellar parameters on the stars. To do that we have selected 50 different

[12] problem of oscillation at the edges of an interval that occurs when using polynomial interpolation with polynomials of high degree.

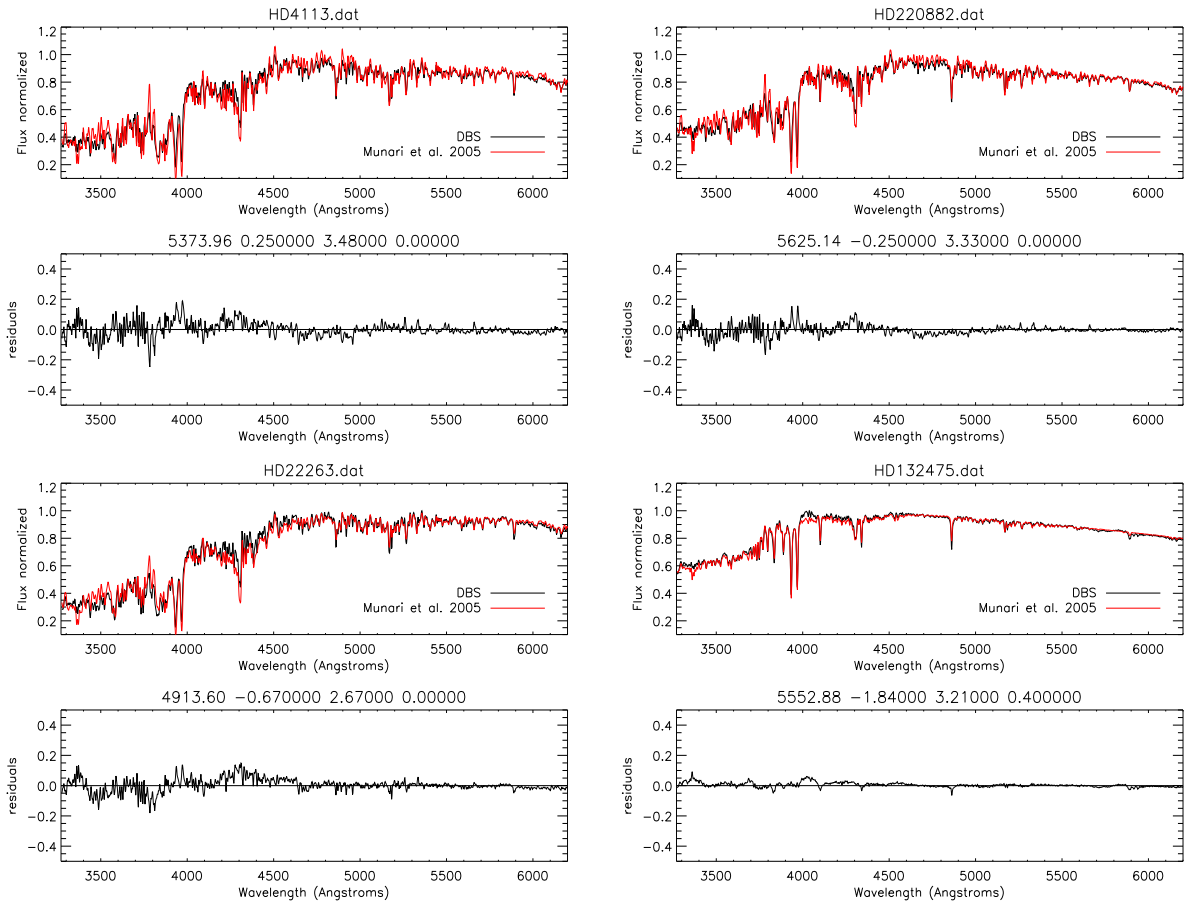

Figure 3.18: Four observed spectra (black line) and the closest model (red line) via χ^2 minimization. The figure also presents the T_{eff}, [m/H], log g and [α/Fe] we get for the four stars. We find some discrepancies in the blue region.

models from the original library to test the interpolation and degraded them to a common and typical resolution (FWHM = 9 Å). The χ^2 pipeline is be able to find the best match for the right stellar parameters for these models using the interpolated grid.

We have tested the surface of the χ^2 around the minimum for the 50 models. In Fig. 3.19 we show the χ^2 profile for two different models for [α/Fe] = 0.0 and [α/Fe] = 0.4. We find that the interpolated library provides clear χ^2 profiles and allows us to find the right stellar parameters. We see that the points close to the minimum represent a well defined surface suggesting that the interpolation of the library works well.

Fig. 3.20 shows the contour plots for the χ^2 surface in the two dimensional parameter space. Note how the interpolated library traces a more precise χ^2 surface than the raw grid as one would expect because the steps of the grid are smaller. There is a strong covariance between the metallicity and the temperature, pushing hot stars to look more metal-rich.

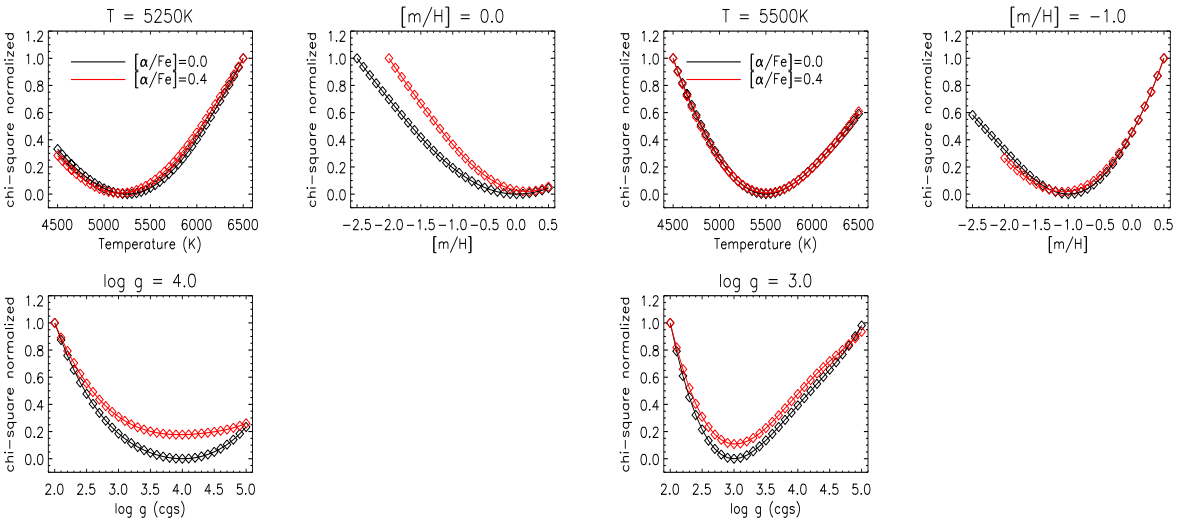

Figure 3.19: The χ^2 profile for two different models (5250/0.0/4.0/+0.0 and 5500/-1.0/3.0/+0.0 being temperature/metallicity/gravity/[α/Fe] respectively) for two values of [α/Fe] = 0.0 (black) and +0.4 (red). There is no α-enhancement models for stars more metal-poor than -2.0.

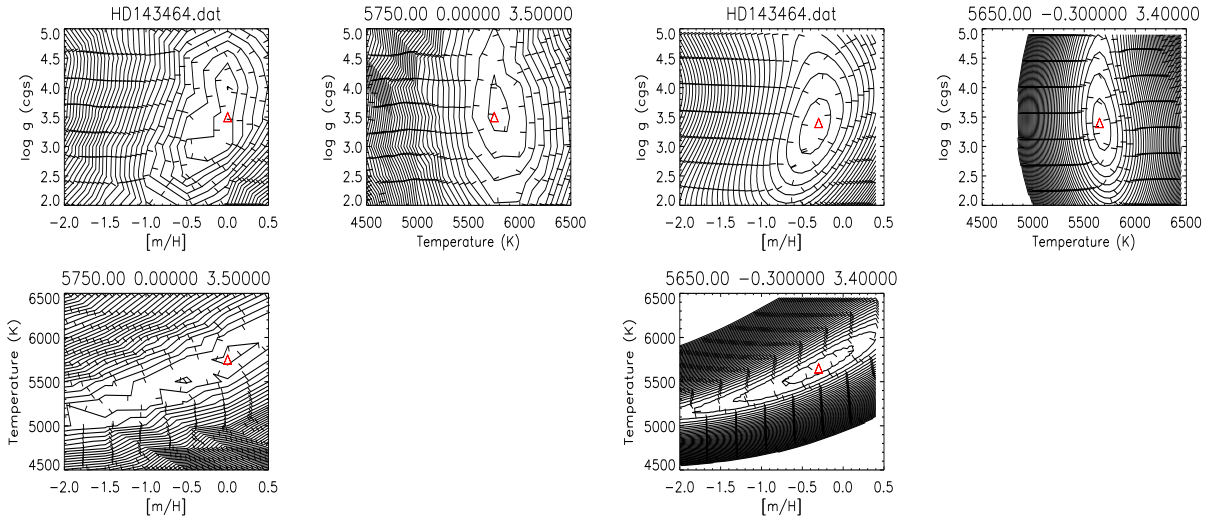

Figure 3.20: The contour plots for HD143464 computed using Munari et al. (2005) library. On the left using the raw grid and on the right the interpolated one. In both cases the red triangle indicates the minimum χ^2 value. Note how the interpolated grid traces a better defined surface.

The red triangles represent the minimum of the χ^2 surface giving the stellar parameters of the best match model. To get the final stellar parameters we use a *weighted mean* of the parameters. Formally, the weighted mean of non-empty set of data $\{x_1,x_2,...,x_n\}$ with non-negative weights $\{\omega_1,\omega_2,...,\omega_n\}$ is defined by

$$\overline{x} = \frac{\sum_{i=1}^{n} \omega_i x_i}{\sum_{i=1}^{n} \omega_i} \tag{3.48}$$

In our case the data is $\{T_{eff}$,[m/H],log g,[α/Fe]$\}$ and the general weight is $\omega = 1/\chi^2$. The stellar parameters coming from the models that match the observed stars better, contribute with a bigger weight (low χ^2) to the final result. We use the 10 stars with the lowest χ^2 to compute the stellar parameters using the weighted mean.

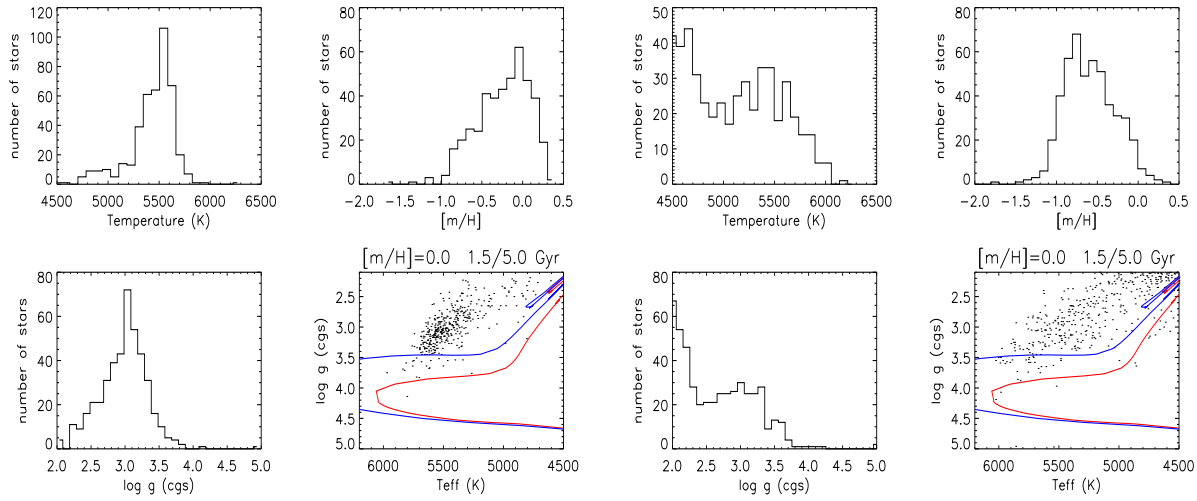

Figure 3.21: Distribution of the stellar parameters for the GCS (left) and RAVE sample (right). We also show the T_{eff} - log g plane with two isochrones from Girardi et al. (2000) at solar metallicity for 1.5 (blue) and 5.0 Gyr (red) respectively. Note that the gravities are underestimated according to the isochrones.

Fig. 3.21 shows the distribution of the stellar parameters for the observed stars using Munari et al. (2005) stellar library. The distribution shows the selection effects described in Sect. 2.2; those effects are very clear in temperature and gravity. Unfortunately, the gravities are completely underestimated ($\sim$ 0.3 dex). Note how the stars are clearly out of the subgiant region in the T_{eff} - log g plane (bottom right panels) according to the isochrones at the indicated metallicity and two different ages for both samples. The metallicity distribution function for the RAVE sample shows a huge number of metal-poor stars. This sample covers a bigger volume and we could find more stars belonging to the thick disk, which we know contains more metal-poor stars compared to the thin disk (see Sect. 1.3), but this distribution is very likely unrealistic. It is more likely that the fact that we find more cool stars is driving the stars to look more metal-poor due to the strong covariance between these two observables.

From these results, the subgiant candidates selected from the RAVE survey are contaminated by giants and the stars from the GCS are mainly subgiants. That could be because

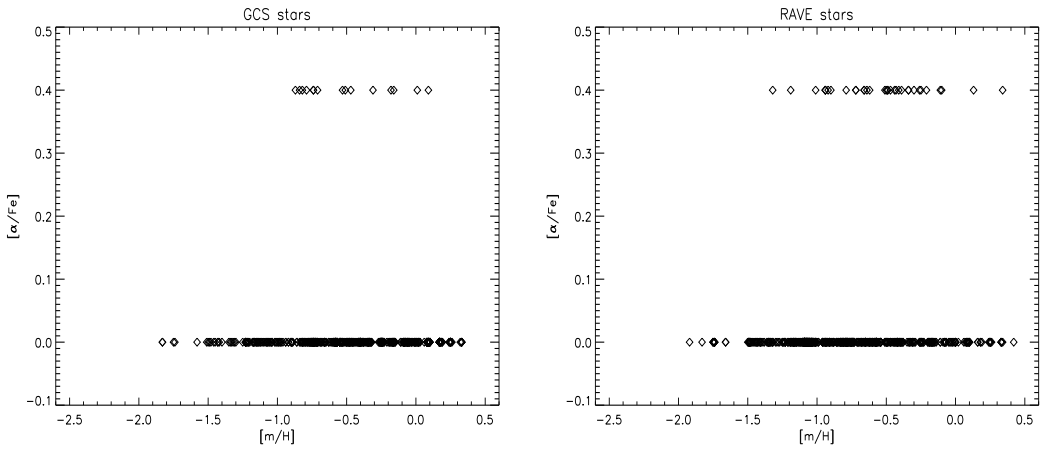

Figure 3.22: [α/Fe] vs [m/H] for the observed stars. On the left the stars selected from GCS and on the right the those selected from RAVE survey. The method employed allows us to label a few stars with [α/Fe] different from solar.

the M_V we use to select the stars from the Hipparcos catalogue are more precise than the gravities obtained from the RAVE spectra, making the subgiants candidates selection more robust. We have tried to understand the underestimation of log g. This atmosphere parameter is crucial to get the ages of stars. In the next section we study the effect of reddening on the observed spectra and their stellar parameters. There is indeed an effect from reddening on the shape of the energy distribution of the stars but our targets are a few parsecs away and the stars with high distances ($\sim$ 500 - 1000 pc) have $|b| \geq 25°$. In principle we do not expect a big impact of the reddening on the stellar parameters. Prof. M. Bessell has also found that there are some indications for a systematically low values ($\sim$ 0.2) for log g when they are determined with the mixing-length parameter to the scale height of α=1.25 (private communication).

The library offers two values for α-enhancement ([α/Fe] = 0.0, +0.4). The features sensitive to [α/Fe] are also sensitive to gravity (see Fig. 3.5 and Fig. 3.7), especially Mgb and Ca II H & K lines. The Ca lines also carry metallicity information. We expect a degeneracy between [α/Fe] and log g. In Fig. 3.22 we show the results for the [α/Fe] determination; just in a few stars the model with [α/Fe] = +0.4 has a lower χ^2. From different studies we know that metal-poor stars ([m/H] < -0.5) usually experience a clear α-enhancement (see Sect. 1.3). Our results indicate that a few stars with a metallicity range -1.0 < [m/H] < 0.4 show α-enhancement but as mentioned the results could indicate degeneracy between the observables.

3.4.7 Interstellar absorption

We cannot observe all the light which is emitted from the star because the interstellar gas and the interstellar grains, called dust, have absorbed part of the light. The main two processes that dim the light from distant stars are *scattering* and *absorption*. We refer to this dimming as *extinction*. This effect is relevant in our studies as we work with a flux calibrated spectra. The interstellar extinction depends on the wavelength ($\sim \lambda^{-1}$) hence the extinction modifies the shape of the spectrum. We need to correct for this effect to determine the atmosphere parameters. The extinction is defined by

$$A_\lambda = (m - m_0)_\lambda \tag{3.49}$$

where the extinction A_λ of a star at some wavelength is defined to be the difference between the observed magnitude $m(\lambda)$ and the magnitude $m_0(\lambda)$ that would be observed in the absence of dust. The *reddening* or *color excess* E(X-Y) in some color X-Y is the difference between the observed color m(X) - m(Y) and the intrinsic color m_0(X) - m_0(Y), using Eq. 3.49:

$$E(X-Y) \equiv (m(X) - m(Y)) - (m_0(X) - m_0(Y)) = A_X - A_Y \tag{3.50}$$

For this project we use the most often cited extinction A_V, and the most often cited color excess E(B-V). The reddening curve[13] is that of Cardelli et al. (1989). The slope of the extinction curve near the V band is $A_V/(A_J R_V)$, where

$$R_V \equiv \frac{A_V}{A_B - A_V} = \frac{A_V}{E(B-V)} \tag{3.51}$$

R_V quantifies whether the extinction curve is rising steeply into the UV. We have adopted the classical value for lines of sight that do not pass through dense clouds, R_V = 3.1 (Schultz & Wiemer (1975)). We can approximate the reddening curve by $a(\lambda)$ + $b(\lambda)/R_V$, where a and b are polynomials in λ^{-1} (Cardelli et al. (1989)). To derive the unreddened flux we use the expression $F_\lambda^{unred} = F_\lambda^{obs} \times 10^{0.4A_\lambda}$

From the relationship between B-V and temperature (e.g. Bessell et al. (1998)), one would expect to find a change in temperature of about 30 K for each 0.01 change in reddening. In Fig. 3.23 we see clearly that reddening has an important effect on the shape of the energy distribution on the observed spectra as one would expect from the wavelength dependence of the extinction.

[13] the ratio A_λ/A_J of the extinction at wavelength λ to that in the Johnson J-band is called reddening or extinction curve.

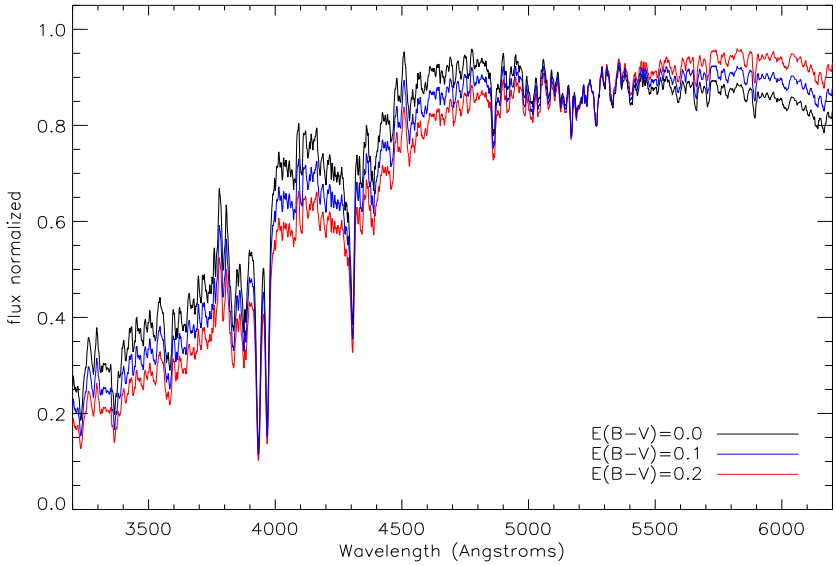

Figure 3.23: Effect of reddening (E(B-V) = 0.1-0.2) on a flux calibrated spectrum using the reddening curve derived by Cardelli et al. (1989).

The Schlegel et al. (1998) dust maps

The *Maps of Dust Infrared Emission for Use in Estimation of Reddening and Cosmic Microwave Background Radiation Foregrounds* (Schlegel et al. (1998)), hereafter the Schlegel map, is a full-sky 100 μm map that is a reprocessed composite of the COBE/DIRBE and IRAS/ISSA maps, with the zodiacal foreground and confirmed point sources removed. Schlegel et al. (1998) combined the strengths of IRAS and COBE/DIRBE to create a relatively high resolution 100-micron intensity map of the sky that is free of striping and accurately recalibrated to the absolute photometry of COBE/DIRBE. The maps can be used to derive the opacity, and hence, extinction, along the line of sight assuming a standard reddening law. This dust map is normalized to E(B-V) reddening using the colors of background galaxies and the spatial resolution is about 6.1 arcmin.

Schlegel et al. (1998) made an important simplification -all of the dust is at one single temperature. This approximation works well at high latitudes but not for large extinctions at intermediate and low latitudes, where the dust emission spectrum is not well fitted by a single temperature (Lagache et al. (1998)). The stars selected from the GCS cover the whole latitude range but they are a few parsecs away, hence, for these stars we expect a small extinction effect. The stars selected from the RAVE catalogue have a $|b| \geq 25°$. The approximation of one single temperature of the dust could work for our stars. Schlegel et al. (1998) do not provide the interstellar extinction as a function of distance r from the Sun. To do that we follow the work done by Chen et al. (1999). Suppose that the large-scale

volume density of the absorbing material, n(r), follows a decaying exponential law away from the galactic plane, as given by,

$$n(r) = n_0 exp(-|Z|/h_{red}) \tag{3.52}$$

where Z = Z_{Sun} + r sin(b). Z_{Sun} is the distance of the Sun from the galactic plane, and h_{red} is the scale height of the absorbing material. We adopt h_{red} = 100 pc for the medium in this study (Sandage (1972), Spitzer (1978)). Chen et al. (1999) use the optical-depth expressed in terms of the number volume density of the absorbing material n(r), the average extinction cross-section, and the Eq. 3.52 to derive the reddening via the equation:

if b $\geq 0°$,

$$\frac{E(B-V)(r,l,b)}{E(B-V)(\infty,l,b)} = 1 - exp(-rsin(b)/h_{red}) \tag{3.53}$$

if b $< 0°$ and r|sin(b)| $\leq Z_{Sun}$,

$$\frac{E(B-V)(r,l,b)}{E(B-V)(\infty,l,b)} = \frac{1 - exp(-rsin(b)/h_{red})}{1 - 2exp(Z_{Sun}/h_{red})} \tag{3.54}$$

if b $< 0°$ and r|sin(b)| $> Z_{Sun}$,

$$\frac{E(B-V)(r,l,b)}{E(B-V)(\infty,l,b)} = \frac{1 - 2exp(Z_{Sun}/h_{red}) + exp((2Z_{sun} + rsin(b))/h_{red})}{1 - 2exp(Z_{Sun}/h_{red})} \tag{3.55}$$

where E(B-V)(∞, l, b) is the reddening at r $\rightarrow \infty$, which is obtained directly from the Schlegel map. Most of the studies constrained Z_{Sun} in the range of 15 to 30 pc in the north direction of the galactic plane (see Joshi (2007)). For this study we use Z_{Sun} = 24.2 $\pm$ 2.1 pc, this value was determined by Maíz-Apellániz (2001) using a sample of about 3400 O-B5 stars with accurate distances obtained from the Hipparcos catalogue. Chen et al. (1999) make the approximation that the distribution of absorbing material is homogeneous along the line of sight to derive the extinction model presented above.

The distances come from the trigonometric parallaxes, generally of very good accuracy, from Hipparcos for the majority of our relatively nearby programme stars (Perryman & ESA (1997)) selected from the GCS. Their relative errors (σ_π/π); most are better than 10% and nearly all better than 20%. For the stars selected from the RAVE survey the distances are taken from the work done by Zwitter et al. (2010). In this work they estimate the distances using the parameters derived from the RAVE spectra and the closest matching isochrone by minimizing the χ^2 and assuming that the star has followed a standard stellar evolution. The accuracy of these distances is not better than 20%. In Fig. 3.24 we show

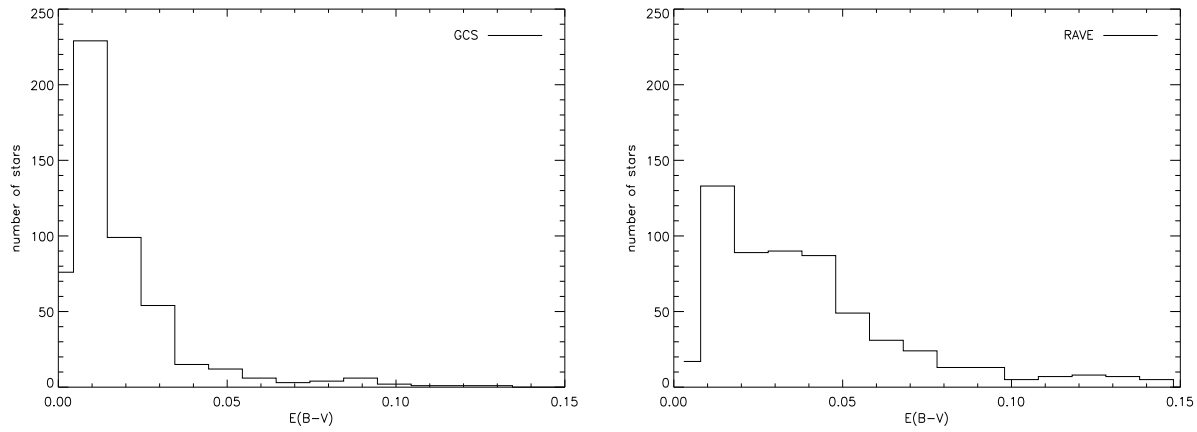

Figure 3.24: The distribution of reddening, E(B-V), for the programme stars derived using the Schlegel map, their distances and the extinction model from Chen et al. (1999). On the left the distribution of the color excess for the stars selected from the GCS. On the right the color excess for the RAVE selected stars.

the distribution of the reddening for the observed stars. For the Hipparcos stars E(B-V) peaks around 0.01 and around 90% of the stars have E(B-V) < 0.05. For the RAVE stars the color excess also peaks around 0.01 but we find more stars in the range between 0.02 $<$ E(B-V) < 0.05 indicating that these stars are more affected by the absorption of the Galactic medium; some of these stars have distances up to a few kpc. Chen et al. (1999) estimate that the total relative error in the extinction model for an object inside the dust plane is 23%. We estimate the formal errors for the color excess using a standard error propagation of the reddening expression; we find that for the GCS stars ΔE(B-V) < 0.01 but for the RAVE objects the accuracy in E(B-V) is typically 0.02.

Once we know the E(B-V) from the Schlegel map we reddened the fluxes of the library. For a given observed star with a specific E(B-V) we reddened all the models before the χ^2 determination at this given E(B-V) and we re-computed the stellar parameters. In this way we are taking into account the effect of reddening in our spectra and in the determination of the atmosphere parameters without introducing another free parameter in the χ^2 minimization.

There is not a big effect of the reddening on the stellar parameters as we can see in Fig. 3.25. The value of the χ^2 is lower after the correction for some stars and it never gets higher. Hence the correction for reddening allows the χ^2 minimization to get a better match between the observed spectra and the model. After applying the reddening correction the distribution of temperature gets slightly hotter, the distribution of metallicity slightly more metal-rich and the stars have a slightly higher gravity. Even after the extinction correction the gravities are still underestimated when using a theoretical spectral library from Munari et al. (2005).

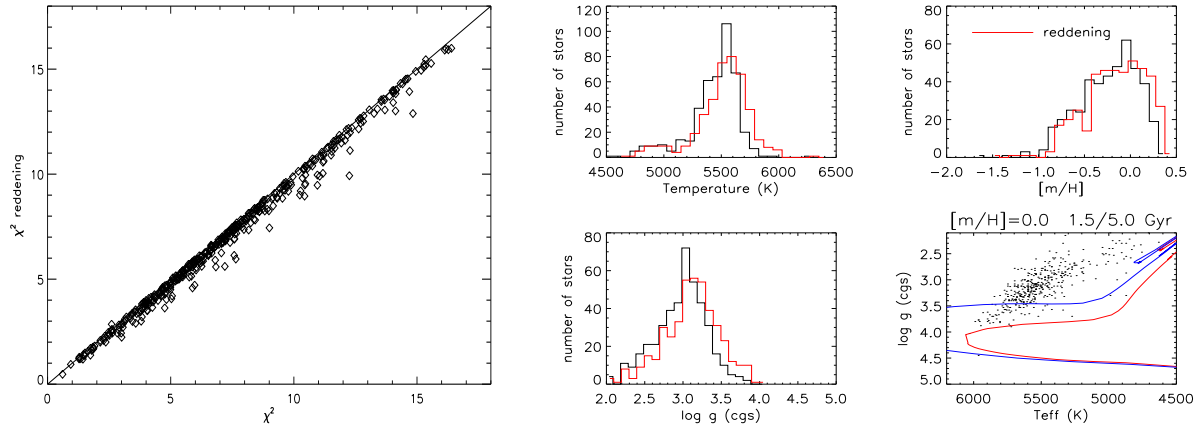

Figure 3.25: Left panel: the χ^2 values using the spectra without and with reddening correction. The spectra taking account the reddening is giving similar or lower χ^2 values. Right panels: the distribution of the stellar parameters with (red) and without (black) reddening correction. In the bottom right panel, the T_{eff} - log g plane after reddening correction. We also show two isochrones from Girardi et al. (2000) at solar metallicity for 1.5 (blue) and 5.0 Gyr (red) respectively. Note that the gravities are still underestimated after the reddening correction.

3.4.8 Stellar parameters using an empirical library

We discussed some properties of the MILES empirical library in Sect. 3.4.2. We have used the flux calibrated spectra presented in this library as model to estimate the atmosphere parameters of the observed stars. In the MILES library the stellar spectra are available in a rest frame. They were corrected for interstellar reddening, using literature values when available or following *uvby-β*, DDO photometry calibrations or the Schlegel map (see Sánchez-Blázquez et al. (2006) for details). The stellar spectra in the library have a higher resolution than the observed spectra. We used the method explained in Sect. 3.4.3 to get the exact resolution we need to degrade the stellar spectra from the empirical library to match the observed spectra. For this exercise we use the stellar spectra of MILES library as template. For the interstellar reddening we have reddened the fluxes of the MILES library using the E(B-V) obtained as explained in Sect. 3.4.7.

One may expect a good agreement between an empirical library and the stellar spectra collected for this project. MILES, as explained in Sect. 3.4.2, is tied back to stellar atmosphere parameters derived from high resolution spectroscopy. With this method we built a bridge between high resolution and low resolution spectroscopy. This method presents the advantage of the fast-taking data from spectrophotometry in small-to-medium size telescopes and shows how a simple statistical method of a minimum distances or χ^2 minimization could give accurate results. In Fig. 3.26 we present four observed spectra and the closest stellar spectra from the MILES library. The agreement is quite good for all of them as one can see in the residual plots. The differences between the MILES and observed

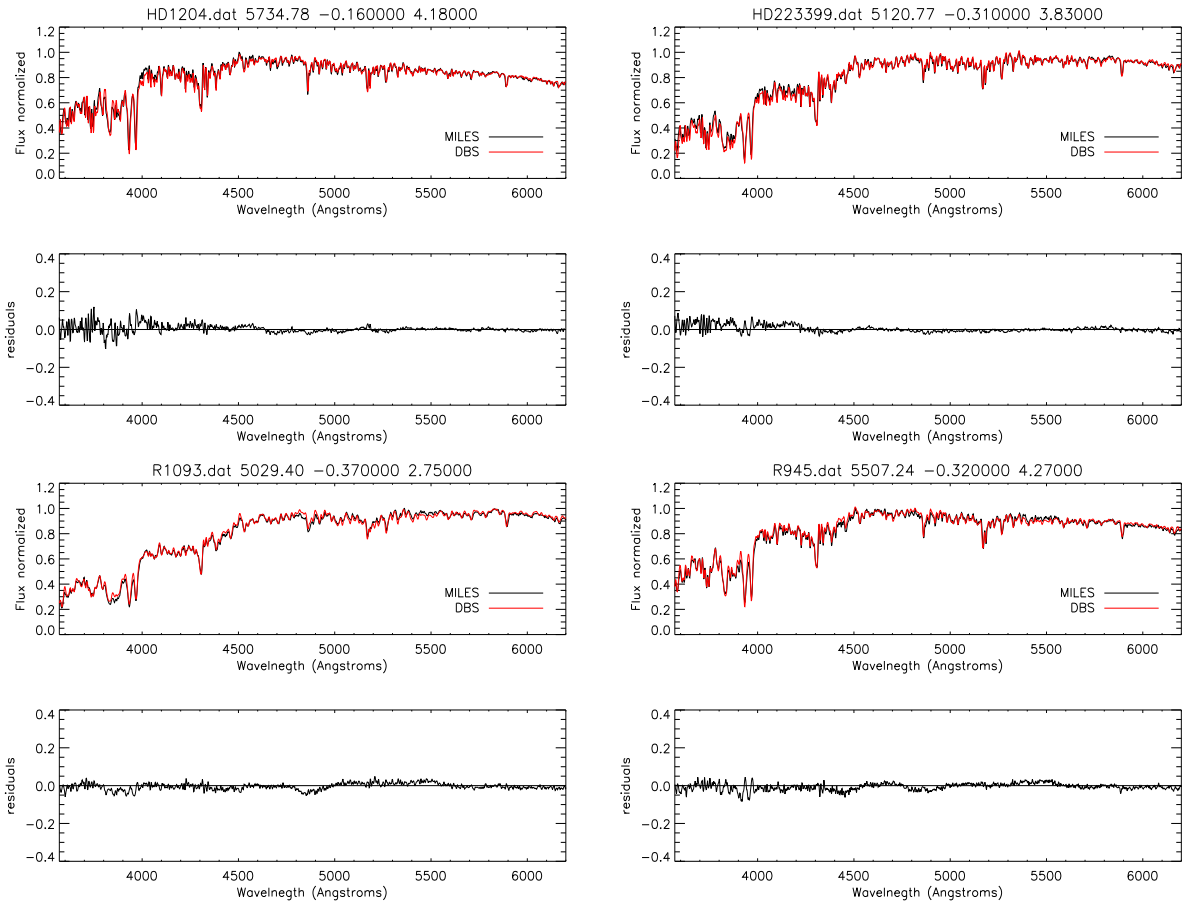

Figure 3.26: Flux calibrated stellar spectra for four program stars (red) and the closest spectra from the MILES library (black). There is a good agreement between the library and the observed spectra as we can see in the residual plots.

spectra are up to 10% for the worst cases.

The handicap with this method would be the irregular grid of the parameters space of the MILES library. However, the library was carefully created trying to fill the major gaps in T_{eff}, [m/H] and log g present in other empirical libraries as we explained in Sect. 3.4.2. Moreover to get the final stellar atmosphere parameters we use the five stars with the lowest χ^2 using a weighted mean as we explained in Sect. 3.4.6. This method allows us to expand the parameter space and smooth our uncertainties associated with the observables in the empirical library. Fig. 3.27 shows these stellar parameters for both samples, for stars selected from the GCS and RAVE surveys. Note the number of giant stars we got from the RAVE survey and some red clump stars around $T_{eff} \sim 4900$ K and log g ~ 2.7. Those type of stars were out of the initial selection criteria indicating that the surface gravities in the RAVE survey may present large uncertainties.

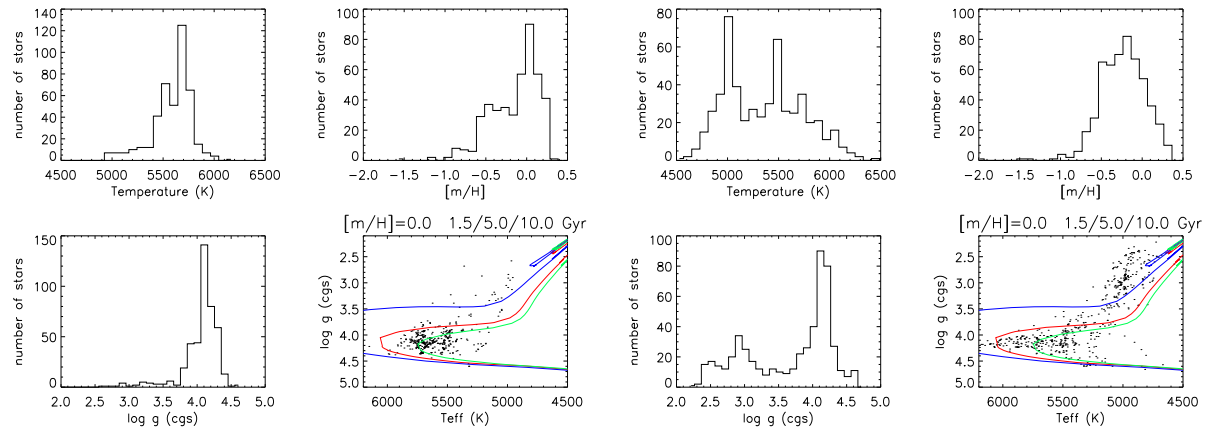

Figure 3.27: Left panel: the distribution of the stellar parameters, T_{eff}, [m/H] and log g, for the stars selected from the GCS. Bottom right panel shows the T_{eff}-log g plane with isochrones at solar metallicity for three given ages 1.5 (blue), 5.0 (red) and 10 Gyr (green) (Girardi et al. (2000)). The sample is dominated for turn-off stars and some subgiants. Right panels: the distribution of the stellar parameters and the T_{eff}-log g plane for the stars selected from RAVE. Here the sample presents a significant number of giants, subgiants and turn-off stars.

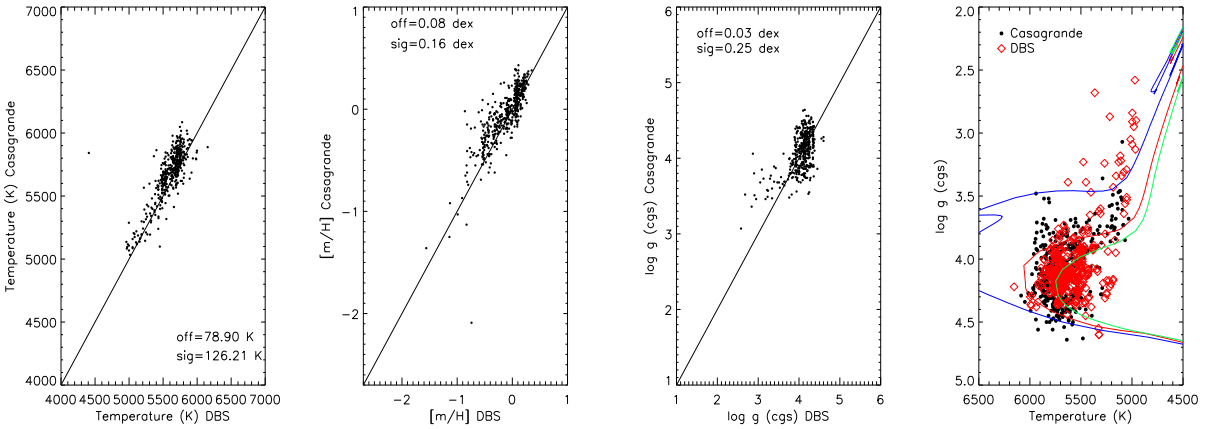

Figure 3.28: Comparison between the stellar parameters (T_{eff}, [m/H] and log g) derived in the present work and the ones obtained in Casagrande et al. (2011) for 436 stars in common. The figure also shows the T_{eff}-log g plane for both samples with isochrones at solar metallicity for three given ages 1.5 (blue), 5.0 (red) and 10 Gyr (green) (Girardi et al. (2000)).

Casagrande et al. (2011) present a re-analysis of the Geneva-Copenhagen survey, which benefits from the infrared flux method (IRFM) to improve the accuracy of the derived stellar effective temperatures and uses the latter to build a consistent and improved metallicity scale. For all stars, log g is determined from the fundamental relation,

$$log\frac{g}{g_\odot} = log\frac{M}{M_\odot} + 4log\frac{T_{eff}}{T_\odot} - log\frac{L}{L_\odot} \tag{3.56}$$

where L is the bolometric luminosity and M is the mass of the star, obtained by interpolating over isochrones. Fig. 3.28 shows the comparison between the stellar parameters derived in the present work and the atmosphere parameters from Casagrande et al. (2011). There is a correlation between the two samples. For temperature we find a RMS $\sim$ 125 K while for metallicity and gravity the RMS is 0.16 dex and 0.25 dex respectively. There is an offset in temperature of 80 K and in metallicity $\sim$ 0.1 dex. The stars in Casagrande et al. (2011) are systematically hotter and more metal-rich than our results. Fig. 3.28 also shows the T_{eff}-log g plane. Both samples present a similar distribution. They clearly show the selection effects discussed in Sect. 2.2. Note that our results find a few stars with lower gravities in the RGB while Casagrande et al. (2011) derive higher gravities for these stars.

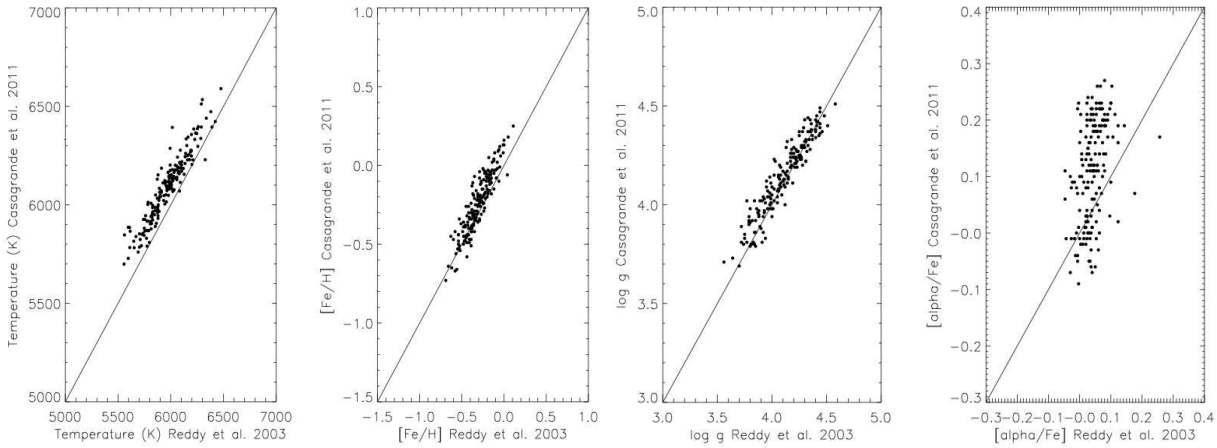

Figure 3.29: Comparison between the stellar parameters (T_{eff}, [m/H], log g and [α/Fe]) derived in Reddy et al. (2003) and those derived in Casagrande et al. (2011). There is a clear correlation for all the parameters except for the [α/Fe].

The comparison between T_{eff}, [m/H], log g and [α/Fe] derived using high-resolution spectroscopy (Reddy et al. (2003)) and the parameters derived in Casagrande et al. (2011) using photometry for the GCS show a clear and tight correlation (see Fig. 3.29). Note that the comparison shows the same offsets we see in Fig. 3.28. High-resolution results reveal stars as cooler and more metal-poor than the results from Casagrande et al. (2011). These result are similar to our findings. Casagrande et al. (2011) are able to derive a proxy for [α/Fe] from Strömgren photometry. The GCS uses the [α/Fe] to derive the age of stars and to get a clean sample of thin/thick disk stars to derive the age-metallicity and age-velocity relations in the solar vicinity. The comparison in Fig. 3.29 shows that there is no correlation between the [α/Fe] measured using high-resolution spectroscopy and the α-elements from

Casagrande et al. (2011), casting doubt on the use of the Strömgren photometry to derive a proxy for [α/Fe].

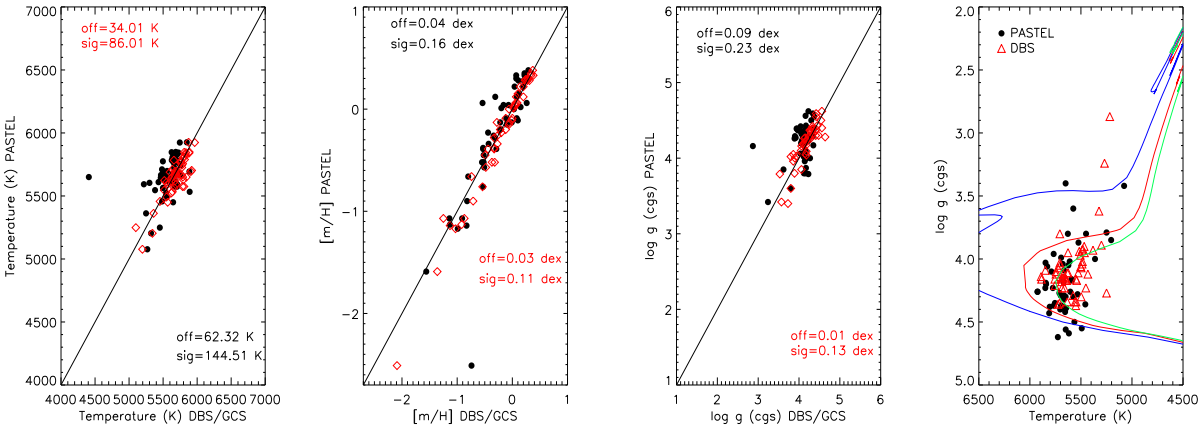

Figure 3.30: Comparison between T_{eff}, [m/H] and log g derived in the present work (DBS) and those from PASTEL catalogue (black points) and the stellar parameteres from GCS (Casagrande et al. (2011)) compared with PASTEL (red squares) for 56 stars in common between the three samples. We also show the T_{eff}-log g panel for both samples with isochrones from Girardi et al. (2000) at solar metallicity for three given ages 1.5 (blue), 5.0 (red) and 10 Gyr (green). In black the offset and the RMS between PASTEL and this work and in red between GCS and PASTEL.

We have 56 stars in common with PASTEL catalogue (Soubiran et al. (2010)). PASTEL is a bibliographical compilation of stellar atmospheric parameters providing T_{eff}, log g and [Fe/H] determinations obtained from the analysis of high resolution and high signal-to-noise spectra. In many cases PASTEL provides several measurement of the parameters for the same star from different authors and techniques. In that case we take the mean of the stars with the lowest uncertainties, after reject the values that are clearly discrepant. The comparison between the present work and PASTEL shows a good correlation for the three main atmosphere parameters (see Fig. 3.30). The RMS is $\sim$ 145 K, 0.16 and 0.23 dex for temperature, metallicity and gravity respectively. *This is a good result; with very low resolution spectroscopy (R = 400) we are be able to get accurate stellar atmosphere parameters using the spectral energy distribution of the stellar atmospheres.* There is a star (HD140283) that is clearly out of the correlation but there is a good agreement between PASTEL and GCS. For this star we get 4408/-0.74/0.81 for T_{eff}/[m/H]/log g respectively while PASTEL show 5650/-2.51/3.40. We find some ripples in the shape of the spectrum suggesting that this star saturated during the observations. Hence the parameters we get for HD140283 are very likely incorrect.

The new parameters of GCS derived by Casagrande et al. (2011) clearly correlate with those from high-resolution spectroscopy (Reddy et al. (2003), Soubiran et al. (2010)) as one can see in Fig. 3.29 and Fig. 3.30. Note that when comparing PASTEL and GCS

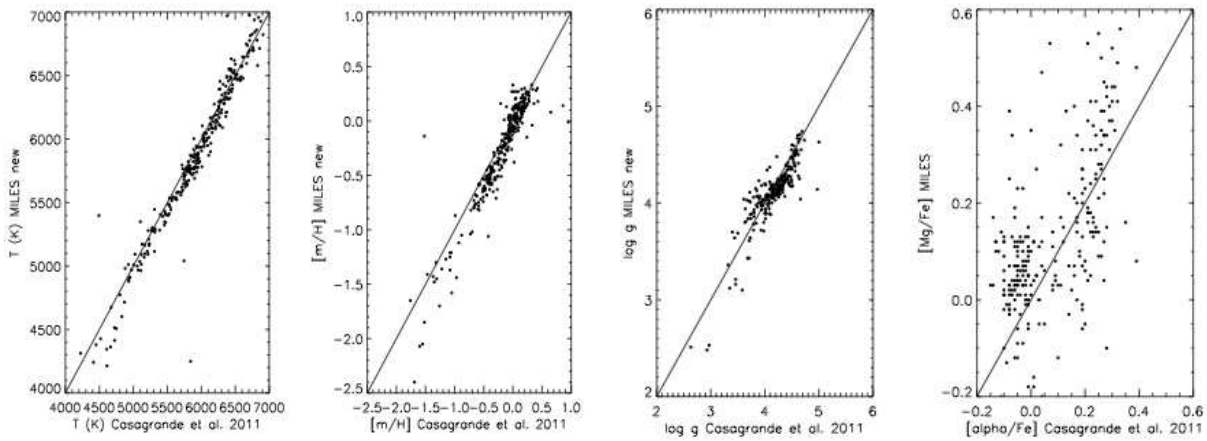

Figure 3.31: 1:1 relation for T_{eff}, [m/H], log g and [α/Fe] from MILES and those from GCS catalogue for $\sim$ 300 stars in common.

(red squares in Fig. 3.30) the RMS is 86 K, 0.11 dex and 0.13 dex for temperature, metallicity and gravity respectively. As mention above GCS uses the IRFM to improve the precision by employing Tycho2 $B_T V_T$ and 2MASS JHK_S photometry to simultaneously recover the bolometric flux and the effective temperature of each star. For the metallicity determination GCS uses the *uvby* photometric system Strömgren (1963) but they build a large and homogeneous high-resolution spectroscopic catalogue, which they use to derive their metallicity calibration. The catalogues they use are mainly Valenti & Fischer (2005), Sousa et al. (2008), Reddy et al. (2003). Valenti & Fischer (2005) fit observed echelle spectra with synthetic spectra (Kurucz (1992b)) yielding effective temperature, surface gravity and metallicity. In Sousa et al. (2008) spectroscopic analysis was completed assuming LTE with a grid of Kurucz atmosphere models measuring line equivalent widths. Finally, Reddy et al. (2003) use also the equivalent widths with a grid of 1D LTE atmosphere models called MARCS (Gustafsson et al. (1975)) to derive the temperature and the metallicity. For the surface gravity they use Eq. 3.56 where stellar masses were estimated from the evolutionary tracks by Girardi et al. (2000) and Salasnich et al. (2000). These three studies are the reference system for the new GCS and they are also part of the PASTEL catalogue compilation. That could explain the good correlation between the stellar parameters from GCS and Reddy et al. (2003) that we see in Fig. 3.29 and also the good correlation between PASTEL and GCS.

We saw in Sect. 3.4.2 that the MILES catalog was calibrated using the high-resolution spectroscopy work of Katz et al. (1998) and this study relies on the existence of a library of high quality, which covers as well as possible the parameters space. Katz et al. (1998) use a least-square comparison of the spectrum of a target star to a library of 211 spectra of reference stars for which the atmospheric parameters are well known and which were observed with the same instrument (ELODIE). Unfortunately, Katz et al. (1998) do

not explain how the atmosphere parameters were obtained for these 211 reference stars. Fig. 3.31 shows the 1:1 relation for the stellar parameters from the new MILES library (Prugniel et al. (2011)) and those from the new GCS (Casagrande et al. (2011)). MILES present stars sligly hotter and more metal-poor than GCS. There is a good agreement for gravities. Unfortunately, we do not find a good correlation for the [α/Fe]. We represent the [Mg/Fe] derived by de Castro Milone et al. (2011) for the MILES stars and the [α/Fe] from GCS. In principle there should be a correlation as Mg is a α-element.

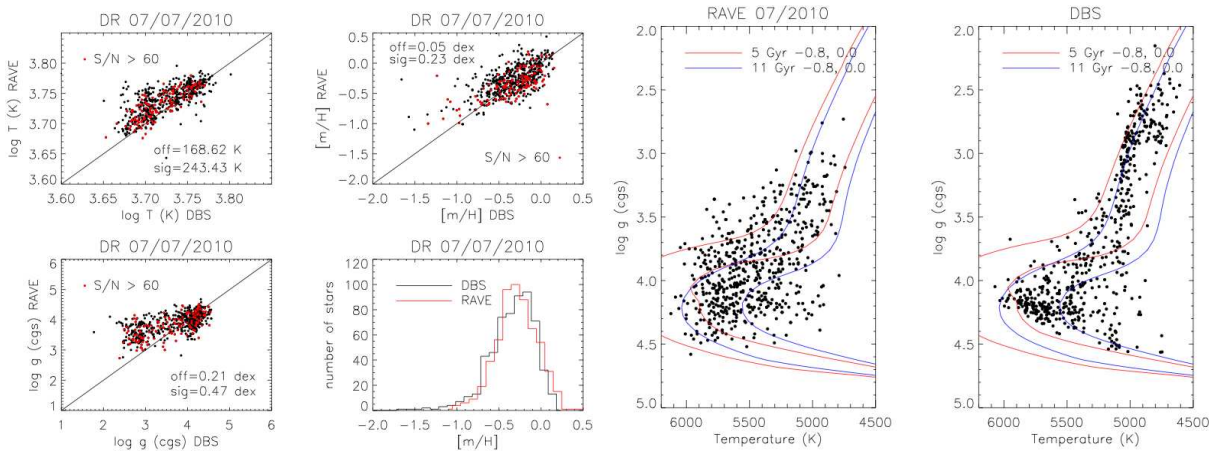

Figure 3.32: Correlation between the stellar parameters derived in the present work (DBS) and those obtained in the RAVE survey. The figure also shows the metallicity distribution function for the common stars and the T_{eff}-log g plane for both samples. The isochrones (Demarque et al. (2004)) present two ages, 5 and 11 Gyr, for solar metallicity and -0.8 dex.

An interesting exercise is to compare our results with the parameters from the RAVE survey. RAVE works with an effective resolution of R = 7,500 in a 385 Å wide spectral interval around the near-infrared calcium triplet ($\lambda\lambda$8410 - 8795 Å), a different spectral region to the one used in our spectra. The RAVE pipeline relied on the Munari et al. (2005) synthetic spectra library. There have been some modifications on the RAVE pipeline (see Boeche et al. (2011) and Siebert et al. (2011) for more details), here we use the results from the internal release 07.07.2010 for the comparison. Fig. 3.32 shows the comparison between RAVE and our results. There is a clear offset in temperature ($\sim$ 170 K) with a big scatter ($\sim$ 250 K). Metallicity looks good with a scatter $\sim$ 0.2 dex but the surface gravity present some problems. The metallicity distribution function is very similar for both samples. The red dots are stars with S/N $>$ 60. Note that the stars with S/N $<$ 60 follow the same trend we see for the stars with high S/N. On the right in Fig. 3.32 we show the T_{eff}-log g plane for the common stars. This figure suggests that RAVE surface gravities suffer from substantial uncertainties.

3.4.9 The estimation of [Mg/Fe] and [Ca/Fe] ratios of the observed spectra

The determination of the α-element abundances with respect to iron from our spectra would allow us to explore the evolution of the Galactic disk in much more detail as thin and thick disk show a different chemical evolution history, and hence different [α/Fe] ratios. The very low resolution of the spectra present this problem as a real challenge. However, in Fig. 3.7 Ca and Mg lines show a clear variation when we modify the [α/Fe] abundances in the flux calibrated spectra. de Castro Milone et al. (2011) obtained [Mg/Fe] measurements for $\sim$ 76% of the stars in the MILES spectral library. These abundance ratios were obtained through a compilation of values from the literature using abundances from high-resolution spectroscopic studies and a robust spectroscopic analysis using the MILES mid-resolution optical spectra.

Our spectra clearly show the Mgb triplet around 5200 Å and the Ca II H & K lines around 3900 Å and the NaD line at 5890 Å. We use these features to estimate the [Mg/Fe], [Ca/Fe] and [Na/Fe] ratios. For the [Mg/Fe] we use the abundances ratios obtained in de Castro Milone et al. (2011). In the present work they emphasize the small average uncertainties in the calibrated [Mg/Fe] values ($\sim$ 0.1 dex) and the good coverage of the stars with [Mg/Fe] abundances. For the [Ca/Fe] and [Na/Fe] we use the compilation made by Venn et al. (2004). Venn's catalogue is a compilation of data from different sources. The effect of combining the data sets is likely to be a larger spread in the abundances ratios on the order of 0.1 to 0.2 dex. Venn et al. (2004) do not attempt to homogenize the error analyses for all elements, however, and instead adopt representative uncertainties of Δ[Fe/H] = $\pm$ 0.05, Δ[X/(Fe or H)] = $\pm$ 0.10, and Δ[X/Y] = $\pm$ 0.15 (where X,Y represent any element or combination of elements other than H and Fe). Venn's catalogue has 204 stars in common with the MILES library in the temperature range from 4500 K to 6500 K covering a large range in metallicity and gravity. For these 204 stars we have flux calibrated spectra with accurate values of T_{eff}, [m/H], log g and [X/Fe]. We implement the individual abundances into the MILES library and we use the χ^2 minimization procedure to get the individual abundances using the entire spectrum to estimate all the parameters.

We used the 5 closest stars according to the χ^2 together with the weighted mean procedure explained in Sect. 3.4.6 to estimate the abundance ratios. We also estimated [Fe/H], [Ti/Fe] and [Ni/Fe] using the common stars between MILES and Venn's catalogue. Very likely the Ni and Ti lines could give a small signal and at low resolution they are blended with other close lines, hence we do not expect a very reliable results for those elements. Fig. 3.33 shows a good correlation between the [Fe/H] of our observed stellar spectra obtained using MILES and Venn's catalogue. Some stars are out of the correlation, mainly for those selected from RAVE. These stars are mainly giants covering a small region in temperature between 4900 and 5200 K, Venn's catalogue present fewer stars than MILES library for that region and that could drive the small discrepancies we see. We get a significant scatter for [Mg/Fe] ratio (see Fig. 3.33). This scatter seems to be real; results

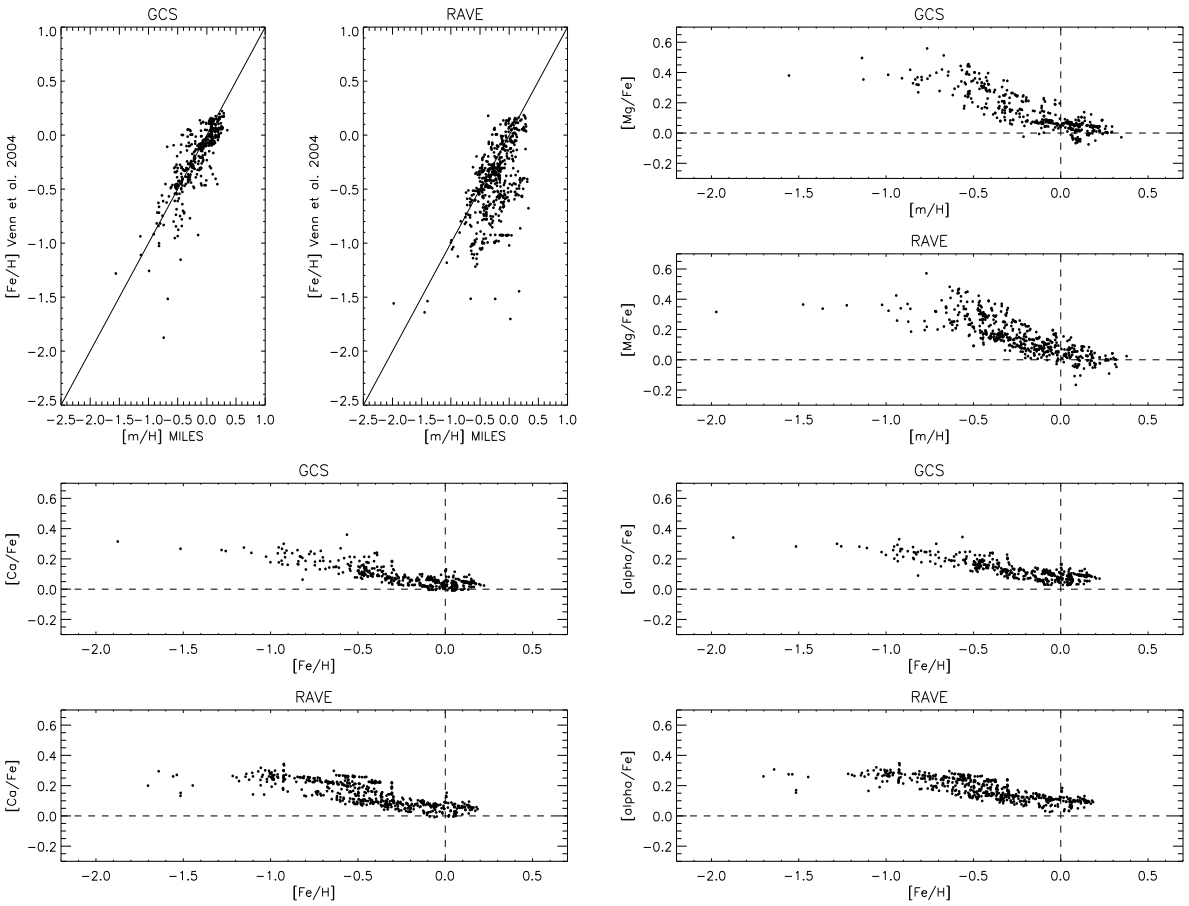

Figure 3.33: Top left: Comparison between the metallicity derived using MILES library and Venn et al. (2004) for the observed stellar spectra selected from GCS and RAVE. Top right: [Mg/Fe] vs [Fe/H] for the observed stars derived using the abundances from de Castro Milone et al. (2011). Bottom panels show the [Ca/Fe] and [α/Fe] vs [Fe/H].

from very high-resolution spectroscopy also find a significant scatter in this abundance ratio Fuhrmann (2008). Fig. 3.33 also shows the [Ca/Fe] and the [α/Fe] vs [Fe/H]. The [α/Fe] - [Fe/H] relation is much tighter than the [Mg/Fe]-[Fe/H] relation. This suggests that some other element (probably Ca) is carrying a lot of weight for the [α/Fe], maybe the Ca II H & K lines are getting a lot of weight in the χ^2 process. In Fig. 3.34, we show [Ti/Fe], [Na/Fe] and [Ni/Fe] against [Fe/H]. The results for these elements ratios do not look as good as for [Mg/Fe] and [Ca/Fe]. The reason could be that these lines are blended with other equally strong lines making it difficult to get a good estimation. We have 18 stars in common with Reddy et al. (2006). The present work presents individual chemical abundances for 176 nearby stars obtained from high-resolution spectra (R $\sim$ 60,000) in the optical range. In Fig. 3.34 we show that our stars follow the same trend in the abundance space as those from Reddy et al. (2006). In both datasets the [Mg/Fe] exhibits a significant

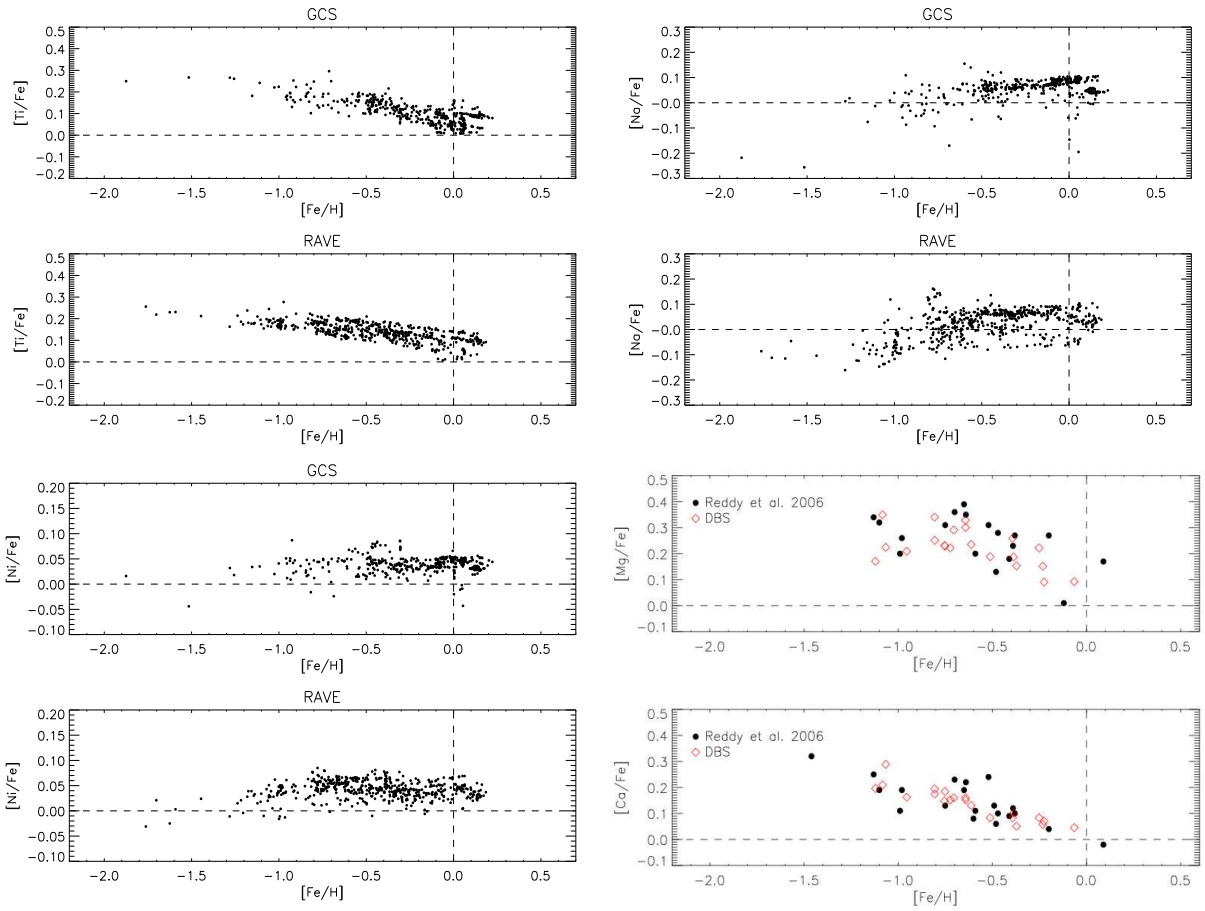

Figure 3.34: Top panel: [Ti/Fe] and [Na/Fe] vs [Fe/H] for the whole sample separated for GCS and RAVE selection. In the bottom the [Ni/Fe]-[Fe/H] relation and the [Mg/Fe]-[Fe/H] and [Ca/Fe]-[Fe/H] relation for common stars with a sample observed with high-resolution (Reddy et al. (2006)). Note we get the same trend in the abundances space and those from high-resolution spectroscopy begin the red squares our data and the black dots high resolution data.

scatter and the [Ca/Fe] shows a more tight relation with respect to [Fe/H].

In summary, strictly speaking we are not measuring the individual abundances of the stellar spectra but we are be able to make a good estimation using the shape and the lines together with a well known sample (MILES and Venn's catalogue) as pattern to get the information for our spectra and, indeed, this is very useful. Our spectra have a very high signal-to-noise hence almost every single feature in the stellar spectra is real. The fact that we are getting a good estimation of [Mg/Fe] and [Ca/Fe] allows us to get [α/Fe] for our sample of subgiants. α-abundances play an important role in determining the age of stars (see next Chapter) and it is clear that thick and thin disk stars of the same [Fe/H] show different abundances, relative to Fe, of other elements (Fuhrmann (1998), Reddy et al. (2006), Navarro et al. (2011)). We could also use the [α/Fe] ratio to perform a tentative

dissection of the chemical thin and thick disk. Unfortunately, that is not easy in this study as the differences in the abundances space are very small between the two disks (< 0.2 dex) and the accuracy of our [α/Fe] and [Fe/H] is around 0.1 to 0.2 dex. On the other hand, using empirical libraries has the limitation that they are sampled from the solar neighborhood, and therefore are limited to what nature provides in this small region of the Galaxy.

Chapter 4

The age of stars

4.1 Introduction

How old is a star? This is a fundamental question for our understanding on the evolution of the Galaxy. Unfortunately, determining the age of stars is still difficult and imprecise. Low-mass stars live long enough to be present from all epochs of star formation, making them attractive for Galactic studies. FGK stars have been widely applied to the age-metallicity-velocity relation problem with conflicting results (e.g., Edvardsson et al. (1993), Rocha-Pinto et al. (2000a), Nordström et al. (2004), Soubiran et al. (2008) and references therein) mainly due to the disparity of the age of the field stars. A very common method for dating the Galaxy is to place a star on model isochrones in the Hertzsprung-Russell diagram. Isochrone placement uses models that are based on well-understood stellar physics, especially for stars similar to the Sun. Chromospheric activity has also been used as an age indicator for age-metallicity studies (Rocha-Pinto et al. (2000a), Pace & Pasquini (2004)). By far the most frequently observed manifestation of activity is the chromospheric reversals seen in the cores of resonance lines in optical spectra, particularly Ca II H & K. In this Chapter we discuss briefly the results from different authors using those methods and we also discuss our results on the observed subgiants and the value of these for dating the Galactic disk and its application for understanding the evolution of the disk.

4.2 Dating the Galactic disk

The age-metallicity relation (AMR) and the age-velocity relation (AVR) are still not completely understood, mainly due to the important discrepancies in the age of the field stars from different authors. F and G-type dwarf stars are favorite tracer populations of the history of the disk. They are relatively numerous and sufficiently long-lived to survive from the formation of the Galactic disk. Evolved stars from the main sequence (MS) are the

most common objects and isochrone fitting the most popular method for dating purposes (e.g., Twarog (1980), Feltzing et al. (2001), Nordström et al. (2004), Bensby et al. (2004), Karataş et al. (2005)).

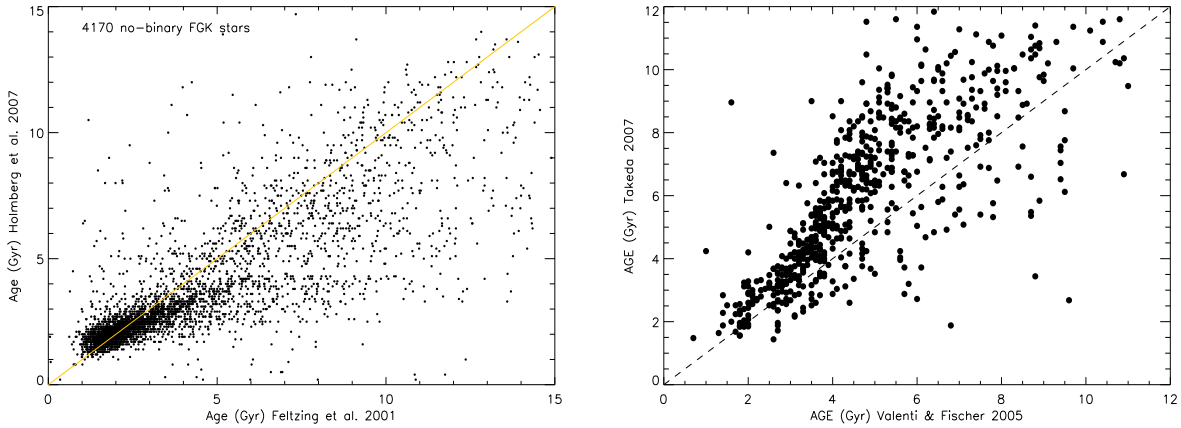

Figure 4.1: On the left: comparison between the ages derived in Feltzing et al. (2001) and Holmberg et al. (2009). Note the systematic discrepancy around 4.5 Gyr. On the right: comparison between the ages derived in Valenti & Fischer (2005) and Takeda (2007).

We find remarkable differences between different authors and techniques for the same stars (see Fig. 4.1). Nordström et al. (2004) for every point in a dense grid of interpolated Padova isochrones (Salasnich et al. (2000), Girardi et al. (2000)) with α-enhancement equal zero. They compute the probability that the star could in reality be located on the isochrones space (and thus have the corresponding age), given its nominal position in the three dimensional space defined by log T_{eff}, M_V, and [Fe/H]. Nordström et al. (2004) assume that the associated observational errors have a Gaussian distribution. The method is described in greater detail by Jørgensen & Lindegren (2005). This work uses a Bayesian approach with priori star-formation rate (SFR), a priori metallicity distribution as function of age, and a priori initial mass function (IMF) as function of metallicity and age. In Feltzing et al. (2001), for each star they have the observationally determined quantities of metal abundance, [m/H], absolute magnitude, M_V, and effective temperature, $\log T_{eff}$ which define a point on the Hertzsprung-Russell diagram. The stellar evolution algorithm is then used to provide a theoretical mass and age appropriate to this point by minimizing the quantity between the observed quantities (M_V, T_{eff}, [m/H]) and those predicted by theoretical isochrones (Pols et al. (1998)). On the left panel of Fig. 4.1 we find important differences between the derived ages for the same stars in Holmberg et al. (2007) and Feltzing et al. (2001). Note that there is a clear systematic effect for the ages derived in Holmberg et al. (2007) around 4.5 Gyr. See the age distribution function in the next section and note how Holmberg et al. (2007) find a minimum around 4.5 Gyr while Feltzing et al. (2001) find many stars around this age. This effect could be driven by the prior functions in the Bayesian approach.

Valenti & Fischer (2005) used also a minimum-distance method through Y^2 isochrones (Demarque et al. (2004)) taking account the α-enhancement isochrones. Takeda (2007) computed their ages using the spectroscopically determined T_{eff} along with the photometrically derived L (from the apparent magnitude, the bolometric correction, and the Hipparcos parallax) and the metallicity represented by [Fe/H] (i.e., $z \equiv 0.019 \times 10^{Fe/H}$), while adopting the stellar evolution tracks computed by Girardi et al. (2000). Takeda (2007) used a Bayesian method that they applied to a large sample of G dwarfs with masses from about 0.8 to 1.3 $M_{\odot}$. Right panel in Fig. 4.1 shows the 1:1 relation for the ages derived in Valenti & Fischer (2005) and Takeda (2007). There is a correlation for stars younger than 4.0 Gyr but for older stars Takeda (2007) is systematically older than Valenti & Fischer (2005).

Casagrande et al. (2011) re-analysis the ages derived in Nordström et al. (2004) and Holmberg et al. (2007) for the GCS. They use the method developed by Burnett & Binney (2010) to compute the ages, Burnett & Binney (2010) used a similar Bayesian technique derived by Jørgensen & Lindegren (2005) and Pont & Eyer (2004). Fig. 4.2 we compare the ages in the new GCS and those derived by Feltzing et al. (2001), Valenti & Fischer (2005), Takeda (2007) and Rocha-Pinto & Maciel (1998). We have described some of these works above. The systematic effect comparing Casagrande et al. (2011) and Feltzing et al. (2001) is less obvious than using the ages from Holmberg et al. (2007) (see Fig. 4.1). However it is not completely under control with the new ages as one can see in Fig. 4.2. This figure also shows the lack of correlation for a large number of common stars between the new ages from GCS and other authors. Rocha-Pinto & Maciel (1998) used theoretical isochrones from the work of Vandenberg & Bell (1985) to estimate the ages of about 700 stars. Fig. 4.2 shows the comparison of these ages with Casagrande et al. (2011) and we find no correlation.

Rocha-Pinto & Maciel (1998) also made use of the chromospheric emission (CE) in these stars. There is evidence that the stellar chromospheric activity can be associated with the stellar age (e.g., Soderblom et al. (1991) and references therein). Young stars consistently show CE levels higher than those of older stars. However, activity can be difficult to detect in older stars, and the portion of the signal to be attributed to age (as opposed to a basal level expected to be present in a minimally active star) is uncertain. We know the Sun has experienced periods such as the Maunder minimum in which spots are rare, but we do not know the activity level one would observe in those cases (see Soderblom (2010) for more details). Rocha-Pinto & Maciel (1998) estimated chromospheric ages using equation (3) of Soderblom et al. (1991). Unfortunately, that equation relies on ages derived using isochrones, i.e., the chromospheric ages are calibrated to ages derived via isochrone fitting using the T_{eff} and ΔM_{bol}, the displacement of a star above the zero-age main sequence (ZAMS), calculated from its gravity. Soderblom et al. (1991) used theoretical isochrones of Maeder (1976). In Fig. 4.3 we see there is no correlation between the ages derived using chromospheric emission (Rocha-Pinto & Maciel (1998)) and the ages derived via theoretical isochrones fitting (Valenti & Fischer (2005), Casagrande et al. (2011)). Another important issue is that derived uncertainties in ages from isochrone placement are significant. In their analysis, Jørgensen & Lindegren (2005) were able to recover ages to

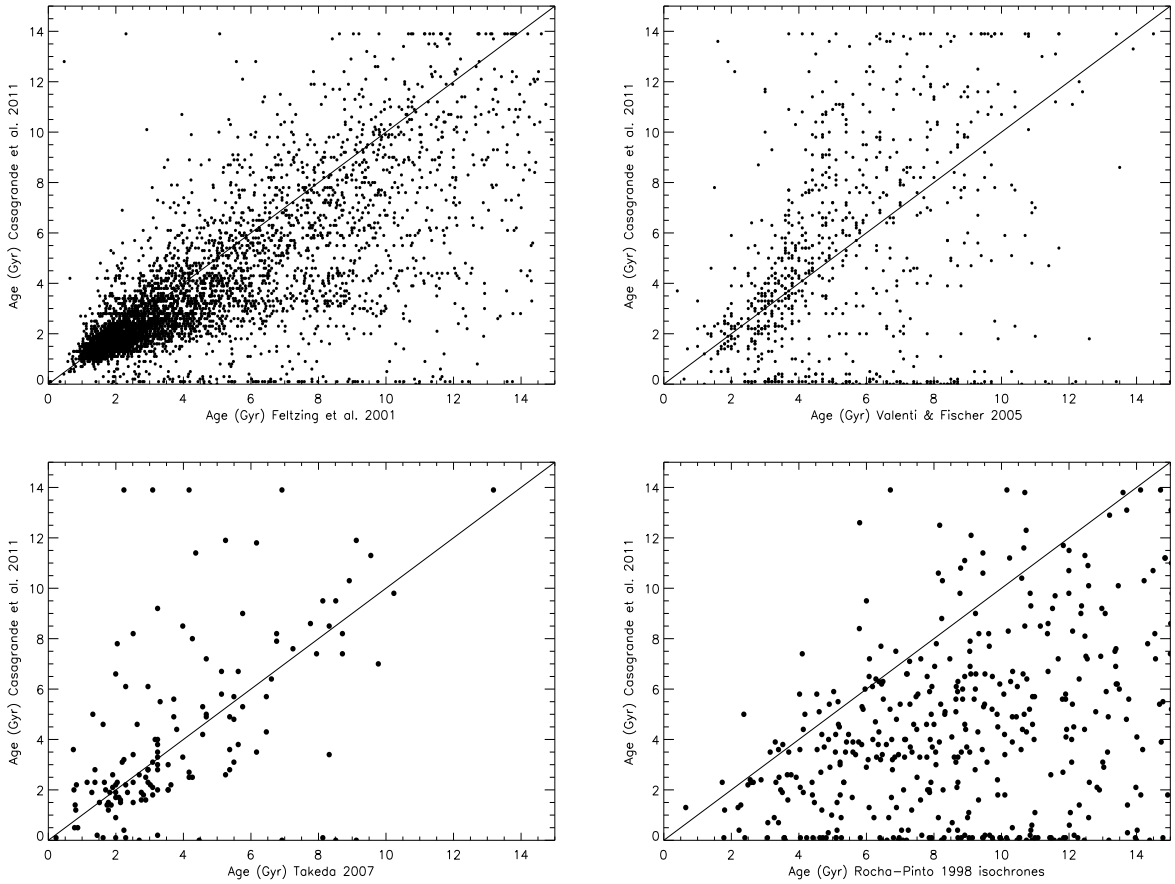

Figure 4.2: Top left: comparison between the ages derived in Feltzing et al. (2001) and Casagrande et al. (2011). Note that the systematic discrepancy around 4.5 Gyr is still there. Top right: comparison between the ages derived in Feltzing et al. (2001) and Casagrande et al. (2011). Bottom left: 1:1 relation between the ages from Takeda (2007) and Casagrande et al. (2011). Bottom right: comparison between the ages derived using isochrones in Rocha-Pinto & Maciel (1998) and Casagrande et al. (2011).

better than 20% only for relatively massive and well-evolved stars. Less-evolved stars had ages good to about 50%, and stars near the ZAMS were indeterminate.

In summary, no reliable ages seem to have been obtained, especially for those older than 3.0 - 4.0 Gyr. We do not have an independent method to get stellar ages. From the results presented here we do not have a good number of stars with well known ages that could be used as a reference or calibration purposes and the different methodologies being used for dating the Galaxy clearly conflict with one another. Moreover, the determination of the ages relies on theoretical isochrones using quantities such a temperature, metallicity, bolometric magnitude, etc., that are calculated using theoretical spectral libraries. Even for the Sun the age is an indirect quantity, obtained using radiogenic dating of meteorites.

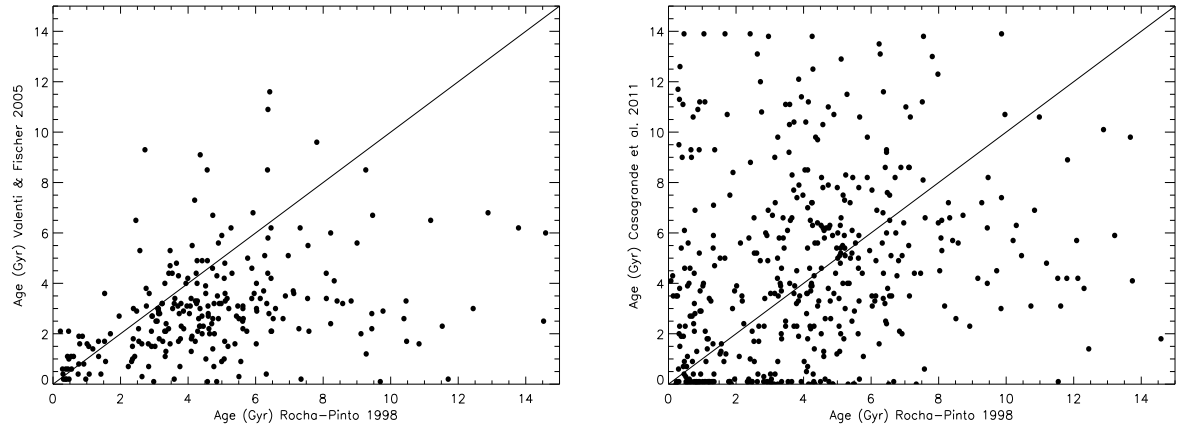

Figure 4.3: On the left: comparison between the ages derived using chromospheric activity ((Rocha-Pinto et al. 2000a)) and Valenti & Fischer (2005). On the right: comparison between the ages derived using chromospheric activity ((Rocha-Pinto et al. 2000a)) and Casagrande et al. (2011)).

WMAP measured the age of the Universe with an extraordinary precision, 13.7 ± 0.2 Gyr (Bennett et al. (2003)), the theoretical models, based on our knowledge on stellar evolution, we use to estimate the ages present a conflict with this result as we find stars older than 14 Gyr. Recently, space missions such as *Kepler* (Christensen-Dalsgaard et al. (2009)) with unprecedented photometric precision bring new opportunities for dating the Galaxy, for example, using asteroseismology -the detection of oscillation modes in stars- is especially promising for single solar-type stars and for older stars because the low-order modes that can be detected in an unresolved object pass through or near the star's center, making them an indicator of the star's central density, which is to say its age. However, asteroseismology is also model-dependent. For more details and methods on the age of stars, see Soderblom (2010).

Finally, we want to emphasize that an important goal of this thesis is to estimate the ages for a sample of subgiants. The previous works, as indicated above, mainly have been using evolved stars. Using subgiants we minimize the systematic effects that arise due to crowded regions in the isochrones space and reduce the uncertainties in the estimation of the ages, making subgiants suitable stars for understanding the evolution of the Milky Way (see Thorén et al. (2004)).

4.2.1 The age distribution function and the star formation history in the solar volume

The star formation history (SFH) in the nearby disk is still a poorly known function (e.g. Twarog (1980), Scalo (1987), Barry (1988), Rocha-Pinto et al. (2000b), Cignoni et al. (2006)). The most efficient way to find the SFH is to use the age distribution function (ADF), which can be transformed into star formation history by various corrections, especially if the sample is not volume-limited and the sample comprises stars with different masses.

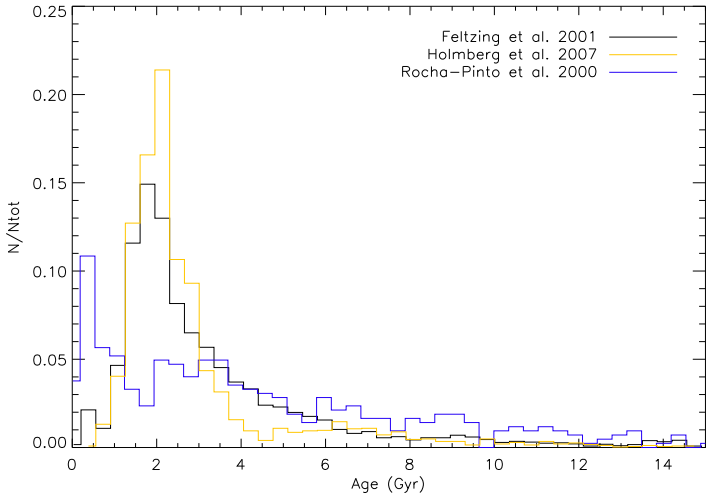

Figure 4.4: The age distribution function derived in three different works, Rocha-Pinto & Maciel (1998), Feltzing et al. (2001) and Holmberg et al. (2007).

It is common in the Bayesian estimation method for stellar ages to use as a prior function the SFH in the Milky Way disk (e.g., Pont & Eyer (2004), Jørgensen & Lindegren (2005), da Silva et al. (2006), Burnett & Binney (2010)). This prior is also called *the age prior*. These authors assumed an SFH that has been globally constant or slightly decreasing. It seems we are in a vicious circle: due to the lack of accurate stellar ages we do not fully understand the SFH in the solar volume, but the Bayesian methods assume a flat SFH as a good approximation for the age prior to determine the stellar ages. Maybe a constant age prior is a good approximation just because it is a demonstration of our ignorance in this point. Moreover, the thin and thick disk present clearly a different chemical evolution picture, hence the SFH of the Galactic disk might be complex. The ADF in Fig. 4.4 is not a constant distribution. Two authors, Feltzing et al. (2001) and Holmberg et al. (2007), found a clear peak around 2.0 Gyr. The distribution decreases rapidly from 2.0 to 8.0 Gyr and after that time the ADF becomes quite flat. Rocha-Pinto & Maciel (1998) found a different distribution for the solar volume. This ADF is irregular with some

peaks at different ages. These ADFs suffer from selection effects, but in any case they are not globally constant, which suggests an inconsistency of the data with a constant SFH. Finally, there is evidence for three extended periods of enhanced star formation in the disk (Rocha-Pinto et al. (2000a) present a brief review about this question).

Bayesian approaches are powerful methods and the priors can help to control biases due to many effects, including star formation history, galactic distribution, IMF, etc., but we need to understand the impact of the prior functions on the final results and how reliable are they. We discuss these points further in the next sections.

4.3 Dating the disk with subgiant stars

Strömberg (1930) used the term *subgiants* to refer to stars of intermediate luminosity between the main sequence and the giants, with absolute magnitudes between $M_V = +2.5$ and +4 and spectral types from G0 to K3. Since then subgiants have played a fundamental role in the field of stellar astrophysics. Very briefly, as hydrogen is used up in the core of a star, a discontinuity in molecular weight develops, which causes the star to move upwards from the ZAMS in the HR diagram. When core hydrogen is exhausted, the entire star undergoes homologous contraction, which heats the interior to the point where hydrogen is ignited in a shell and the star begins to expand again. For stars with $M \geq 1.4$ $M_\odot$ Schönberg & Chandrasekhar (1942) found an upper limit to the fraction of the total mass of hydrogen which can be thus exhausted. This limit gives the maximum mass of a non-fusing, isothermal core which can support an enclosing envelope. The star in this region moves quickly across the *Hertzsprung gap* and begins its ascent of the red-giant branch (RGB) where its evolutionary lifetime is of the order of 0.1 that of stars on the main-sequence.

The facts that the isochrones separate nicely for different ages in the subgiant region (see Fig. 4.5), and that they run almost horizontally make the stars particularly suitable for dating purposes. This requires a good determination of M_{bol}, i.e. the stellar parallaxes, or of the surface gravity. Subgiants are 1-2 mag brighter than dwarfs, which opens up larger volumes for study.

4.3.1 Selection of stellar evolutionary isochrones and its composition

Isochrones are defined as the locus of coeval (equal age) points on the evolutionary tracks of stars of different masses in the Hertzsprung-Russell diagram (HRD). An older isochrone has a fainter and redder main-sequence turnoff (MSTO), because the brighter and bluer massive stars evolve and die earlier. Selecting an appropriate set of theoretical evolution models is the first step in any determination of isochrone ages. The extension of the convective

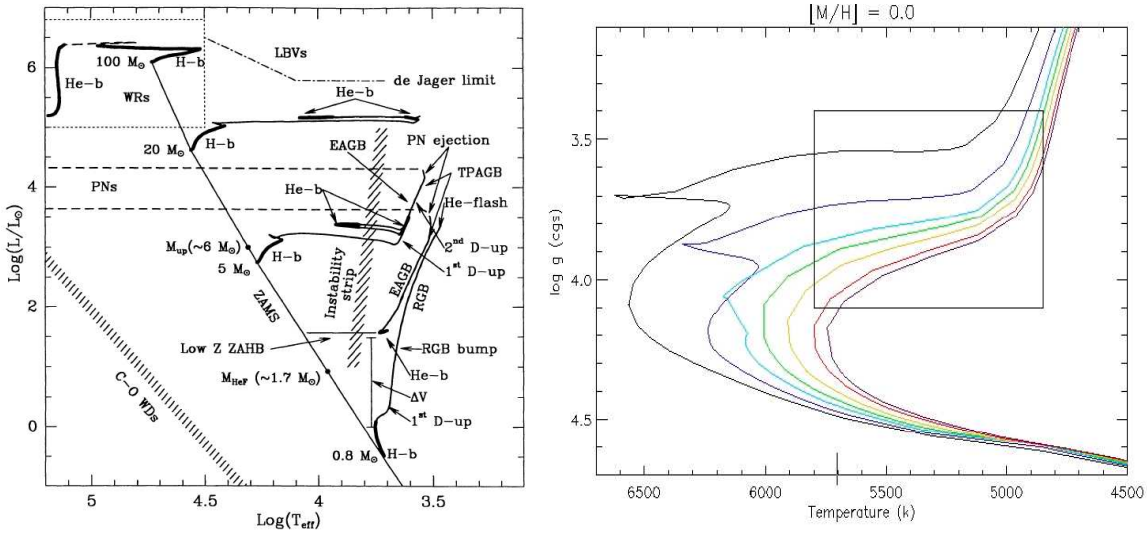

Figure 4.5: On the left: the evolutionary paths in the HR diagram of model stars of composition Y = 0.25 and Z = 0.008 and on initial mass 0.8 $M_\odot$, 5 $M_\odot$, 20 $M_\odot$, and 100 $M_\odot$. Note that our stars are in the mass region from 0.8 $M_\odot$ to 1.2 $M_\odot$ in a very small range of temperature from $\log(T_{eff})$ = 3.69 to $\log(T_{eff})$ = 3.75 (see Chiosi et al. (1992) for details in stellar evolution). On the right: T_{eff} - log g plane, the big square give us an idea of our range of interest. The isochrones (Girardi et al. (2000)) show and age of 1.99 Gyr, 3.16 Gyr, 4.46 Gyr, 5.62 Gyr, 7.01 Gyr, 8.90 Gyr and 10 Gyr respectively for a solar composition [Z=0.019, Y=0.273]. Note that the multiple-valued region near the turnoff, stars of different ages inhabit almost the same location in the T_{eff} - log g plane.

regions, either cores or envelopes, is determined in presence of convective overshoot. The extension of the overshoot regions is governed by a parameter that varies with the mass range. Our subgiant stars have very likely a small range in mass (0.8 $M_\odot \leq M_{star} \leq$ 1.2 $M_\odot$); to incorporate convective core overshooting in the models is fundamental for massive stars but may not be so important for low mass stars. Nordström et al. (2004) compared the models from both the Geneva (Mowlavi et al. (1998), Lejeune & Schaerer (2001)) and Padova groups (Girardi et al. (2000), Salasnich et al. (2000)). The two sets of models yield essentially the same ages (to within 10%). Breddels et al. (2010) compared the theoretical evolution models from Demarque et al. (2004) (Y^2), Girardi et al. (2000) (Padova) and Dotter et al. (2008) (Dartmouth) in the T_{eff} - log g plane and they found a very good agreement for the subgiants region (see Fig. 15 in that work). Pont & Eyer (2004) remarked that the agreement between the predicted isochrones from the different groups is generally good on or near the main sequence, so that using one set of models rather than another does not introduce dramatic differences in the derived stellar ages.

However, when comparing stellar evolutionary isochrones with observations, there are some problems still unsolved; the observed distribution of massive stars in the HR diagram, the study of the color-magnitude diagrams (CMD) and luminosity functions (LF) of inter-

mediate age clusters, and the determination of the basic parameters of globular clusters (Chiosi et al. (1992)). For this work we explore the results using three different grids of isochrones: Bertelli et al. (1994), Girardi et al. (2000) and Demarque et al. (2004).

Theoretical isochrones from models with new radiative opacities (Bertelli et al. (1994))

It is convenient to define the fractions by mass of hydrogen X, of helium Y and of heavy elements Z. Z = (mass of heavy elements)/(total mass of all nuclei). By definition we have X + Y + Z = 1. Solar abundances give X = 0.70; Y = 0.28; Z = 0.02 by mass. Recently, Asplund (2008) claimed that C, N, O and Ne abundances in the Sun have been lowered by almost a factor of two. He concludes that the mass fraction of metals Z decreases to from 0.0194 to 0.0122. This last point is currently under debate.

Bertelli et al. (1994) presented large grids of theoretical isochrones for the initial chemical compositions [Z=0.0004, Y=0.23], [Z=0.004, Y=0.24], [Z=0.008, Y=0.25], [Z=0.02, Y=0.28], and [Z= 0.05, Y=0.352] and ages in the range 4×10^6 yr to 16×10^9 yr. These isochrones were derived from stellar models computed with radiative opacities by Iglesias et al. (1992). In addition to this they presented another set with chemical composition [Z=0.001, Y=0.23]. All the stellar models are followed from the zero age main sequence (ZAMS) to the central carbon ignition for massive stars or to the beginning of the thermally pulsing regime of the asymptotic giant branch phase (TP-AGB) for low and intermediate mass stars. The choice of the chemical composition parameters Y and Z is made according to the law $\Delta Y/\Delta Z = (Y - Y_p)/Z = 2.5$[1], where Y_p is the primordial helium abundances, that represents a lower limit to the estimates given by Pagel (1989). Theoretical luminosities and effective temperatures along the isochrones are translated to magnitudes and colors using extensive tabulations of bolometric corrections (BC) and colors obtained from properly convolving the spectral energy distributions (SEDs) contained in the library of stellar spectra made by Kurucz (1992b).

Evolutionary tracks and isochrones for low- and intermediate-mass stars: from 0.15 to 7 $M_\odot$, and from Z=0.0004 to 0.03 (Girardi et al. (2000))

The library present grids for the initial chemical compositions [Z=0.0004, Y=0.23], [Z=0.001, Y=0.23], [Z=0.004, Y=0.24], [Z=0.008, Y=0.25], [Z=0.019, Y=0.273] (solar composition), and [Z=0.03, Y=0.30]. They are computed with updated opacities and equation of state, and a moderate amount of convective overshoot. The range of initial masses goes from 0.15 $M_\odot$ to 7 $M_\odot$, and the evolutionary phases extend from the zero age main sequence

[1]For the solar neighborhood, Jimenez et al. (2003) determine $\Delta Y/\Delta Z = 2.1 \pm 0.4$ from K dwarfs, a value similar to that found by studying H II regions in both the Milky Way and external galaxies (e.g. Balser (2006)). Recent results, however, suggest that the naive assumption that $\Delta Y/\Delta Z$ varies linearly and with a universal law might not be correct (see e.g. Casagrande et al. (2007) for more details).

(ZAMS) to either the thermally pulsing AGB regime or carbon ignition. The radiative opacities are from the OPAL group (Iglesias & Rogers (1993)) for temperatures higher than log(T/K) = 4.1, and from Alexander & Ferguson (1994) for log(T/K) < 4.0. The energy transport in the outer convection zone was described according to the mixing-length theory of Böhm-Vitense (1958). They calibrated the mixing length parameter α means of the solar model, and they adopted for the Sun the metallicity of Z = 0.019, i.e. a value almost identical to the $Z_\odot$ = 0.01886 favored by Anders & Grevesse (1989). Theoretical luminosities and temperatures along the isochrones are translated to magnitudes and colors using extensive tabulations of bolometric corrections and colors, as in Bertelli et al. (1994). The tabulations were obtained from convolving the spectral energy distributions contained in the library of stellar spectra of Kurucz (1992b) with the response function of several broad-band filters.

Salasnich et al. (2000) presented four large sets of evolutionary tracks for stars with initial chemical compositions [Y = 0.250, Z = 0.008], [Y = 0.273, Z = 0.019], [Y = 0.320, Z = 0.040] and [Y = 0.390, Z = 0.070] and enhancement of α-elements with respect to the solar pattern. The metallicities and the helium-to-metal enrichment ratio $\Delta Y/\Delta Z$ are chosen in such a way as to secure consistency with the Girardi et al. (2000) models. In general α-enhanced isochrones have fainter and hotter turn-offs (TO).

Y^2 (Yonsei-Yale) Isochrones (Yi et al. (2001), Kim et al. (2002), Yi et al. (2003), Demarque et al. (2004))

The Y^2 isochrones covers a wide range in metallicity and age. They use the OPAL opacities for the temperature range of log T $\geq$ 4.1. For log T $\leq$ 3.75, they use the Alexander & Ferguson (1994) opacities. In the temperature region of 3.75 < log T < 4.1, they use a value linearly interpolated between these two sets of tables. The equation of state was taken from Rogers et al. (1996), i.e., OPAL EOS. These models are based on the solar mixture of Grevesse et al. (1993). Their new solar metal-to-hydrogen ratio is $(Z/X)_\odot$ = 0.0245, while the previous value from Anders & Grevesse (1989), based on the meteoritic Fe, was 0.0267. The value they have finally adopted is 0.0244 from the even more up-to-date value from Grevesse et al. (1996). They have set the initial chemical composition to $(Y,Z)_0$ = (0.23, 0.00). Their solar calibration suggests the initial solar chemical composition of $(Y,Z)_\odot$ = (0.267025, 0.018100). This indicates $\Delta Y/\Delta Z \sim 2.0$. It should be noted that $\Delta Y/\Delta Z$ is not a precisely determined quantity. Adoption of a slightly different value does not greatly modify the stellar evolution when Z is low. However, it can lead to unrealistic stellar models when Z is very large ($> 2Z_\odot$), because helium abundance is the prime factor in setting the pace of stellar evolution. In this sense, the extremely metal-rich models based on a crude value of $\Delta Y/\Delta Z$ may not have the same accuracy as their metal-poor counterparts. Helium diffusion and convective core overshoot were taken into account. They found a good agreement between the isochrones and the MS stars in the field as well as in an open clusters. They found that the isochrones combined with their

LFs reproduce the Galactic globular clusters integrated colors quite well at their generally accepted ages.

Kim et al. (2002) derived isochrones in which the effect of the α-element enhancement is fully incorporated. The range of chemical compositions covered is $0.00001 \leq Z \leq 0.08$ and the age range of the full isochrone set is 0.1 - 20 Gyr. They have made the assumption of a constant enhancement, as chosen by VandenBerg (2000). In the α-enhanced case, they adopt a mixture in which the α-elements were enhanced by a constant factor with respect to the solar abundance ratios. They found that inclusion of α-enhancement effects further reduces the age estimates of globular clusters by approximately 8%. Finally, Demarque et al. (2004) provided a patch to the Y^2 Isochrones with an improved treatment of convective core overshoot. The new tracks cover the transition mass range from no convective core to a fully developed convective core.

4.3.2 Dating techniques and results

When main-sequence stars evolve off of their ZAMS position, their luminosity slowly increases while their effective temperature also changes. The position in the HR diagram may thus be used to determine the age of the star. Isochrones fitting method may work better for subgiant stars. We use theoretical isochrones described above and the stellar atmosphere parameters derived from spectrophotometry, to estimate the age of the observed stars. We measured [m/H] and [α/Fe] from our spectra. The metal mass fraction Z is related to the measured abundance [m/H] by

$$[m/H] = log(\frac{Z}{X}) - log(\frac{Z}{X})_{\odot} \tag{4.1}$$

where Z = 1 - X - Y and X and Y are the hydrogen and helium mass fraction, respectively. It follows that for any given star with measured [m/H] the corresponding metal mass fraction is $Z = \epsilon Z_{\odot} 10^{[m/H]}$ where

$$\epsilon = \frac{(1-Y)/X_{\odot}}{1 + (Z/X)_{\odot} 10^{[m/H]}} \tag{4.2}$$

It is clear that the use of such a correction has negligible effect for standard helium values; hence $Z = Z_{\odot} 10^{[m/H]}$ could be a good first estimation of the metal mass fraction used for interpolating over the grid of isochrones. When using isochrones enhancement of α-elements we need to study the relationship between Z and [m/H] for different chemical mixtures. When interior opacity tables were only available for the solar mixture, in studies of very metal-poor systems, there was interest in mimicking the effects of α-enhancement by correcting the metallicity Z used in the opacities (e.g. Chieffi et al. (1991), Salaris et al. (1993)). We can write

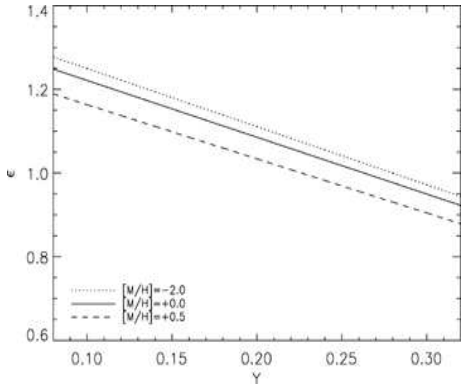

Figure 4.6: On the left: Change in metal mass fraction for different [M/H] and helium abundances Y (Casagrande et al. (2007)).

[m/H]	Z([α/Fe]=0.0)	Z([α/Fe]=+0.3)	Z([α/Fe]=+0.6)
-2.5	0.000062	0.000102	0.000182
-2.0	0.000195	0.000321	0.000574
-1.5	0.000615	0.001012	0.001807
-1.0	0.001935	0.003174	0.005627
-0.5	0.006021	0.009774	0.016990
0.0	0.018120	0.028557	0.047000
0.5	0.049711	0.072793	0.106471
1.0	0.110798	0.142689	0.177489

Table 4.1: Conversion from [m/H] to Z for the solar mixture and the two α-enhanced mixtures assuming that $\Delta Y/\Delta Z = 2$ for the chemical enrichment (Kim et al. (2002)).

$$Z = Z_0(0.638 \cdot 10^{[\alpha/Fe]} + 0.362) \tag{4.3}$$

where $Z_0 = Z_{odot}10^{[m/H]}$ and Z_0 is the heavy element abundance by mass for the solar mixture. Several authors (Chaboyer et al. (1992), VandenBerg (2000)) noted that simple scaling formulae are adequate at low metallicities. However such scalings and even simple interpolations turn out to be very unreliable at high metallicities. Kim et al. (2002) shows the conversion from [m/H] to Z for the solar mixture and the two α-enhanced mixtures used in their calculations.

Departing from the solar mixture can create confusion in assigning chemical abundance parameters to the isochrones, and in making comparisons with observations. [m/H] is the quantity we have measured observationally by spectrophotometry in the present work. Kim et al. (2002) developed Tab. 4.1 for a conversion from [m/H] to Z for the solar mixture and the two α-enhanced mixtures assuming that $\Delta Y/\Delta Z = 2$ for the chemical enrichment. For the present work we use the results in Tab. 4.1 to convert the isochrones into the

observed metallicity system.

Determination of stellar ages

We could write a function (F) relating physical parameters from stellar evolution isochrones to observable quantities (we use the formalism like in Pont & Eyer (2004)),

$$Y[T_{eff}, [m/H], \log g] = F(X[m, age, Z]) \tag{4.4}$$

where X are the physical input parameters, namely, mass, age and abundance and where Y are the observed quantities, in our case, the temperature, metallicity and surface gravity we obtained from the DBS spectra (see Sect. 3.4.8). An interpolation between the models is needed to yield a value of F for all (m,age,z) triplets. Given the observed values T_{eff}, [m/H] and log g; we want to find F^{-1}

$$(m, age, Z) = F^{-1}(T_{eff}, [m/H], \log g) \tag{4.5}$$

In general, the function F is not strictly bijective[2] because isochrones do cross each other in the Y space. However, we expect to avoid this problem in the subgiant region if we are be able to break the age-metallicity degeneracy by having a robust determination of metallicity. The approach we use to determine the ages is to compute F^{-1} over the whole (T_{eff},[m/H],log g) space, and to assign to each point the probability given by the distribution function of the observational uncertainties. Our method resembles that described by Lachaume et al. (1999), Reddy et al. (2003) and Allende Prieto et al. (2004). Adopting a Gaussian probability density for T_{eff}, log g and [m/H] centered at the measured values, we determine the probability density distribution for the age. The procedure makes no assumption on the initial mass function, the metallicity distribution, or the star formation rate. We can write the Gaussian probability density for T_{eff}, log g and [m/H] as follows,

$$\begin{aligned} P(T_{eff}, [m/H], logg) &= \frac{1}{\sigma_{T_{eff}}\sigma_{[m/H]}\sigma_{logg}((2\pi)^{3/2}} \times exp[-(\frac{T_{eff} - T^*_{eff}}{\sqrt{2}\sigma_{T_{eff}}})^2] \\ &\times \quad exp[-(\frac{[m/H] - [m/H]^*}{\sqrt{2}\sigma_{[m/H]}})^2] \times exp[-(\frac{\log g - \log g^*}{\sqrt{2}\sigma_{\log g}})^2] \end{aligned} \tag{4.7}$$

This likelihood is the conditional probability of a point being observed at (T_{eff}, [m/H], log g) given a true value of (T, [m/H], log g), or P(observed,true) $\equiv$ prob(observed | true)

[2]function giving an exact pairing of the elements of two sets

where the '|' symbol denotes conditional probabilities. The terms on the right result from the Gaussian distribution of the uncertainties. Instead of simply inverting the F function at the value of the data point, an age probability distribution function (PDF) can be obtained from the histogram in age of the likelihood over all possible ages,

$$P(age) = \int_R P(T_{eff}, [m/H], \log g) dT d[m/H] d\log g \tag{4.8}$$

where R is the region in (T_{eff}, [m/H], log g) space where the $F^{-1}(T_{eff}$, *[m/H], log g) = age*. The maximum of *P(age)* can be used as an estimator. This is often called the maximum-likelihood method. To find the best estimate for each star we sample the isochrones of Bertelli et al. (1994), Girardi et al. (2000) and Demarque et al. (2004) with constant steps of 0.05 dex in log age and 0.1 dex in [m/H]. We queried a total of 26 metallicities from the database, which was created by interpolating among the available metallicities, ranging from [m/H] = -2.2 to [m/H] = +0.3 for Girardi et al. (2000) and Demarque et al. (2004) isochrones and 17 metallicities, ranging from [m/H] = -1.65 to [m/H] = +0.35 in steps of 0.125 dex for Bertelli et al. (1994) isochrones.

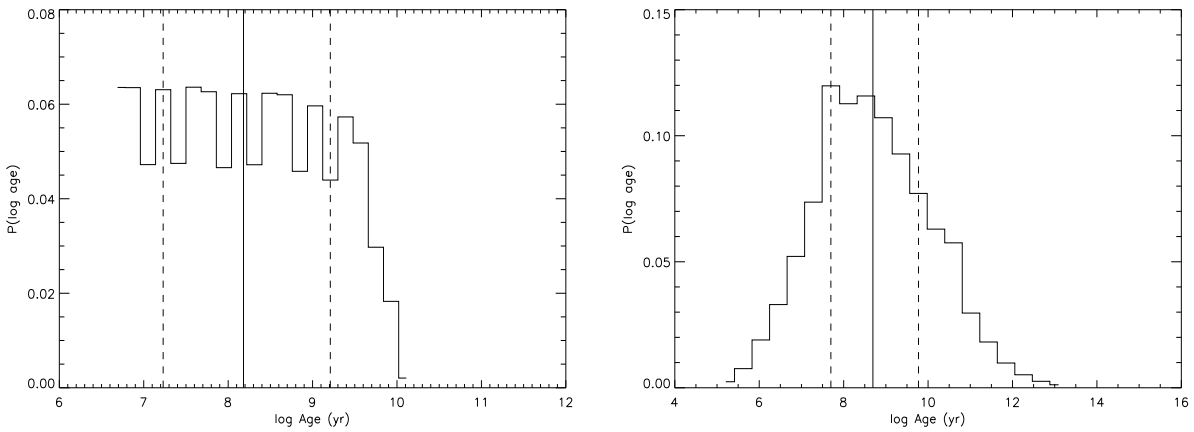

Figure 4.7: The age probability distribution function for a typical star in the MS (5777/0.0/4.4). On the right, the distribution function for a star in the subgiant region (5600/0.0/3.8). The thick solid vertical line shows the best estimate for the age and the broken vertical lines mark the 1σ limits.

We converted Eq. 4.8 into a sum over the area confined by an ellipsoid centered at the adopted values of T_{eff}, [m/H] and log g. The semi-axes of the ellipsoid are giving by the 1σ uncertainties in these parameters. Finally, we normalized the derived P(age) and, whenever appropriate, fitted with a Gaussian to derive the mean and a 1σ uncertainty for the age of the star. Fig. 4.7 shows that a star with the solar parameters is too close to the ZAMS and almost all the ages are equally probable. For instance, using a subgiant star is possible to constrain the age much more precisely.

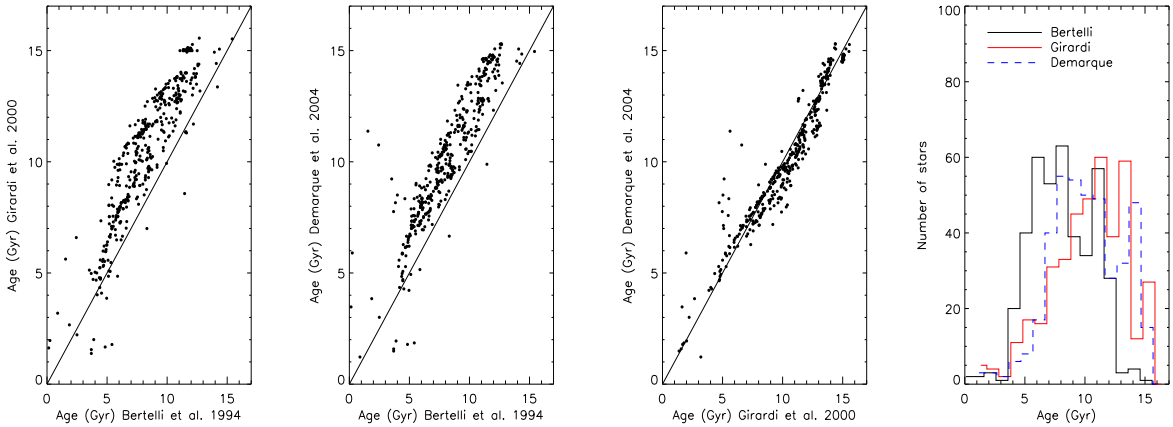

Figure 4.8: Comparison between ages derived using different set of isochrones for the GCS selected stars. The last panel shows the ADF for the ages derived using different isochrones.

We have computed the ages using the method described above for three different set of isochrones Bertelli et al. (1994), Girardi et al. (2000) and Demarque et al. (2004). We find different absolute ages using different isochrones, see Fig. 4.8 for the GCS star. The ages derived using Bertelli et al. (1994) show a correlation with those derived from Girardi et al. (2000) and Demarque et al. (2004) but we find a clear offset. The ages from Bertelli et al. (1994) are systematically younger. The ages from Girardi et al. (2000) and Demarque et al. (2004) show a clear correlation. The ADFs show the clear offset we see in the 1:1 relations. Note that we find only a very few stars younger than 4.0 Gyr. Girardi et al. (2000) and Demarque et al. (2004) gave ages older than 14.0 Gyr for a large number of stars.

For instance, if the observational uncertainties are described by Gaussian functions with dispersions σ([Fe/H]), σ(log T) and σ(log L), then the recovered age distribution function is based on the likelihood function: Adopting a Gaussian probability density for T_{eff}, log g and [m/H] centered at the measured values we determine the probability density distribution for the age . The procedure makes no assumption on the initial mass function, the metallicity distribution, or the star formation rate.

In Fig. 4.9 we show a similar study but now using the stars selected from the RAVE survey. We find very similar results for the RAVE stars. The absolute ages from Bertelli et al. (1994) are systematically younger. The ADFs show that with this sample we find more young stars. Note that, using Bertelli et al. (1994) we find a large number of stars around 1.5 Gyr, while using Girardi et al. (2000) and Demarque et al. (2004) isochrones we find a large range of ages for these stars. That would suggests that there is a systematic effect coming from the ages derived using Bertelli et al. (1994) isochrones for the youngest stars.

To understand better this systematic effect we have selected those stars and we represented them on the T_{eff}-log g plane (see Fig. 4.10). We see that the stars of 1.5 Gyr

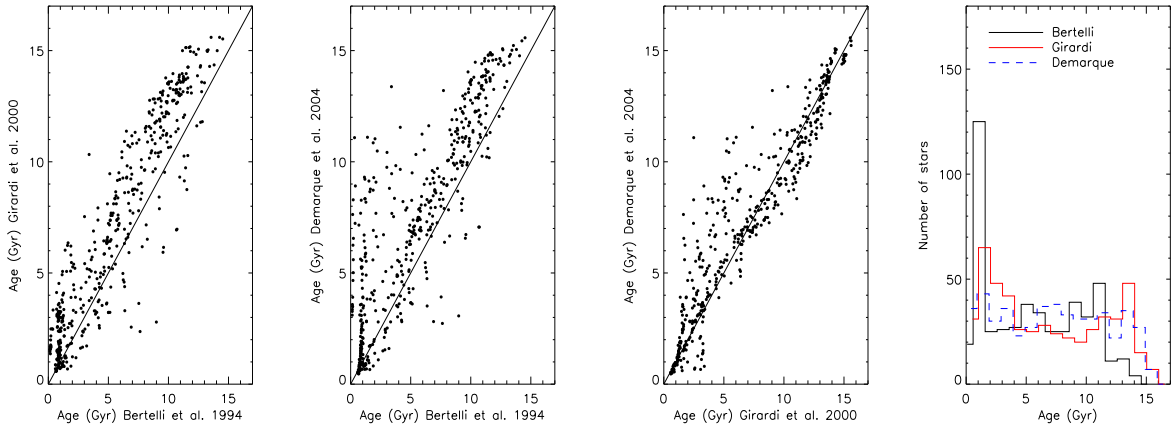

Figure 4.9: Comparison between ages derived using different set of isochrones for the RAVE selected stars. The last panel shows the ADF for the ages derived using different isochrones.

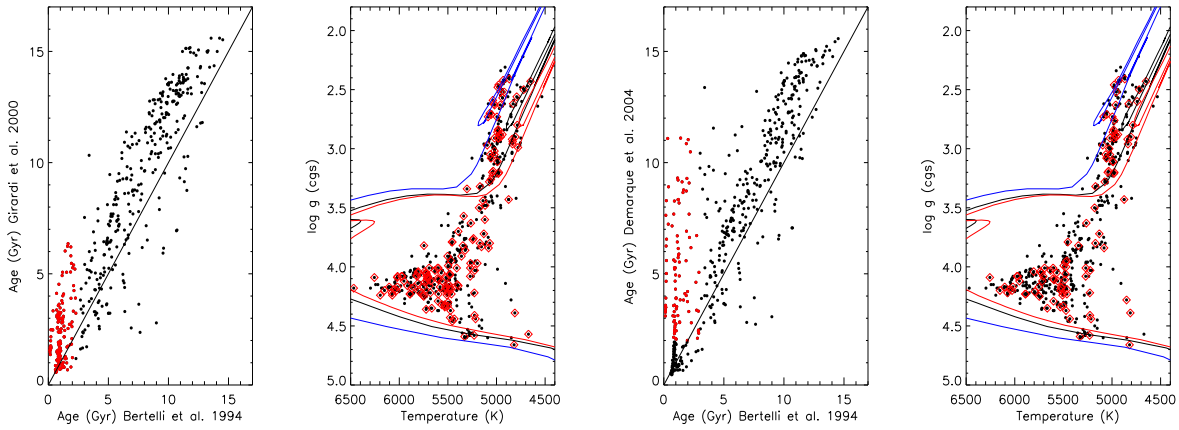

Figure 4.10: 1:1 relations and T_{eff}-log g plane for the stars selected from RAVE. The red points are stars with an age around 1.5 Gyr according to Bertelli et al. (1994) isochrones. Those stars are represented by red triangles in the T_{eff}-log g plane.

according to Bertelli et al. (1994) isochrones (red points) cover a large range in temperature and gravity indicating that those stars very likely present a large range in ages, as we find when using Girardi et al. (2000) and Demarque et al. (2004) isochrones. We find a large number of intermediate-old stars. That may be due to the nature of the sample but it could be also an artifact from the maximum likelihood method. This effect is also called the *age terminal bias*. For a given metallicity the isochrones for the old ages get clearly more crowded than the young ones. This effect would modify the PDF pushing the stars to look older than they are and thus explain why we find stars older than 14.0 Gyr. Pont & Eyer (2004) made an extensive analysis on this bias. In the next chapter we make

Monte Carlo simulations to understand the age-metallicity relation we obtain. We will see that this effect is coming out naturally from the maximum likelihood method.

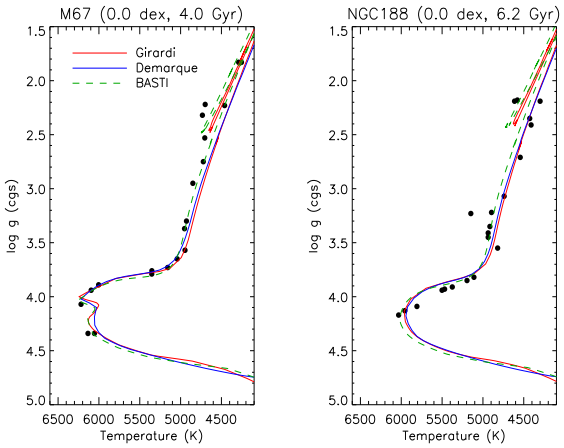

Figure 4.11: T_{eff}-log g plane for a few members of M67 and NGC188 with accurate stellar parameters. The figure also shows three different models for a given metallicity and age.

A temperature mismatch between the models and observed stars will enter directly into the derived ages (see e.g. Lebreton et al. (2001)). This effect is more important when trying to determine the ages for evolved stars. In the subgiant region, the isochrones run almost horizontally. Hence the mismatch in temperature for that region might be less harmful. However, a gravity mismatch could give unrealistic ages for the subgiants. For example, Nordström et al. (2004), Casagrande et al. (2011) and Schuster et al. (2011) amount of others have adjusted the temperature scales of the isochrones before the determination of the ages. Casagrande et al. (2011) suggest that that a correction of $\sim$ 100 K should be applied to the spectroscopic temperatures. Note that our temperatures are systematically cooler than those derived by Casagrande et al. (2011), see Fig. 3.28. We have used members of two old open clusters to determine the mismatch in temperature between the models and the observed stars. The star members of the clusters were selected from an empirical library in the near-IR Ca II triplet (Cenarro et al. (2001a), Cenarro et al. (2001b), Cenarro et al. (2002)). This library provides accurate stellar atmosphere parameters for around 20 members of the clusters. There two main reasons why we have selected the stars from this library. First, the stellar parameters are tied back to the same work that MILES library uses as reference (Soubiran et al. (1998)), hence the reference system for the present work. Second, for both clusters we have a very well defined subgiant trace (see Fig. 4.11). The clusters are M67 and NGC188. Both clusters present solar metallicity and an age of about 4.0 and 6.2 Gyr respectively (Magic et al. (2010), Meibom et al. (2009)). Fig. 4.11 shows that there is a good agreement between the members of the cluster and the isochrones for a given metallicity and age. Note also the minor differences in the subgiant branch for the three models represented, Girardi et al. (2000), Demarque et al. (2004) and BASTI (Pietrinferni et al. (2004)). BASTI is slightly hotter than Girardi et al.

(2000) and Demarque et al. (2004) in the turn-off and in the RGB. We have made this simple test only for solar metallicity. The empirical library in the near-IR Ca II triplet and MILES present stars that are members of globular clusters, but all of them belong to the upper part of RGB (log g $\sim$ 2.5), far from our area of interest for this study. However, Demarque et al. (2004) made an extensive comparison between isochrones and observed stars for intermediate-age open clusters at different metallicities. Fig. 3 in Demarque et al. (2004) shows that the models fit fairly well the subgiant branch of four Galactic open clusters in the color-magnitude diagram. For the reasons explained above we have not adjusted the temperature scales of the models before the determination of the ages, as we see that they are consistent with the stellar parameters derived using MILES library.

From the probability distribution we find the mean (true value) and the 1σ lower and upper limits for the age of a star. We have computed the total relative error as,

$$\sigma_{total} = \sqrt{(\sigma_{age}^{upper} - age)^2 + (age - \sigma_{age}^{lower})^2} \tag{4.9}$$

Fig. 4.12 shows the behavior of σ_{total} for three set of isochrones used to determinate the ages of the stars. For the three models we see clearly that old ages suffer bigger uncertainties. The uncertainty increases with the age (see left panels in Fig. 4.12). That is to be expected: as mentioned above, the isochrones at a given metallicity become crowded for the old ages, thus making the age determination less accurate. Around 80% of the stars present a total relative error lower than 4.0 Gyr for the three models (right panel in Fig. 4.12). The total age relative error shows a clear peak around 3.0 Gyr using Bertelli et al. (1994) isochrones, around 2.5 Gyr for Girardi et al. (2000) and 1.5 Gyr for Demarque et al. (2004) isochrones. Quantitatively, the lowest errors come from Demarque et al. (2004) isochrones, while Bertelli et al. (1994) have the most significant uncertainties. The differences we see using different sets of models could arise from the nature of the models themselves but also from the interpolation of the grids.

The importance of the [α/Fe]

Kim et al. (2002) showed that inclusion of α-enhancement effects in the models further reduces the age estimates of globular clusters by approximately 8%. The inclusion of α-enhancement in the isochrones does have an impact on the age determination. Ramírez et al. (2007) found that the differences between ages computed with and without the α-element enhancement effects are more important for the oldest stars.

We use the Y^2 isochrones in which the effect of the α-element enhancement is fully incorporated (Kim et al. (2002)). We compute the ages using isochrones with [α/Fe] = 0.0, +0.1, +0.2 and +0.4. Fig. 4.13 shows the isochrones with the same metallicity ([m/H] = 0.0 and -0.5 respectively) for two ages (4.0 and 10.0 Gyr) for two [α/Fe] values, 0.0 and +0.2. Note that the difference between models with solar and [α/Fe] = +0.2 is more

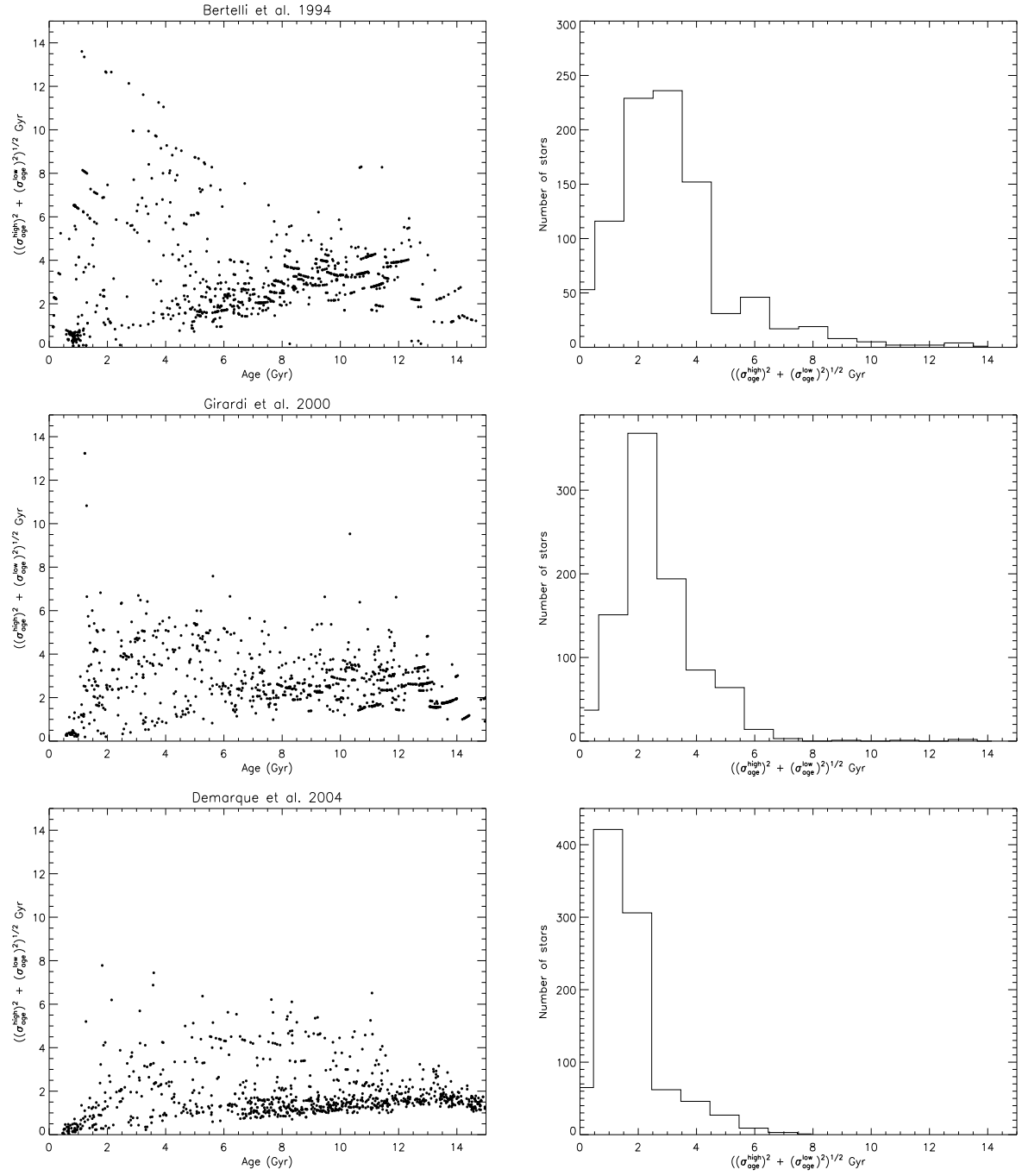

Figure 4.12: Left: relative total age error vs. age for the whole sample using three set of isochrones. Right: The distribution of the total relative errors for the ages.

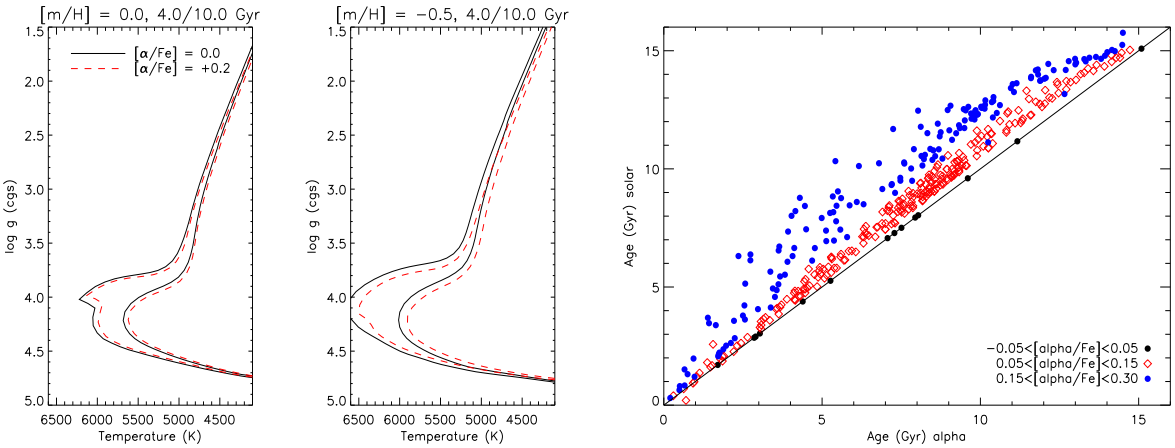

Figure 4.13: Left: isochrones of two different ages (4.0 and 10.0 Gyr) for a given metallicity ([m/H] = 0.0 and -0.5) with [α/Fe] = 0.0 (black) and [α/Fe] = +0.2 (red). Right: 1:1 relation for ages derived taking account the α-elements and ages derived using solar models. The color code shows different values of [α/Fe].

evident for metal-poor abundances. The figure also shows the difference in the ages using only isochrones with α-solar and [α/Fe] = +0.1, +0.2 for a sub-sample of stars. There is a clear effect on the ages taking into account models with α-enhancement. The difference on the ages could sum up to 5.0 Gyr. Not taking into account the [α/Fe] values in the isochrones is pushing the stars to look older, i.e. α-element enhancement models reduce the ages estimates of the field stars.

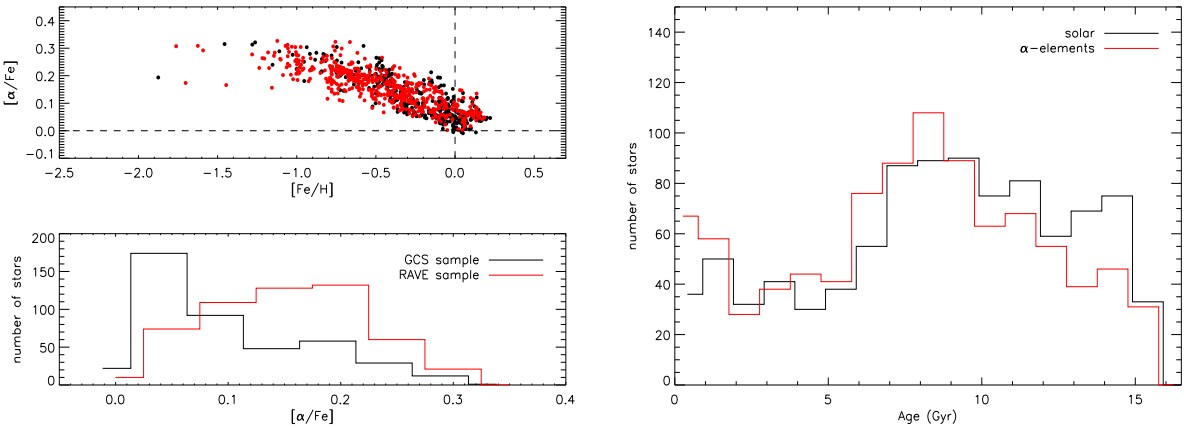

Figure 4.14: On the left the [α/Fe] vs. [Fe/H] for the sample of study and the distribution of the α-values for the GCS and RAVE sub-sample. On the right the ADFs for ages derived with (red) and without (black) taking account the effect of the α-element enhancement.

Fig. 4.14 shows the [α/Fe] - [Fe/H] relation for the whole sample of this study. Note that the RAVE sample covers a larger volume than the GCS. RAVE sample presents a peak around [α/Fe] $\sim$ +0.2 while GCS sample show a clear peak close to solar abundances. Fig. 4.14 also shows the ADF for ages derived both taking into account α-elements and also by not taking them into account. For stars with -0.05 $\leq$ [α/Fe] $\leq$ 0.05 we use the isochrones with [α/Fe] = 0.0. For stars with 0.05 $<$ [α/Fe] $\leq$ 0.15 we use the isochrones with [α/Fe] = +0.1. For stars with 0.15 $<$ [α/Fe] $\leq$ 0.30 we use the isochrones with [α/Fe] = +0.2 and for stars with [α/Fe] $\geq$ 0.30 we use the isochrones with [α/Fe] = +0.4. The two ADFs are quite similar for stars younger than 10.0 Gyr. For the oldest stars ($>$ 10.0 Gyr) we find fewer stars when taking into account the α-elements.

Maximum likelihood vs. Bayesian approach

Pont & Eyer (2004) argued that prob(observed | true) is not really the probability that one is trying to determine when performing the age of a star. One is attempting to estimate the value of the true quantity, given the observation, i.e. prob(true | observed). Another argument in favor of the Bayesian approach is the unrealistic assumption of Gaussian uncertainties for temperature, luminosity and metallicity in the maximum likelihood. As mention already Casagrande et al. (2011) estimate the ages for the GCS using a Bayesian method. Using the stellar parameters derived by Casagrande et al. (2011) we have estimated the ages for those stars with our maximum likelihood approach with the goal to compare both methods.

Casagrande et al. (2011) use two set of isochrones to determine the ages of the GCS, Padova (Bertelli et al. (2008), Bertelli et al. (2009)) and BASTI (Pietrinferni et al. (2004)). We use the three set of isochrones described in Sect. 4.3.1. There is mostly agreement between the maximum likelihood and the bayesian approach, except for some systematic effects for the very young population in both methods. We find different results when using different isochrones, especially for intermediate-old population (see Fig. 4.15). In general the Bayesian approach produces greater ages than the maximum likelihood method for the stars older than $\sim$ 4.5 Gyr. Is that an artifact of the prior functions? We see this effect more clear for the subgiants. We selected stars between 5000 K and 5700 K and between 4.1 and 3.4 in log g. That is just the region where we expect to obtain more precise ages for the subgiants. Those stars are the red squares in Fig. 4.15. Note that the subgiants show a different behavior for stars younger than $\sim$ 4.5 Gyr; the Bayesian method is pushing the stars to look younger than they do with the maximum likelihood approach. However, for the subgiants older than $\sim$ 4.5 Gyr we find the opposite behavior. Are the prior functions driving this behavior? Why does the trend change just around 4.5 Gyr? We should understand better the effect of the priors when we use the Bayesian approach for dating the Galaxy. Yonsei-Yale isochrones with α-elements present good agreement between the two methods but still we find a different trend for stars younger and older than 4.5 Gyr. This study presents a general agreement between two dating methods but

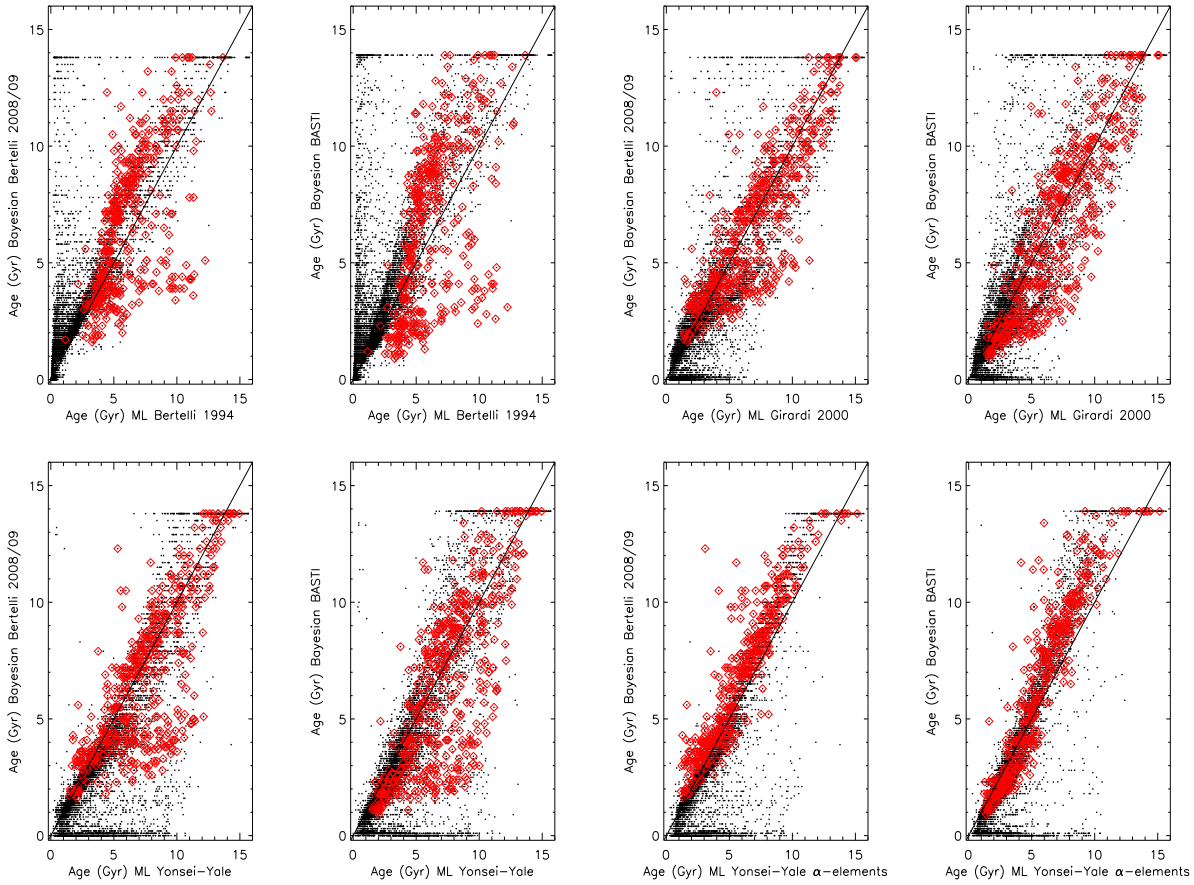

Figure 4.15: Comparison between the maximum likelihood and the bayesian approach for the GCS. The red triangles are subgiants selected using the T_{eff} and log g plane.

it does not tell us that those ages are right. We have seen in Sect. 4.2 that there is a significant disagreement between different authors in the age for field stars. Ages are extremely sensitive to discrepancies in the stellar parameters (see Haywood (2006) for a study in systematic biases in metallicities and effective temperatures and the repercussion on the age-metallicity relation). To get some security where we are we have selected stars that are members of the Hyades star cluster.

The GCS present a clear overdensity of stars around $\delta \sim$ -26º. Those stars are members of the Hyades open cluster. We selected stars from this overdensity in the galactic latitude-longitude plane, and then we cleaned the sample using the radial velocities (rv $\sim$ 40 km/s). We represent the ADF for around 100 stars that very likely are members of the cluster (see Fig. 4.16). On the final sample there is a clear group of stars that present over-solar metallicities (cluster members) but there are few stars with sub-solar abundances. Those few metal-poor stars are probably field stars. The ADFs in Fig. 4.16 present a clear peak

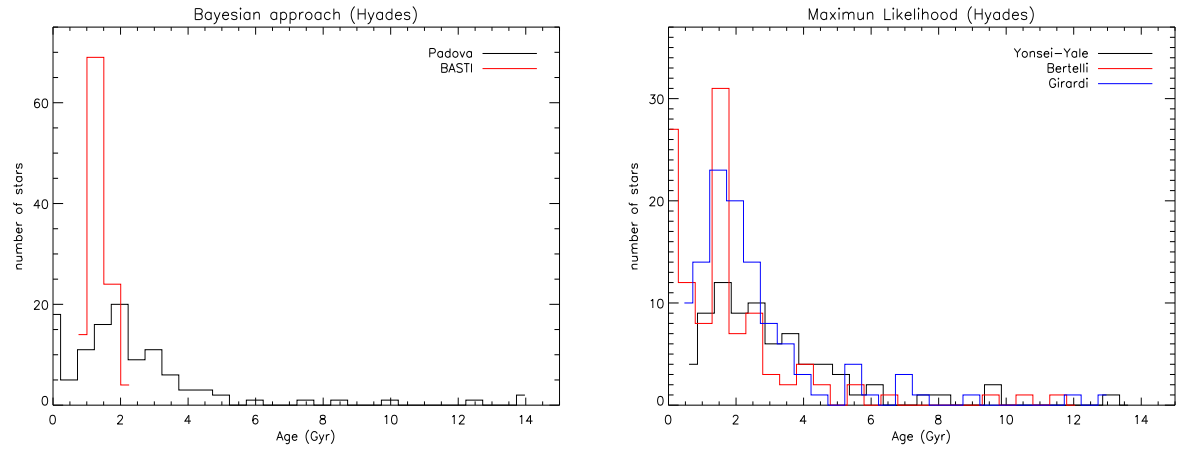

Figure 4.16: Histogram of the ages of the members of the Hyades open cluster using the maximum likelihood and the bayesian approach.

between 1.5 and 2.0 Gyr for all the isochrone sets. Both age determination methods are be able to identify those stars as a young group. The Hyades open cluster is around 650 Myr old (Lebreton et al. (2001) and references therein). The ADFs show few stars of intermediate-old ages. Those stars present sub-solar abundances, hence it is likely they are not members of the Hyades cluster. Some stars are in the MS where the isochrones do not separate well for different ages and some of them are slightly evolve. Note that we do not try in this exercise to test the effectiveness of the age determination methods for the older subgiant stars in the RAVE and GCS samples. However, we could get a clue in terms of absolute ages. Note also that BASTI isochrones are giving ages younger than 2.0 Gyr for all the stars. Both methods present the ages of those stars systematically older of about 1.5 - 2.0 Gyr.

4.3.3 Choosing an age system

We have seen that some of the isochrone comparisons in the previous section look worse than others. An external check was also made by comparing with the ages from the GCS derived by Casagrande et al. (2011). We have compared the ages for 436 stars in common with GCS. We have seen above that the maximum likelihood and the Bayesian approach present a general correlation when estimating the ages but also we see systematic effect coming out.

The stellar parameters derived in Casagrande et al. (2011) correlate with those derived in the present work (see Fig. 3.28) but the stars in Casagrande et al. (2011) are systematically hotter and more metal-rich than our results. Note also that we see a trend when comparing the gravities. In Fig. 4.15 we see that both methods correlate but in Fig. 4.17

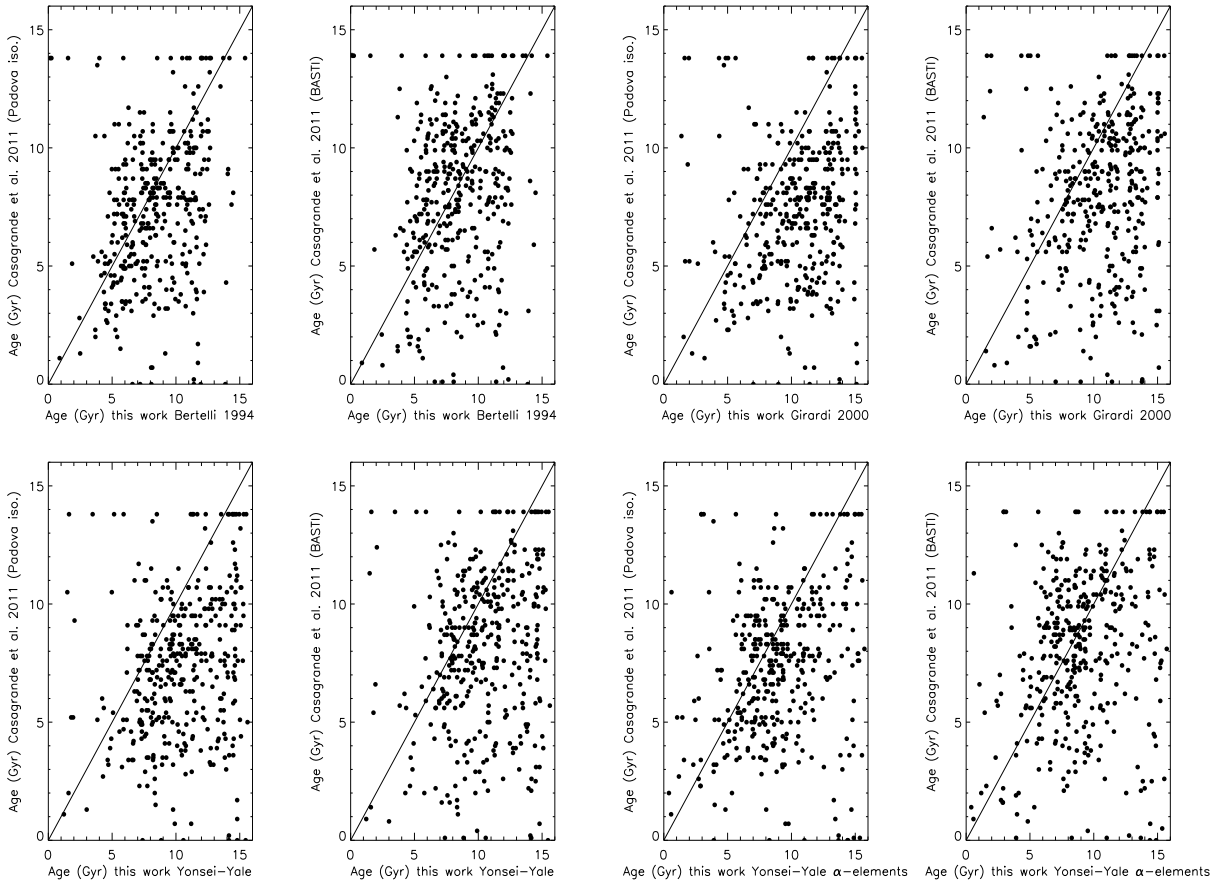

Figure 4.17: 1:1 relation for the ages derived in this work and those derived in Casagrande et al. (2011). We compare the results for different set of isochrones. All the comparison present a significant scatter.

the correlations is poor. Hence what we see in Fig. 4.17 is mainly the differences of the ages due to the differences on the stellar parameters between the two samples. Fig. 4.17 shows correlation between the two sample but there is a significant scatter. We find the best correlation result when using Yonsei-Yale isochrones and taking account the α-elements and Casagrande et al. (2011) using the BASTI isochrones. There are some arguments for going with the ages derived using the Y^2 theoretical isochrones. Fig. 4.12 shows that the uncertainties in age are smallest if we use the Y^2 isochrones. We have seen in Sect. 3.4.9 we are be able to get useful [α/Fe]. Fig. 4.15 shows also that Y^2 isochrone ages using the [α/Fe] values give ages that are most consistent with the Bayesian estimates. These arguments suggest that the ages derived with the Y^2 isochrones are more robust. We make use of these ages for understanding the evolution of the Galactic disk.

Chapter 5

The evolution of the Galactic disk

5.1 Introduction

In this chapter we gather the previous results in an attempt to understand the evolution of the Galactic disk through the age-metallicity and the age-velocity relation (AMR and AVR hereafter). The ages of field stars are one of the main problems on the determination of the shape of the AMR; and if the AVR present an evidence of rapid saturation of the heating mechanism in the disk or it increases steadily with time. Using subgiants, we have derived more accurate ages for field stars, and we expect thereby to derive a new AMR and AVR. We also comment on the impact of the selection effects in the final results.

5.2 The age-metallicity relation

The AMR is a record of the chemical enrichment of the star-forming local interstellar medium during the evolution of the Galactic disk. The progressive chemical enrichment of the interstellar medium suggest that the younger generation of stars is more enriched in heavy elements. According to this simple chemical picture we may expect to find an AMR in which the older stars in the disk are metal-poor and the young population metal-rich. We refer the reader to Chapter 1 for an introduction on the AMR problem.

We have represented the AMRs for the GCS and RAVE sample using the Y^2 set of isochrones and the Y^2 isochrones taking account the α-elements (see Fig. 5.1). The shape of the AMR depends on the isochrone models we use, i.e. our observational results depend on how well we understand the theoretical framework. In general the RAVE sample presents a larger scatter in metallicity than the GCS sample. The two set of isochrones show a gently declining AMR, especially for the GCS sample. Note a clear AMR for stars between 4.0 and 12.0 Gyr for the GCS sample using the Y^2 not taking account the α-elements. For

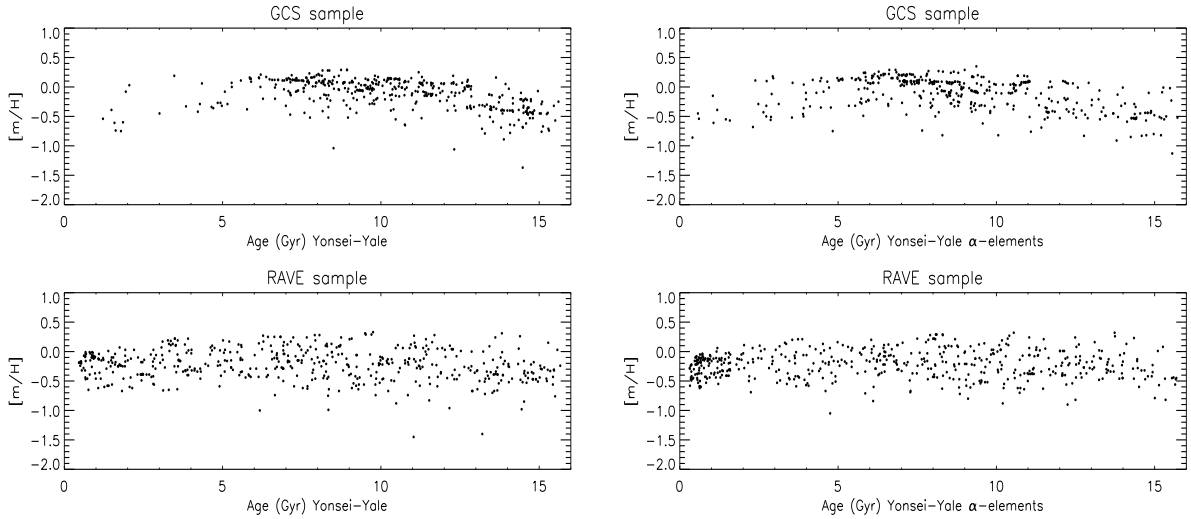

Figure 5.1: Left panel: the age-metallicity relation for the GCS and RAVE sample using Yonsei-Yale set of isochrones. Right panel: the age-metallicity relation for the GCS and RAVE sample using Yonsei-Yale set of isochrones taking into account the α-elements.

stars older than 11.0 Gyr the relation between the age and the metallicity is more evident. Our sample was contaminated by some stars in the turn-off and in the RGB, especially the sample from RAVE. Those stars in the turn-off and in the RGB are younger than the GCS sample which is dominated by subgiants (see Fig. 5.1). As discussed in the previous chapter, the accuracy of ages for the stars in the turn-off and in the RGB could suffer for systematic effects, so we have selected some subgiants in a small range of temperature and gravity to secure the ages.

We have selected stars according to 5000 K $<$ T$_{eff}$ $<$ 5700 K and 3.4 $<$ log g $<$ 4.2. Fig. 5.2 show the AMR using a sub-sample of subgiants. The trend on the AMR is more evident. For the GCS sample we see a clear relation between the age and metallicity. The RAVE sample presents the same trend but the scatter is larger compare with the results from the GCS sample. The stellar parameters for the GCS sample may be more precise as those stars are very bright and hence present very high S/N for the whole spectral range. Note we do not see many young subgiants. Young subgiants are more massive than the stars in our sample and they cross the subgiant region relatively quickly, so it is difficult to observe them. We try to reconstruct the young part of the AMR using Galactic open clusters. Vande Putte et al. (2010) presented a catalogue of 439 Galactic clusters with accurate ages. Information on metallicity is present for 111 of the set of 439. We have selected the clusters older than 0.5 Gyr with metallicity information.

The red points in Fig. 5.3 are the selected open clusters from the Vande Putte et al. (2010) catalogue. The metallicity and the ages of these clusters are quite accurate. The typical uncertainties are 0.11 dex for the metallicity and 0.44 Gyr for the age. Friel et al.

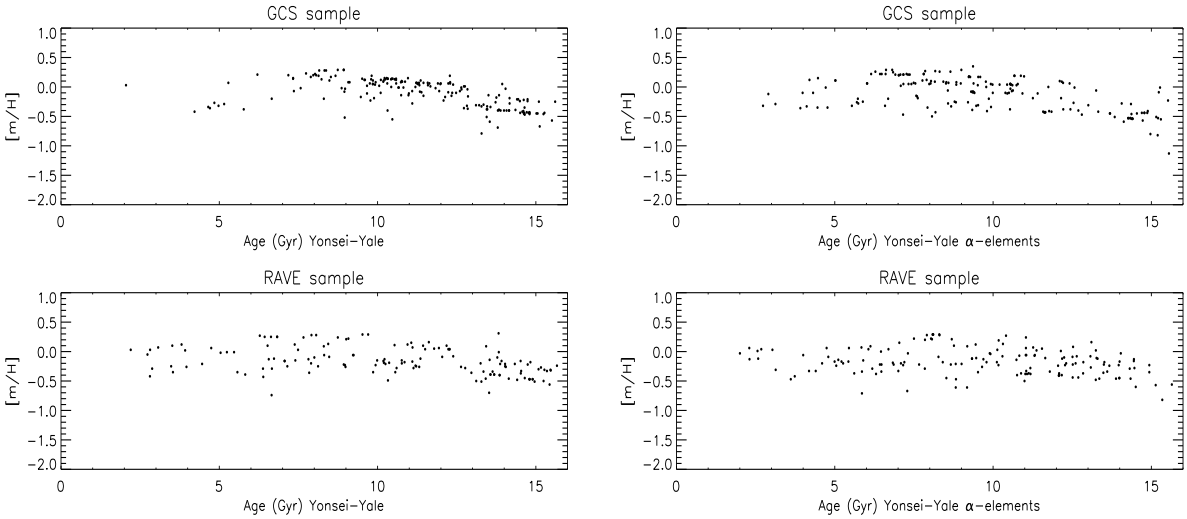

Figure 5.2: Left panel: the age-metallicity relation for a sample of subgiants using Yonsei-Yale set of isochrones. Right panel: the age-metallicity relation for a sample of subgiants using Yonsei-Yale set of isochrones taking into account the α-elements.

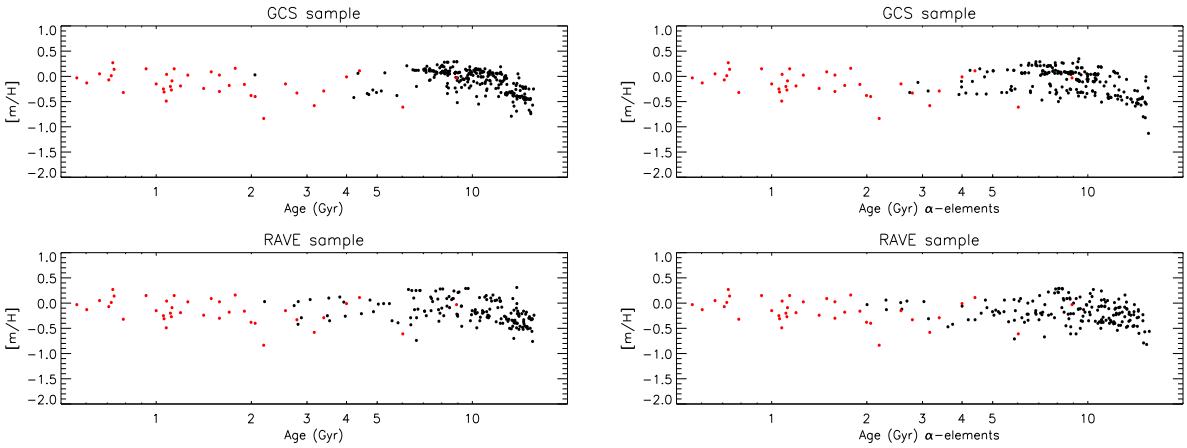

Figure 5.3: The age-metallicity relation for the whole sample of subgiants. The red dots represent open cluster from the Vande Putte et al. (2010) catalogue.

(2002) using 24 open cluster older than 0.7 Gyr found that there is no clear correlation between metallicity and age; the oldest open clusters are as metal-rich as the youngest. The 44 open clusters presented in Fig. 5.3 show a declining AMR. Note that clusters younger than 1.0 Gyr present mainly solar or up-solar metallicity. For clusters older than 1.0 Gyr the sample presents mainly sub-solar metallicity. Note also that we find a very old open cluster (8.9 $\pm$ 2.3 Gyr) called Collinder 261 at solar metallicity ([m/H] = -0.03 $\pm$ 0.03). However, the number of open clusters older than 2.5 Gyr is fairly small. Only a very

few massive clusters could survive for long the internal and external dynamical processes (Lamers et al. (2005)). Note that the age-axis in Fig. 5.3 is scaled logarithmically. Fig. 5.3 shows also the AMR for the GCS and RAVE subgiants sample. The field subgiants show a clear AMR for stars older than 5.5 Gyr. The correlation between the age and the metallicity is clear in the GCS sample when using the Y^2 isochrones with $[\alpha/Fe] = +0.0$. The RAVE sample presents the same trend but the scatter is larger. Using isochrones taking into account the α-elements introduce scatter on the AMR.

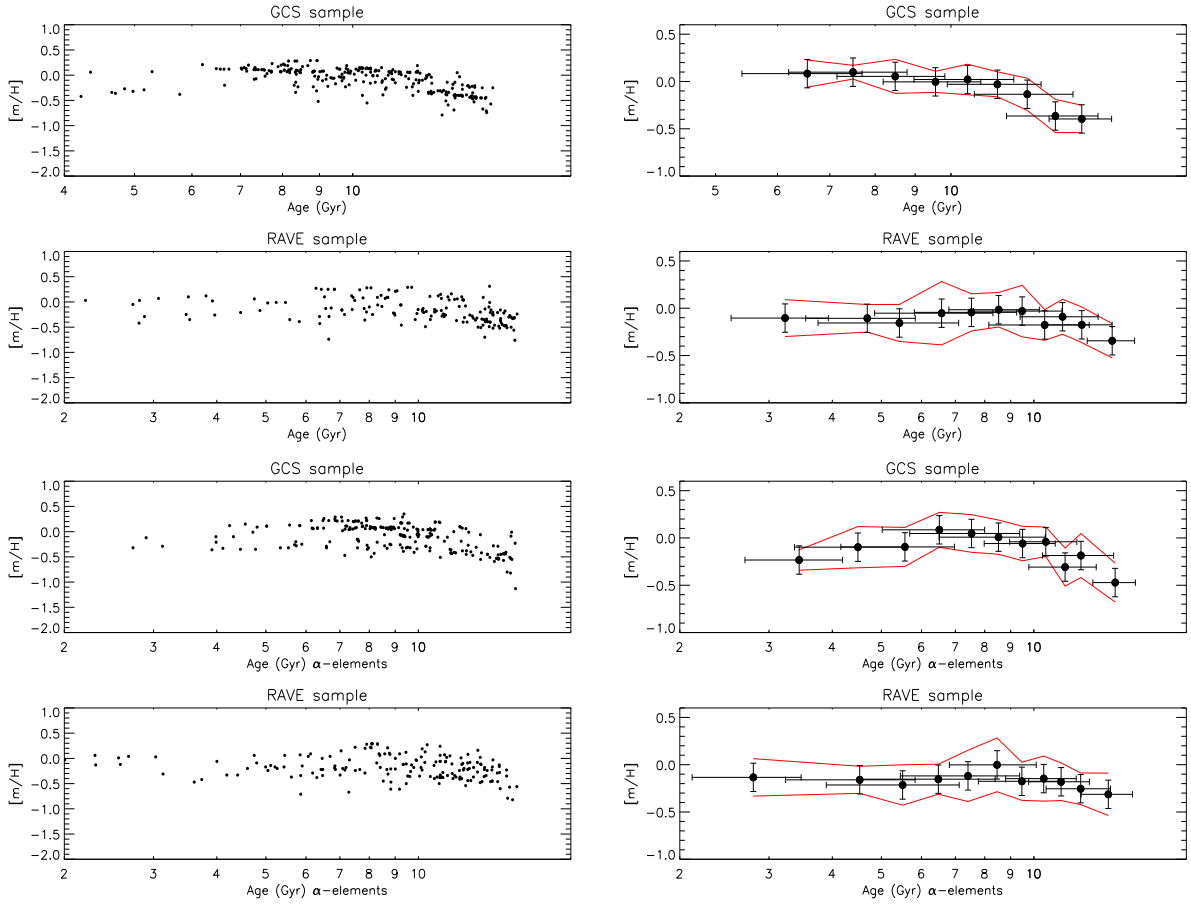

Figure 5.4: Left panels: the age-metallicity relation for the GCS and RAVE sample of subgiants taking and not taking into account the α-elements. Right panels: the big dots represent the mean value in metallicity and age for a 1.0 Gyr bin. The error bars are also represented for both quantities and the scatter (red line) in metallicity for a 2.0 Gyr bin.

Fig. 5.4 shows the AMR for the GCS and RAVE sample. We make also simple statistics on the data. We have computed the mean and the standard deviation for the stars in the age-metallicity plane in 1.0 Gyr bins. The typical uncertainties in metallicity are around 0.16 dex; and for the ages we find easily uncertainties of 1.5 - 2.0 Gyr. The uncertainties on the age we see in Fig. 5.4 are the mean value of the individual errors in the 1.0 Gyr

Age (Gyr)	N (GCS sample)	$< [m/H] >$	$\sigma_{<[m/H]>}$
6 - 7	6	+0.08	0.14
7 - 8	27	+0.09	0.07
8 - 9	43	+0.05	0.17
9 - 10	30	-0.01	0.11
10 - 11	34	+0.02	0.16
11 - 12	26	-0.03	0.13
12 - 13	26	-0.13	0.17
13 - 14	24	-0.36	0.17
> 14	39	-0.39	0.14

Table 5.1: Mean age, mean metallicity and dispersion for a 1.0 Gyr bin for the GCS sample.

bin. Note the clear AMR using the GCS sample. The red lines represent the scatter in a 1.0 Gyr bin. The AMR using the GCS sample does not show the large scatter present in other studies using Hipparcos stars (e.g. Edvardsson et al. (1993), Feltzing et al. (2001), Ibukiyama & Arimoto (2002), Casagrande et al. (2011)). The RAVE sample and the isochrones for different values of $[\alpha/Fe]$ increase the scatter on the AMR. Our estimation of $[\alpha/Fe]$ has an associated uncertainty of about 0.1 dex. That would contribute to find an AMR with a large scatter. Note that the age-axis scale in Fig. 5.4 for the GCS sample starting at 4.0 Gyr. Few stars younger than 4.0 Gyr are in the GCS sample. We want to emphasize a clear AMR for stars older than 5.5 Gyr.

The AMR for the GCS sample is presented in Tab. 5.1, which gives the number of stars in each metallicity bin, the average [m/H] and the metallicity dispersion. A comparison between the present work and PASTEL shows a good correlation for the metallicity (see Fig. 3.30). The RMS is 0.16 dex; hence the measuring errors for the metallicity are ≤ 0.16 dex. Note also that for the subgiant sample the uncertainties in age are ≤ 2.0 Gyr. We find a mean scatter for the AMR of 0.14 dex. *From this one might be tempted to conclude that the observed scatter on the AMR reflects the measuring errors in the abundances of the observed stellar atmospheres, which would suggest a relation between the abundances and the ages of the stars in the Galactic disk.*

The scatter on the AMR tends to be large for metal-poor stars (see Fig. 5.5). That could be explained by a mixing of stars by *orbital diffusion* from different Galactocentric distances in our sample, as we find that stars more metal-poor than -0.3 dex are older than 12.0 Gyr (e.g. Wielen (1977)). Edvardsson et al. (1993) based on Wielen (1977) study of kinematic properties of K and M dwarfs with estimated ages showed that a scatter of about 0.1, 0.2 and 0.3 dex in metallicity is expected for stars in the solar volume with ages = 1.0, 5.0 and 10.0 Gyr respectively. Note that we do not find this significant scatter on our data. Even for the oldest stars we find small scatter on the AMR. The results presented here would suggest that the diffusion process may not be very efficient, or else that the kinematical assumption made by Wielen (1977) about an steady increase of the dispersion of stellar space velocities with age may not be completely correct, as Edvardsson et al.

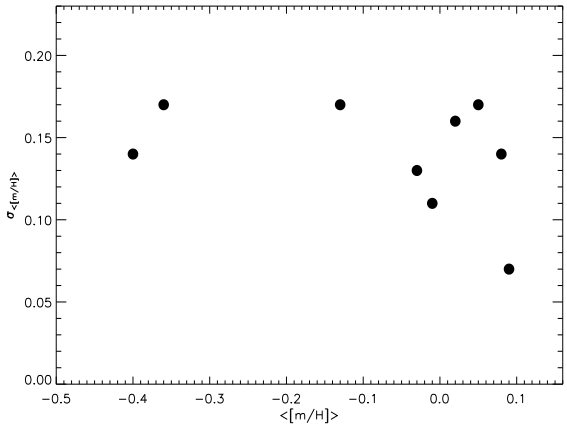

Figure 5.5: The scatter on the AMR as a function of mean metallicity for the GCS sample.

(1993) use the kinematical results from Wielen (1977) for their estimation. Models taking into account the chemical enrichment and the dynamical evolution of the system present a significant scatter in the AMR (Raiteri et al. (1996)). Sellwood & Binney (2002) proposed a theory called *radial mixing*. According to this theory the stars could migrate over large radial distances due to the resonant interactions with spiral density waves. Radial mixing theory predicts an AMR with a high degree of scatter (Roškar et al. (2008)) where half of stars of the solar neighbourhood came from large radial distances (> 2 kpc) according to their simulations and most of the metal rich stars in the solar volume originate from the inner disk (Haywood (2008)). In fact, radial mixing was invoked in attempts to explain the width of the MDF at a given age that some authors found on the AMR (see Chapter 1). The results presented about the AMR in this work suggest a less need for radial migration in the Galactic disk. Note also that other authors such as Rocha-Pinto et al. (2000a), Pont & Eyer (2004) and Soubiran et al. (2008) have found the existence of an AMR with a low scatter for the solar vicinity.

Fig. 5.6 shows the MDF for four different ranges in age for the GCS sample. The population with an intermediate age is dominated by metal-rich stars while the old population presents mainly metal-poor stars. Note the two populations for the age range between 11.0 and 13.5 Gyr. We have also tried to understand the AMR using the data from Casagrande et al. (2011). Using the whole catalogue they found the same constant mean metallicity and large scatter at all ages. We have selected a group of subgiants using the same criteria on temperature and gravity used in the present work.

Fig. 5.7 shows the AMR for the whole sample and the AMR for a sample of subgiants. The black line is the mean and the red lines are the dispersion with respect to the mean. Note that when using the whole sample, the AMR is nearly flat and the scatter is up to 0.22 dex, while using only subgiants, the AMR gently declines and the scatter in metallicity is around 0.15 dex. Note also the large number of metal-rich stars in the subgiant region

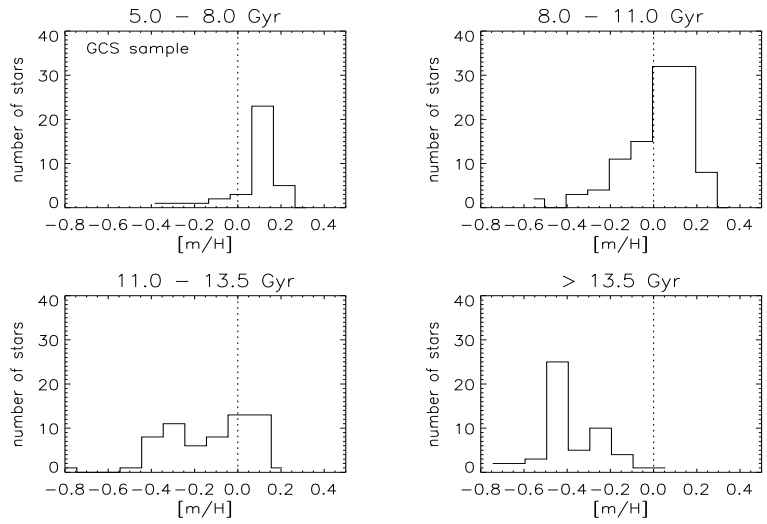

Figure 5.6: Metallicity distribution function for four different age bins.

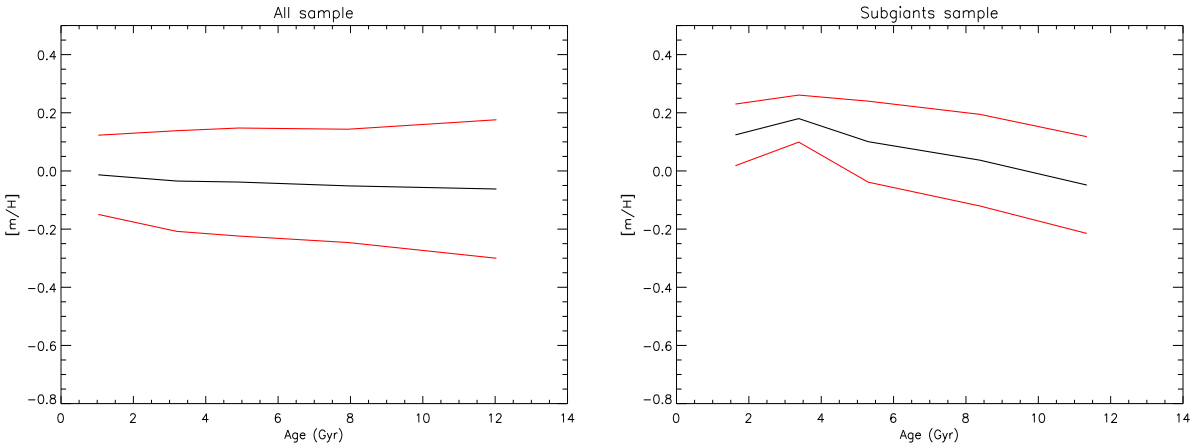

Figure 5.7: The age-metallicity relation for the whole sample and the subgiants respectively using the data from the last GCS version. The black line is the mean and the red lines are the dispersion with respect to the mean.

when using the Casagrande et al. (2011) sample. Stars out of the subgiant region add scatter to the AMR, flattening it.

5.2.1 The age-[α/Fe] relation

We now investigate the relation between the [α/Fe] and age. We mentioned in Chapter 1 that the vertical distribution of stars in the solar cylinder is best approximated by two

exponential laws suggested the presence of two components of different scaleheights, the Galactic thin and thick disk (Gilmore & Reid (1983)). The finding that thick disk stars are substantially older and more highly enriched in α-elements than their thin disk counterparts supports the two-component nature of the Galactic disk (Gratton et al. (1996), Prochaska et al. (2000), Bensby et al. (2007), Fuhrmann (2008)). The thin and thick disks differ, at given metallicity, in their kinematics, age and α-content. We will now explore this dichotomy.

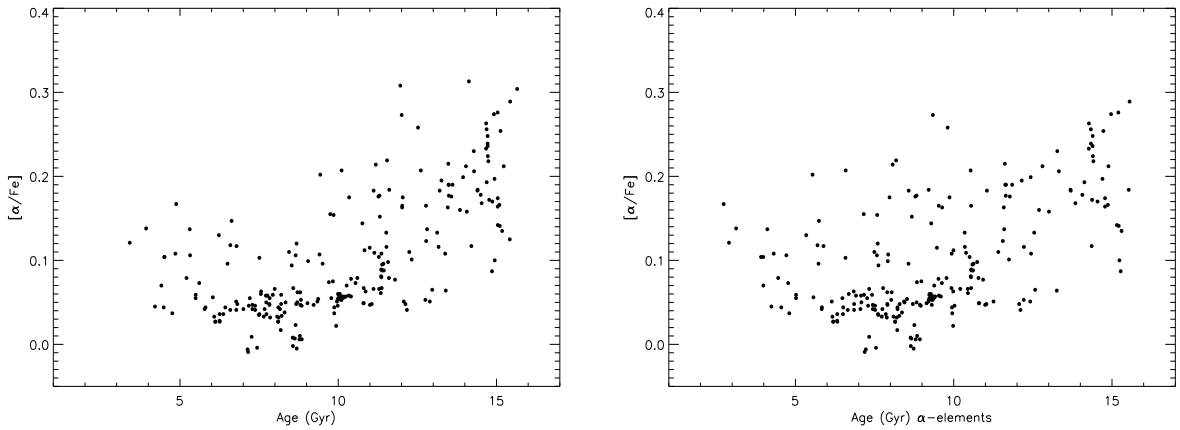

Figure 5.8: Relation between the α-elements and the age using the GCS sample. The ages were computing not taking into account the α-elmements (left panel) and taking it into account (right panel).

Fig. 5.8 shows a clear relation between the α-elements and the age for the thin disk stars using the GCS sample. For the oldest stars there is clearly an increase in the scatter of [α/Fe]. Very likely these old stars are part of the thick disk. Using the ages derived by taking into account the α-elements, the relation is still present but there is also more scatter.

With the RAVE sample we find similar results but the relation is less obvious due to the larger uncertainties in the α-elements (see Fig. 5.9). The results using the GCS sample are in good agreement with Edvardsson et al. (1993). They wrote: *apart from a possible increase in σ([α/Fe]) for stars older than 10.0 Gyr there is hardly any significant scatter in [α/Fe] at a given age and galactocentric distance.* Edvardsson et al. (1993) pointed out the clear conflict between the substantial scatter in the AMR and the astonishing small scatter in the age-[α/Fe] relation for stars younger than 10.0 Gyr. Note that in the present work we also find small scatter in the age-metallicity relation. As discussed in Edvardsson et al. (1993) this small amount scatter in the age-[α/Fe] for the thin disk stars would exclude local bursts of star formation, because such bursts would be expected to produce a large scatter in [α/Fe] (e.g. Gilmore & Wyse (1991)). Fig. 5.8 suggests that our *absolute ages* are overestimated around 2.0 Gyr, as we discussed in the previous chapter. Generally,

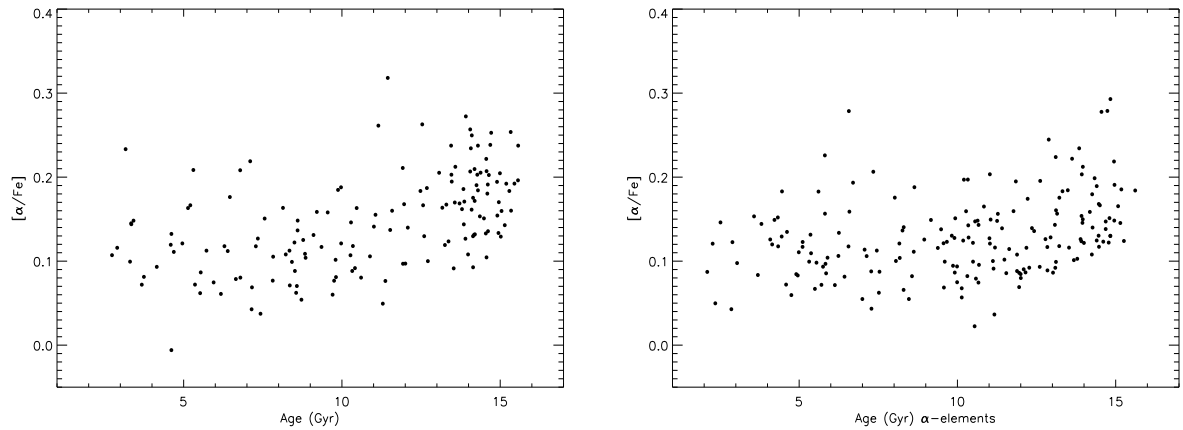

Figure 5.9: Relation between the α-elements and the age using the RAVE sample. The ages were computing not taking into account the α-elmements (left panel) and taking it into account (right panel).

estimates of the age of the thin disk using the luminosity function of white dwarfs attain a lower limit for the age of around 9.0 Gyr (e.g. Leggett et al. (1998), Knox et al. (1999)) while the thick disk is in general found to be exclusively old, where "old" means as old as the globular clusters of the same metallicity (e.g. 47 Tuc), or at least 10.0 Gyr, and probably 12.0 Gyr (see Feltzing & Bensby (2009), Wyse (2009a) and references therein) as we discussed in chapter 1. There is a gradient in [α/Fe] for the thin disk stars. We find that stars around 5.5 Gyr present [α/Fe] slightly higher than solar ($\sim$ +0.02) while the oldest thin disk stars show values around +0.1 dex. For the thick disk stars we find values from +0.1 up to +0.3 dex in [α/Fe].

5.2.2 Selection effects

In this section we check the systematic effects and bias that the isochrones could introduce in the ages for the selected subgiants and hence in the age-metallicity relation. We created a synthetic AMR, covering the range in metallicity from -1.5 to +0.5 in steps of 0.1 and the ages from 0.1 to 16 in steps of 0.1 Gyr.

We use Y^2 isochrones with [α/Fe] = +0.0 to compute the temperature and gravity for a given metallicity and age using the synthetic AMR we have created. A single point in the age-metallicity plane defines a whole isochrone for that age and metallicity and the step size for temperature and gravity come from the isochrone. We selected stars in the following range: $4900 < T_{eff} < 5900$ K and $3.1 <$ log g < 4.2, and compute the ages using the maximum likelihood method already described for a given temperature, metallicity and gravity. Fig. 5.10 shows the synthetic AMR and the AMR recovered. We also show the age

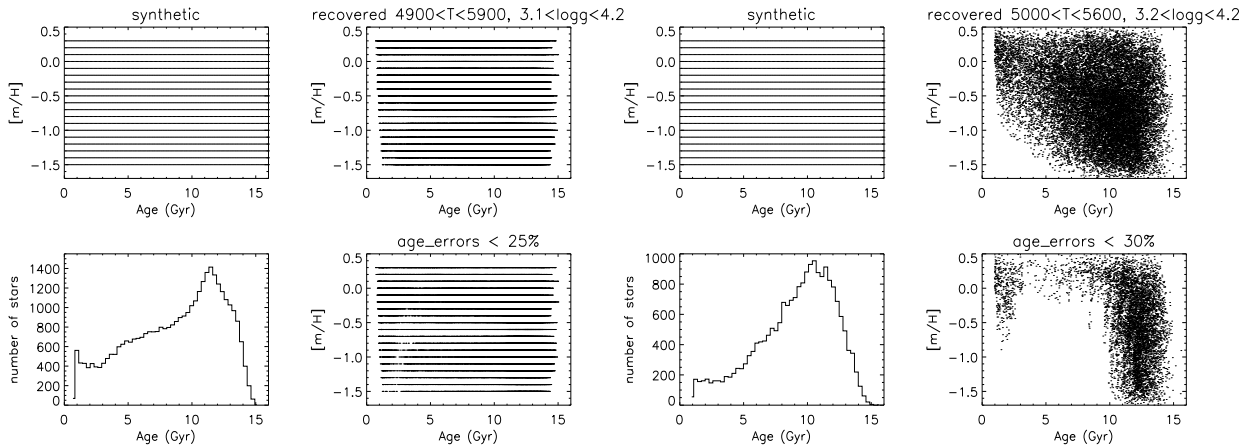

Figure 5.10: Left panels: synthetic and recovered AMRs not taking into account the errors in the stellar parameters. The ADF and the AMR for the stars with a age error < 25 % are also represented. Right panels: synthetic and recovered AMRs taking into account the errors in the stellar parameters. Note the severe bias we find when slecting stars with low errors in age.

distribution function. Ideally that distribution should be flat, but the nature of isochrones and the age mechanism push the star ages up. We have selected stars in the range 5000 $<$ T$_{eff}$ $<$ 5600 K and 3.1 $<$ log g $<$ 4.2. The use of a restricted range of temperature will produce a bias against young stars, which tend to be hotter. This effect is therefore less if we extend the range to hotter stars. We can see this effect in Fig. 5.10; the simulation using the temperature range between 4900 - 5900 K shows a smaller bias against young stars. This bias is inevitable if we want to avoid the turn-off stars but the important point for the AMR is not the bias against young stars, but wheter there is a bias against stars of a given age which depends on metallicity. For the AMR is not important how many stars there are at each age -that is affected by the star formation history (which is another problem). We want the form of the MDF at each age and to know whether MDF could be modified by our selection. The bias in the age direction would reduces the overall number of younger stars, so the statistics for the AMR at the young end are worse. We stress that our sample will not represent an age distribution: we seek to obtain the MDFs as a function of age. Note also that in the right panel, Gaussian errors in temperature -σ = 100 K, and 0.1 dex in metallicity and gravity, were applied before the age computation. The last panel is the AMR, selecting stars with low errors in age. We see clearly that selecting stars according with the errors in age introduces a severe bias in the shape of the AMR. This bias depletes the number of young metal poor stars relative to the number of young metal rich stars. An interesting point is that the bias effect selecting stars with lower errors is less evident when we do not introduce Gaussian errors in the stellar parameters (see Fig. 5.10 left and righ panels). To take a selection of stars with low age errors is a common practice when studying the AMR in the solar vicinity (e.g. Feltzing et al. (2001), Nordström et al. (2004), Holmberg et al. (2009), Casagrande et al. (2011)). This bias together with the *terminal*

age bias already mentioned was also pointed out by Pont & Eyer (2004).

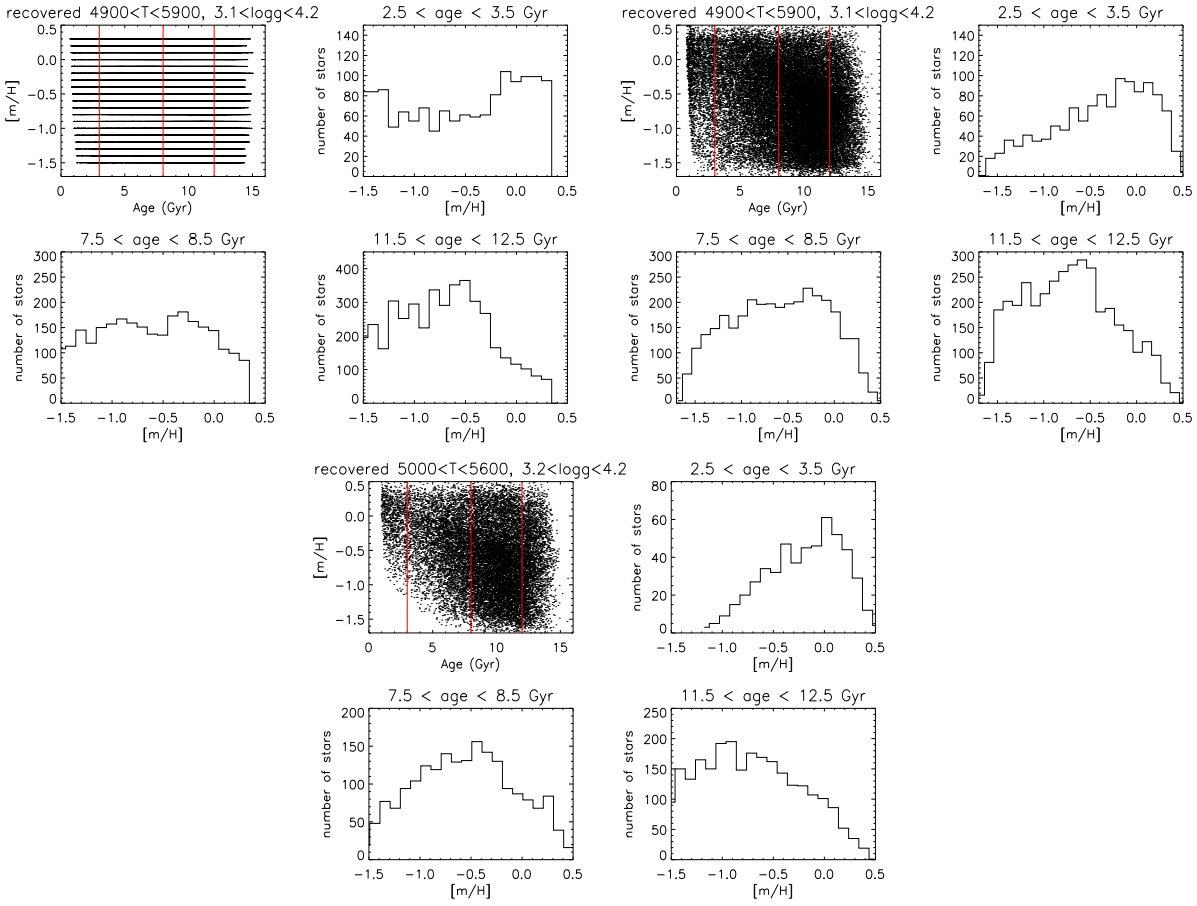

Figure 5.11: Top left: recovered MDFs for three different range in ages from the synthetic AMR without taking into account the errors in the stellar parameters. The vertical red lines in the recovered AMR represent the age range for the ADF. Top right: recovered MDFs for three different range in ages from the synthetic AMR taking into account the errors in the stellar parameters. Bottom panels: recovered MDFs for three different range in ages from the synthetic AMR taking into account the errors in the stellar parameters for a restricted range of temperatures (e.g. 5000 - 5600 K).

Fig. 5.11 presents the recovered MDFs for three different age ranges from the synthetic AMR. The metallicity distribution is nearly flat for young and intermediate stars, but for the oldest stars there is gradient for metal-rich stars. Without a bias, these histograms should be flat. The addition of Gaussian errors to the stellar parameters recovered from the isochrones results in the MDF being dominated by metal-rich stars for the young ages and for metal-poor stars for the old ages (see the right panels in Fig. 5.11). Using a restricted range of temperatures (e.g. 5000 - 5600 K) the effect mention above is more evident. The age machinery is be able to recover the synthetic AMR reasonably well, however there are

some effects on the MDFs for a given age due to the nature of the isochrones in this range and the maximum likelihood method itself taking account the measuring errors on the stellar parameters. Note also that, for the temperature range between 5000 K and 5600 K, there are not stars more metal-poor than -1.0 in the range between 1.0 and 4.0 Gyr in the recovered AMR. This effect comes about because the very low metallicity stars are hotter, so more are lost due to the selection criteria in temperature and gravity.

5.3 The evolution of the Galactic disk through the kinematics of its stellar components

We often applied the term *disk heating* to the sum of the effects that may cause larger velocity dispersions in the disk stars. In principle, one may expect that the heating processes inject kinetic energy into the random component of the stellar motion over time. In order to understand the origin of the present assemblage of disk stars, it is necessary to to quantify the kinematic properties of the populations in the disk and characterize the properties of their stars as accurately as possible. Using very accurate kinematics from the GCS and RAVE survey together with the reliable ages from the the selected sample of subgiants, we will investigate the kinematical evolution of the Galactic disk.

5.3.1 Distances and space motions

The stars selected from GCS are nearby and have trigonometric parallaxes of excellent quality from Hipparcos (Perryman & ESA (1997)). For the selected RAVE stars we use the photometric distances derived by Zwitter et al. (2010) assuming a standard stellar evolution scenario.

The re-reduction of the raw Hipparcos data by van Leeuwen (2007) reduced the parallax errors by a factor ~ 1.5 on average -a substantial improvement on the original results. Fig. 5.12 show the distribution of the new parallaxes in the GCS sample. For the RAVE sample, Zwitter et al. (2010) derived the most likely distance to the star. They assumed that a star follows stellar evolution as mirrored by theoretical isochrones. They also use the knowledge on stellar evolution to compensate for some of the errors in values of stellar parameters as derived by RAVE. Note in Fig. 5.12 that RAVE distances present significant uncertainties. Accurate proper motions are available from the Tycho-2 catalogue (Høg et al. (2000). This catalogue is constructed by combining the Tycho star-mapper measurements of the Hipparcos satellite with the Astrographic Catalogue based on measurements in the Carte du Ciel and other ground-based catalogues. The typical mean error in the total proper motion vector is 1.8 milliarcsec/year. Proper motions of varying accuracy are available for most of the RAVE stars via Starnet 2.0, Tycho-2, or the SuperCOSMOS Sky Survey (see Steinmetz et al. (2006) for more details). The radial

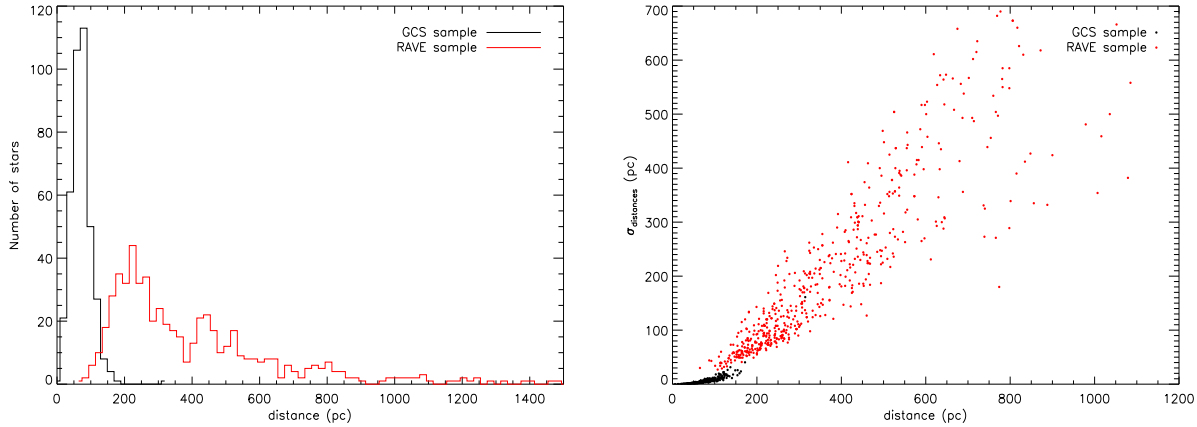

Figure 5.12: Left: the distribution of the distances for the GCS ans RAVE samples. Note the very local volume sampled by GCS stars. Right: relation between the distances and their associated error for the GCS sample (black) and for the RAVE sample (red).

velocities for the GCS stars was obtained with the photoelectric cross-correlation spectrometers CORAVEL (Baranne et al. (1979), Mayor (1985)). Operated at the Swiss 1-m telescope at Observatoire de Haute-Provence, France, and the Danish 1.5-m telescope at ESO, La Silla. The typical mean error in the radial velocity is $\sim$ 0.3 km/s. The radial velocities for the RAVE survey have uncertainties better than 3.4 km/s (Steinmetz et al. (2006), Zwitter et al. (2008), Siebert et al. (2011)).

Velocities in a cylindrical galactic system were obtained following the method developed by Johnson & Soderblom (1987). From the observed radial velocities, proper motions and parallaxes we derive the space velocity components (U,V,W). (U,V,W) are defined in a right-handed Galactic system with U pointing towards the Galactic center, V in the direction of rotation, and W towards the north Galactic pole. No correction for the Solar motion has been made in the tabulated velocities. The average error of the Tycho-2 proper motions corresponds to only 0.7 km/s in the tangential velocities, so the dominant source of error in the space motions is the distance (Nordström et al. (2004), Holmberg et al. (2007), Holmberg et al. (2009)). Accounting for all these sources, we find the average error of our spatial motions to be 1.5 km/s in each component (U, V, and W) for the selected GCS stars. For the RAVE sample, we find that the average error to be around 10 km/s in each component. Fig. 5.13 show the U-V, U-W, and V-W diagrams for all stars in our GCS sample. The velocity space has been widely used to find structures (classic moving groups or stellar streams[1]) in the Galactic disk (e.g. Dehnen (1998), Skuljan et al. (1999), Antoja et al. (2008), Williams et al. (2009)). The plane U-V in Fig. 5.13 show members of the *Sirius stream* and *Pleiades stream* together around (U,V) = (0,0) km/s and some

[1]These streams, or moving groups are thought to be vestiges of the clusters and associations in which most stars form.

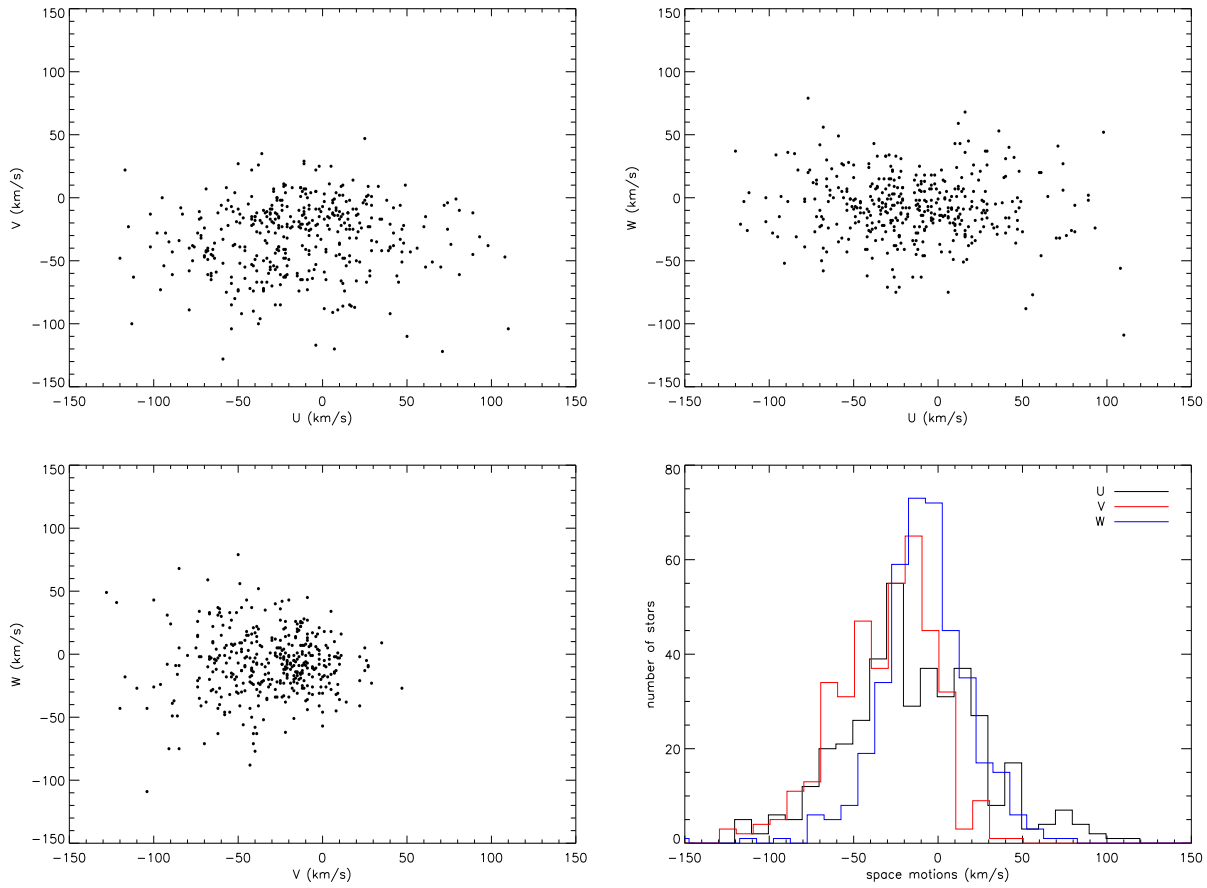

Figure 5.13: U-V, U-W, and V-W diagrams for all stars in our GCS sample and the distribution of U,V and W.

stars from the *Hyades stream* around (U,V) = (-30,-40) km/s.

Fig. 5.13 also show the histograms of U, V and W. The V distribution show a long tail towards negative V. This is a consequence of the so called asymmetric drift (Dehnen & Binney (1998), Binney & Merrifield (1998)). Fig. 5.14 show the U-V, U-W, and V-W diagrams for all stars in our RAVE sample and the histograms of U,V and W. Note the two sub-groups we could see in Fig. 5.13 they are not so evident with the RAVE data. The average velocity error in our sample does not allow us to distinguish these substructures. This fact could blur the sub-groups in the velocity space. In Fig. 5.14 we also show the histograms of U, V and W for the RAVE sample. Note that the V distribution also shows the long tail towards negative V.

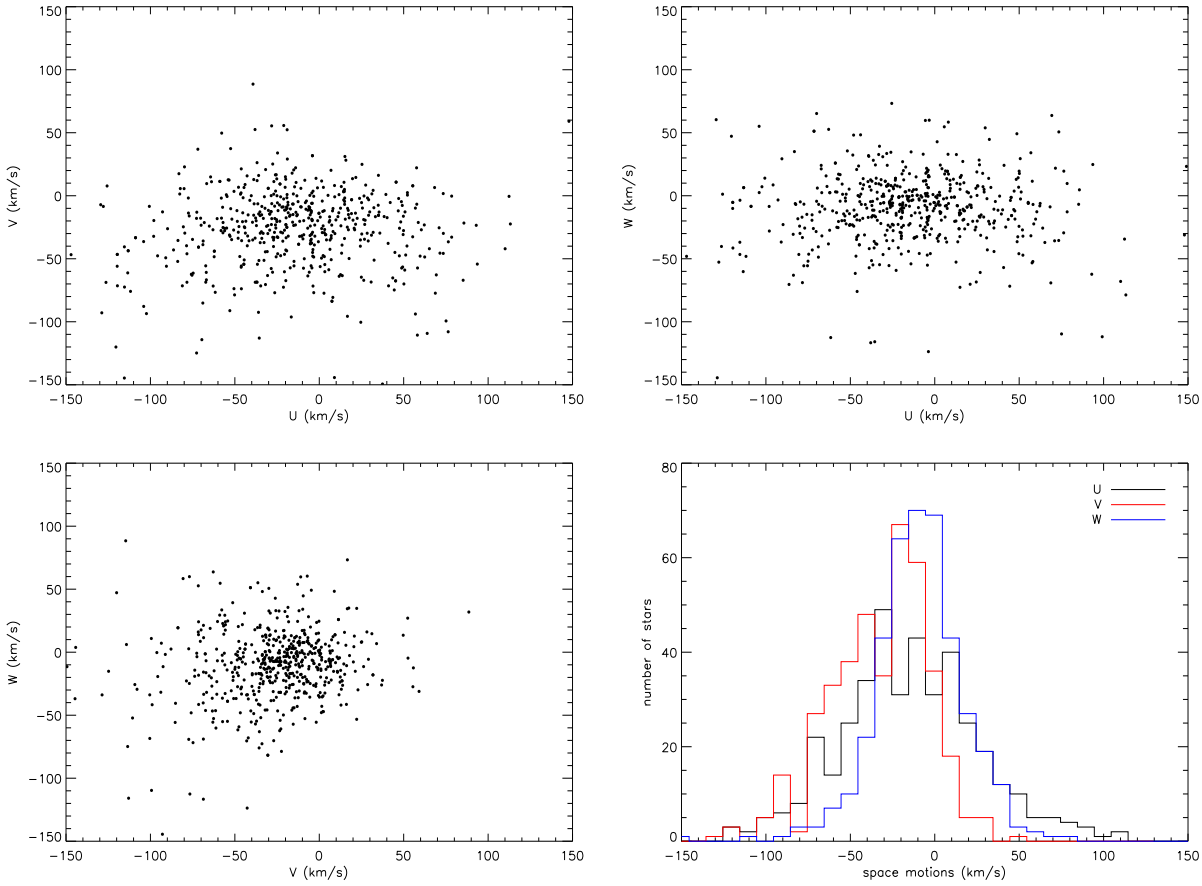

Figure 5.14: U-V, U-W, and V-W diagrams for all stars in our RAVE sample and the histograms of U,V and W.

5.3.2 The metallicity-velocity relation

The metallicity-velocity relation for our data is discussed. Previous studies have found that the velocity dispersion increases as metallicity decreases. For example, Stromgren (1987) showed the variation of σ_R and σ_Z with metallicity for 1294 stars in the metallicity range from +0.2 to -0.8 dex. At solar metallicity, they found $\sigma_Z \sim 18$ km/s while around [m/H] = -0.7, $\sigma_Z \sim 38$ km/s. It is well establish that the thick disk stars are more metal-poor and present a higher velocity dispersion than the thin disk stars (e.g. Gratton et al. (2000), Venn et al. (2004), Soubiran & Girard (2005), Veltz et al. (2008), Navarro et al. (2011)). That would suggests that the increase in the velocity dispersion is just a result of decreasing fraction of thin/thick disk stars as the metallicity decreases. We will further explore this issue.

In Fig. 5.15 we represent the spatial motions versus the metallicity for the GCS sample.

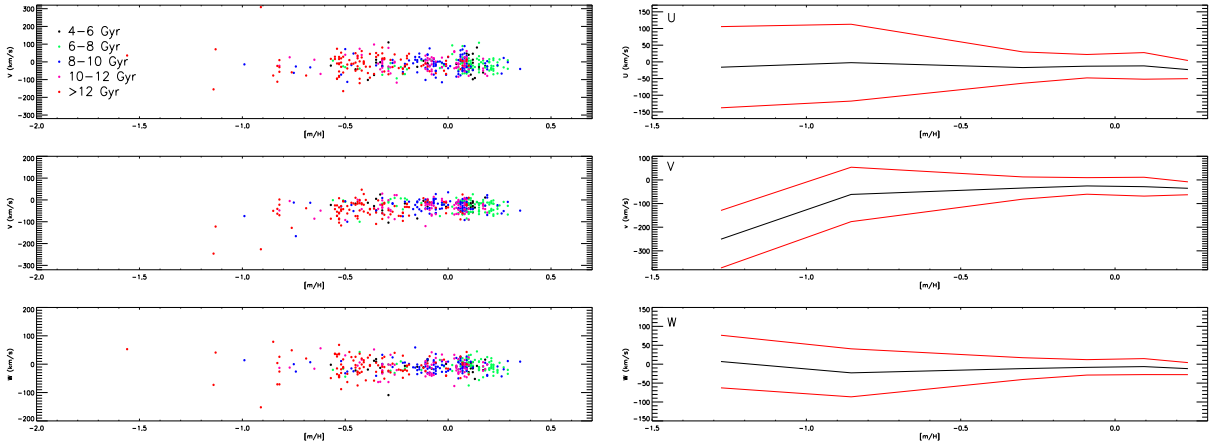

Figure 5.15: Metallicity-velocity relation for the GCS sample. Left panels: space velocities versus metallicity, the colors indicate different range of ages. Right panels: the black line represents the mean velocity and the red line represents the velocity dispersion for U, V and W.

We color-code these stars binned by age. We use the ages computed with the Yonsei-Yale stellar evolution models. Note that the metal-rich stars are dominated by the young population. For +0.1 < [m/H] < -0.3 there is a mixture of intermediate-old stars and around -0.5 dex the population is dominated by old stars. Fig. 5.15 that U, V and W-velocities are independent of metallicity for a range between +0.2 and -0.7 dex. Furthermore the velocity dispersion (red line) remains roughly constant for a metallicity range from +0.2 to -0.5 dex for this GCS sample. This results are very similar to those we found in Navarro et al. (2011) using the catalogue presented in Venn et al. (2004). For metal-poor stars ([m/H] < -0.7 dex and older than 10 Gyr), the velocity dispersion clearly increases for the three velocity components. Note also how the V-component for these metal-poor stars lag behind, indicating that these stars have a rotational velocity lower than the metal-rich population.

Fig. 5.16 shows the same study for the RAVE sample. In accordance with our computed ages, stars with metallicity lower than -0.4 dex are mainly quite old for this RAVE sample. The V-velocity do not show evidence of a gradient until we reach the very metal-poor population. The velocity dispersion is independent of the metallicity in U and V for a big range in metallicity (+0.2 < [m/H] < -0.8). The velocity dispersion in the W-velocity increase for metallicities lower than -0.4 dex.

In Fig. 5.17 we represent the velocity dispersion versus the metallicity for the GCS and RAVE sample. Fig. 5.17 shows clearly that the velocity dispersion for the three velocity components (U,V,W) increase as metallicity decreases. Note that the dispersion is nearly constant for stars with [m/H] > -0.2. For stars more metal-poor than -0.4 there is an abrupt increase of the velocity dispersion. Is that because the sample starts to be dominated by thick disk stars? In Fig. 5.8 we see a clear relation between [α/Fe] and the age of the stars for the thin disk. We use this relation to get a clean sample of thin disk stars.

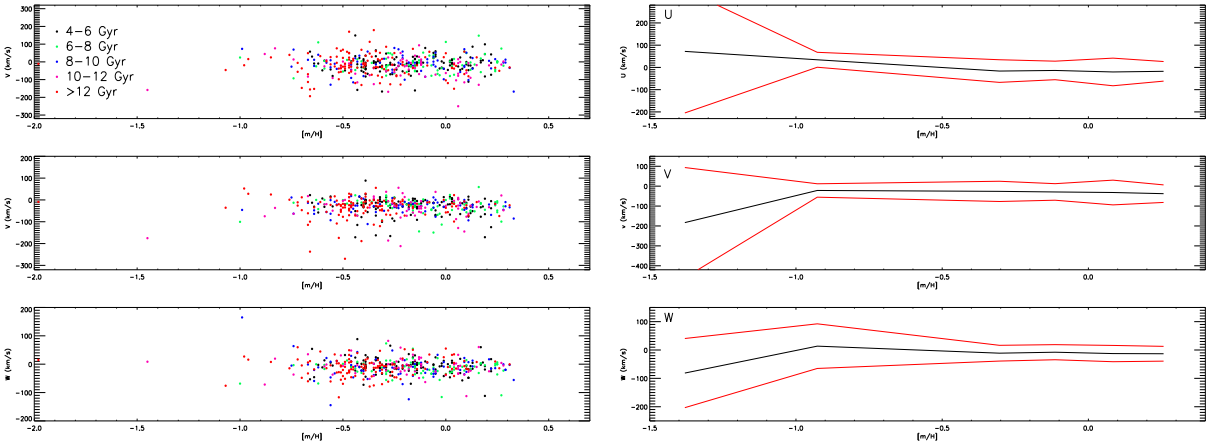

Figure 5.16: Metallicity-velocity relation for the RAVE sample. Left panels: space velocities versus metallicity, the colors indicate different range of ages. Right panels: the black line represent the mean velocity and the red line represent the velocity dispersion for U, V and W.

Fig. 5.18 shows the velocity dispersion as a function of metallicity for stars identified as belonging to the thin disk component (age $\leq$ 12.0 Gyr and [α/Fe] $\leq$ 0.15 dex). We find little or no correlation between velocity dispersion and metallicity, over the range in metallicity spanned for the selected thin disk stars. Stars more metal rich than the Sun present $\sigma_V \sim$ 25 km/s while stars with [m/H] < -0.2 show a $\sigma_V \sim$ 28 km/s. However, with this selection criteria based on the age-[α/Fe] relation the most metal-poor stars are around -0.44 dex. Some authors have found that the thin disk could be as metal-poor as -0.6 dex (Navarro et al. (2011) and references therein). We find that the velocity dispersion is roughly independent of metallicity for the thin disk. These results are in good agreement with Navarro et al. (2011). See that work for a good discussion on the implications of these results. Note that in Navarro et al. (2011) we explored the value of the *r-process* element Eu to separate into two groups that delineate the traditional thin and thick disk components of the Milky Way. However, Haywood (2008) and Lee et al. (2011) found a clear gradient for the rotational velocity with metallicity for a thin disk population selected using [Mg/Fe] and [α/Fe] respectively. It is an open question if this gradient for the thin disk is real, or due to the "clean thin disk" sample still containing a fraction of stars belonging to the thick disk.

We investigate the dependence of the the axial ratios σ_V/σ_U, σ_W/σ_U and the asymmetric drift with the metallicity of the stellar group. In Fig. 5.19, we represent the value of the ratio between the semi-axes of the velocity ellipsoid, σ_V/σ_U and σ_W/σ_U versus metallicity. σ_V/σ_U is nearly constant for stars with [m/H] > -0.5 dex being $\sigma_V/\sigma_U = 0.68$. However, for metal-poor stars ([m/H] < -0.6 dex) σ_V/σ_U clearly increases. For this metal-poor population we have $\sigma_V/\sigma_U \sim 0.97$. That would suggest a significant change on the shape of the velocity ellipsoid. σ_W/σ_U is independent of the metallicity as we see in Fig. 5.19. σ_W/σ_U

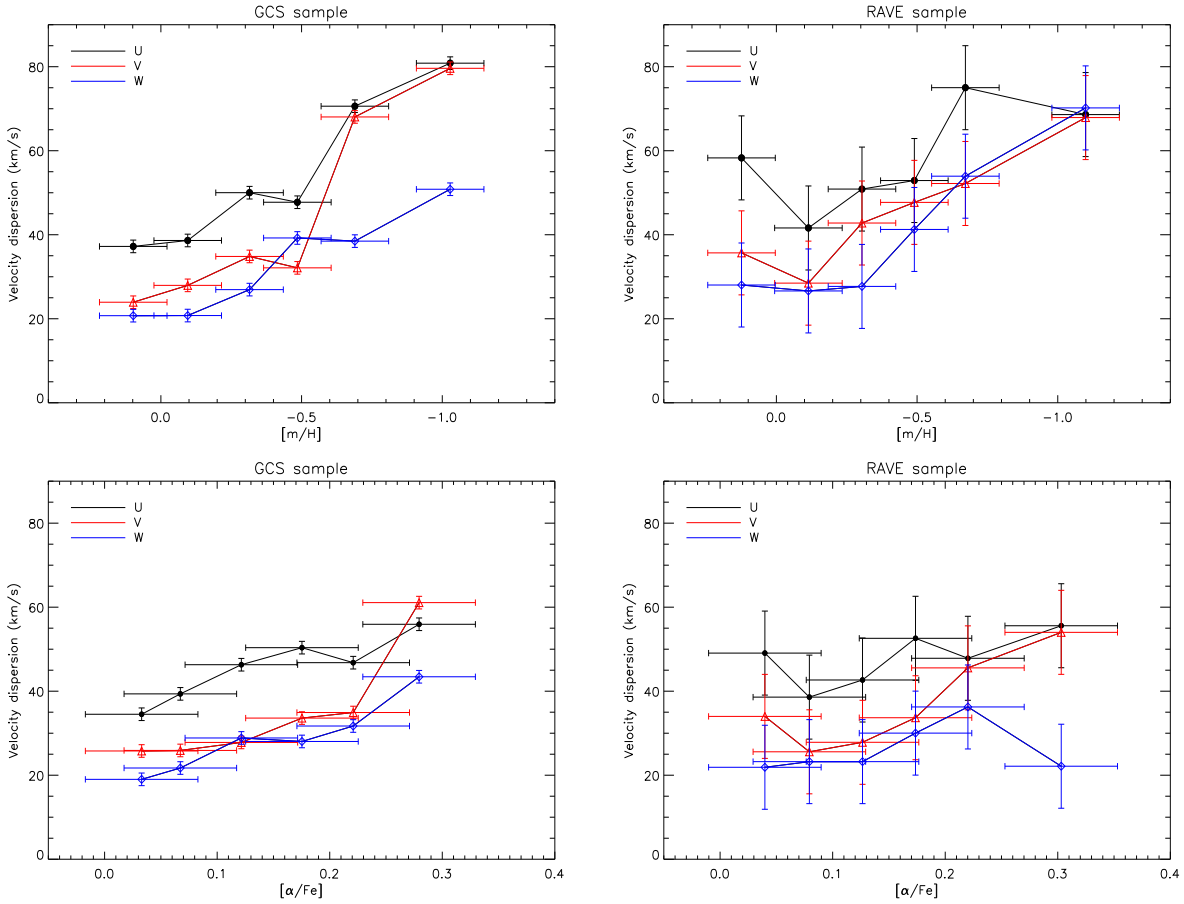

Figure 5.17: Top panels: velocity dispersion versus metallicity for the GCS and RAVE sample. Bottom panels: velocity dispersion versus [α/Fe] for the GCS and RAVE sample.

slightly increases for very metal-poor stars ([m/H] < -0.8). A common value for σ_W/σ_U is 0.55. For stars with [m/H] $\sim$ -0.5 dex we find that σ_W/σ_U = 0.82. We do not know if this feature is real, as for stars more metal-poor than -0.5 dex we recover the common value of 0.5 dex. For a pure thin disk stars (right panels in Fig. 5.19) the ratio between the semi-axes of the velocity ellipsoid are independent of the metallicity. Fig. 5.19 also shows the asymmetric drift as a function of metallicity for the whole sample and for thin disk stars. The figure shows how the mean rotation velocity of the metal-poor population (larger velocity dispersion) lag behind that of the metal-rich stars. For the thin disk, we find that <V> is nearly constant. These results are in good agreement to those in Gomez & Mennessier (1977), as well as those presented in Binney & Merrifield (1998). We have made the same study using [α/Fe]. σ_V/σ_U is nearly constant for stars with [α/Fe] < +0.2 dex being the axial ratio around 0.68 while for stars with [α/Fe] $\geq$ +0.25 dex, $\sigma_V/\sigma_U \sim 1.0$. σ_W/σ_U is independent of [α/Fe] for values $\leq$ +0.2 dex. σ_W/σ_U increases for stars more α-enhancement than +0.2 dex (see Fig. 5.19). Note that the mean rotational

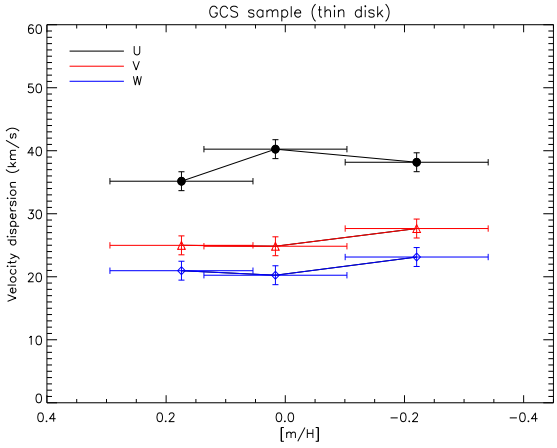

Figure 5.18: Velocity dispersion as a function of metallicity for stars identified as belonging to the thin disk

$< [m/H] >$	N	σ_V/σ_U	σ_W/σ_U	<V> (km/s)
+0.10	161	0.64 ± 0.06	0.55 ± 0.06	-30.29
-0.10	106	0.72 ± 0.07	0.53 ± 0.05	-25.75
-0.31	77	0.69 ± 0.04	0.54 ± 0.04	-32.53
-0.48	40	0.67 ± 0.04	0.82 ± 0.06	-40.80
-0.68	16	0.96 ± 0.05	0.54 ± 0.04	-68.50
-1.02	5	0.98 ± 0.03	0.62 ± 0.03	-112.00

Table 5.2: Mean metallicity, number of stars per metallicity bin, axial ratios and asymmetrical drift.

velocity is also independent of [α/Fe] for values $< +0.2$ dex. The stars with [α/Fe] $> +0.2$ dex clearly lag behind.

We present the characterization of the kinematical sample with a velocity ellipsoid as a function of the metallicity in Tab. 5.2. The values we have found for the ratio between the semi-axes of the velocity ellipsoid are closer to those in Dehnen & Binney (1998) for MS stars. Dehnen & Binney (1998) found a typical value for $\sigma_V/\sigma_U \sim 0.6$ and $\sigma_W/\sigma_U \sim 0.5$. Note, as mentioned above, that for the metal-poor population we find that σ_V/σ_U is close to one.

Tab. 5.3 presents the characterization of the kinematical sample with a velocity ellipsoid as a function of the [α/Fe]. Stars with [α/Fe] $> +0.2$ show higher values for the axial ratios, indicating that the velocity ellipsoid may be different for thin and thick disk. These stars present also a lower velocity rotation.

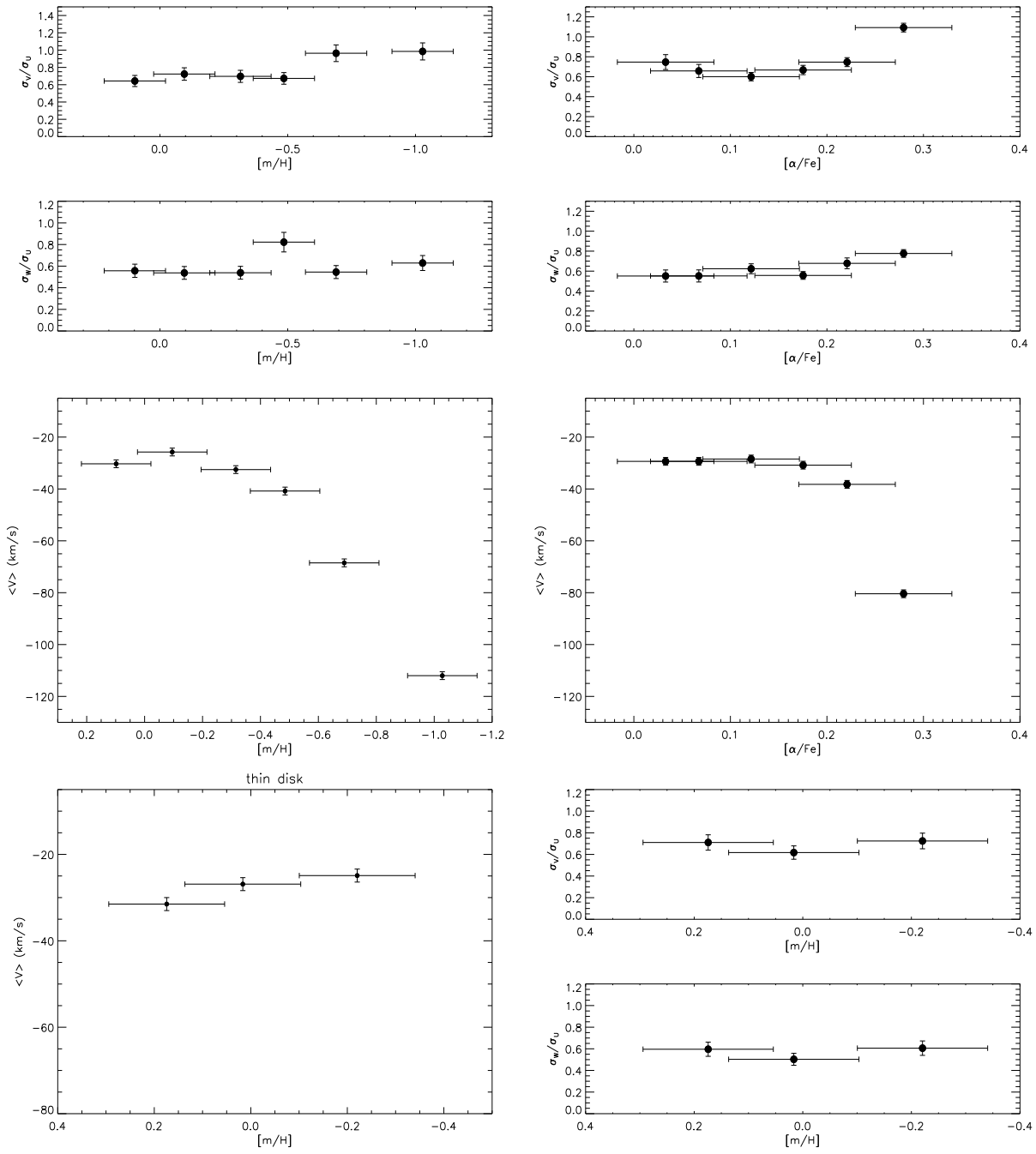

Figure 5.19: Velocity ellipsoid and mean rotational velocity as a function of metallicity and [α/Fe]. Top panels show the ratio between the semiaxis of the velocity ellipsoid versus [m/H] and [α/Fe]. In the middle we have the mean rotational velocity as a function of metallicity and [α/Fe]. Bottom panels: semiaxis of the velocity ellipsoid and the mean rotational velocity as a function of metallicity and [α/Fe] for stars identified as belonging to the thin disk.

$< [\alpha/Fe] >$	N	σ_V/σ_U	σ_W/σ_U	<V> (km/s)
+0.03	108	0.74 ± 0.07	0.55 ± 0.06	-29.36
+0.06	134	0.65 ± 0.05	0.55 ± 0.05	-29.35
+0.12	60	0.60 ± 0.05	0.62 ± 0.05	-28.45
+0.17	45	0.66 ± 0.04	0.55 ± 0.04	-30.82
+0.22	36	0.75 ± 0.05	0.67 ± 0.04	-38.22
+0.28	17	1.09 ± 0.05	0.77 ± 0.04	-80.41

Table 5.3: Mean [α/Fe], number of stars per [α/Fe] bin, axial ratios and asymmetrical drift.

5.3.3 The age-velocity relation

Gravitational perturbations experienced by the stars during their translations around the Galactic center could be understood using the relation between the age and the velocity of a stellar group. Many authors have studied this relation with conflicting results (e.g. Wielen (1974), Mayor (1974), Carlberg et al. (1985), Stromgren (1987), Meusinger et al. (1991), Freeman (1991), Dehnen & Binney (1998), Quillen & Garnett (2001), Rocha-Pinto et al. (2004), Nordström et al. (2004), Seabroke & Gilmore (2007), Soubiran et al. (2008)). Moreover, the disk heating mechanisms such as massive perturber of the disk from the Galactic halo (Wielen (1977)), molecular clouds (Lacey (1984)), transient spiral arms (Sellwood & Carlberg (1984), Binney & Lacey (1988)), the resonance overlap of multiple spiral patterns (Minchev & Quillen (2006)), disrupting satellite galaxies (Toth & Ostriker (1992), Velazquez & White (1999), Villalobos & Helmi (2008), House et al. (2011)) are not yet completely well understood. In this section we make use of the ages derived for the selected subgiants to investigate the kinematical evolution of the nearby disk.

We represent the spatial velocities as a function of age. In order to calculate the velocity dispersion we further examine our stellar sample. For the GCS sample see Fig. 5.20. We have selected the stars according to 5000 K < T_{eff} < 5700 K and 3.4 < log g < 4.2 and we use the ages derived using Y^2 isochrones. The disk heating can be seen in this figure for the very old group. We also represent the mean velocity of each component, <U>, <V> and <W> as function of age. <U> and <W> are constant for all the ages. <V> versus ages shows the asymmetric drift we already mentioned. The fact that we find a similar trend for <V> versus metallicity and age (see Fig. 5.19 and Fig 5.20) would suggests that, indeed, there is a relation between the age and the metallicity. The stars lagging behind are more metal-poor than -0.5 dex and older than 11.0 Gyr. Note that our absolute ages could be systematically older by about 2.0 Gyr, as we already commented.

Fig. 5.21 represents the spatial velocities as a function of age for the RAVE sample. We also find that <U> and <W> are constant for all the ages. The RAVE sample also shows the asymmetric drift for the V-velocity (red line in Fig. 5.21).

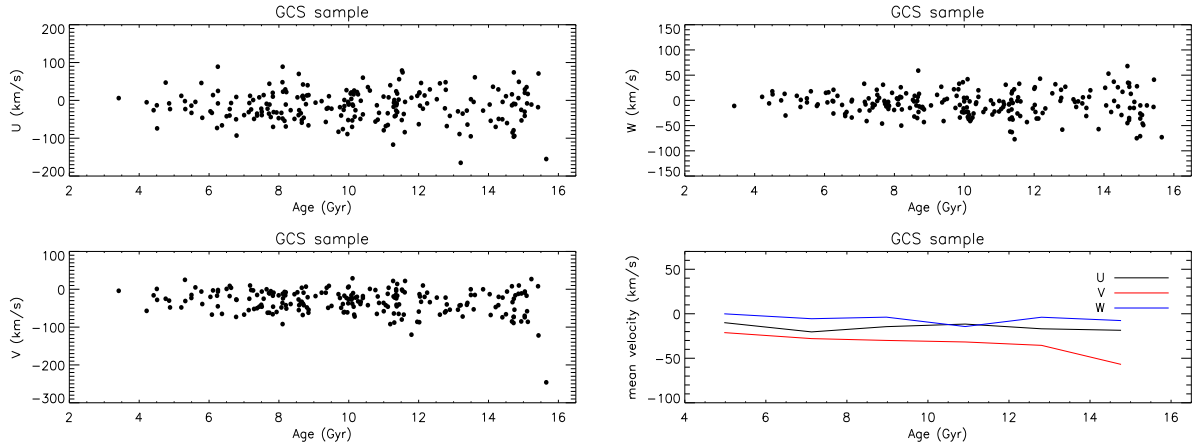

Figure 5.20: Age-velocity diagrams for the GCS sample. Bottom right panel represents the mean velocity for the three components.

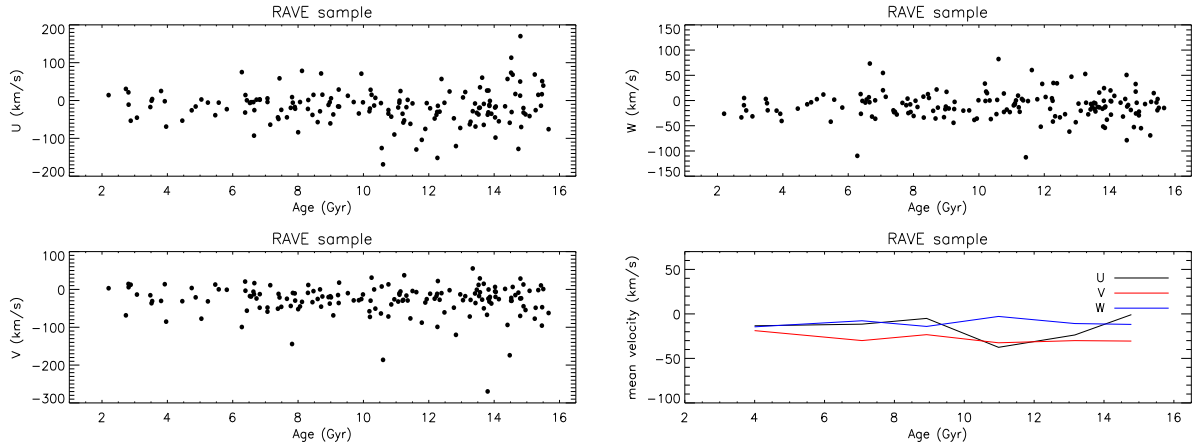

Figure 5.21: Age-velocity diagrams for the RAVE sample. Bottom right panel represents the mean velocity for the three components.

We ilustrate the kinematical evolution of the Galactic disk in Fig. 5.22. We present the age-velocity dispersion relation of the three velocity components and the total velocity dispersion, i.e. the quadratical velocity dispersion of the three velocity components, for the GCS and RAVE sample respectively. Each component of the velocity dispersion is calculated in equal range bins of 1.0 Gyr for the GCS and 2.0 Gyr for the RAVE sample. Do the results depend on how the data was binned? We explore this point in the next section. The oldest stars present clearly a higher velocity dispersion. The tangential velocity dispersion using the GCS sample is independent of the age for the young-intermediate population. Do we see two populations in the vertical velocity dispersion? The typical value for $\sigma_W \sim$ 20 km/s for thin disk stars while for the thick disk $\sigma_W > 30$ km/s (Robin et al. (2003)

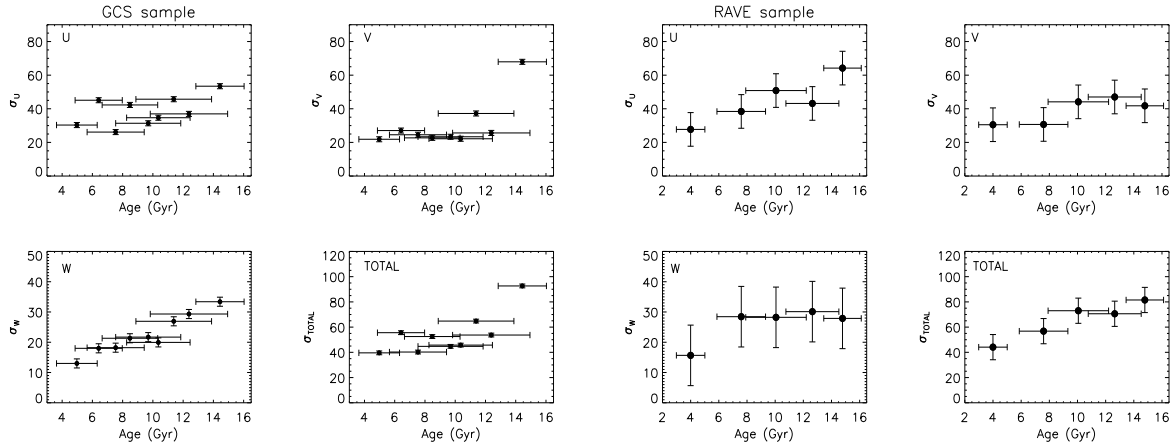

Figure 5.22: Age-velocity dispersion relation of the three velocity components and the total velocity dispersion for the GCS (left) and RAVE sample (right).

and references therein). Stromgren (1987), Freeman (1991), Quillen & Garnett (2001), Soubiran et al. (2008) suggested that the AVR for the thin disk is inconsistent with a continuously increase of the velocity dispersion with time. These authors show that the Milky Way stellar thin disk was relatively quiescent, suffering little heating or dispersion increase between 3.0 and 9.0 Gyr and that σ_W saturates around 20.0 km/s. Moreover, Veltz et al. (2008) combined star counts with kinematic data from the RAVE survey discovered a gap between the vertical velocity dispersions of thin disk components with σ_W less than 21 km/s and a dominant thick disk component at $\sigma_W = 45.5$ km/s. We study this point in more detail in the next section.

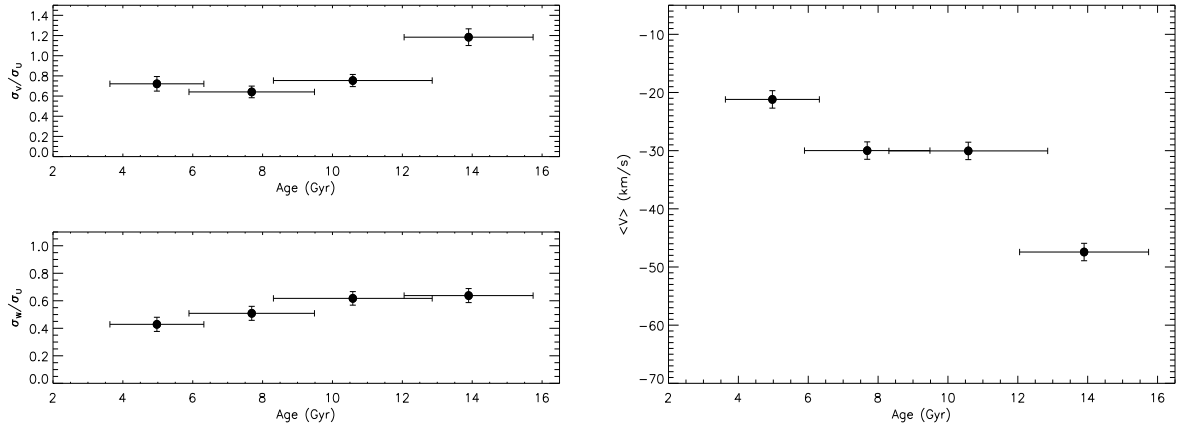

Figure 5.23: Semiaxis of the velocity ellipsoid and asymmetric drift as a function of age.

We explore the evolution of the axial ratios σ_V/σ_U and σ_W/σ_U of the velocity ellipsoid.

$< Age > (Gyr)$	N	σ_V/σ_U	σ_W/σ_U	<V> (km/s)
4.9	16	0.72 ± 0.07	0.42 ± 0.05	-21.18
7.6	70	0.64 ± 0.06	0.50 ± 0.05	-29.98
10.5	73	0.73 ± 0.06	0.61 ± 0.04	-30.04
13.8	61	1.18 ± 0.08	0.64 ± 0.05	-47.42

Table 5.4: Mean age, number of stars per age bin, axial ratios and asymmetrical drift.

We also show the asymmetrical drift as a function of age (see Fig. 5.23). The ratio σ_V/σ_U is related to the Oort constants and is expected to be ∼0.5 and the ratio σ_W/σ_U is related to the scattering process responsible for the dynamical heating of the disk. σ_V/σ_U is nearly constant for the young-intermediate population but there is a clear increase of σ_V/σ_U for the oldest stars. This result is consistent with what we have found in Fig. 5.19. Stars in our sample older than 12.0 Gyr, more metal-poor than -0.6 dex and $[\alpha/Fe] > +0.25$ dex present an axial ratio $\sigma_V/\sigma_U \sim 1.0$ while younger and more metal-rich stars show that $\sigma_V/\sigma_U \sim 0.68$. These results would suggest that σ_V/σ_U is higher for the thick disk stars, $\sigma_V/\sigma_U)_{thick} > (\sigma_V/\sigma_U)_{thin}$. Our results show that σ_W/σ_U increases with time. For stars younger than 6.0 Gyr, $\sigma_W/\sigma_U = 0.42$ and for stars older than 12.0 Gyr the ratio is around 0.62. We have also seen in Fig. 5.19 that metal-poor stars and stars with $[\alpha/Fe] > +0.2$ dex present a ratio $\sigma_W/\sigma_U > 0.6$. We could conclude that the axial ratios σ_V/σ_U and σ_W/σ_U are independent of abundances and ages for the thin disk and they present a lower values compare with the axial ratios we find for the thick disk stars. In an axisymmetric Galaxy these ratios are supposed to be constant, there are previous reports of variations related to color or spectral type (e.g. Mignard (2000)) and age (Soubiran et al. (2008)). Note that in this study we find variations in both abundances and age. Fig. 5.23 also shows the asymmetrical drift as a function of age.

Tab. 5.4 presents the characterization of the kinematical sample with a velocity ellipsoid as a function of the age. Old stars show higher values for the axial ratios and a lower velocity rotation.

5.3.4 Disk heating

The processes which change the velocities in any direction of initially slow-moving young stars into higher dispersion orbits (hotter) with time are called disk heating mechanisms and are fundamental aspects of disk galaxy evolution. The vertical velocity (W) is a suitable component to investigate the disk heating problem. Whether heating is continuous or saturates with time requires separate consideration in the plane (σ_U and σ_V) and out of the plane (σ_W). Seabroke & Gilmore (2007) show that observationally measured σ_U and σ_V can only be used to constrain in-plane disk heating models if we are be able to exclude

the dynamical streams. They also conclude that the age-σ_W relation can be constrained because the dynamical streams are well phase-mixed in W.

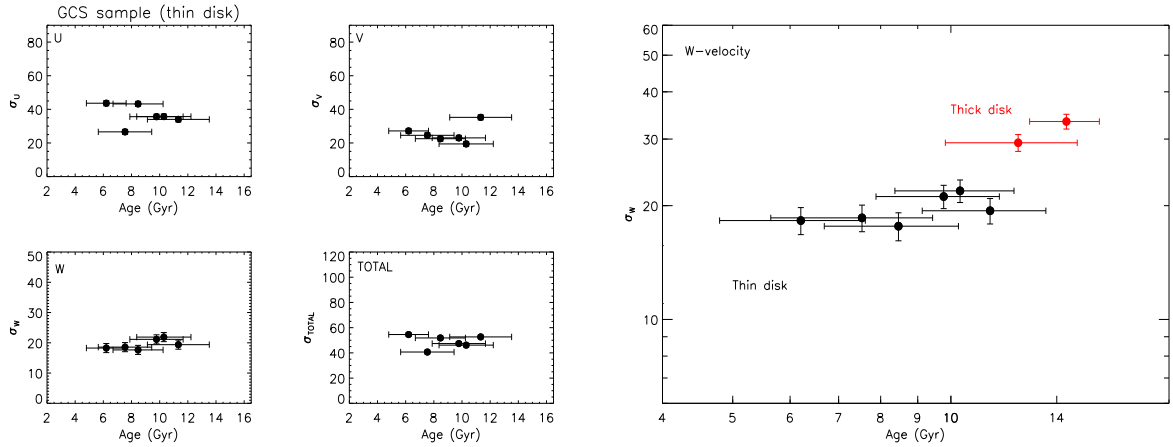

Figure 5.24: Age-velocity dispersion relation for the thin disk. On the right panel we show the W-velocity for the thin (black) and thick disk (red).

We make a selection of thin/thick disk stars using the age-[α/Fe] relation we get for the GCS sample (see Fig. 5.8). The space motions in the GCS sample are very accurate, the average error in each component is 1.5 km/s. We take advantage of the accuracy in kinematics and the precise ages we get for the selected subgiants to explore the heating for a thin disk sample. Fig. 5.24 shows the AVR for stars belonging to the thin disk. On the right panel we show the W-velocity for the thin (black) and thick disk (red). *The results presented here suggest that σ_W would saturates around 20.0 km/s for the thin disk, for the oldest stars (thick disk) there is an abrupt increase (by almost a factor of 2) in the stellar velocity dispersion.* These results would indicate that the heating mechanisms for the thin disk may operate promptly and saturate after a few Gyr. We have mentioned already that in terms of absolute ages, our results using the Y^2 isochrones not taking into account the [α/Fe] seem to be systematically older by 2.0 Gyr. That would set the youngest stars between 3.0 and 4.0 Gyr. However, taking into account the uncertainties in the age of stars the idea of a continuous heating in σ_W is not completely discarded.

To reconstruct the young part of the Galactic disk we use the catalogue of open clusters with kinematic information (Vande Putte et al. (2010)). 481 open clusters have the data on distance, proper motion and radial velocity, with 439 of these also having the age. The average error in each velocity component is around 5.0 km/s and the average uncertainty in age is < 0.5 Gyr. We have selected the clusters older than 0.5 Gyr. Fig. 5.25 shows the evolution of the vertical velocity with time for the Galactic disk. The blue dots are the selected open clusters, the black points are the subgiants belonging to the thin disk and the red points, thick disk stars according to our selection criteria on the age-[α/Fe] relation. For the AVRs of different authors for the thin disk, we find power laws with indices 0.37

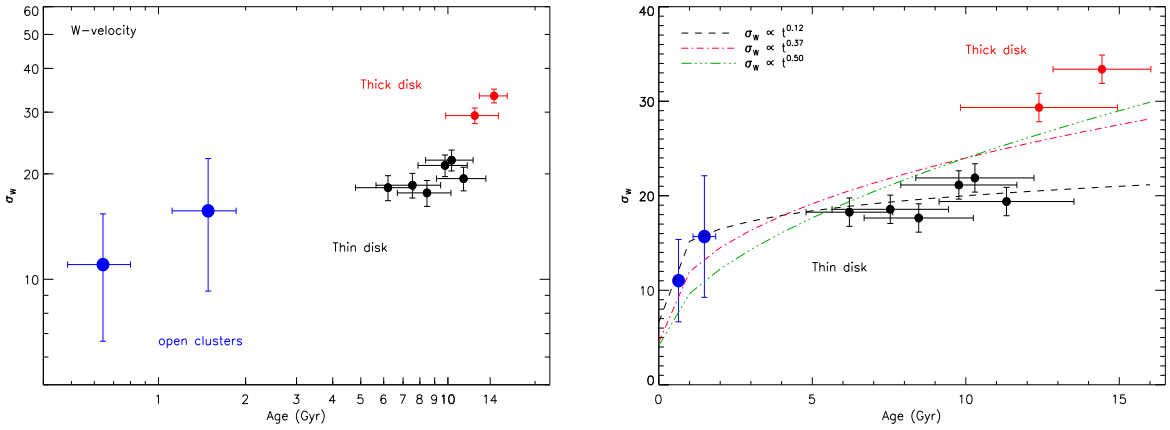

Figure 5.25: Age-velocity dispersion relation for the W-component. The blue dots are the selected open clusters. On the right panel we show three different power laws with indices 0.12 (black) , 0.37 (red) and 0.50 (green).

$< \alpha < 0.50$ for σ_W. This is in the range of the classical value of 0.5 (Wielen (1977)), of 0.53 (Holmberg et al. (2007)) and of 0.45 derived by Aumer & Binney (2009). Right panel on Fig. 5.25 shows the AVR for the W-velocity together with three different power laws with indices 0.10, 0.37, 0.50 respectively. Newly born stars ($\sim$ 300 Myr) present $\sigma_W \sim 5.0$ km/s (Torra et al. (2000)). Open cluster older than 1.0 Gyr show a $\sigma_W \sim 15.0$ km/s and field stars older than 4.0 Gyr present a $\sigma_W \sim 20.0$ km/s. That would suggest that the heating mechanisms are very efficient the first 3.0 Gyr. According with the classical values for α the maximum velocity dispersion of the oldest thin-disk stars is 25 - 30 km/s. Our findings suggest that this result is clearly lower than 25 km/s indicating that the heating mechanisms in the thin disk become inefficient after 3.0 - 4.0 Gyr. Note that a power law with $\alpha \sim 0.1$ would fit the data nicely. Despite the fact we have improved the age of stars by using subgiants, the uncertainties in age are still large to make a robust conclusion.

Fig. 5.26 shows the cumulative diagram of the absolute value of the vertical velocity as a function of age. In this way we look at the evolution of dispersion with age that avoids binning. We also correct W for the measuring errors before calculate the cumulative diagram. If all of the stars come from a population with the same dispersion, then this cumulative diagram will be an approximately straight line with some fluctuations. The steeper the line, the larger the dispersion. If the dispersion increases steadily with age, then the cumulative diagram will show curvature: the sum will increase with age more rapidly than a straight line. Fig. 5.26 present the results for the GCS and RAVE samples respectively. When using the whole sample we find clearly curvature in the cumulative diagram. Selecting thin disk stars we find that the cumulative diagram is a straight line. These results would confirm that σ_W saturates after 3.0 - 4.0 Gyr and the heating mechanisms in the thin disk become inefficient after that time.

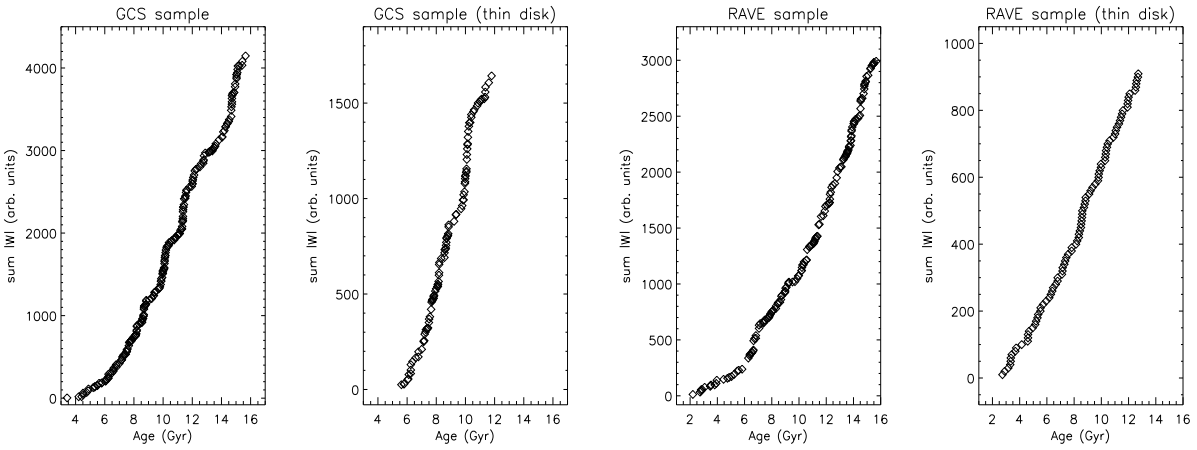

Figure 5.26: Cumulative diagram of the absolute value of the vertical velocity as a function of age for the GCS sample (left panels) and RAVE sample (right panels).

5.4 Clues about the evolution of the disk

The AMR for nearby stars is a standard constraint for modeling the chemical evolution of the solar neighbourhood. The AMR is a trace of the progressive storage of heavy elements in the star-forming interstellar medium. Simple chemical models predicts a monotonic increase in the abundance of any robust element with time. Edvardsson et al. (1993) using very accurate abundances ($\Delta[X/Fe] \sim 0.05$ dex) for almost 200 stars found the presence of a significant scatter with respect to the average trend. As a result after this very highly cited work the average AMR no longer represents a tight constraint for chemical evolution models; hence the new challenge was in reproducing the dispersion of the data. More complex chemical models are therefore required, which should include mechanisms inducing the observed scatter. *Different galactic substructures* (halo, thick disk, thin disk and bulge), each with its own AMR, might overlap in the solar vicinity. Pardi et al. (1995) followed the parallel evolution of a halo, a thick disk and a thin disk with different evolutionary rates, and the resulting mixture of stars shows a scatter in the AMR. Another mechanism invoked to explain the observational scatter was the *non-instantaneous mixing*, non-instantaneous mixing of stellar nucleosynthesis products in the surrounding gas allows for self-enrichment in molecular clouds and for local inhomogeneities (Pilyugin & Edmunds (1996)). Francois & Matteucci (1993) conclude that the observed scatter in the AMR could be the consequence of the overlapping of different stellar populations observed in the solar vicinity, possibly caused by *orbital diffusion.* Diffusion of stellar orbits allows stars to move away from their birthplaces because of scattering of molecular clouds, density waves in the disk or infalling satellite galaxies. It is interesting that the orbital diffusion phenomenon is revealed by the observed relation between the age and the velocity dispersion of disk stars (Wielen (1977); Wielen et al. (1992)), we will be back to this point later. Diffusion of stars

from different birthplaces into nearby orbits results in a spread of metallicities with respect to the expected "local" metallicity for a given age. Following this point, Sellwood & Binney (2002) introduced a new theoretical concept called *radial migration* that could explain the lack of correlation between the ages and metallicities of stars that some authors found. The typical radial excursions for a population of stars with rms radial velocity σ_U are $\Delta \propto \sigma_U/\kappa$, where κ is the epicycle frequency. For old stars in the thin disk near the Sun we have that $\Delta \sim 1.3$ kpc. Sellwood & Binney (2002) pointed out that migration over distances of this order proves insufficient to explain the weakness of the correlation between age and metallicity found by Edvardsson et al. (1993). Wielen et al. (1996) based on the AMR from Edvardsson et al. (1993) concluded that the Sun has migrated from its birth-place in the inner part of the Galaxy outwards by 1.9 ± 0.9 kpc during its lifetime of 4.5 Gyr. They also concluded that stars have migrated by more than their epicycle size from their radii of birth. Since the home radius is determined by the specific angular momentum of a star, L, about the symmetry axis of the Galaxy, the latter possibility requires L to be changed (Sellwood & Binney (2002)). Stars oscillate radially with increasing larger amplitude, but keep the same mean orbital radius.

However, Ng & Bertelli (1998) and Pont & Eyer (2004) computed new ages for the stars from the Edvardsson et al. (1993) data set and they found that the intrinsic dispersion in the AMR is at most 0.15 dex and probably lower, suggesting the existence of a AMR in the solar vicinity. Other authors like Rocha-Pinto et al. (2000a) and Soubiran et al. (2008) also found a small scatter in the AMR in clear conflict with recent results from Casagrande et al. (2011) where they show a lack of correlation between the ages and the abundances of the stars. We have seen in this thesis that a good determination of the age of stars is tricky and the uncertainties are still large. There is a weak correlation between the ages derived from different authors. Is the lack of relation between ages and abundances an artifact of an imprecise determination of ages? In this study we use subgiants, these type of stars are suitable for dating the Galaxy as one could get a well defined age probability distribution function in this region of the Hertzsprung-Russell diagram as we have seen in this work. Using a pure subgiants data set we find the existence of a relation between the abundances and the ages. We find a mean scatter for the AMR of 0.14 dex. If there were no stellar migration, there would be a correlation between the ages and metallicities of stars. Those results would suggest that there is less need for radial mixing. Moreover, using Casagrande et al. (2011) data we find the existence of a correlation between the ages and the metallicity with a mean scatter, $\sigma_{[m/H]} \leq 0.15$ dex. Even using subgiants the uncertainties in the ages are still large ($\sigma_{age} \leq 2.0$ Gyr), again, much of the difference in view in the AMR problem goes back to the difficulty of measuring stellar ages. Radial migration theories are very popular in our days (Roškar et al. (2008), Schönrich & Binney (2009a), Minchev & Famaey (2010), Loebman et al. (2011)) and, indeed, radial mixing is potentially an important feature of the evolution of the disk but the main observational constrains of this theory is the AMR and the relation is still under debate. It is an open question if we need to invoke stars coming from large radial distances (> 2 kpc), as some authors have found in their simulations (e.g. Roškar et al. (2008)), to explain the

chemical evolution we see in the solar volume. We also find that <V> - [m/H] do not show a correlation for the thin disk; recent models taking account the radial migration (e.g. Schönrich & Binney (2009a)) predict a gradient in the mean rotational speed of $\sim$ 100 km/s as the metallicity in the thin disk increases. Note also that the Sun has often been cited as evidence that stars move from their initial orbits, however in this work we find that stars around 5.0 Gyr present <[m/H]> $\sim$ +0.08 dex. The Sun is < 0.1 dex away from the mean metallicity of stars of the same age. However, the number of stars is this work with ages around 5.0 Gyr is small to make a robust conclusion. Accurate ages from asteroseismology could help to put some light into the AMR problem.

The age-velocity dispersion relation (AVR) is another fundamental constraint on the evolution of the Galactic disk. In this study we find that the heating for the thin disk takes place for the first $\sim$ 3.0 Gyr, but then saturates when $\sigma_W \sim$ 20 km/s because the stars of higher velocity dispersion spend most of their orbital time away from the Galactic plane where the sources of heating lie. The heating of the stellar disk is fitted with a simple power law of the form $\sigma_W \propto t^{\alpha}$, many authors find α in the range 0.35 - 0.60 (Hänninen & Flynn (2002)). In this study we find that $\sigma_W \propto t^{0.12}$ would fit the data nicely. That would support the idea that after the first 3.0 - 4.0 Gyr the heating processes in the Galactic disk are inefficient. As the amplitude of the random motions increases, the star becomes less vulnerable to heating by transient spiral waves, and the heating process is expected to saturate. Lacey (1984) showed that Giant Molecular Clouds (GMCs) are highly effective in scattering stars. Hänninen & Flynn (2002) derived a heating $\sigma_{total} \propto t^{0.21}$ for the heating of the stellar disk caused by GMCs using simulations of the orbits of tracer stars embedded in a path of the local Galactic disk. These results suggest that GMCs are very efficient heaters only the first 2.0 - 3.0 Gyr. Another heating mechanism that has been widely proposed is caused by transient spiral arms in the disk (Barbanis & Woltjer (1967), Carlberg (1987), De Simone et al. (2004), Minchev & Quillen (2006)). This heating mechanism was too low compared with the vertical heating from observations (Carlberg (1987)), that leads the idea that the observed heating could be explained by the combined effect of the GMCs and transient spiral arms (Jenkins & Binney (1990), Binney (2001)). Note that all the previous studies have assumed that $\sigma_W \sim t^{0.45\pm0.1}$ as a true behavior for the Galactic disk. The results presented in this work are consistent with inefficient heating caused by scattering from tightly wound transient spiral structure and with the very efficient heating mechanism caused by the GMCs during the first 3.0 Gyr. Other possible heating mechanisms, poorly understood, include scattering by massive compact halo objects or halo substructure, mergers with dwarf galaxies or the outer Lindblad resonance from the Galactic bar (see Binney & Tremaine (2008)). Note that inefficient heating would actually be easier to reconcile with theoretical models, which have struggled to explain the rapid increase in velocity dispersion with age inferred from earlier observations.

The shape of the velocity ellipsoid is also investigated. The rate of axial ratios of the velocity ellipsoid is another constraint on theories for disk heating. We find $\sigma_V/\sigma_U \sim 0.68$ for stars more metal-rich than -0.5 dex, [α/Fe] < +0.2 and younger than 12 Gyr (again, in terms of absolute ages our results could be overestimated easily by 2 Gyr), i.e. thin disk

stars. For the rest of the stars, i.e. thick disk, we find $\sigma_V/\sigma_U \sim 1.0$. In the case of σ_W/σ_U we find that for the thin disk, $\sigma_W/\sigma_U \sim 0.55$ while for the thick disk, $\sigma_W/\sigma_U \sim 0.70$. σ_V/σ_U and σ_W/σ_U show little dependence on age except for the oldest groups. We observe the same behavior with respect to metallicity and [α/Fe]. We can conclude that for the thin disk we find $\sigma_U : \sigma_V : \sigma_W \sim 1.0{:}0.7{:}0.5$ and for the thick disk we have $\sigma_U : \sigma_V : \sigma_W \sim 1.0{:}1.0{:}0.7$. In the following, we consider velocity dispersions with respect to a cylindrical coordinate system, where r, θ and z represent the radial, azimuthal and vertical components of the space velocity, respectively. For solar neighborhood stars we can adopt $\sigma_W/\sigma_U = \sigma_z/\sigma_r$. Spitzer & Schwarzschild (1953) and Lacey (1984) bases on scattering from GMCs found that $\sigma_z/\sigma_r \sim 0.8$. The result suggested that the velocity ellipsoid was too round. **?** and Carlberg (1987) found that transient spiral arms can give $\sigma_z/\sigma_r \sim 0.5$ with inefficient vertical heating ($\sigma_z \sim t^{0.2}$) in good agreement with our results. Jenkins & Binney (1990) combined the scattering from clouds and spiral waves. In the presence of spiral waves the clouds are more efficient vertical heaters, but still obtained $\alpha < 0.3$. Even with the combination of spiral arms and GMCs they do not find the continuous heating through the life of the disk. That led to Jenkins (1992) to add disk accretion to the heating mechanisms. He obtained $\alpha \sim 0.4$ and $\sigma_z/\sigma_r \sim 0.65$. This is interesting, if the spiral arms are the main heating mechanisms, $\sigma_z/\sigma_r \sim 0.5$ with an inefficient vertical heating. This is in a good agreement with our results for the thin disk. Taking into account satellite accretion they found that the vertical heating is more efficient and $\sigma_z/\sigma_r \sim 0.65$; in good agreement with our results for the thick disk where we find $\sigma_z/\sigma_r \sim 0.7$. Yasutomi & Fujimoto (1991) presented a very sophisticated treatment of the scattering problem. They found that dynamical friction lead to important systematic accelerations and decelerations of the stars, as a consequence they found a very slow growth of the velocity dispersion for ages $>$ 1.0 Gyr, with $\alpha \sim 0.2$ when the clouds are uniformly distributed and even small values $\sim$ 0.10 to 0.15 for clouds distributed in an annulus or spiral arms. Note that even theoretical treatment of the disk heating mechanism present problems to find α in the range from 0.35 to 0.60, as many observational results suggested. Another valid mechanism would be the stochastic heating due to minor mergers. This process has been studied numerically by a large number of authors (e.g. Velazquez & White (1999), Taylor & Babul (2001), Villalobos & Helmi (2008)). There are observational evidences for merger activity in the past (Ibata et al. (1994), Newberg et al. (2002), Rocha-Pinto et al. (2003), Williams et al. (2011)), and minor mergers could have imprinted changes in the slope of the AVR but their role is not yet fully understood (see Rocha-Pinto et al. (2004) for a discussion). Recently, House et al. (2011) using a suite of simulations run with different particle- and grid-based cosmological hydrodynamical codes trying to reproduce a Milky Way galaxy found that merger/assembly activity has a clear impact on the shape of the AVR. Understanding the disk heating mechanisms is complex (e.g. Binney (2012)), accurate kinematics and abundances together with accurate ages for the stellar components of the Galaxy could be very useful to clarify the observational disagreements and develop a robust theoretical treatment of the problem.

5.5 Thick disk formation

Finally we discuss the possible formation scenarios for a thick disk in the Galaxy and what our results could say about it. A number of formation scenarios have been proposed, e.g.: thick disks are a normal part of early disk settling, and form through energetic early star forming events, e.g. in gas-rich mergers (Brook et al. (2004)); thick disks are made up of accretion debris (Abadi et al. (2003)); thick disks come from the heating of the thin disk via disruption of its early massive clusters (Kroupa (2002)); thick disks come from early partly-formed thin disks, heated by accretion events such as the accretion event which is believed to have brought omega Centauri into the Galaxy (Bekki & Freeman (2003)); stars on more energetic orbits migrate out from the inner galaxy to form a thick disk at larger radii where the potential gradient is weaker (Schönrich & Binney (2009b)).

We find a big spread in [α/Fe], from +0.1 to +0.3 dex for the thick disk in our age-[α/Fe] relation. α elements are thought to form mainly in massive stars with short lifetimes and are ejected by SN II events, while iron is produced in both SN II and SN Ia events. Very simple prediction is that stars that form shortly after the interstellar medium has been enriched by SNe II should have enriched [α/Fe] ratios, while those that form sometime after the SNe Ia contribute will have higher iron abundances and lower [α/Fe] ratios. The large value and spread in α elements suggest that the formation of the thick disk was rather fast ($\sim$ 2 Gyr) and these results would support a formation scenario for this primitive disk where a gas-rich merger is accreted to the galaxy during a chaotic period of hierarchical clustering at high redshift (Brook et al. (2004)). Two recent studies based on RAVE (Wilson et al. (2011)) and SDSS data (Dierickx et al. (2010)) used the observed eccentricity distribution to favor the gas-rich merging scenario. Our results also confirm that the thick disk is an old component ($\geq$ 10 Gyr) of the Milky Way and that rotates slower than the thin disk with a clear gradient from $\sim$ -50 km/s for the metal-rich thick disk (-0.6 dex) to $\sim$ -100 km/s for the metal-poor thick disk (-1.0 dex). In the other hand, the fact that we find a saturation for the AVR suggests a discontinuity in σ_W and that would present some problems for a pure thick disk formed via secular evolution (e.g. migration). Having in mind that secular processes indeed are important during the life of the disk we find that mechanisms of formation of the thick disk such as accretion events remain compatible with our findings.

Chapter 6

Summary and future work

6.1 Summary

How the Galactic disk has evolved with time in the last 10 Gyr is still an open question. To address this question we have investigated the evolution of the Galactic disk via the age-metallicity and the age-velocity relations using a sample of subgiant stars.

Our sample of subgiants was selected from the RAVE survey and the GCS using the M_V/log g - T_{eff} plane. We made follow-up observations to improve the stellar parameters in order to identify the pure subgiants in the sample and get accurate ages. We obtained 1253 low resolution spectra from the Double Beam Spectrograph (DBS) on the ANU 2.3-m telescope at Siding Spring Observatory (Australia). The resolving power is 400, with a spectral range from 3200 to 6200 Å. During the observations we used a wide slit of 5". A wide slit assures that 100% of the star light is collected and mitigates tracking problems and differential refraction that could affect the flux calibration. To get an accurate flux calibration we have secured spectra of standard stars at different zenith distances, i.e. different airmass, for every night. The accuracy of the flux calibration was tested using DDO bands, ensuring that the flux calibration is quite precise when comparing with photometric catalogues. We derive the main stellar atmosphere parameters by using the spectral energy distribution of the stellar atmospheres. Simple spectroscopic observations can yield accurate values for *log g* through comparison of the Balmer jumps of low-resolution spectra with recent grids of synthetic flux spectra (Bessell 2007). We need to degrade the models to the observed resolution to get a good match in order to secure the stellar atmosphere parameters via the minimum chi-square method. We used the Fourier space to understand the behavior and the impact of the conditions of the night on the final resolution of the observed spectra. We degrade the model at different resolutions from 2 Å to 15 Å (FWHM) in steps of 0.1 Å by convolving the model with a Gaussian profile. We work out the Power Spectrum and using a minimum distances method we get the best fit in the Fourier domain, i.e. we get the FWHM of the Gaussian we need to degrade the model

to the exact resolution of the observed spectrum. Using synthetic stellar libraries we find that log g are underestimated ($\sim$ 0.3 dex). A comparison between the stellar parameters derived using an empirical stellar library (MILES) and those from a high-resolution catalogue (PASTEL) present a rms $\sim$ 145 K, 0.16 and 0.23 dex for temperature, metallicity and gravity respectively. We also estimate [Mg/Fe] and [Ca/Fe] from spectrophotometry using the abundances ratios obtained in de Castro Milone et al. (2011) and Venn et al. (2004), as reference.

The facts that the isochrones separate nicely for different ages in the subgiant region, and that they run almost horizontally make these stars particularly suitable for dating purposes. We determine the age of stars via isochrones fitting. For this work we explore the results using three different grid of isochrones: Bertelli et al. (1994), Girardi et al. (2000) and Yonsei-Yale (Demarque et al. 2004). Adopting a Gaussian probability density for T_{eff}, log g and [m/H] centered at the measured values we determine the probability density distribution for the age. The procedure makes no assumption on the initial mass function, the metallicity distribution, or the star formation rate. We find different absolute ages using different isochrones. The ages derived using Bertelli et al. (1994) show a correlation with those derived from Girardi et al. (2000) and Demarque et al. (2004) but we find a clear offset. The ages from Bertelli et al. (1994) are systematically younger. The ages from Girardi et al. (2000) and Demarque et al. (2004) show a clear correlation. Quantitatively the lowest errors come from Demarque et al. (2004) isochrones while Bertelli et al. (1994) are giving the most significant uncertainties.

The age-metallicity relation (AMR) is a record of the chemical enrichment of the star-forming local interstellar medium during the evolution of the Galactic disk. In this study we derive an age-metallicity relation with an intrinsic cosmic dispersion in metal abundances of 0.14 dex, a factor of two smaller than those found by Edvardsson et al. (1993), Nordström et al. (2004), Casagrande et al. (2011). The mean metallicity shows a slow, steady increase with time. We also find a relation between the α-elements and the age for the thin disk stars. Stars around 5.0 Gyr old present [α/Fe] slightly higher than the solar value ($\sim$ +0.02) while the oldest thin disk stars show values around +0.1 dex. For the thick disk stars we find values from +0.1 dex up to +0.3 dex in [α/Fe]. These results suggest a less need for radial migration in the Galactic disk.

We find that <V> versus [m/H] do not show a correlation for the thin disk; recent models taking into account the radial migration (e.g. Schönrich & Binney (2009a)) predict a gradient in the mean rotational speed of $\sim$ 100 km/s as the metallicity in the thin disk increases. Furthermore, the velocity dispersion remains roughly constant for a metallicity range from +0.2 to -0.5 dex. For metal-poor stars ([m/H] < -0.7 dex) the velocity dispersion clearly increases for the three velocity components. These results are in good agreement with those found by Navarro et al. (2011). In this study we find that the heating for the thin disk takes place for the first $\sim$ 3.0 Gyr, but then saturates when $\sigma_W \sim$ 20 km/s because the stars of higher velocity dispersion spend most of their orbital time away from the Galactic plane where the sources of heating lie. We find an abrupt increase of the

velocity dispersion for stars older than 10.0 Gyr. The shape of the velocity ellipsoid is also investigated. For the thin disk we find $\sigma_U : \sigma_V : \sigma_W \sim 1.0{:}0.7{:}0.5$ and for the thick disk, $\sigma_U : \sigma_V : \sigma_W \sim 1.0{:}1.0{:}0.7$. Mechanisms of formation of the thick disk such as accretion events remain compatible with our findings.

6.2 Future work

The future of Galactic astronomy is *Gaia* (Perryman 2005). ESA Gaia mission will build on the observational principles of Hipparcos to measure detailed properties of the brightest 1 billion stars in the sky. Astrometric accuracies of around 10 microarcsec at 15 mag should lead to 20 million stars measured with distance accuracies of better than 1 per cent, and more than 100 million better than 5 per cent. Tangential velocities will be measured astrometrically at better than 1 km/s for about 100 million stars, while the dedicated radial velocity spectrometer will gather radial velocities to 1-10 km/s down to 16-17 mag, depending on spectral type. Gaia will provide multi-color (in 11 medium and 5 broad bands), multi-epoch (of order of 100 epochs over 5 years) photometry for each object to 20 mag.

The synergy between space missions like Gaia and ground based surveys opens up a new era in astrophysics. Massive stellar surveys like, HERMES ((Freeman 2010)), Gaia-ESO survey, WAVES (Balcells et al. 2010), LAMOST (Hu & Jiang 2005), 4MOST (de Jong et al. 2012) among others will work with medium-high resolution spectrographs. In a few years we will have catalogues with extremely accurate distances (kinematics) and individual abundances for millions of stars in the Galaxy. However, we still do not know how to get very precise ages for the field stars. In this thesis we showed that the subgiant region is a good alternative but that would reduce the number of stars to work with and we will have to live with uncertainties of $\sim$ 2 Gyr for the best cases. Asteroseismology has been recognized for a long time as a very powerful mean to probe stellar interiors. The oscillations frequencies are closely related to stellar internal structure properties via the density and the sound speed profiles. Since these properties are in turn tightly linked with the mass and evolutionary state, one could expect to determine the age and mass of a star from the comparison of its oscillation spectrum with the predictions of stellar models (see Lebreton & Montalbán (2009) for more details and current work on this topic). These precise ages from asteroseismology will be very welcome. The combination of very accurate kinematics, abundances and ages will allow us to determinate very precise age-metallicity-velocity diagrams for pure thin/thick disk data sets (*chemical labeling*), to find the siblings of the Sun and others stars (*chemical tagging*) and find new stellar streams around us. Those results will help to understand the mechanisms that drive the evolution of the Galactic disk.

We conclude that we are in a golden moment for Galactic astronomy and the future is just promising. The Milky Way as springboard in our understanding of galaxy formation

and evolution in the Cosmos. Stay tuned!

Bibliography

Abadi, M. G., Navarro, J. F., Steinmetz, M., & Eke, V. R. 2003, ApJ, 597, 21 141

Alexander, D. R. & Ferguson, J. W. 1994, ApJ, 437, 879 96

Allende Prieto, C., Barklem, P. S., Lambert, D. L., & Cunha, K. 2004, A&A, 420, 183 99

Anders, E. & Grevesse, N. 1989, Geochim. Cosmochim. Acta, 53, 197 47, 96

Anderson, L. S. 1989, ApJ, 339, 558 44

Antoja, T., Figueras, F., Fernández, D., & Torra, J. 2008, A&A, 490, 135 123

Asplund, M. 2005, ARA&A, 43, 481 39, 43

Asplund, M. 2008, in IAU Symposium, Vol. 252, IAU Symposium, ed. L. Deng & K. L. Chan, 13–26 49, 95

Asplund, M., Nordlund, Å., Trampedach, R., & Stein, R. F. 1999, A&A, 346, L17 44

Aumer, M. & Binney, J. J. 2009, MNRAS, 397, 1286 136

Avni, Y. 1976, ApJ, 210, 642 66

Balcells, M., Benn, C. R., Carter, D., et al. 2010, in Society of Photo-Optical Instrumentation Engineers (SPIE) Conference Series, Vol. 7735, Society of Photo-Optical Instrumentation Engineers (SPIE) Conference Series 145

Balser, D. S. 2006, AJ, 132, 2326 95

Baranne, A., Mayor, M., & Poncet, J. L. 1979, Vistas in Astronomy, 23, 279 123

Barbanis, B. & Woltjer, L. 1967, ApJ, 150, 461 139

Barry, D. C. 1988, ApJ, 334, 436 92

Bautista, M. A. 1997, A&AS, 122, 167 44

Beifiori, A., Maraston, C., Thomas, D., & Johansson, J. 2010, ArXiv e-prints 53

Bekki, K. & Freeman, K. C. 2003, MNRAS, 346, L11 141

Bennett, C. L., Halpern, M., Hinshaw, G., et al. 2003, ApJS, 148, 1 91

Bennett, C. L., Hill, R. S., Hinshaw, G., et al. 2011, ApJS, 192, 17 2

Bensby, T., Feltzing, S., & Lundström, I. 2004, A&A, 421, 969 88

Bensby, T., Zenn, A. R., Oey, M. S., & Feltzing, S. 2007, ApJL, 663, L13 3, 118

Bertelli, G., Bressan, A., Chiosi, C., Fagotto, F., & Nasi, E. 1994, A&AS, 106, 275 95, 96, 100, 101, 102, 104, 144

Bertelli, G., Girardi, L., Marigo, P., & Nasi, E. 2008, A&A, 484, 815 107

Bertelli, G., Nasi, E., Girardi, L., & Marigo, P. 2009, A&A, 508, 355 107

Bertone, E. 2005, Memorie della Societa Astronomica Italiana Supplementi, 8, 180 45

Bessell, M. S. 2007, PASP, 119, 605 7, 46, 143

Bessell, M. S., Castelli, F., & Plez, B. 1998, A&A, 333, 231 71

Binney, J. 2001, in Astronomical Society of the Pacific Conference Series, Vol. 230, Galaxy Disks and Disk Galaxies, ed. J. G. Funes & E. M. Corsini, 63–70 139

Binney, J. 2012, ArXiv e-prints 140

Binney, J. & Lacey, C. 1988, MNRAS, 230, 597 6, 131

Binney, J. & Merrifield, M. 1998, Galactic Astronomy, ed. Binney, J. & Merrifield, M. 124, 128

Binney, J. & Tremaine, S. 2008, Galactic Dynamics: Second Edition, ed. Binney, J. & Tremaine, S. (Princeton University Press) 139

Boeche, C., Siebert, A., Williams, M., et al. 2011, ArXiv e-prints 7, 81

Böhm-Vitense, E. 1958, ZAp, 46, 108 96

Bovy, J., Rix, H.-W., & Hogg, D. W. 2011, ArXiv e-prints 3

Bowen, G. H. 1988, ApJ, 329, 299 44

Brault, J. W. & White, O. R. 1971, A&A, 13, 169 63

Breddels, M. A., Smith, M. C., Helmi, A., et al. 2010, A&A, 511, A90 94

Brook, C. B., Kawata, D., Gibson, B. K., & Freeman, K. C. 2004, ApJ, 612, 894 141

Burnett, B. & Binney, J. 2010, MNRAS, 407, 339 89, 92

Bšhm-Vitense, E. 1990, Introduction to Stellar Astrophysics: Volume 2 (Cambridge University Press) 40

Carbon, D. F. & Gingerich, O. 1969, in Theory and Observation of Normal Stellar Atmospheres, ed. O. Gingerich, 377–+ 44

Cardelli, J. A., Clayton, G. C., & Mathis, J. S. 1989, ApJ, 345, 245 71, 72

Carlberg, R. G. 1987, ApJ, 322, 59 139, 140

Carlberg, R. G., Dawson, P. C., Hsu, T., & Vandenberg, D. A. 1985, ApJ, 294, 674 4, 131

Carney, B. W., Yong, D., Teixera de Almeida, M. L., & Seitzer, P. 2005, AJ, 130, 1111 3

Casagrande, L., Flynn, C., Portinari, L., Girardi, L., & Jimenez, R. 2007, MNRAS, 382, 1516 95, 98

Casagrande, L., Schönrich, R., Asplund, M., et al. 2011, A&A, 530, A138+ xiii, xiv, xix, 5, 6, 76, 77, 78, 79, 81, 89, 90, 91, 103, 107, 109, 110, 115, 116, 117, 120, 138, 144

Castelli, F. & Kurucz, R. L. 2003, in IAU Symposium, Vol. 210, Modelling of Stellar Atmospheres, ed. N. Piskunov, W. W. Weiss, & D. F. Gray, 20P–+ 47

Cenarro, A. J., Cardiel, N., Gorgas, J., et al. 2001a, MNRAS, 326, 959 103

Cenarro, A. J., Gorgas, J., Cardiel, N., et al. 2001b, MNRAS, 326, 981 54, 103

Cenarro, A. J., Gorgas, J., Cardiel, N., Vazdekis, A., & Peletier, R. F. 2002, MNRAS, 329, 863 103

Cenarro, A. J., Peletier, R. F., Sánchez-Blázquez, P., et al. 2007, MNRAS, 374, 664 53, 54, 55, 56, 57

Chaboyer, B., Sarajedini, A., & Demarque, P. 1992, ApJ, 394, 515 98

Chang, C.-K., Ko, C.-M., & Peng, T.-H. 2011, ApJ, 740, 34 3

Chen, B., Figueras, F., Torra, J., et al. 1999, A&A, 352, 459 72, 73, 74

Chieffi, A., Straniero, O., & Salaris, M. 1991, in Astronomical Society of the Pacific Conference Series, Vol. 13, The Formation and Evolution of Star Clusters, ed. K. Janes, 219 97

Chiosi, C., Bertelli, G., & Bressan, A. 1992, ARA&A, 30, 235 94, 95

Christensen-Dalsgaard, J., Arentoft, T., Brown, T. M., et al. 2009, Communications in Asteroseismology, 158, 328 91

Cignoni, M., Degl'Innocenti, S., Prada Moroni, P. G., & Shore, S. N. 2006, A&A, 459, 783 92

Clark, J. P. A. & McClure, R. D. 1979, PASP, 91, 507 28, 29

Coelho, P., Barbuy, B., Meléndez, J., Schiavon, R. P., & Castilho, B. V. 2005, A&A, 443, 735 45

Colina, L. & Bohlin, R. C. 1994, AJ, 108, 1931 23

Colina, L., Bohlin, R. C., & Castelli, F. 1996, AJ, 112, 307 45, 46, 54, 55

da Silva, L., Girardi, L., Pasquini, L., et al. 2006, A&A, 458, 609 92

de Castro Milone, A., Sansom, A. E., & Sanchez-Blazquez, P. 2011, ArXiv e-prints xix, 65, 81, 82, 83, 144

de Jong, R. S., Chiappini, C., & Schnurr, O. 2012, Assembling the Puzzle of the Milky Way, Le Grand-Bornand, France, Edited by C. Reylé; A. Robin; M. Schultheis; EPJ Web of Conferences, Volume 19, id.09004, 19, 9004 145

De Simone, R., Wu, X., & Tremaine, S. 2004, MNRAS, 350, 627 139

Dehnen, W. 1998, AJ, 115, 2384 123

Dehnen, W. & Binney, J. J. 1998, MNRAS, 298, 387 124, 129, 131

Demarque, P., Woo, J.-H., Kim, Y.-C., & Yi, S. K. 2004, ApJS, 155, 667 81, 89, 94, 95, 96, 97, 100, 101, 102, 103, 104, 144

Dierickx, M., Klement, R., Rix, H.-W., & Liu, C. 2010, ApJL, 725, L186 141

Dotter, A., Chaboyer, B., Jevremović, D., et al. 2008, ApJS, 178, 89 94

Edvardsson, B. 2008, Physica Scripta Volume T, 133, 014011 xii, 45, 47

Edvardsson, B., Andersen, J., Gustafsson, B., et al. 1993, A&A, 275, 101 xix, 4, 5, 87, 115, 118, 137, 138, 144

Eggen, O. J. 1964, Royal Greenwich Observatory Bulletin, 84, 111 28

Englmaier, P., Pohl, M., & Bissantz, N. 2011, Memorie della Societa Astronomica Italiana Supplementi, 18, 199 3

Feltzing, S. & Bensby, T. 2009, in IAU Symposium, Vol. 258, IAU Symposium, ed. E. E. Mamajek, D. R. Soderblom, & R. F. G. Wyse, 23–30 119

Feltzing, S., Holmberg, J., & Hurley, J. R. 2001, A&A, 377, 911 xiii, 4, 6, 88, 89, 90, 92, 115, 120

Francois, P. & Matteucci, F. 1993, A&A, 280, 136 137

Freeman, K. 2011, ArXiv e-prints 3

Freeman, K. & Bland-Hawthorn, J. 2002, ARA&A, 40, 487 3

Freeman, K. C. 1991, in Dynamics of Disc Galaxies, ed. B. Sundelius, 15 131, 133

Freeman, K. C. 2010, in Galaxies and their Masks, ed. D. L. Block, K. C. Freeman, & I. Puerari, 319 145

Freytag, B. 2001, in Astronomical Society of the Pacific Conference Series, Vol. 223, 11th Cambridge Workshop on Cool Stars, Stellar Systems and the Sun, ed. R. J. Garcia Lopez, R. Rebolo, & M. R. Zapaterio Osorio, 785–+ 44

Friel, E. D., Janes, K. A., Tavarez, M., et al. 2002, AJ, 124, 2693 4, 112

Fuhrmann, K. 1998, A&A, 338, 161 84

Fuhrmann, K. 2008, MNRAS, 384, 173 3, 83, 118

Garnett, D. R. & Kobulnicky, H. A. 2000, ApJ, 532, 1192 4

Genzel, R. 2009, in IAU Symposium, Vol. 254, IAU Symposium, ed. J. Andersen, J. Bland-Hawthorn, & B. Nordström, 33–34 2

Gilmore, G. & Reid, N. 1983, MNRAS, 202, 1025 3, 118

Gilmore, G. & Wyse, R. F. G. 1991, ApJL, 367, L55 118

Girardi, L., Bressan, A., Bertelli, G., & Chiosi, C. 2000, A&AS, 141, 371 69, 75, 77, 79, 80, 88, 89, 94, 95, 96, 100, 101, 102, 103, 104, 144

Gomez, A. & Mennessier, M. O. 1977, A&A, 54, 113 128

Gratton, R., Carretta, E., Matteucci, F., & Sneden, C. 1996, in Astronomical Society of the Pacific Conference Series, Vol. 92, Formation of the Galactic Halo...Inside and Out, ed. H. L. Morrison & A. Sarajedini, 307 3, 118

Gratton, R. G., Carretta, E., Matteucci, F., & Sneden, C. 2000, A&A, 358, 671 125

Gray, D. F. 2008, The Observation and Analysis of Stellar Photospheres, ed. D. F. Gray 49

Gray, D. F. & Toner, C. G. 1987, ApJ, 322, 360 48

Gregg, M. D., Silva, D., Rayner, J., et al. 2004, in Bulletin of the American Astronomical Society, Vol. 36, American Astronomical Society Meeting Abstracts, 1496–+ 53

Grevesse, N., Noels, A., & Sauval, A. J. 1993, A&A, 271, 587 96

Grevesse, N., Noels, A., & Sauval, A. J. 1996, in Astronomical Society of the Pacific Conference Series, Vol. 99, Cosmic Abundances, ed. S. S. Holt & G. Sonneborn, 117 96

Grevesse, N. & Sauval, A. J. 1998, Space Sci. Rev., 85, 161 48

Guedes, J., Callegari, S., Madau, P., & Mayer, L. 2011, ApJ, 742, 76 2

Gustafsson, B., Bell, R. A., Eriksson, K., & Nordlund, A. 1975, A&A, 42, 407 80

Gustafsson, B., Edvardsson, B., Eriksson, K., et al. 2008, A&A, 486, 951 39, 44

Hamuy, M., Suntzeff, N. B., Heathcote, S. R., et al. 1994, PASP, 106, 566 15, 23, 24

Hänninen, J. & Flynn, C. 2002, MNRAS, 337, 731 139

Hayes, D. S. 1985, in IAU Symposium, Vol. 111, Calibration of Fundamental Stellar Quantities, ed. D. S. Hayes, L. E. Pasinetti, & A. G. D. Philip, 225–249 24

Hayes, D. S. & Latham, D. W. 1975, ApJ, 197, 593 24

Haywood, M. 2006, MNRAS, 371, 1760 5, 6, 108

Haywood, M. 2008, MNRAS, 388, 1175 116, 127

Hoffleit, D. 1964, Catalogue of bright stars, ed. Hoffleit, D. 28

Høg, E., Fabricius, C., Makarov, V. V., et al. 2000, A&A, 355, L27 122

Holmberg, J., Nordström, B., & Andersen, J. 2007, A&A, 475, 519 5, 10, 11, 88, 89, 92, 123, 136

Holmberg, J., Nordström, B., & Andersen, J. 2009, A&A, 501, 941 xiii, 5, 88, 120, 123

Horne, K. 1986, PASP, 98, 609 21

House, E. L., Brook, C. B., Gibson, B. K., et al. 2011, MNRAS, 415, 2652 7, 131, 140

Hu, J. & Jiang, B. 2005, in American Institute of Physics Conference Series, Vol. 752, Stellar Astrophysics with the World's Largest Telescopes, ed. J. Mikolajewska & A. Olech, 84–87 145

Ibata, R. A., Gilmore, G., & Irwin, M. J. 1994, Nature, 370, 194 140

Ibukiyama, A. & Arimoto, N. 2002, A&A, 394, 927 4, 5, 115

Iglesias, C. A. & Rogers, F. J. 1993, ApJ, 412, 752 96

Iglesias, C. A., Rogers, F. J., & Wilson, B. G. 1992, ApJ, 397, 717 95

Jehin, E., Bagnulo, S., Melo, C., Ledoux, C., & Cabanac, R. 2005, in IAU Symposium, Vol. 228, From Lithium to Uranium: Elemental Tracers of Early Cosmic Evolution, ed. V. Hill, P. François, & F. Primas, 261–262 53

Jenkins, A. 1992, MNRAS, 257, 620 140

Jenkins, A. & Binney, J. 1990, MNRAS, 245, 305 139, 140

Jimenez, R., Flynn, C., MacDonald, J., & Gibson, B. K. 2003, Science, 299, 1552 95

Johnson, D. R. H. & Soderblom, D. R. 1987, AJ, 93, 864 123

Jørgensen, B. R. & Lindegren, L. 2005, A&A, 436, 127 88, 89, 92

Joshi, Y. C. 2007, MNRAS, 378, 768 73

Karataş, Y., Bilir, S., & Schuster, W. J. 2005, MNRAS, 360, 1345 88

Katz, D., Soubiran, C., Cayrel, R., Adda, M., & Cautain, R. 1998, A&A, 338, 151 53, 80

Keller, S. C., Schmidt, B. P., Bessell, M. S., et al. 2007, Publications of the Astronomical Society of Australia, 24, 1 12

Kim, Y.-C., Demarque, P., Yi, S. K., & Alexander, D. R. 2002, ApJS, 143, 499 96, 97, 98, 104

Klypin, A., Zhao, H., & Somerville, R. S. 2002, ApJ, 573, 597 2

Knox, R. A., Hawkins, M. R. S., & Hambly, N. C. 1999, MNRAS, 306, 736 119

Kroupa, P. 2002, MNRAS, 330, 707 141

Kurtz, M. J. & Mink, D. J. 1998, PASP, 110, 934 38, 39

Kurucz, R. 1999, H2O linelist from Partridge and Schwenke (1997), part 1 of 2. Kurucz CD-ROM No. 25. Cambridge, Mass.: Smithsonian Astrophysical Observatory, 1999., 25 48

Kurucz, R. L. 1979, ApJS, 40, 1 45

Kurucz, R. L. 1992a, , 23, 45 48

Kurucz, R. L. 1992b, in IAU Symposium, Vol. 149, The Stellar Populations of Galaxies, ed. B. Barbuy & A. Renzini, 225–+ 80, 95, 96

Kurucz, R. L. & Avrett, E. H. 1981, SAO Special Report, 391 47

Lacey, C. G. 1984, MNRAS, 208, 687 6, 131, 139, 140

Lachaume, R., Dominik, C., Lanz, T., & Habing, H. J. 1999, A&A, 348, 897 99

Lagache, G., Abergel, A., Boulanger, F., & Puget, J.-L. 1998, A&A, 333, 709 72

Lamers, H. J. G. L. M., Gieles, M., Bastian, N., et al. 2005, A&A, 441, 117 114

Le Borgne, J.-F., Bruzual, G., Pelló, R., et al. 2003, A&A, 402, 433 53

Lebreton, Y., Fernandes, J., & Lejeune, T. 2001, A&A, 374, 540 103, 109

Lebreton, Y. & Montalbán, J. 2009, in IAU Symposium, Vol. 258, IAU Symposium, ed. E. E. Mamajek, D. R. Soderblom, & R. F. G. Wyse, 419–430 145

Lee, Y. S., Beers, T. C., An, D., et al. 2011, ApJ, 738, 187 127

Leggett, S. K., Ruiz, M. T., & Bergeron, P. 1998, ApJ, 497, 294 119

Lejeune, T. & Schaerer, D. 2001, A&A, 366, 538 94

Lemasle, B., François, P., Piersimoni, A., et al. 2008, A&A, 490, 613 3

Lobel, A. 2008, Journal of Physics Conference Series, 130, 012015 50

Loebman, S. R., Roškar, R., Debattista, V. P., et al. 2011, ApJ, 737, 8 138

Luck, R. E., Kovtyukh, V. V., & Andrievsky, S. M. 2006, AJ, 132, 902 3

Maeder, A. 1976, A&A, 47, 389 89

Magic, Z., Serenelli, A., Weiss, A., & Chaboyer, B. 2010, ApJ, 718, 1378 103

Maíz-Apellániz, J. 2001, AJ, 121, 2737 73

Martins, L. P. & Coelho, P. 2007, MNRAS, 381, 1329 45

Martins, L. P., González Delgado, R. M., Leitherer, C., Cerviño, M., & Hauschildt, P. 2005, MNRAS, 358, 49 45

Mayor, M. 1974, A&A, 32, 321 131

Mayor, M. 1985, in Stellar Radial Velocities, ed. A. G. D. Philip & D. W. Latham, 35–48 123

McClure, R. D. 1976, AJ, 81, 182 29

McClure, R. D. & Forrester, W. T. 1981, Publications of the Dominion Astrophysical Observatory Victoria, 15, 439 xi, 28, 29, 30, 31, 32, 33, 34

McClure, R. D. & van den Bergh, S. 1968, AJ, 73, 313 28

Meibom, S., Grundahl, F., Clausen, J. V., et al. 2009, AJ, 137, 5086 103

Mermilliod, J. C. & Nitschelm, C. 1989, A&AS, 81, 401 xi, 32, 33

Meusinger, H., Stecklum, B., & Reimann, H.-G. 1991, A&A, 245, 57 4, 5, 131

Mignard, F. 2000, A&A, 354, 522 134

Mihalas, D. 1978, Stellar Atmospheres (A Series of books in astronomy and astrophysics) (W H Freeman & Co (Sd)) 40

Mihalas, D., Auer, L. H., & Mihalas, B. R. 1978, ApJ, 220, 1001 43

Minchev, I. & Famaey, B. 2010, ApJ, 722, 112 138

Minchev, I. & Quillen, A. C. 2006, MNRAS, 368, 623 6, 131, 139

Mo, H. J., Mao, S., & White, S. D. M. 1998, MNRAS, 295, 319 2

Mortara, L. & Fowler, A. 1981, in Society of Photo-Optical Instrumentation Engineers (SPIE) Conference Series, Vol. 290, Society of Photo-Optical Instrumentation Engineers (SPIE) Conference Series, 28–+ 15

Mowlavi, N., Schaerer, D., Meynet, G., et al. 1998, A&AS, 128, 471 94

Munari, U., Sordo, R., Castelli, F., & Zwitter, T. 2005, A&A, 442, 1127 xii, 7, 38, 45, 46, 47, 48, 66, 68, 69, 74, 81

Nakanishi, H. & Sofue, Y. 2006, PASJ, 58, 847 3

Navarro, J. F., Abadi, M. G., Venn, K. A., Freeman, K. C., & Anguiano, B. 2011, MNRAS, 412, 1203 3, 84, 125, 126, 127, 144

Navarro, J. F. & Benz, W. 1991, ApJ, 380, 320 2

Navarro, J. F., Frenk, C. S., & White, S. D. M. 1997, ApJ, 490, 493 2

Newberg, H. J., Yanny, B., Rockosi, C., et al. 2002, ApJ, 569, 245 140

Ng, Y. K. & Bertelli, G. 1998, A&A, 329, 943 4, 138

Nissen, P. E., Edvardsson, B., & Gustafsson, B. 1985, in European Southern Observatory Conference and Workshop Proceedings, Vol. 21, European Southern Observatory Conference and Workshop Proceedings, ed. I. J. Danziger, F. Matteucci, & K. Kjar, 131–147 4

Nordlund, A. & Dravins, D. 1990, A&A, 228, 155 44

Nordström, B., Mayor, M., Andersen, J., et al. 2004, A&A, 418, 989 xix, 5, 6, 10, 87, 88, 89, 94, 103, 120, 123, 131, 144

Oke, J. B. 1990, AJ, 99, 1621 15, 23

Pace, G. & Pasquini, L. 2004, A&A, 426, 1021 87

Pagel, B. E. J. 1989, in Evolutionary Phenomena in Galaxies, ed. J. E. Beckman & B. E. J. Pagel, 201–223 95

Pardi, M. C., Ferrini, F., & Matteucci, F. 1995, ApJ, 444, 207 137

Payne, P. 1985, Proceedings of the Astronomical Society of Australia, 6, 182 12, 13

Perryman, M. A. C. 2005, in Astronomical Society of the Pacific Conference Series, Vol. 338, Astrometry in the Age of the Next Generation of Large Telescopes, ed. P. K. Seidelmann & A. K. B. Monet, 3 145

Perryman, M. A. C. & ESA, eds. 1997, ESA Special Publication, Vol. 1200, The HIPPARCOS and TYCHO catalogues. Astrometric and photometric star catalogues derived from the ESA HIPPARCOS Space Astrometry Mission 73, 122

Pettini, M. 2009, in IAU Symposium, Vol. 254, IAU Symposium, ed. J. Andersen, J. Bland-Hawthorn, & B. Nordström, 21–32 2

Pietrinferni, A., Cassisi, S., Salaris, M., & Castelli, F. 2004, ApJ, 612, 168 103, 107

Pilyugin, L. S. & Edmunds, M. G. 1996, A&A, 313, 792 137

Plez, B., Brett, J. M., & Nordlund, A. 1992, A&A, 256, 551 44

Pols, O. R., Schroder, K.-P., Hurley, J. R., Tout, C. A., & Eggleton, P. P. 1998, MNRAS, 298, 525 88

Pont, F. & Eyer, L. 2004, MNRAS, 351, 487 89, 92, 94, 99, 102, 107, 116, 121, 138

Press, W. H. 1993, Science, 259, 1931 61, 66

Prochaska, J. X., Naumov, S. O., Carney, B. W., McWilliam, A., & Wolfe, A. M. 2000, AJ, 120, 2513 118

Prugniel, P. & Soubiran, C. 2001, A&A, 369, 1048 45, 53, 54

Prugniel, P., Vauglin, I., & Koleva, M. 2011, A&A, 531, A165+ 54, 55, 56, 57, 81

Quillen, A. C. & Garnett, D. R. 2001, in Astronomical Society of the Pacific Conference Series, Vol. 230, Galaxy Disks and Disk Galaxies, ed. J. G. Funes & E. M. Corsini, 87–88 6, 131, 133

Raiteri, C. M., Villata, M., & Navarro, J. F. 1996, A&A, 315, 105 116

Ramírez, I., Allende Prieto, C., & Lambert, D. L. 2007, A&A, 465, 271 104

Reddy, B. E., Lambert, D. L., & Allende Prieto, C. 2006, MNRAS, 367, 1329 83, 84

Reddy, B. E., Tomkin, J., Lambert, D. L., & Allende Prieto, C. 2003, MNRAS, 340, 304 xii, 78, 79, 80, 99

Robin, A. C., Reylé, C., Derrière, S., & Picaud, S. 2003, A&A, 409, 523 132

Rocha-Pinto, H. J., Flynn, C., Scalo, J., et al. 2004, A&A, 423, 517 131, 140

Rocha-Pinto, H. J. & Maciel, W. J. 1998, MNRAS, 298, 332 xiii, 5, 89, 90, 92

Rocha-Pinto, H. J., Maciel, W. J., Scalo, J., & Flynn, C. 2000a, A&A, 358, 850 5, 87, 91, 93, 116, 138

Rocha-Pinto, H. J., Majewski, S. R., Skrutskie, M. F., & Crane, J. D. 2003, ApJL, 594, L115 140

Rocha-Pinto, H. J., Scalo, J., Maciel, W. J., & Flynn, C. 2000b, ApJL, 531, L115 92

Rodgers, A. W., Conroy, P., & Bloxham, G. 1988, PASP, 100, 626 13

Rogers, F. J., Swenson, F. J., & Iglesias, C. A. 1996, ApJ, 456, 902 96

Roman, N. G. 1950, ApJ, 112, 554 6

Roškar, R., Debattista, V. P., Quinn, T. R., Stinson, G. S., & Wadsley, J. 2008, ApJL, 684, L79 116, 138

Royer, F., Grenier, S., Baylac, M.-O., Gómez, A. E., & Zorec, J. 2002, A&A, 393, 897 48

Salaris, M., Chieffi, A., & Straniero, O. 1993, ApJ, 414, 580 97

Salasnich, B., Girardi, L., Weiss, A., & Chiosi, C. 2000, A&A, 361, 1023 80, 88, 94, 96

Sánchez-Blázquez, P., Peletier, R. F., Jiménez-Vicente, J., et al. 2006, MNRAS, 371, 703 7, 45, 47, 53, 75

Sandage, A. 1972, ApJ, 178, 1 73

Scalo, J. M. 1987, in Starbursts and Galaxy Evolution, ed. T. X. Thuan, T. Montmerle, & J. Tran Thanh van, 445–465 92

Scannapieco, C., Tissera, P. B., White, S. D. M., & Springel, V. 2008, MNRAS, 389, 1137 2

Schlegel, D. J., Finkbeiner, D. P., & Davis, M. 1998, ApJ, 500, 525 66, 72

Schönberg, M. & Chandrasekhar, S. 1942, ApJ, 96, 161 93

Schönrich, R. & Binney, J. 2009a, MNRAS, 396, 203 138, 139, 144

Schönrich, R. & Binney, J. 2009b, MNRAS, 399, 1145 141

Schultz, G. V. & Wiemer, W. 1975, A&A, 43, 133 71

Schuster, W. J., Moreno, E., Nissen, P. E., & Pichardo, B. 2011, ArXiv e-prints 103

Schwenke, D. W. 1998, Faraday Discussions, 109, 321 48

Seabroke, G. M. & Gilmore, G. 2007, MNRAS, 380, 1348 131, 134

Seaton, M. J., Yan, Y., Mihalas, D., & Pradhan, A. K. 1994, MNRAS, 266, 805 44

Sellwood, J. A. & Binney, J. J. 2002, MNRAS, 336, 785 116, 138

Sellwood, J. A. & Carlberg, R. G. 1984, ApJ, 282, 61 6, 131

Siebert, A., Williams, M. E. K., Siviero, A., et al. 2011, AJ, 141, 187 7, 11, 81, 123

Skuljan, J., Hearnshaw, J. B., & Cottrell, P. L. 1999, MNRAS, 308, 731 123

Soderblom, D. R. 1982, ApJ, 263, 239 48

Soderblom, D. R. 2010, ARA&A, 48, 581 89, 91

Soderblom, D. R., Duncan, D. K., & Johnson, D. R. H. 1991, ApJ, 375, 722 89

Soubiran, C., Bienaymé, O., Mishenina, T. V., & Kovtyukh, V. V. 2008, A&A, 480, 91 6, 87, 116, 131, 133, 134, 138

Soubiran, C. & Girard, P. 2005, A&A, 438, 139 125

Soubiran, C., Katz, D., & Cayrel, R. 1998, A&AS, 133, 221 53, 103

Soubiran, C., Le Campion, J.-F., Cayrel de Strobel, G., & Caillo, A. 2010, A&A, 515, A111+ 79

Sousa, S. G., Santos, N. C., Mayor, M., et al. 2008, A&A, 487, 373 80

Spitzer, L. 1978, Physical processes in the interstellar medium, ed. Spitzer, L. 73

Spitzer, Jr., L. & Schwarzschild, M. 1953, ApJ, 118, 106 140

Stein, R. F. & Nordlund, A. 1998, ApJ, 499, 914 44

Steinmetz, M. & Muller, E. 1995, MNRAS, 276, 549 2

Steinmetz, M., Zwitter, T., Siebert, A., et al. 2006, AJ, 132, 1645 7, 11, 122, 123

Stempels, H. C., Piskunov, N., & Barklem, P. S. 2001, in Astronomical Society of the Pacific Conference Series, Vol. 223, 11th Cambridge Workshop on Cool Stars, Stellar Systems and the Sun, ed. R. J. Garcia Lopez, R. Rebolo, & M. R. Zapaterio Osorio, 878–+ 44

Stewart, K. R., Bullock, J. S., Wechsler, R. H., Maller, A. H., & Zentner, A. R. 2008, ApJ, 683, 597 2

Stix, M. 2004, The sun : an introduction, ed. Stix, M. 45

Stone, R. P. S. 1977, ApJ, 218, 767 24

Stone, R. P. S. & Baldwin, J. A. 1983, MNRAS, 204, 347 24

Strömberg, G. 1930, ApJ, 71, 175 93

Strömgren, B. 1963, QJRAS, 4, 8 80

Stromgren, B. 1987, in NATO ASIC Proc. 207: The Galaxy, ed. G. Gilmore & B. Carswell, 229–246 6, 125, 131, 133

Takeda, Y. 2007, PASJ, 59, 335 xiii, 88, 89, 90

Taylor, B. J. 1984, ApJS, 54, 259 24

Taylor, J. E. & Babul, A. 2001, ApJ, 559, 716 140

Thorén, P., Edvardsson, B., & Gustafsson, B. 2004, A&A, 425, 187 8, 91

Thuillier, G., Floyd, L., Woods, T. N., et al. 2004, Advances in Space Research, 34, 256 46, 47

Tonry, J. & Davis, M. 1979, AJ, 84, 1511 xi, 38, 39

Torra, J., Fernández, D., & Figueras, F. 2000, A&A, 359, 82 136

Toth, G. & Ostriker, J. P. 1992, ApJ, 389, 5 7, 131

Tripicco, M. J. & Bell, R. A. 1991, AJ, 102, 744 31

Twarog, B. A. 1980, ApJ, 242, 242 4, 5, 88, 92

Valdes, F., Gupta, R., Rose, J. A., Singh, H. P., & Bell, D. J. 2004, ApJS, 152, 251 45, 53

Valenti, J. A. & Fischer, D. A. 2005, ApJS, 159, 141 xiii, 80, 88, 89, 91

van Leeuwen, F. 2007, A&A, 474, 653 122

Vande Putte, D., Garnier, T. P., Ferreras, I., Mignani, R. P., & Cropper, M. 2010, MNRAS, 407, 2109 112, 113, 135

VandenBerg, D. A. 2000, ApJS, 129, 315 97, 98

Vandenberg, D. A. & Bell, R. A. 1985, ApJS, 58, 561 89

Velazquez, H. & White, S. D. M. 1999, MNRAS, 304, 254 7, 131, 140

Veltz, L., Bienaymé, O., Freeman, K. C., et al. 2008, A&A, 480, 753 125, 133

Venn, K. A., Irwin, M., Shetrone, M. D., et al. 2004, AJ, 128, 1177 xix, 82, 83, 125, 126, 144

Villalobos, Á. & Helmi, A. 2008, MNRAS, 391, 1806 7, 131, 140

Wall, J. V. & Jenkins, C. R. 2003, Practical Statistics for Astronomers, ed. Wall, J. V. & Jenkins, C. R. 66

White, S. D. M. 2009, in IAU Symposium, Vol. 254, IAU Symposium, ed. J. Andersen, J. Bland-Hawthorn, & B. Nordström, 19–20 2

Wielen, R. 1974, Highlights of Astronomy, 3, 395 131

Wielen, R. 1977, A&A, 60, 263 6, 115, 116, 131, 136, 137

Wielen, R., Dettbarn, C., Fuchs, B., Jahreiss, H., & Radons, G. 1992, in IAU Symposium, Vol. 149, The Stellar Populations of Galaxies, ed. B. Barbuy & A. Renzini, 81–92 137

Wielen, R., Fuchs, B., & Dettbarn, C. 1996, A&A, 314, 438 138

Williams, M. E. K., Freeman, K. C., Helmi, A., & the RAVE collaboration. 2009, in IAU Symposium, Vol. 254, IAU Symposium, ed. J. Andersen, J. Bland-Hawthorn, & B. Nordström, 139–144 123

Williams, M. E. K., Steinmetz, M., Sharma, S., et al. 2011, ApJ, 728, 102 140

Wilson, M. L., Helmi, A., Morrison, H. L., et al. 2011, MNRAS, 413, 2235 141

Wood, P. R. 1979, ApJ, 227, 220 44

Wood, P. R., Rodgers, A. W., & Russell, K. S. 1995, Publications of the Astronomical Society of Australia, 12, 97 12

Worthey, G. & Lee, H.-c. 2011, ApJS, 193, 1 45

Wyse, R. F. G. 2009a, in IAU Symposium, Vol. 254, IAU Symposium, ed. J. Andersen, J. Bland-Hawthorn, & B. Nordström, 179–190 2, 3, 119

Wyse, R. F. G. 2009b, in IAU Symposium, Vol. 258, IAU Symposium, ed. E. E. Mamajek, D. R. Soderblom, & R. F. G. Wyse, 11–22 2

Yasutomi, M. & Fujimoto, M. 1991, PASJ, 43, 9 140

Yi, S., Demarque, P., Kim, Y.-C., et al. 2001, ApJS, 136, 417 96

Yi, S. K., Kim, Y.-C., & Demarque, P. 2003, ApJS, 144, 259 96

Zwitter, T., Castelli, F., & Munari, U. 2004, A&A, 417, 1055 66

Zwitter, T., Matijevič, G., Breddels, M. A., et al. 2010, A&A, 522, A54+ 73, 122

Zwitter, T., Siebert, A., Munari, U., et al. 2008, AJ, 136, 421 7, 11, 123

Acknowledgments

I would like to extend warm thanks to Prof. Ken Freeman and Prof. Matthias Steinmetz that with absolute respect have been helping and supporting me in this thesis. I would also express my thanks to those people that with their real love have made this thesis something real. Especial thanks to the *Leibniz Institute for Astrophysics Potsdam*, the *University of Potsdam* and the *Milky Way and the Local Volume* group. Many thanks also go to *Mount Stromlo and Siding Spring Observatory.*

26.03.2012 Potsdam

Borja Anguiano

Selbstständigkeitserklärung

Hiermit versichere ich, dass ich die vorliegende Arbeit selbstständig verfasst und keine anderen als die im Literaturverzeichnis angegebenen Quellen und Hilfsmittel benutzt habe. Die Arbeit wurde an keiner weiteren Universität eingereicht.

Borja Anguiano